Characterizing Real-life Graphene through the Latest First-principles Methodological Developments

Lucía Rodrigo Insausti

Prof. Rubén Pérez Pérez and Dr. Pablo Pou Bell Supervisors

Departamento de Física Teórica de la Materia Condensada

Universidad Autónoma de Madrid

This dissertation is submitted for the degree of

Doctor en Física

Facultad de Ciencias March 2016

TABLE OF CONTENTS

RESUMEN

¿Sigue habiendo esperanzas para una tecnología basada en grafeno?

El grafeno ha suscitado mucho interés en los últimos años. Su síntesis en un laboratorio de Manchester por Novoselov y Geim fue el pistoletazo de salida hacia la carrera por controlar sus extraordinarias propiedades debidas a su naturaleza bidimensional y la dispersión lineal de sus estados electrónicos alrededor del nivel de Fermi. Trás la alegría inicial de la comunidad científica, algunas voces decepcionadas clamaban que el grafeno no era tan especial como se esperaba. Un ejemplo paradigmático de ello, aunque no es objeto de estudio en esta tesis, es la ausencia de una banda prohibida, necesaria para su aplicación como sustitutivo del silicio en transistores tradicionales.

Hay que tener en cuenta que las propiedades del grafeno prístino son muy diferentes de las que podemos encontrar en una muestra común en el laboratorio. En un entorno realista hay que contar con cómo este material se ve afectado por defectos o distorsiones de la red, cómo se comporta en la cercanía de bordes o contactos con otros materiales o cómo afecta el sustrato en el que se ha crecido a sus propiedades. Estos y otros medios de alterar las propiedades del grafeno ideal, lejos de ser un obstáculo o inconveniente, representan una oportunidad de modular espacialmente sus propiedades electrónicas y de ajustar su respuesta mecánica. Con esta idea en mente, en esta tesis: (i) caracterizamos los contactos entre grafeno y platino que aparecen naturalmente en los escalones de este metal al crecer grafeno en su superficie, (ii) estudiamos la influencia tanto en las propiedades magnéticas como mecánicas de la presencia de defectos puntuales en grafeno y, finalmente, (iii) analizamos el mecanismo de formación de monocapas autoensambladas (*SAMs*) de moléculas sencillas en grafeno –sistemas poco interactuantes– a través del balance energético entre las interacciones molécula-sustrato e intermolecular. Para ello, en esta tesis se han realizado cálculos de de primeros principios basados en la teoría del funcional de la densidad (*DFT*) en estas tres líneas de investigación que a continuación describimos con más detalle.

En la primera de ellas, aprovechamos los primeros experimentos, realizados con microscopía de efecto túnel (*STM*), que consiguen información a escala atómica sobre la caracterización de la estructura de contactos metal-grafeno en escalones de Pt(111) para estudiar sus propiedades. La combinacion de teoría y experimento nos permite identificar un estado electrónico asociado al borde del grafeno y que está localizado en una de las subredes de grafeno que aparece justo en el contacto. Además analizamos la estructura de ese contacto y, en particular, como se modifican los estados de borde del grafeno por la presencia del metal sobreviviendo al contacto y transmitiéndose incluso a la primera fila de átomos del metal. También estudiamos como la estructura de la interfase entre el grafeno y el metal está relacionada con la frecuencia con la que ciertos patrones de Moiré se encuentran en los experimentos, demostrando que no sólo influye la estabilidad intrínseca que dicta el *mismatch* entre redes sino también qué geometría u orientación fomentan los escalones de metal que es donde principalmente comienza la nucleación de la lámina de grafeno. Con este estudio hemos contribuido a entender las propiedades de los contactos entre grafeno y metales cuya caracterización es imprescindible para el desarrollo de tecnologías de precisión atómica basadas en el grafeno.

En segundo lugar estudiamos las propiedades tanto mecánicas como electrónicas de monovacantes en grafeno a través de simulaciones *ab initio* de gran escala. Desde el punto de vista electrónico, experimentalmente se había observado que las láminas de grafeno tienen propiedades magnéticas. Teóricamente se predijo que las monovacantes podían ser la explicación de ese magnetismo inducido en el grafeno, pero no estaba bien entendido el tipo de magnetismo que producen. En la literatura había controversia entre varios trabajos teóricos que predecían distintos valores para el momento magnético inducido por una monovacante que ni siquiera las evidencias experimentales habían sido capaces de dilucidar. Mientras que cálculos *DFT* basados en *clusters* predecían un valor de 2 μ_B, cálculos análogos en sistemas extendidos afirmaban que era 1 μ_B. Nuestros cálculos en sistemas extendidos con tamaños de celda de hasta $G(30\times30)$ para los cuales se emplearon mallas de varios miles de puntos k –lo que convierte este problema en un reto computacional hasta ahora no atacado– muestran una clara convergencia del momento magnético local inducido por una pequeña concentración de vacantes –límite diluido– a un valor de 2 μ_B que resuelve las discrepancias previas de la literatura. En cuanto a las propiedades mecánicas, hay evidencias experimentales que afirman que se produciría un incremento inesperado de la rigidez del grafeno en presencia de una baja concentración de vacantes. Sin embargo, no existía aún un argumento atomístico y fundamental que apoyara estos resultados. Gracias a nuestros cálculos concluímos que, incluso cuando la presencia de monovacantes prácticamente no afecta a las deformaciones dentro del

plano, sí que inducen un campo de tensiones que claramente amortigua las vibraciones fuera del plano, haciendo que una muestra con defectos sea más rígida que su versión prístina incluso a temperatura ambiente. Por tanto, esto no sólo afectaría a la rigidez sino también otras propiedades mecánicas que dependan de las fluctuaciones.

Por último se estudia la formación de *SAMs* en sistemas débilmente interaccionantes. Hemos estudiado el sistema más sencillo que permite la formación de *SAMs* –debido a la presencia de puentes de hidrógeno– sobre un sustrato débilmente interaccionante. En particular analizamos monocapas de 1,3,5-Triacina sobre grafito y sobre G/Pt(111) mediante una exhaustiva caracterización teórica que se apoya en evidencias experimentales. En ambos casos los experimentos con *STM* muestran grandes islas de moléculas que forman patrones de Moiré. Sin embargo, por efecto del sustrato sobre el que el grafeno está crecido, tanto las barreras de difusión de las moléculas como la distancia entre ellas cambia. Gracias a esta información experimental, hemos podido entender bien cómo está controlado el balance energético entre la adsorción de las moléculas en el sustrato, para la que serán importantes la atracción debida a van der Waals y repulsión de Pauli; y la interacción intermolecular entre ellas, que está mediada por puentes de hidrógeno y van der Waals. En nuestros cálculos *DFT* hemos explorado los límites de precisión de las técnicas actuales usando tanto diferentes funcionales –PBE estándar e híbridos– como distintas implementaciones de fuerzas dispersivas para modelizar el sistema. Además hemos tenido que desarrollar una metodología que nos permitiera caracterizar cada interacción dado que, debido al gran tamaño de los Moirés experimentales, una simulación directa del sistema era computacionalmente inalcanzable. De nuestro estudio concluimos que, aunque la interacción con el sustrato mediada por los orbitales π es débil, aún así es suficientemente alta como para determinar cual es la orientación relativa de las moléculas con respecto al sustrato. Sin embargo, tenemos unas discrepancias en las barreras de disfusión que salen sistemáticamente más bajas que en los experimentos, además de con las diferencias que genera el cambio de sustrato. Esta exhaustiva caracterización muestra las limitaciones teóricas que aparecen a la hora de describir estos sistemas débilmente interactuantes incluso haciendo uso de los métodos más vanguardistas. Por este motivo estos sistemas representan un buen test para el desarrollo de las de estas teorías.

Desde el punto de vista teórico, hay que destacar que trabajar sobre estos temas ha exigido llevar las técnicas de cálculo hasta el límite. Eran todos sistemas cuyo estudio venía acompañado de grandes retos para las simulaciones. Ya sea el caso de los escalones, en el que la falta de simetría del sistema precisa generar superceldas complejas que sean una buena descripción del problema y en el que hemos tenido que utilizar nuestro propio método de simulación de imágenes *STM* para reproducir los resultados experimentales;

o la caracterización de los defectos puntuales, que ha requerido celdas de tamaños no antes alcanzados para este tipo de sistemas y un número de puntos k inusitadamente alto incluso para los tamaños más grandes de celda; hasta el estudio del crecimiento de *SAMs* en grafeno, para el que hemos explorado las últimas implementaciones de fuerzas dispersivas, imprescindibles en el cálculo, y alcanzado precisiones del orden del meV/molécula en las energías; estos problemas son un gran reto teórico de gran complejidad.

En resumen, este conjunto de estudios son una contribución en la búsqueda de los métodos que nos permitirán controlar y modificar las propiedades del grafeno. Se trata de trabajos con doble utilidad. Desde el punto de vista del objeto de estudio, hemos caracterizado cómo cambian las propiedades del grafeno a través de la interacción con otros materiales o la deformación de su red bidimensional ideal. Por otra parte, en relación con las técnicas de cálculo utilizadas, hemos puesto a prueba los últimos avances en métodos de simulación para los que este tipo de análisis en sistemas realistas resultan muy útiles de cara a continuar con su desarrollo.

ABSTRACT

Is there still hope for graphene-based technologies? Looking at real, defective graphene.

Graphene has attracted a lot of interest in the last few years. Its first synthesis on a laboratory in Manchester by Novoselov and Geim was the starting pistol for a race towards controlling the extraordinary properties associated with its bidimensional structure and the linear dispersion of its electronic states around the Fermi level. After the initial joy of the scientific community, some disappointed voices started to arise claiming that graphene was not as promising as expected. A paradigmatic example of the problems to apply it as a replacement for silicon in traditional transistors, although not directly related with the content of this thesis, is the absence of a band gap.

The properties of pristine graphene are very different to those of common samples found in the laboratory. In a realistic environment, one has to take into account how this material is affected by defects and structural distortions, how the electronic properties change near edges or interfaces with other materials, and what is the influence of the substrate on which graphene is grown. These modifications, far from being an obstacle or a disadvantage, represent an opportunity to spatially tune its electronic properties and to control its mechanical response. This is the route that we follow in this thesis, where we (i) characterize the graphene-platinum contacts that appear naturally on the metal steps during graphene growth, (ii) study the influence, both in the magnetic and mechanical properties, of the presence of point defects in graphene and, finally, (iii) analyze the formation mechanisms of self-assembled molecular layers (SAMs) of a simple molecule, triazine, on different graphene-based substrates, addressing how subtle differences in the molecule-substrate interaction determine the final Moiré periodicity. To this end, we have performed first principle calculations based in density functional theory (DFT) for these three research lines as described below.

In the case of graphene-platinum contacts, we take advantage of the first experiments, performed with scanning tunneling microscopy (STM), which obtain atomic-scale resolu-

tion on metal-graphene contacts at Pt(111) steps. Using the lateral periodicity revealed by the experiments as an input, we determine the structure of the contact and analyze how graphene edge states are modified by the presence of the metal and how they delocalize across the metal atoms in the contact. The combination of experiment and STM simulations beyond the usual Tersoff-Hamman approximation allows us to unveil the zig-zag graphene termination and the existence of an unoccupied electronic state that is mostly localized on the C-edge atoms of one particular graphene sublattice and the first row of metal atoms. The confinement in both energy and real space of this essentially 1D state makes it a suitable candidate for building multichannel nanowires. Our study of the metal-graphene interface structure has also implications for the frequency on which certain Moirés appear during graphene growth. We prove that, apart from the influence of the intrinsic stability dictated by the mismatch between the two lattices, the geometry and orientation favored by the metal steps –which is where the nucleation of the graphene sheet preferentially starts– also play an important role. With this study we have contributed to understand the properties of metal-graphene contacts, whose characterization is a necessary step for developing atomically precise graphene-based electronic applications.

Next, we study the electronic and mechanical properties of graphene in the presence of a low concentration of single-atom vacancies (monovacancies) through large scale *ab initio* simulations. Experiments support that the presence of these defects may confer magnetic properties to graphene. Theory predicted that magnetic moments associated to each of these monovacancies could be the explanation for this induced-magnetism, but the type of magnetism produced is still not well understood. There was controversy in the literature on the value for the local magnetic moment which the experimental evidences were unable to elucidate. While DFT calculations based on clusters predicted a value of 2 μ_B, similar calculations in extended systems claimed a 1 μ_B in the low-concentration limit. Our calculations on systems with up to a $G(30 \times 30)$ cell size and with several thousand k-point meshes –which make them a challenging computational problem– show a clear tendency to converge the local magnetic moment in the diluted limit to 2 μ_{B}. Regarding the mechanical properties, there is a growing experimental evidence that supports an unexpected increase of the graphene stiffness in the presence of a low concentration of monovacancies. Our calculations provide an atomistic, fundamental explanation that was still missing. We conclude that, even when the presence of monovacancies does not practically affect the in-plane deformations, they induce a strain field that clearly quenches the out-of-plane vibrations, making the defective sample stiffer than its pristine version for a low concentration of vacancies even at room temperature. This result has

implications not only for the stiffness of the sheet but also for many mechanical properties that depend strongly on the presence of these intrinsic out-of-plane fluctuations.

Finally, we study the formation of SAMs on weakly interacting substrates. We have considered the simplest aromatic molecule –1,3,5-Triazine (from now on referred simply as triazine), a benzene ring where three of the carbons are replaced by nitrogen atoms– that presents sizeable intermolecular interactions through the N-H hydrogen bonds. The formation of triazine SAMs on both graphite and G/Pt(111) has been characterized experimentally. STM experiments identify in both substrates large molecular islands showing a clear Moiré pattern. However, the Moire periodicity, the intermolecular distance and the molecular diffusion barriers depend on the substrate. We have performed an exhaustive theoretical characterization of the energy balance between molecule-substrate interaction –controlled by the interplay of the van der Waals (vdW) attraction and Pauli electronic repulsion–, and the intermolecular interaction mediated by vdW and hydrogen bonding. The large size of the experimental Moirés and the high precision needed in the energy convergence preclude a direct simulation of the triazine/substrate system. Therefore, we developed a methodology to characterize each interaction independently from calculations on smaller unit cells. Our simulations test the accuracy of state-of-the-art *ab initio* DFT methods, considering different exchange-correlation (XC) functionals (the standard PBE and hybrid functionals including a contribution from exact exchange) and several approaches to include vdW dispersive forces (from semi-empirical to recent many-body approaches). We conclude that, although the molecule-substrate interaction mediated by π orbitals is weak, it plays a key role in the determination of the molecular orientation with respect to the substrate. However, our results yield diffusion barriers that are systematically lower than in the experiments, and predict almost no difference between the two substrates, irrespective of the XC functional or vdW implementation used. These discrepancies highlight the limitations of current theoretical approaches to describe these weakly interacting systems and point them out as excellent test beds for the development of new methods.

As already hinted above, the theoretical methodology plays an important role in this thesis. Making progress on these problems has demanded to push the calculation techniques to their limit. All of the systems considered in this thesis represent a simulation challenge. Starting with the case of the G/Pt steps, the lack of symmetry imposed by the step and the need to simulate the graphene flake require the ingenious design of a complex, non-orthogonal supercell to make the simulations possible. The characterization of point defects called for cell sizes not previously achieved for such systems, and unusually dense k-point meshes even for the largest cells that we have managed to handle with an efficient,

well-parallelized local orbital code. The study of SAMs formation on graphene-based substrates rested upon the use of the most recent implementations to include dispersive forces implementations and demanded very stringent convergence parameters in order to reach an energy accuracy of the order of a meV/molecule in the energies.

In summary, this set of studies are a contribution in the search for methods to control and modify the properties of graphene. Its relevance is twofold. We have characterized how the properties of graphene can be tuned through the interaction with other materials or the presence of defects. On the other hand, we have shown how to apply the latest advances in simulation methods to these challenging systems. We believe that both our implementation and comprehensive tests will be useful in future studies dealing with other 2D materials in a realistic environment.

CHAPTER 1

GRAPHENE: THE FUTURE OF MATERIALS SCIENCE?

Graphene has emerged as a new material with a very bright future. Since its early days, graphene has attracted a great deal of attention due to its extraordinary properties as a real two-dimensional (2D) material. Even if it has come a long way since it was first isolated in 2004 [1], there is still a long road ahead until it becomes a commercial success story [2].

Its origin

Graphene, a one-atom thick carbon layer with an hexagonal lattice, was first isolated in 2004 by the group of K. Novoselov and A. K. Geim in Manchester by mechanical exfoliation of highly oriented pyrolytic graphite (HOPG), using a simple scotch tape for removing the topmost layers of a commercial HOPG sample [1]. The first proof of the Dirac fermion nature of electrons near the Fermi level [3] was provided with graphene obtained by this technique.

The original idea of working with HOPG was to see if it could be used as a transistor, the fundamental switching device at the heart of computing. They had almost given up with HOPG when they heard about how microscopy researchers used Scotch tape to clean the mineral and leave it free of involuntary contaminants before putting it under the lens. The inventive step was to look at the remains attached to the Scotch tape and to find a way of transferring the ultra-thin flakes of graphene from Scotch tape to a silicon wafer, the material of microprocessors. Once they did this, the extraordinary electrical properties of graphene could be witnessed and explored, proving the existence of the first purely 2D system.

However, graphene had already been isolated long before that, in 1859, by means of graphite oxidation [4]. Today we know that, what B. Brodie then called *graphon* and thought to be a new form of carbon with a molecular weight of 33, were tiny crystals of graphene oxide (GO). A century after B. Brodie experiments, the study of dried graphite

oxide droplets by means of transmission electron microscopy (TEM) was started by G. Ruess and F. Vogt[5] and continued by U. Hofmann's group[6,7]. In 1962[7] he and H. P. Boehm identified some of the thinnest possible fragments as monolayers. Furthermore, it was H. P. Boehm and his collegues[8] who, in 1986, introduced the term *graphene*, deriving it from the word *graphite* and the suffix *-ene* that refers to polycyclic aromatic hydrocarbons. The strong dependence of the TEM contrast with the focusing conditions cast some doubts about those studies which made this remarkable observations to receive little attention. Thank to some new developments of this experimental technique, they were finally unambiguously identified in TEM by counting the number of folding lines in the early 2000s[9–11]. However, these studies had to wait until the graphene electronic properties were experimentally described[1,3,12–14] to become relevant. Since graphene was discovered, thousands of scientific papers have been devoted to the topic.

The material of the future

Graphene is nowadays one of the most promising materials of this nanotechnological era. It was the last of the carbon allotropes to be synthesized, and the first pure 2D material ever isolated. Its unique physicochemical properties have attracted a huge attention, not only among the scientific community but also in the industrial sector which is interested on its many potential applications. These excellent properties are a direct consequence of the combination of its dimensionality, the particular honeycomb symmetry of the lattice and also the nature of its bonds –sp^2 hybridized covalent bonds (σ band) which accommodate three of the valence electrons, while the forth one is hosted in p_z orbitals (forming the π and π^* bands)–. Some of graphene's properties are a consequence of its 2D nature (transparency, flexibility) while other properties are due to its chemical and electronic structure (electronic mobility, thermal conductivity).

This new material combines many interesting aspects. Never before did a single material comprise so many interesting properties with a wide range of potential applications. Some of its main properties are listed below.

- It is the best heat conductor known to date, with thermal conductivity values up to $(5.30 \pm 0.48) \times 10^3$ W/mK, outperforming carbon nanotubes at room temperature[15] and allowing very efficient heat dissipation.

- It is one of the best electrical conductors ever described. Charge carriers in graphene can travel for μm without scattering even at room temperature. As a consequence graphene presents very high charge carrier mobility values (>$2{\cdot}10^5$ cm^2/Vs)[1]. It

can stand current densities up to 10^8 A/cm^2, six orders of magnitude higher than copper[16], without suffering of electromigration problems.

- It presents electrical spin-current injection and detection for temperatures up to 300 K[17–19].
- It is nearly transparent. Graphene absorbs 2.3% of light over a broad range of the visible spectrum[20].
- It has very good mechanical properties. It is the thinnest material known and also the strongest –substantially times stronger than steel by weight and 10 times better than steel at scattering kinetic energy[21]– with a Young's modulus (different to that of 3D graphite) of 1.0 ± 0.1 TPa[22] and it is very flexible. Even when patches of graphene are stitched together, it remains the strongest known material[22].
- Researchers have also identified the bipolar transistor effect[23] and large quantum oscillations in the material[24].

Scientists and engineers predict that many future applications can be realized using graphene from electronics, optoelectronics, energy storage, photonics to lighting and up to aerospace[25]. Among the main ones are:

- Its very high carrier mobility has raised expectations in many fields such as high-speed electronics, photonics, and biodevices[1,14].
- It can be used for making strong and durable touch-screens for smartphones. It has led to the production of lower costs of display screens in mobile devices by replacing indium-based electrodes in organic light emitting diodes (OLED)[26] which also lower power consumption.
- Pristine and porous 2D graphene membranes with and without functionalization have been investigated for gas purification[27–29] and for more efficient separation of gases[30], which could be used to build explosive detectors or even for low cost water desalination.
- It can be used to build pressure sensors[31,32].
- Transparent electrodes[20] can be built with this material.
- It can be used in the production of lithium-ion batteries that recharge faster[33]. These batteries use graphene on the anode surface.

- Graphene needs less light energy to get the electrons to jump between layers than silicon. In the future, that property could give rise to very efficient solar cells[34]. Using graphene would also allow cells that are hundreds of thousands of times thinner and lighter than those that rely on silicon.

- It can be a way to store hydrogen for fuel cell powered cars[35–37].

- It can be very useful for chip making[38].

All that glitters is not gold

Its nice properties render graphene with a great potential to be applied in many different fields. However, in order for academic interest to be translated into commercial success, there are a number of requirements that have to be fulfilled such as the availability of suitable production methods (cost effective, scalable, reliable), the overcoming of some problems related to its intrinsic properties that prevent certain applications, market awareness, etc.

The main issue is still the production methods (we will comment on the most common methods to synthesize it later on). There is no good general synthesis method that produces graphene quickly, precisely and in large enough quantities. Until this problem is solved, we will not see graphene on the mass-market. There are also issues with the intrinsic properties of graphene that need to be fully sorted out. The main electronic disadvantage to build new graphene-based transistors is the lack of a band gap. There has been a lot of effort in trying to open its gap through different techniques[39], but still is an open problem. A different issue, related with its usage as a catalyst, is its low resilience to oxidative environments which could be avoided by means of functionalization[40]. Another example deals with potential biological applications on which issues surrounding biocompatibility and cytotoxicity are still to be fully addressed with different studies contradicting each other[41].

Moreover, in term of its applications, there is a characterization problem: graphene has been extensively studied in ideal conditions reaching a deep understanding of its properties[42,43]. However, in realistic environments, due to their higher complexity, very relevant basic features of real-life graphene are not well understood yet.

Studies on graphene in more realistic situations are crucial to extract the full potential of this material and design suitable applications, which can still be very interesting. In these studies is necessary to characterize the effects of the interaction with other materials and the presence of defects, which is the main goal of this thesis.

1.1 Synthesis

There are two main graphene manufacturing techniques that could supply graphene in relatively large scales. Chemical vapour deposition (CVD) has been identified as the technique to produce graphene films in large scale, while liquid phase exfoliation techniques are suitable to manufacture graphene platelets –smaller flakes in form of powder– in an industrial scale at low cost, although more defective than CVD-produced samples. We will comment on this and other of the most used graphene production techniques below.

Mechanical exfoliation from HOPG

As we have already said, graphene was first isolated using the "Scotch tape" or micromechanical exfoliation method[1]. This is the method that produces best quality freestanding graphene, however the size and morphology of the samples is not well controlled and the production price is relatively high. This is not an industrially scalable technique, as an experimented researcher has to look the by-products of HOPG exfoliation one by one with an optical microscope searching flakes with a precise optical absorbance to check that it is indeed a monolayer. The exfoliated graphene can be transferred onto an arbitrary substrate, such as a SiO_2/Si wafer, on which characterization experiments can be performed.

Epitaxial growth on silicon carbide by thermal annealing

Graphene films were initially produced using transfer-free wafer-scale graphene growth by the thermal decomposition of silicon carbide[44] (SiC). When SiC is heated to high temperatures (>1500K) in a vacuum or in an argon atmosphere, only the silicon atoms leave the surface due to the difference in the vapour pressures of silicon and carbon. The remaining carbon atoms form epitaxial graphene spontaneously on the surface. This method produces high purity areas of graphene on top of a wide gap semiconductor and it is the most promising for being used in future graphene based nanoelectronics. However, the main drawback of this method is the high cost and limited size of the starting SiC wafers.

Graphite oxide reduction through chemical methods

The graphene synthesis method based on reduction of graphene oxide (GO) is among the liquid phase exfoliation methods developed to fabricate graphene platelets. The basic procedure was developed by Hummers *et al.* in the 1950's[45]. The GO, which is oxidized

chemically from a graphite crystal and is dissolved in aqueous solution, can be easily deposited on an arbitrary substrate in monolayer or few-layer form[46]. The resulting product is a highly dispersed carbon powder with a few percent of single layer planes. The monolayer GO can be reduced –chemically, thermally or via irradiation with ultraviolet (UV) or infrared (IR) light– into graphene in order to restore up to some extent the electronic properties of the starting material. These sheets are, however, highly functionalized through –OH, -COOH, -O- and other oxygen-rich groups due to the oxidation process. This reduced GO is based on the solution technique, and so is most suitable for printed electronics and chemical applications.

Chemical vapour deposition on metal substrates

One promising larger-scale graphene growth technique is chemical vapour deposition (CVD) on metal substrates[47,48]. A carbon-containing gas such as methane, ethane, or propane, decomposes at high-temperatures and turns into graphene on the catalytic metal surface. This technique can provide wafer-scale graphene at low cost, which is appropriate for industrial applications.

It was already known in the 1970's that the carbon atoms diffuse into a nickel substrate at a high temperature and precipitate to form multi-layer graphene on its surface during cooling[49]. Recently, a copper substrate was found to be better for the monolayer graphene growth, because of the low carbon solubility[50]. Moreover, studies in 2012[51–53] found, by analysing graphene's interfacial adhesive energy, that it is possible to effectually separate graphene from the metallic board on which it is grown, whilst also being able to reuse the board for future applications theoretically an infinite number of times, therefore reducing the toxic waste previously created by this process. Growing large-area single crystal graphene without grain boundaries, and removing defects and impurities due to the transfer process are, then, the remaining problems.

This experimental method naturally provides a playground to study G-metal contacts and tune its properties through the metal influence. This G-metal systems could have a wide range of applications, in particular those related with electronics. This is the reason why there are plenty of works dealing not only with the growth mechanisms of graphene on metals, but also with the new properties that arise from the combination of both materials. In this thesis we have followed this research line and, in particular, we have studied weakly interacting G-metal systems.

1.2 Properties of graphene

In simple terms, graphene, is a thin layer of pure carbon or, in other words, a single, tightly packed layer of carbon atoms that are bonded together in a honeycomb lattice. In this section we will introduce and explain its main properties, focusing on those that will be relevant for this thesis.

Structure

Graphene is a 2D crystalline allotrope of carbon. Its carbon atoms are densely packed in a regular honeycomb lattice (see Fig. 1.1a). It is not a Bravais lattice because two neighbouring sites are not equivalent. This hexagonal lattice can be regarded as two interleaving triangular lattices and one may view it as a triangular Bravais lattice with a two-atom basis (A and B). The distance d between nearest neighbour carbon atoms is 1.42 Å. The magnitude of the lattice vectors is, then, $|\mathbf{a}_1| = |\mathbf{a}_2| = \sqrt{3} \cdot 1.42$ Å$= 2.46$ Å. They can be written as

$$\mathbf{a}_1 = \frac{3d}{2}\left(\hat{x} + \frac{1}{\sqrt{3}}\hat{y}\right);\ \mathbf{a}_2 = \frac{3d}{2}\left(\hat{x} - \frac{1}{\sqrt{3}}\hat{y}\right). \tag{1.1}$$

The reciprocal lattice vectors have magnitude $8\pi/3d$ and can be written as

$$\mathbf{b}_1 = \frac{2\pi}{3d}\left(\hat{x} + \sqrt{3}\hat{y}\right);\ \mathbf{b}_2 = \frac{2\pi}{3d}\left(\hat{x} - \sqrt{3}\hat{y}\right). \tag{1.2}$$

Hence, the first Brillouin Zone (BZ) is an hexagon (see Fig. 1.1a) of which the sides are at a distance $4\pi/3d$ from its center. The positions of the two Dirac points, $\mathbf{K}$ and $\mathbf{K}'$, located symmetrically at the corners of the BZ (of which the significance is to be explained later) are

$$\mathbf{K} = \frac{2\pi}{3d}\left(\hat{x} + \frac{1}{\sqrt{3}}\hat{y}\right);\ \mathbf{K}' = \frac{2\pi}{3d}\left(\hat{x} - \frac{1}{\sqrt{3}}\hat{y}\right). \tag{1.3}$$

1.2.1 Electronic properties

Band structure and density of states

A carbon atom has four valence electrons. In graphene, three of them occupy the in-plane orbitals s, p_x and p_y which are hybridized sp^2 constituting the σ band –which is far from the Fermi level in energy–. The forth electron is in an out-of-plane p_z orbital. All these p_z orbitals hybridize to conform the π and π^* bands (see Fig. 1.1c), which are responsible for most of the peculiar electronic properties of graphene. This band structure was firstly calculated by Wallace in 1947[55].

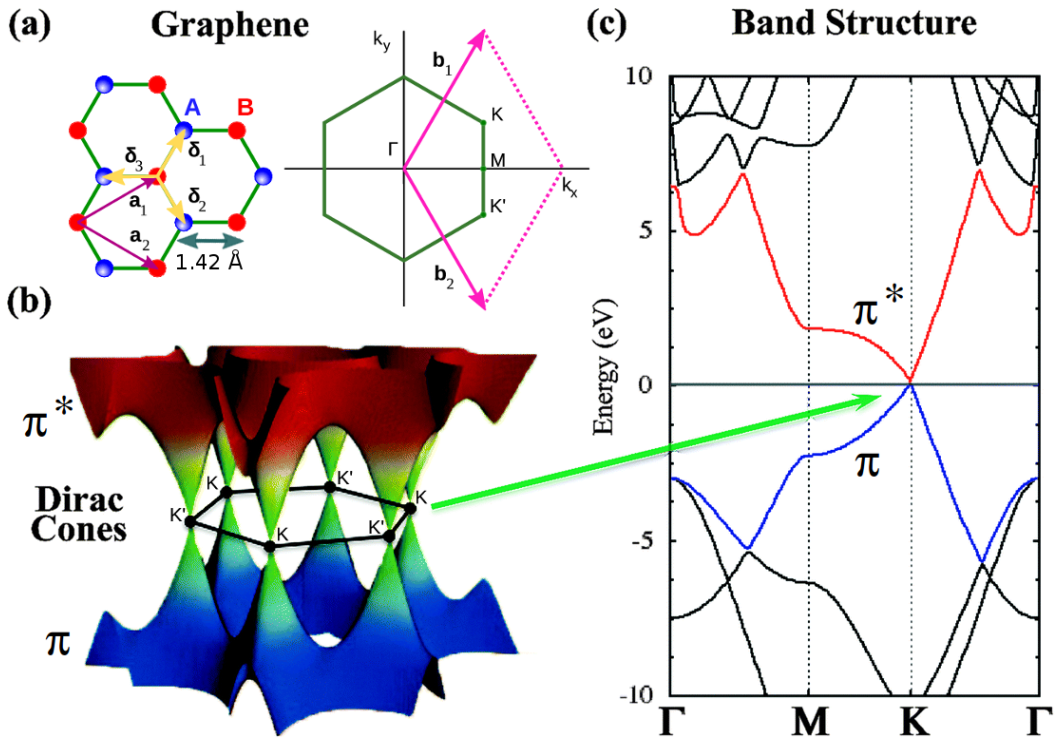

Figure 1.1 a) Graphene structure in the real and reciprocal space. In the real space ball-and-stick scheme the two sublattices A (blue) and B (red) an be clearly distinguished. The lattice vectors $\mathbf{a}_{1,2}$ as well as the vectors $\delta_{1,2,3}$ connecting nearest neighbour atoms are indicated. In the Brillouin zone, the reciprocal lattice vectors $\mathbf{b}_{1,2}$ are also depicted. b) Graphene Dirac cones. c) Graphene band structure. The Fermi level has been shifted to 0 eV. Valence and conduction bands are highlighted in blue and red respectively. This figure has been adapted from[54].

These π and π^* bands present a linear behaviour in the surroundings of the Fermi level and they meet at one point right at this same energy. These two features are the main ingredients for a new type of band structure with massless carriers exhibiting inhibited scattering (mobilities of $\sim 10^5$ cm^2/Vs[1]), which are regarded as Dirac particles. This identification with the Dirac theory[56] –which describe the behaviour of particles at high energy or particle physics– made the scientific community to name the cones formed by the π and π^* bands as Dirac cones and the two equivalent points where they meet, **K** and **K**′, as Dirac points (see Fig. 1.1b). Due to the existence of a pair of Dirac points, the zero-energy states are doubly degenerate (twofold valley degeneracy).

The linear dispersion partially arises from the triangular graphene lattice symmetry with a two-atom basis. This ensures the existence of two bands and the symmetry between them (chiral due to the electrons helicity) makes them to have the same energy (spin degeneration). Some extra symmetry arguments (this honeycomb lattice symmetry combined with and time reversal symmetry) are needed to explain the existence of the zero-energy states[42]. Notice that the inequivalence of the two BZ corners, **K** and **K**′, has nothing to do with the presence of two sublattices, A and B, in the honeycomb lattice. It is just an intrinsic property of the Bravais triangular lattice, independent of the possible presence of more than one atom in the unit cell. The density of states (DOS), then, vanish at this point (see Fig. 1.1c), which makes graphene a zero-gap semiconductor (semimetallic behavior). For energy fluctuations larger than 1 eV away from the Fermi level the behaviour of the DOS is no longer linear and Van Hove singularities[57] can be found. They are essentially non-smooth points where the density of states is not differentiable and they correspond to critical points of the BZ.

Is precisely the linear dispersion found in graphene what make all its extraordinary properties to arise. However, the described behaviour is modified for non-ideal graphene samples. These properties change with the presence of defects or edges, or with the interaction with other materials. Far from being a setback, this represents a perfect opportunity to tune the electronic properties of graphene.

Magnetic properties

The breaking of the perfect 2D periodicity of graphene in the presence of topological defects or in strain relief structures modifies significantly its electronic properties[58,59] producing, in certain cases, the appearance of magnetic features.

There are many examples of graphene-related studies on magnetic properties. Occurrence of high-temperature ferromagnetism in graphite-related materials is a topic of considerable interest. In the case of graphene nanobubbles, it has been found ex-

perimentally that they favour the appearance of pseudo-magnetic fields associated to Landau-levels[60]. It has also been suggested that the zig-zag edges are responsible for some magnetic properties of graphene[61]. Other works have also observed a gradual increase in the magnetic moment, with an increase in the chemisorbed hydrogen content[62].

Experimentally it had been observed that a graphene sheet have magnetic properties. The theory predicted that monovacancies could be the explanation for this induced magnetism in graphene[63], but the type of magnetism produced is still not well understood. In the previous literature there was controversy between theoretical works which predicted a different values for the local magnetic moment induced by monovacancies which the experimental evidences were unable to elucidate. While DFT calculations based on clusters predicted a value of 2 μ_B[64,65], similar calculations in extended systems claimed it was 1 μ_B[66]. In this thesis we have studied this phenomena to clarify this issue (see Chapter 4).

1.2.2 Mechanical properties

Graphene also attracts great attention as the strengthening component in composites[67–69]. Characterization of the mechanical properties of graphene is essential both from a technological perspective for its reliable applications and from a fundamental interest in understanding its deformation physics[70,71]. Its intrinsic mechanical properties could lead to applications such as nanoelectromechanical systems as pressure sensors and resonators[72,73].

Of special importance to the study of these properties on membranes or 2D materials[74,75] is the effect of the temperature which induces much more relevant changes than in 3D solids. In a membrane, the out-of-plane vibrations are very soft and easily excited with temperature. The flexural modes[76,77] –also called the ZA mode, bending mode, or out-of-plane transverse acoustic mode– are the responsible for these out-of-plane deformations that corrugate the graphene membrane (see Fig. 1.2). It is so flexible that its flexural modes are crucial for its thermal and mechanical properties.

The big question here is whether its mechanical behaviour can be explained by the well-known membrane classical theory, since it is a real 2D material, or it behaves more like a solid material, in that it is strongly bound through covalent bonds in contrast with typical biological membranes. To elucidate this, several groups have been measuring different of its characteristic properties.

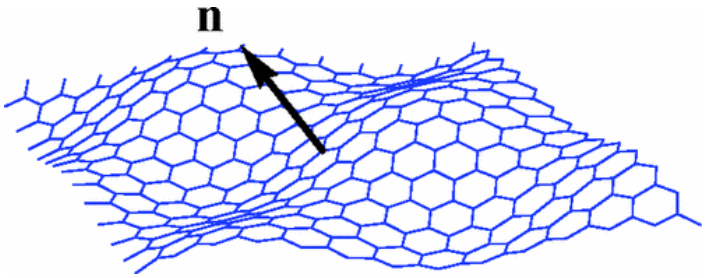

Figure 1.2 Out-of-plane vibration of a graphene lattice due to the excitation of the flexural mode. This figure has been extracted from [78].

Young's modulus and intrinsic strength

Graphene is the strongest material ever tested. The pioneering mechanical testing of graphene has been conducted by Lee *et al.*[22] through nanoindentation of freely suspended graphene films with an atomic force microscope (AFM). Using density functional theory (DFT), Liu *et al.*[79] had earlier undertaken an *ab initio* calculation of the stress–strain curve of a graphene single layer. When comparing the results, there is an extremely good agreement between the theoretical analysis and the experimentally-derived curve.

From these curves the both the Young's modulus, a mechanical property which defines the relationship between stress (force per unit area) and strain (proportional deformation) in a material, and the intrinsic tensile strength, the capacity of a material to withstand loads tending to elongate it, can be calculated. The experimental results reported for the Young's modulus and the intrinsic tensile strength of the mechanically exfoliated pristine graphene are 1.0 ± 0.1 TPa and 130 ± 10 GPa[22], respectively, while the theoretical values are 1.05 TPa and around 107-121 GPa[79].

Fracture Toughness

In spite of these extraordinary values reported, the useful strength of large-area graphene with engineering relevance is usually determined by its fracture toughness, rather than the intrinsic strength that governs a uniform breaking of atomic bonds in perfect graphene. In materials science, fracture toughness is a property that describes the ability of a material containing a crack to resist fracture, and is one of the most important mechanical properties of any material[80,81]. In this same context, the strain energy release rate is the energy dissipated during fracture per unit of newly created fracture surface area.

Theoretical and computational modelling in recent literature has provided important insights into the fracture and strength-controlling mechanisms of graphene with both perfect and defective lattice structures but it was not experimentally measured until

recently[82,83]. The cracked graphene samples exhibited a fast brittle fracture behaviour with the breaking stress much lower than the intrinsic strength of graphene. Zhang *et al.*[82] determined the fracture toughness of graphene measured as the critical stress intensity factor (4.0 ± 0.6 MPa$\sqrt{\text{m}}$) and the critical strain energy release rate of fracture (15.9 ± 0.2 Jm^{-2}). These values were validated with molecular dynamics (MD) simulations. A different work by Hwangbo *et al.* reported an even larger value (10.7 ± 3.3 MPa$\sqrt{\text{m}}$) which is exceptionally high, as compared to other carbon based 3D materials[83].

1.3 Tuning the properties of graphene

In the previous section we have briefly reviewed the main properties of graphene. This material has been extensively studied in its pristine version while some basic features of its characterization in realistic systems are still not well understood. This is an important part of the study of graphene because, in most cases, these properties are altered in real graphene samples. Given that for a range of applications, the next step towards device integration will require modifying graphene for specific functionalities or electronic properties, realistic environments provide an excellent opportunity to do it. The central effort of this thesis has been to characterize different cases of systems on which the graphene properties can be tuned.

There are several ways on which the properties can be modified. In this thesis, we have studied the effects of (i) breaking its perfect 2D structure –exploring point defects and edges properties– and (ii) the interaction with other materials –in particular molecules adsorption and growth on different substrates–. Before getting into details of our specific studies, we will briefly introduce the state-of-the-art on these topics from a more general point of view.

1.3.1 Modifying graphene properties by the interaction with other materials

The study of the interaction of graphene with other materials naturally arises when one wonder about the effect of the substrate on which it is grown or transferred to. It has been explored as a promising way to get the desired band-gap opening in graphene[39]. Apart from the substrates influence, the properties of graphene can also be tuned by the adsorption of other compounds on top of it. In particular, we have analyzed the formation mechanisms of self-assembled molecular layers (SAMs) on graphene.

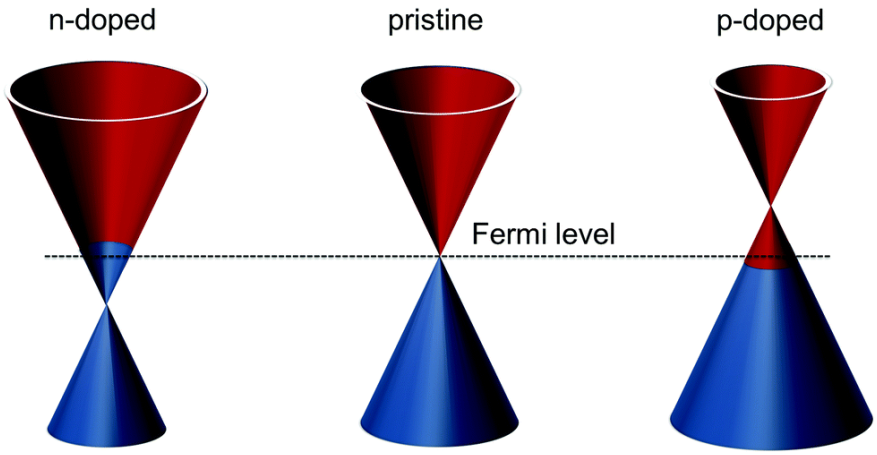

Figure 1.3 A schematic showing the relationship between positions of the HOMO–LUMO levels of dopants with respect to the Fermi level of graphene relevant for n- and p-type doping of graphene. This can be applied to the effects of the substrate on which the graphene is grown and also to the influence of possible molecular adsorbates on graphene. This figure has been adapted from [85].

Depending on the interaction strength of the other material and the graphene, the properties of graphene can be just slightly modified or completely transformed. In this thesis we have dealt with weakly interacting systems on which the properties of graphene are mostly preserved but still some changes are induced which allows to distinguish between different cases of these systems.

Next, we introduce some the cases in the context of what has been studied in this thesis.

Graphene on weakly interacting metals: Moirés

Metal surfaces normally react with carbon by forming surface carbides. However, the less reactive substrates develop graphene upon carbon exposition (by the CVD technique already introduced). When graphene is on top of a metal its electronic structure can be deeply modified when the interaction between them is very strong or barley changed when it is weak. In the first case, the strong graphene-metal interaction corrugates the graphene layer and the π orbitals of the C atoms closer to the substrate are hybridized with the d band of the metal producing a high distortion of the pristine graphene electronic structure. In the weakly interacting cases, the main difference with pristine graphene electronic structure is an energy shift: due to the different work functions of metal and graphene and also to the interaction between them there is a charge redistribution at the interface –a dipole is formed – and a doping is induced in the graphene [84] (see Fig. 1.3).

The least interacting metals are, in progressive order, gold, silver and copper. However, they interact so weakly that it took a lot of effort, and the use of smart growth techniques, to successfully grow graphene on them[86–88]. The next metal in the reactivity scale is the platinum. The G-Pt interaction is still very weak, the graphene layer is only negligibly corrugated, but there is a clear doping effect of the metal[84]. The next metals in low reactivity, on which its effect on the graphene starts to be much more noticeable in structural terms (corrugation), would be iridium and palladium. In the latter, even the electronic properties are affected. Even in early studies in the 1970s, the then called *single layer graphite*[89,90] on transition metal surfaces depicted a very rich landscape of graphitic structures on this sort of weakly interacting metal surfaces.

In general, there is a misalignment between the graphene and the substrate periodic lattices. Therefore, there is not a special orientation favoured by the lattice symmetry. As a consequence, several orientations of the graphene overlayers with respect to the substrate can be found resulting in *superperiodic* structures, the so-called Moiré patterns. They can be characterized by the relative angle between lattices and their superperiodicity (see Fig. 1.4). The formation of these coincidence superstructures has been observed by STM. The exact determination of these structures is difficult to explore from a theoretical point of view since the size of the Moiré patterns can be large, even more than 5 nm[91].

Depending on the reactivity of the substrate, the interaction strength can range from vdW physisorption to strong bonded chemisorption. For the latter cases the interaction can be so strong that just a single Moiré can be found in the experiments; this is the case of rhenium[92], ruthenium[93], cobalt[94] and nickel[95] –these two later cases are slightly different because both lattices are directly commensurated–. However, this is not always the case and, a competition between the interaction and the corrugation energies, allows to find different Moirés in the G-rhodium system[96]. In all these cases, the electronic properties of graphene are clearly modified and the graphene sheet is corrugated by the effect of the metal substrate.

In the case of low interacting metals, the system is more free to explore different rotational configurations producing a set of different Moirés. The two more interacting cases of this group presented before, the iridium[97–99] and the palladium[100], present a single Moiré pattern but it changes depending on the experimental growing conditions. The rest of the cases do not induce a relevant corrugation and, in terms of electronic effects, they only dope the graphene. A good example of low interacting system with a lot of possible Moiré patterns, which is also the case treated in this thesis, is the G/Pt(111) system[101]. The stability of each of these patterns (or how often are they found in the experiments) seems to be correlated with a mismatch minimization as claimed by Merino

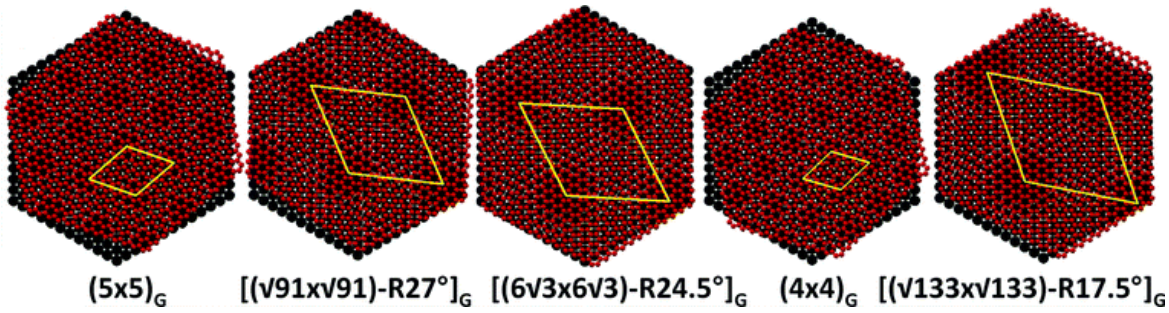

Figure 1.4 Schematic models of the Moirés obtained by STM measurements of graphene grown on Rh(111). This figure has been extracted from [96].

et al. [101]. In this thesis we analyze further factors that can favour the presence of certain Moirés over others.

Graphene vs graphite

Graphite is a commonly found mineral which consists of stacked graphene layers. The distance between layers is roughly 3.35 Å [102], and the most stable state corresponds to Bernal stacking [103] (ABAB) on which the atoms in one layer are placed at the hexagon centres of the layers above and below it. Bonding between layers is driven by weak vdW interaction, which allows the layers to be easily separated or slide across each other, making graphite a soft and malleable material. In graphite, it is well known that, in the uppermost layer a gap is opened in one of the sublattices due to the Bernal stacking. This loss of symmetry converts the massless fermion behaviour characteristic from graphene in massive fermions. This effect can be already seen in the bilayer graphene [42].

From the point of view of the simulations, it has been proved that a four-layer slab with Bernal stacking is enough to reproduce the main features of graphite (see Fig. 1.5d). From this system to the graphene single sheet simulation, the properties gradually change with each layer removal. In Fig. 1.5 the main changes in the band structure can be seen for a different number of layers.

Molecules on graphene

As it was previously introduced, a different way of modifying graphene properties is by the adsorption of atoms or molecules. Covalent or noncovalent chemical functionalization [105,106] can render normally-inert graphene chemically sensitive, which is critical for applications in sensing [2,107], and can allow for bandgap engineering/charge transfer doping from electron donating/accepting organic molecules [108,109]. The electronic effects

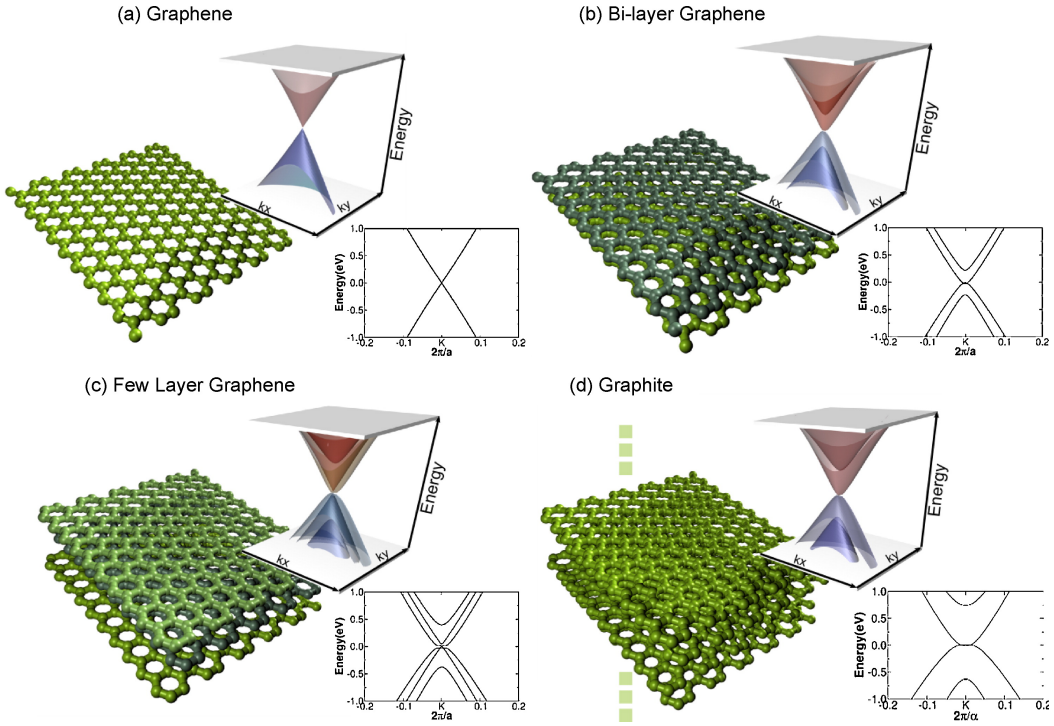

Figure 1.5 Bands around the *K* k-point for a) graphene, b) bilayer graphene, c) trilayer graphene and d) graphite. The Dirac point which can be clearly spotted in graphene, is lost in bilayer graphene, but appears again in trilayer graphene. The graphite exhibits a semimetallic band structure with parabolic-like bands. This figure has been extracted from [104].

produced by organic molecules on graphene have been either included in, or the focus of, a number of recent review papers [105,106].

In the context of the more simple adsorbates, graphene is supposed to be relatively inert to most atmospheric airborne contaminants, this is, low sticking coefficients towards O_2, N_2, and more importantly, H_2O molecular exposition. However, some species can chemisorb on top of in-lattice C atoms. Highly reactive atomic adsorbates, such as O or H, tend to covalent bond the substrate. For example, decoration of graphene surface with hydrogen, oxygen, and fluorine atoms can be used to modulate its electronic properties, such as band gap, electron mobility, and optical absorption [110–112]. Similarly, alkali metal (EM) and alkaline-earth metal (AEM) atoms adsorbed graphene sheets are considered as potential devices for ion batteries, hydrogen storage materials, and superconductors [113–117]. Unlike nonmetal atoms that can perturb the atomic structure of graphene, decoration by AM and AEM has little effect on its geometric structure [115].

More complex compounds can also be absorbed in graphene. In particular, the adsorption of organic molecules [106,118–120] have been extensively studied. The main interest in the adsorption of this kind of molecules is that in many cases they adsorb forming ordered patterns giving rise to what is called a self-assembled monolayer (SAM). This SAMs represent a rapid, scalable route towards the realization of nanoscale architectures with tailored properties.

The low reactivity of graphene makes it the ideal substrate to grow self-assembled monolayers (SAMs) of molecules for whose formation high molecular mobility (low diffusion barriers) and a strong enough intermolecular interaction are needed. On epitaxial graphene, the SAM formation process is sensitive to the interaction between the graphene and the substrate on which it is grown. In the case of graphene that strongly interacts with its substrate, such as graphene/Ru(0001) [121], the inhomogeneous adsorption landscape of the graphene Moiré superlattice provides a unique opportunity for guiding molecular organization, since molecules experience spatially constrained diffusion and adsorption [118].

On weaker-interacting graphene sheets, and on non-epitaxial graphene transferred onto a host substrate, self-assembly leads to monolayers on which the molecules adsorb in a planar geometry. In these systems the balance between the interaction energy with the substrate and the intermolecular interaction is much more delicate. Therefore, graphene presents an appealing testing ground for investigating the basic properties of SAMs. For a fundamental study of this kind, the molecule studied needs also to be the simpler one with self-assembly abilities or, in other words, with a structure which allows the hydrogen bonds formation.

In this thesis we have studied the SAMs formation mechanism on weakly interacting systems analyzing the case of a SAM of simple molecules, as the Azabenzene 1,3,5-Triazine, on top of G-based weakly interacting substrates.

1.3.2 Modifying graphene properties by breaking the lattice symmetry

Even with the most accurate experimental techniques to grow graphene sheets it is impossible to get a completely crystalline sample. The presence of defects is unavoidable. It is common to find either grain boundaries, dislocations of the graphene lattice and, above all in terms of frequency, point defects. Although the presence of disorder in graphene can affect its performance, it also represents a method for tuning its features and functionalize it at convenience inducing new electronic, magnetic, thermal and mechanical properties [122].

Another feature related with breaking the perfect 2D graphene lattice deals with the necessarily finite graphene sample sizes. In this context, the characterization of the edges of the sample, both their structure and electronic properties, or the contacts between the graphene film edge and other materials appears as an obvious matter of study [123]. In particular, termination, chemical functionalization and reconstruction of graphene edges leads to crucial changes in the properties of graphene, so control of the edges is critical to the development of applications in electronics, spintronics and optoelectronics.

In the next sections we introduce the particular features that have been studied in this thesis related with breaking the crystal symmetry of graphene.

Point defects on graphene

Point defects on graphene can be, for simplicity, categorized into three main groups: due to missing atoms (vacancies), due to atom rearrangements (Stone-Wales defect) and atom substitution. More complex combinations of these three types of atoms have also been reported. In Fig. 1.6 some examples on these point defects variety are represented.

These defects naturally appear when graphene is grown in the laboratory and can deeply change its properties. In this sense, a new field based on the modification of graphene by point defects is currently very active and its ultimate goal is to further diversify graphene practical applications in the near future. Techniques such as ion irradiation intentionally induce atomic defects in graphene. By manipulating the conditions of irradiation, it is possible to tune, in a flexible way, the properties of the carbon-based materials. However, precision at the nanoscale on defect formation remains a significant challenge on which there has been a lot of effort [126].

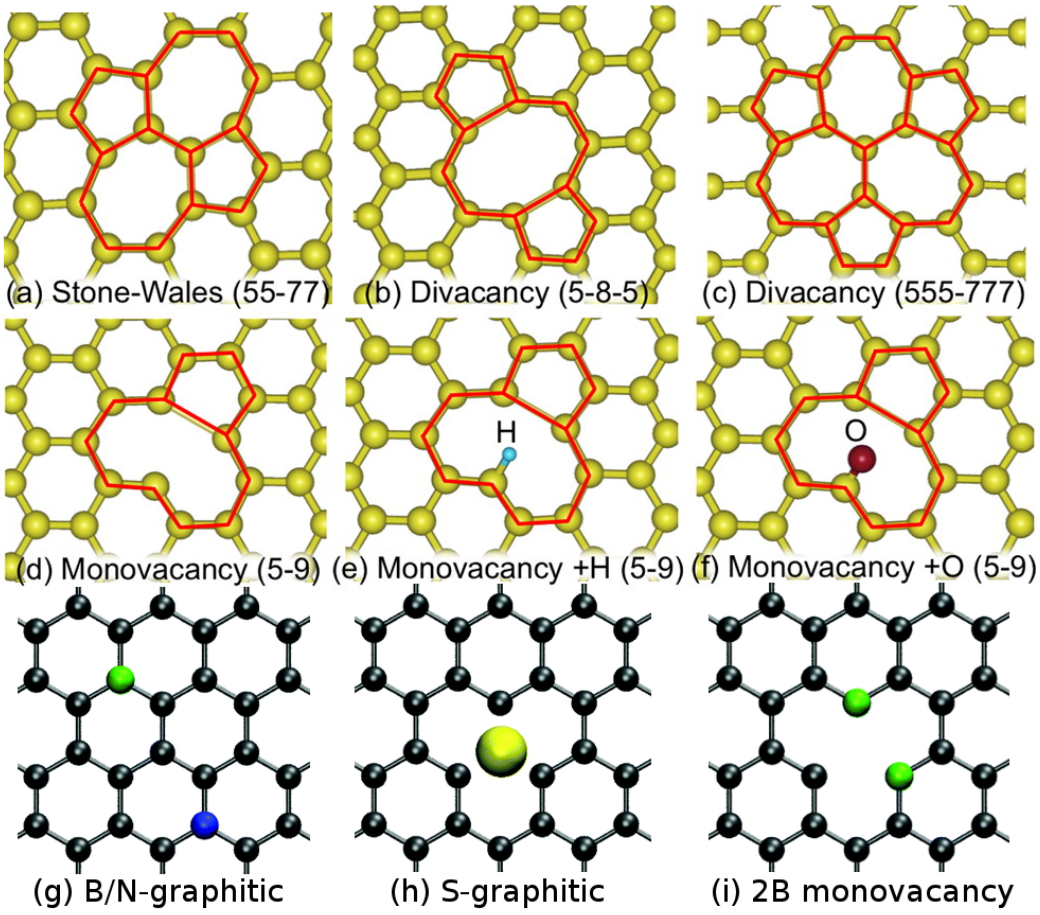

Figure 1.6 Types of native graphene point defects due to missing C atoms and/or atom substitution. These defects can also be funtionalized by different chemical species. This figure has been adapted from [124,125].

An important feature related with graphene defects is related to the asymmetry of the electronic structure of graphene in energy close to the Fermi level (go back to Fig. 1.1c). The absence of electron-hole symmetry shifts the energy of the states localized near defects leading to a transfer of charge from or to the clean regions –depending on the shift of the energy shift–. Hence, the combination of localized defects and the lack of perfect electron-hole symmetry around the Dirac points leads to the possibility of self-doping.

In particular, monovacancies, as it has been previously discussed, have been identify as the origin of the graphene magnetic moment measured experimentally. Moreover, by the presence of a low concentration of these defects, the mechanical properties are modified in an unexpected way[127]. In addition of the experimental evidences on this topic, a more fundamental and atomistic characterization that would explain both the source of this magnetic moment and the unusual modification of the elastic properties of graphene was still missing. For this reason, in this thesis we have addressed this issues.

Graphene edges

Edges can be found not only in graphene samples but also in a wide variety of graphene-based nanostructures which can be terminated by many different types of edges[58]. In this context, the most representative of these structures are graphene nanoribbons (GNRs) which are strips of graphene with ultra-thin width. So is the importance of the edges characterization that GNRs were firstly introduced as a theoretical model by Nakada *et al.* to examine the edge and nanoscale size effect in graphene[58]. Their striking feature is the diversity of electronic structure patterns that can be obtained by changing the structural parameters, like width and crystallographic orientation of the edges[128].

Given the high reactivity of the edges the study of their interaction with the surrounding environment is a very relevant. In particular in graphene, is very important to characterize the edge interaction with the steps of the substrate on which it has been grown. Metals are common substrates for that (CVD) and the study of the G-metal contacts have a double interest: to characterize the contact itself and to analyze how can the contact formation affect to graphene growing mechanisms and, hence, the Moiré formation.

The importance of an edge to a graphene sheet can be compared to that of a surface to a crystal. Cutting through an infinite graphene sheet, one first breaks $C-C$ σ bonds and then obtains two semi-infinite graphene sheets, each with a one-dimensional edge. The dangling σ bonds at the edges can be saturated with hydrogen (so-called hydrogenated or hydrogen-terminated edges) and all the carbon atoms remain sp^2 hybridized. They can also saturate by contacting with a nearby material. Depending on the cutting direction, two main types of edges can be obtained: *zigzag* or *armchair* (see Fig. 1.7). Some other

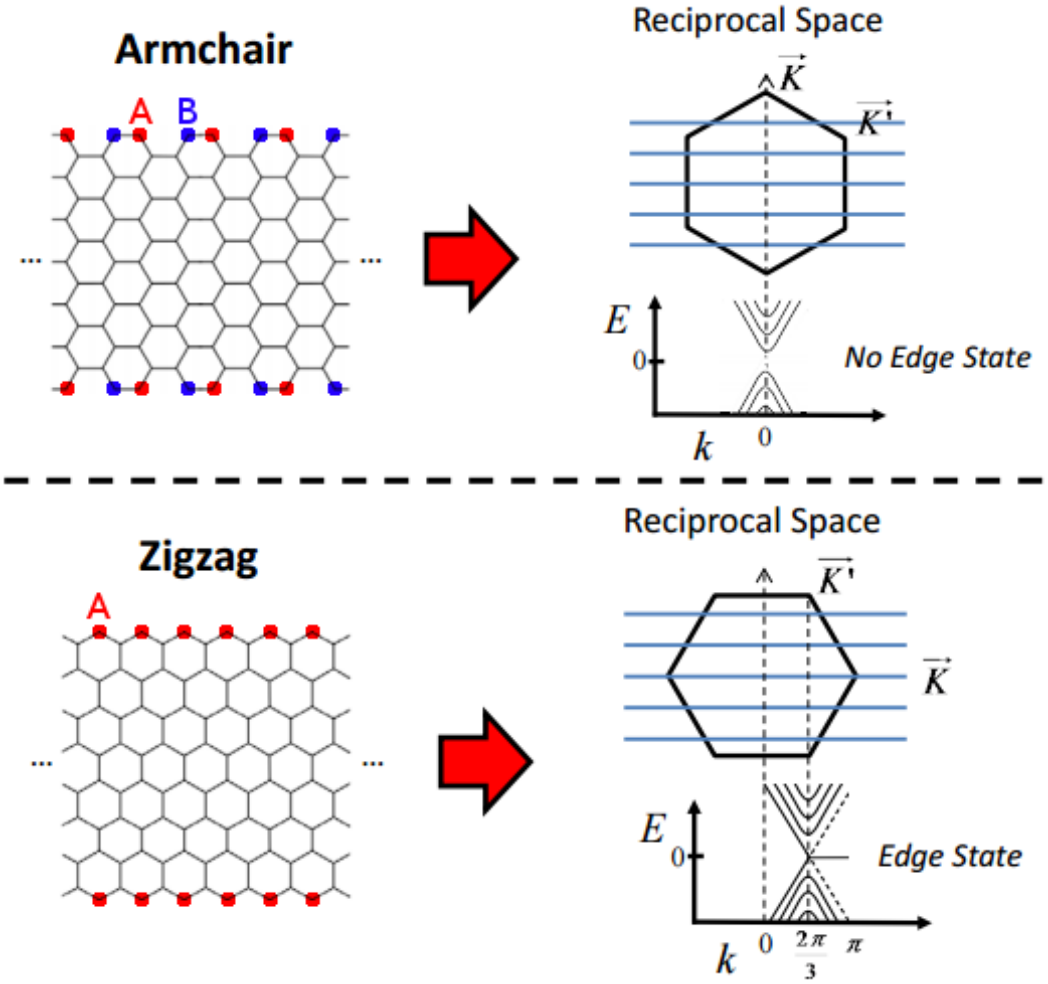

Figure 1.7 Structural and simplified band structure schemes and for the zigzag and armchair edges. On each structure model the sublattice of the ending atoms has been highlighted. Figure adapted from the oral presentation *"Graphene Nanoribbons: A Route to Atomically Precise Nanoelectronics"* by M. Crommie at the *Naval Future Force Science and Technology EXPO* in 2015.

edges reconstructions have been observed[129] as well as mixtures between these to main edge structures.

These edges have a profound influence on the electronic structure and give rise to interesting new phenomena. By constructing an analytical solution to the edge state, Nakada *et al.*[58] showed that the zigzag edge in a semi-infinite graphene sheet gives rise to a so-called localized state at the zigzag edge. These edge states (which are extended along the edge direction) decay exponentially into the centre of the ribbon, with decay rates depending on their momentum[58,130–132]. Such states have been observed experimentally in monoatomic step edges of graphite by using scanning probe techniques[133,134].

The localized edge states form a twofold degenerate flat band at the Fermi energy (E_F), existing in about one-third of the Brillouin zone away from the zone centre[58,130–132] (see Fig, 1.8). This flat band feature and its corresponding localized state are unique to the zigzag edge (they are completely absent from the armchair edge). Indeed, the presence of the zigzag edges gives rise to unique physical and chemical properties, as reported by Son *et al.*[135] and Jiang *et al.*[136], based on the first principles density functional calculations. The origin of this edge state is easy to visualize in terms of symmetry. As we have said, electrons in graphene have the features of massless Dirac fermions. Therefore, the presence of an edge state is a consequence of the broken symmetry of its pseudospin, that is, in the zigzag edge, sites belonging to only one of the two sublattices exist, although sites of A and B sublattices are always paired in the armchair edge (see Fig. 1.7).

The edges are mainly characterized by their morphology and chirality, but there are other distinct features that have an effect on their properties (see Fig. 1.8). The first of them deals with the electron-electron interactions. The edge-state flat band gives rise to a high DOS at the Fermi level, whose associated electronic instability can be relieved by the origin of a peculiar type of magnetic ordering in the zigzag edges. In the ground state, magnetic moments are localized at the edges: the correlations are ferromagnetic along the edge and antiferromagnetic across the honeycomb graphene lattice. Another effect to take into account is the spin-orbit interaction: an effect of relativistic origin that couples electron spin and orbital momentum. In the presence of spin-orbit interactions, the edge states in graphene exhibit the properties of the quantum spin Hall effect boundary states. In graphene, however, the relativistic spin-orbit coupling is very weak[137]. Finally, we find the edge potential effect related to the local electrostatic environment. Potential changes at the edge originate from the interaction of the edge C atom with the substrate or other atoms or functional groups terminating the edge. In general, the edge potential results in either upward or downward broadening of the flat band.

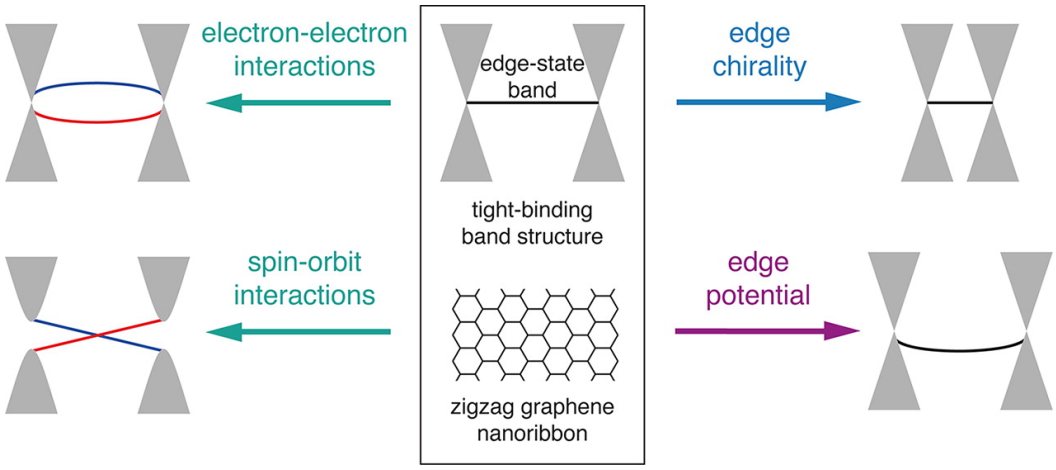

Figure 1.8 Simplified scheme of possible features on the electronic band structure of a graphene nanoribbon: electron-electron and spin-orbit interactions, chirality effects due to the nanoribbon structure (width and crystallographic orientation) and local structure of the edge. This figure has been extracted from [128].

1.4 Thesis hypothesis and main goals

Throughout this introduction to the properties of graphene, we have highlighted the importance of characterizing how the ideal-graphene properties are modified in realistic systems as a way to tune them. The goal of this thesis is to explore different ways to achieve the controlled modification of graphene properties using different strategies: (i) interaction with the underneath substrate –both the effect of having different substrates and the contact between the two materials at the steps of the substrate–, (ii) defect-induced properties on graphene and (iii) adsorption of simple aromatic molecules on graphene to form SAMs.

To analyze these problems, apart from experimental observations, a theoretical atomistic description able to account for the electronic structure of each atom is needed. In order to achieve this, we have used first principle atomistic simulation methods based in the density functional theory (DFT). However, the problem of these systems is that they present a high complexity and their simulation has demanded to push the simulation techniques to their limit. All of them are systems whose study carried great simulation challenges. Starting with the case of the G-edges on substrate steps, on which the lack of symmetry of the system requires to design complex supercells which are still a good description of the problem and on which we had to use our own STM simulation method reproduce the experimental results; or the characterization of point defects, which required simulation cell sizes not previously achieved for such systems and an unusually

high number of k-points even for the largest cell sizes; to the study of the SAMs formation in graphene, for which we have explored the most recent dispersive forces implementations, essential for our calculations, and reached accuracies of the order of a meV/molecule in the energies; these problems are a major theoretical challenge of great computational complexity.

In order to accomplish this goal, in this thesis, we have followed three main research lines:

Study of the interaction of graphene edges with metal steps. In the first of them, we take advantage of the first experiments, performed with scanning tunneling microscopy (STM), which obtain information at the atomic scale about the structural characterization of metal-graphene contacts at Pt(111) steps, to study their properties. The combination between theory and experiment allows us to identify an electronic state associated with the graphene edge which appears just at the contact and which is localized in one of the graphene sublattices. Moreover, we analyze the structure of this contact and, in particular, how the edge states of the graphene are modified by the presence of the metal surviving the contact and even transmitting to the first row of metal atoms. We have also studied how the metal-graphene interface structure is related with the frequency on which certain Moirés appear in the experiments. We prove that apart from the influence of the intrinsic stability dictated by the mismatch between the two lattices, the geometry and orientation favoured by the metal steps –which is where the nucleation of the graphene sheet preferentially starts– also play an important role on this. With this study we have contributed to understand the properties of the metal-graphene contacts whose characterization is a necessary step for developing atomically precise graphene-based technology.

Characterization of arising properties by the presence of monovacancies in graphene. In the next work, we study through large scale *ab initio* simulations the electronic and mechanical properties induced in graphene by the presence of the simplest of all the point defects presented before: the monovacancies. From the point of view of the electric properties, it had been observed experimentally that graphene sheets have magnetic properties. Theoretically it was predicted that monovacancies could be the explanation for this induced-magnetism in graphene[63,122,138,139], but the type of magnetism produced is still not well understood. In the previous literature there was controversy between theoretical works which predicted a different values for the local magnetic moment induced by monovacancies which the experimental evidences were unable to elucidate[38]. While DFT calculations based on clusters predicted a value of 2 μ_B[64], similar calculations

in extended systems claimed it was 1 μ_B [66]. Our calculations on systems with up to a $G(30 \times 30)$ cell size on which we used several thousand k-point meshes –which make them a challenging computational problem– show a clear tendency to converge the local magnetic moment of a low concentration of monovacancies –diluted limit– to 2 μ_B. Regarding the mechanical properties, there are experimental evidences which support an unexpected increasing of the graphene stiffness in the presence of a low concentration of vacancies [127]. However, an atomistic and more fundamental explanation was still missing. Thank to our calculations, we conclude that, even when the presence of monovacancies does not practically affect the in-plane deformations, they induce a strain field that clearly quenches the out-of-plane vibrations, making the defective sample stiffer than its pristine version for a low concentration of vacancies even at room temperatures. Therefore, this would not only affect the stiffness of the sheet but also any other mechanical properties which are dependent on the fluctuations.

Study of the SAMs formation mechanisms on top of graphene on weakly interacting substrates. Finally, we study the SAMs formation on weakly interacting systems. We have studied the most simple case allowing for SAMs formation –due to the presence of hydrogen bonds– on a weakly interacting substrate. In particular, we analyze monolayers of 1,3,5-Triazine on both graphite and G/Pt(111) performing an exhaustive theoretical characterization of these systems supported by experimental evidences [140,141]. In both cases the STM experiments show large molecule islands with Moiré patterns. However, due to the effect of the substrate on which the graphene is grown, both the molecular diffusion barriers and the intermolecular distance changes. Thank to this experimental data, we have been able to understand how the energy balance is controlled between the adsorption of the molecules to the substrate, for which the van der Waals attraction and Pauli repulsion are important; and the intermolecular interaction among them, mediated by hydrogen bonds and van der Waals. In our DFT calculations we have explored the precision limits of the state-of-the-art techniques using both different DFT functionals –standard PBE and hybrids– and several dispersion forces implementations [142–147] to model the system. Moreover, we have had to develop a methodology in order to characterize each interaction since, due to the large size of the experimental Moirés, a direct simulation of the system was computationally out of reach. From our study we conclude that, although the molecule-substrate interaction –mediated by π orbitals– is weak, it is still large enough to determine the relative orientation of the molecules with respect to the substrate. However, we find discrepancies regarding the diffusion barriers –which are systematically lower than in the experiments– and also related to the differences generated by the change of

substrate. This exhaustive characterization shows the theoretical limitations to describe these weakly interacting systems even using the state-of-the-art methods. Therefore, these systems are a good test for the development of these theories.

In summary, this set of studies are a contribution in the search for methods that will allow us to control and modify the properties of graphene. These works have a double usefulness. From the point of view of the object of study, we have characterized how can we change the properties of graphene through the interaction with other materials or the deformation of its ideal two-dimensional lattice. Moreover, regarding the calculation techniques used, we have tested the latest advances in simulation methods for which this type of analysis in realistic systems are very useful for further developments.

CHAPTER 2

CHARACTERIZING GRAPHENE: THEORETICAL AND EXPERIMENTAL TOOLS

Given the nature of this field of research, there is a close-knit relationship between experiments and theory; a study is usually much more fruitful and interesting when it has these two components. In this thesis which is purely theoretical we have performed simulations based in density functional theory (DFT) but there has been a very close collaboration with different experimental groups. The combination between experiment and theory has been decisive to our findings. Therefore, this chapter is fundamentally devoted to give a perspective on the standard theoretical fundamentals and formalisms used and, more specifically, the ones that have been used to deal with these research projects. We do not forget, however, the experimental contributions to these researches whose main techniques will be briefly introduced at the end of the present chapter.

2.1 The origin of Density Functional Theory

Solving the Schrödinger[148] equation for systems of interacting particles is an impossible task except for some very simple cases. This difficulty promoted the appearance of different approaches created to deal with these complex systems. The most accurate way to describe a system is in terms of the many-body wave functions through the Schrödinger equation which contains information about both the ions and the electrons and can be written as

$$E\psi(\mathbf{r},\mathbf{R}) = \left[-\frac{\hbar^2}{2\mu}\nabla^2 + V(\mathbf{r},\mathbf{R})\right]\psi(\mathbf{r},\mathbf{R}), \tag{2.1}$$

where ψ is the wave function for both the electrons ($\mathbf{r}$) and ions ($\mathbf{R}$) of the quantum system and $\hat{H}$ the Hamiltonian operator which characterizes the total energy of any given wave function and which can be written in terms of the kinetic (T) and interaction potentials

(V) of both the electrons (e) and nuclei (N) as

$$\hat{H} = T_e + T_N + V_{ee} + V_{NN} + V_{eN} \tag{2.2}$$

This hamiltonian can be simplified by means of the Born–Oppenheimer (BO) approximation[149] which assumes that the motion of the atomic nuclei and the electrons in a system can be separated. It rests on the fact that the nuclei are much more massive than the electrons, which allows us to say that the nuclei are nearly fixed with respect to electron motion. Thus, this new hamiltonian is purely concerned with electronic dynamics and can be written as

$$\hat{H}_e = T_e + V_{ee} + V_{eN} \tag{2.3}$$

With this approximation the the movement of ions and electrons are decoupled thank to the difference in time regimes for each part of the problem. The ion movement can be treated classically –as if they were affected by an effective potential created by the electrons– and the electronic part will be studied quantum-mechanically.

Although simplified, this problem is still impossible to solve for complex systems due to the electron-electron interaction term. What DFT provides is a way to replace the problem of finding the Schrödinger many-body wave function by the minimization of the energy through the electronic charge density $n(\mathbf{r})$ solving the electron-electron interaction. The so-called *ab initio* or first principle methods solve the Schrödinger equation without the need of including external parameters –unlike semiempirical methods–, but the problem in this case is that you have to know the density functional. Methods based in DFT provide a good balance between accuracy and computational efficiency, a key feature for the practical application of first principles simulation techniques complex material problems.

As it will be detailed below, the starting point for the DFT methods was the two Hohenberg-Kohn theorems[150]. The first one demonstrates that the ground state properties of a many-electron system are uniquely determined by an electron density that depends on only 3 spatial coordinates laying the groundwork for reducing the many-body problem of N electrons with 3N spatial coordinates to 3 spatial coordinates, through the use of functionals of the electron density. The second of these theorems defines an energy functional for the system and proves that the correct ground state electron density minimizes this energy functional. Based on these theorems, the Kohn–Sham equations[151] transform the intractable many-body problem of interacting electrons in a static external potential to a tractable problem of non-interacting electrons moving in an effective potential. The effective potential includes both the external potential and the so-called exchange-correlation interactions. Modeling the latter two interactions becomes the main

difficulty of this method. In order to apply this methodology, several approximations to this exchange-correlation term have been developed over the years. The main ones will be commented in the following sections.

The most standard implementations of DFT methods properly describe covalent, metallic an ionic bonds, but there are other interactions as the van der Waals dispersion forces are not well described by these common approaches. In this context, in this chapter we will pay an extra attention to the inclusion of these dispersion forces [152] in our calculations as they are very relevant interactions in the systems that we have analyzed in this thesis.

In practical terms, there is more ingredients in the DFT simulations that have to be carefully chosen depending in the system that you are dealing with and the features that you want to study. You have to chose a good pseudopotential to describe the core electrons appropriate for what you want to describe; a proper basis set to describe the wave functions, either a more accurate plane-waves basis or a more optimized localized-orbitals basis; and suitable convergence parameters, since the k-point mesh necessary for calculations with periodic boundary conditions (PBC) to the electronic/ionic relaxation criteria and the energy grids/cutoffs among other parameters that can be tunned.

When you are choosing all these parameters you have to think not only to adequate them to your particular problem but also you have to take into account the computational restrictions of your code both in terms of time and resources. The larger you cell-size and your system, and the finer your criteria, the more demanding your calculation will be. However, there are different computational techniques to reduce this computational cost as well as parallelization schemes which are implemented in most of the available codes which enable the user to run a calculation in many processors at the same time. In this chapter we will also talk about the specifics of the codes that we have mainly used in our calculations –Vienna Ab initio Simulation Package (VASP) [153] and Open source package for Material eXplorer (OpenMX) [154,155]–.

In this chapter we will briefly introduce the basis of the DFT methods. We will start with the methodology that make DFT possible (Hohenberg-Kohn, Kohn-Sham), then we will comment how a functional is built and tuned to the system we want to deal with and other ingredients of the calculation. We will finish the theoretical introduction by discussing different ways to simulate STM images. We conclude this chapter presenting the main experimental techniques related with the work of this thesis.

2.1.1 The Hohenberg-Kohn theorems

DFT was given a formal footing by the two theorems introduced by Hohenberg and Kohn[150]. They can be applied to any system consisting of electrons moving under the influence of an external Coulomb potential arising from the nuclei, $V_{ext}(\mathbf{r})$. As a result of the BO approximation[149], it is treated as a static external potential which can be written as follows

$$V_{ext}(\mathbf{r}) = -\sum_{\alpha} \frac{Z_\alpha}{|\mathbf{r}-\mathbf{R}_\alpha|}, \tag{2.4}$$

where Z_α is the potential contribution of the α ion which is at the $\mathbf{R}_\alpha$ position.

First theorem *The external potential, $V_{ext}(\mathbf{r})$, and hence the total energy, is a unique functional of the electron density, $n(\mathbf{r})$, to within an additive constant.*

Hence, the energy functional can be written as follows

$$E[n(\mathbf{r})] = \int n(\mathbf{r})\, V_{ext}(\mathbf{r})\, d\mathbf{r} + F[n(\mathbf{r})], \tag{2.5}$$

where $F[n(\mathbf{r})]$ is an universal (*i.e.* the same for all atoms) functional of the electron density $n(\mathbf{r})$ only. A Hamiltonian $\hat{H}$ for the system can be written as the addition of the external potential, $\hat{V}_{ext}$, and $\hat{F}$, which is the electronic contribution consisting on the kinetic energy, $\hat{E}_k$, and the electron interaction term, $\hat{E}_{e-e}$. Therefore, we have

$$\hat{H} = \hat{F} + \hat{V}_{ext} = \hat{E}_k + \hat{E}_{e-e} + \hat{V}_{ext}, \tag{2.6}$$

where

$$\hat{F} = \hat{E}_k + \hat{E}_{e-e} = -\frac{1}{2}\sum_i \nabla_i^2 + \frac{1}{2}\sum_i \sum_{j\neq i} \frac{1}{|\mathbf{r}_i - \mathbf{r}_j|} \tag{2.7}$$

and

$$\hat{V}_{ext} = \sum_i V_{ext}(\mathbf{r}_i). \tag{2.8}$$

In this equation, $\hat{F}$ is the same for all N-electron systems, so that the Hamiltonian, and hence the ground state $|\psi_0\rangle$, are completely determined by N and $V_{ext}(\mathbf{r})$. The ground state $|\psi_0\rangle$ for this Hamiltonian gives rise to a ground state electronic density $n_0(\mathbf{r})$. Thus, the ground state $|\psi_0\rangle$ and density $n_0(\mathbf{r})$ are both functionals of the number of electrons N and the external potential $V_{ext}(\mathbf{r})$.

Second theorem *The electron density, $n(\mathbf{r})$, that minimizes the total energy, $E[n(\mathbf{r})]$, is the exact ground state density $n_0(\mathbf{r})$.*

Therefore, DFT has replaced the problem of solving the 3N-variable Schrödinger equation by a variational problem of minimising the energy functional $E[n(\mathbf{r})]$ with respect to the electron density $n(\mathbf{r})$. The next step is coming up with a scheme to get a reasonable energy functional to describe our problem.

2.1.2 The Kohn-Sham equations

Although the Hohenberg-Kohn theorems are extremely powerful, they do not offer a way of computing the ground-state density of a system in practice. About one year after Hohenberg and Kohn published their original work, Kohn and Sham[151] devised a simple method for carrying out DFT calculations, that retains the exact nature of DFT. Here we will describe this method.

In order to take advantage of the power of DFT without sacrificing accuracy, they followed a method to map the problem of the system of interacting electrons onto a fictitious system of non-interacting electrons with the same charge density

$$n(\mathbf{r}) = \sum_{i=1}^{N} \left|\psi_i(\mathbf{r})\right|^2, \tag{2.9}$$

being $\psi_i(\mathbf{r})$ the one-electron wave function.

The interacting system energy is written as a functional of the electron density divided in four contributions

$$E[n(\mathbf{r})] = E_k^0[n(\mathbf{r})] + E_{ext}[n(\mathbf{r})] + E_H[n(\mathbf{r})] + E_{xc}[n(\mathbf{r})] \tag{2.10}$$

which are, respectively, the kinetic energy of the non-interacting electron gas (not the same as that of the interacting system), the interaction energy with the external potential, the interaction energy with the Hartree potential (the classical electron-electron energy) and the so-called exchange-correlation energy (which contains the non-classical electron-electron interaction energy and the difference between the kinetic energies of the interacting and non-interacting systems).

The first three are defined as follows

$$E_k^0[n(\mathbf{r})] = \sum_{i=1}^{N} \int d\mathbf{r}\, \psi_i^*(\mathbf{r}) \left[-\frac{\nabla^2}{2}\psi_i(\mathbf{r})\right], \tag{2.11}$$

$$E_{ext}[n(\mathbf{r})] = \int d\mathbf{r}\, n(\mathbf{r})\, V_{ext}(\mathbf{r}) \tag{2.12}$$

and

$$E_H[n(\mathbf{r})] = \frac{1}{2}\int d\mathbf{r}\, d\mathbf{r}' \frac{n(\mathbf{r})\, n(\mathbf{r}')}{|\mathbf{r}-\mathbf{r}'|}. \tag{2.13}$$

On the other hand, the exchange-correlation term is defined as the correction needed to reach the exact solution. By this energy splitting we can separate the first terms, which can be easily dealt with, from the last term, which contains the complex behaviour effects but represents a small contribution to the total energy. The different approximations to the calculation of this unknown E_{xc} term, which will be discussed later, give rise to a wide range of DFT methods and, surprisingly, even the simpler approaches work nicely.

The Kohn-Sham equations are found by varying the total energy expression with respect to a set of orbitals, introducing a Lagrange multiplier μ to constrain the number of electrons to be N, from which the following expression is obtained

$$\frac{\delta E_k^0[n(\mathbf{r})]}{\delta n(\mathbf{r})} + V_{KS}(\mathbf{r}) = \mu, \tag{2.14}$$

in which the Kohn-Sham potential $V_{KS}(\mathbf{r})$ is given by

$$V_{KS}(\mathbf{r}) = V_{ext}(\mathbf{r}) + V_H(\mathbf{r}) + V_{xc}(\mathbf{r}) \tag{2.15}$$

being V_H the electronic interaction hartree potential

$$V_H(\mathbf{r}) = \int \frac{n(\mathbf{r}')}{|\mathbf{r}-\mathbf{r}'|} d\mathbf{r}' \tag{2.16}$$

and the exchange-correlation potential can be, then, defined as

$$V_{xc}(\mathbf{r}) = \frac{\delta E_{xc}[n(\mathbf{r})]}{\delta n(\mathbf{r})}. \tag{2.17}$$

The important point to realize here is that equation 2.14 is precisely the same equation which would be obtained for a non-interacting system of particles moving in an external potential $V_{KS}(\mathbf{r})$. To find the ground state density $n_0(\mathbf{r})$ for this non-interacting system we simply solve the one-electron Schrödinger equations

$$\left[-\frac{1}{2}\nabla^2 + V_{KS}(\mathbf{r})\right]\psi_i(\mathbf{r}) = \varepsilon_i\, \psi_i(\mathbf{r}) \tag{2.18}$$

Since the Kohn-Sham potential, V_{xc}, depends upon the density it is necessary to solve these equations self-consistently for what an initial guess for the form of the density is used to solve the Schrödinger equation obtaining a set of orbitals with which a new

density is calculated. This process is repeated until the input and output densities are the same –according to a certain convergence criterion–. The correspondent energy for the interacting system can be easily obtained from this result and, provided that the exchange-correlation functional form is known, it will be exact. An approach for the electronic structure of the studied system, yielded by the selfenergies, ϵ_i, is also a direct result of this process. Although in this introduction it has not been treated specifically, these theorems can be generalized to treat spin degeneracy.

This electronic self-consistent process combined with a classical treatment of ions embedded in an effective potential created by the electrons enables DFT codes to find the ground-state of the studied system, perform a molecular dynamics simulation or characterize the phonons of the system. This separated treatment of the electronic and ionic part of or problem is provided by the BO approximation as was discussed above.

2.2 Building the energy functional

2.2.1 Chemical description and the exchange-correlation functionals

Kohn-Sham density functional theory is widely used for self-consistent-field electronic structure calculations of the ground-state properties of atoms, molecules and solids. As we have previously said, in this theory, only the exchange-correlation energy $E_{xc} = E_x + E_c$ as a functional of the electron spin densities $n(\mathbf{r})$ must be approximated. The most popular functionals have a form appropriated for slowly varying densities: the Local Density Approximation (LDA)[151] and the Generalized Gradient Approximation (GGA)[156].

However, these approximations are subject to several well-known deficiencies. In the quest for finding an *optimal* electronic-structure method, that combines accuracy and tractability with transferability across different chemical environments and dimensionalities, many new approaches, improvements and refinements have been proposed over the years. These have been classified by Perdew[157] in his *Jacob's ladder* hierarchy (see Fig. 2.1).

Local Density Approximation (LDA)

This approximation, which was proposed already in the famous paper of Kohn and Sham[151], was designed to work with smooth electronic charge densities as in metals or intrinsic semiconductors, although has proven to work too with covalent crystals. Despite its simplicity, produces surprisingly good results. However, its well-know that it overestimates the bond lengths and underestimates binding energies.

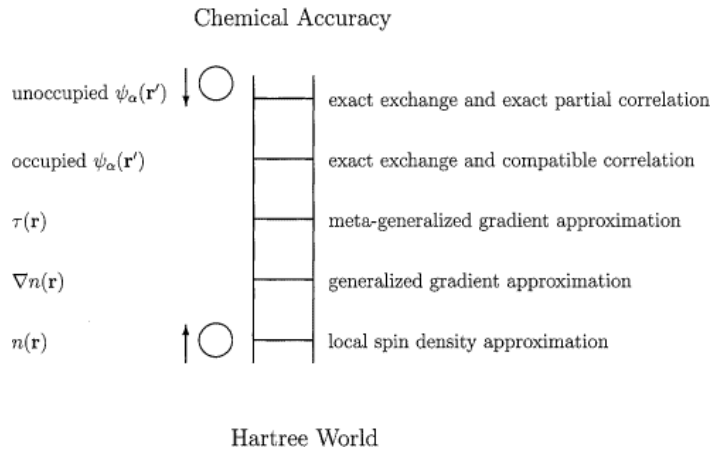

Figure 2.1 In the *Jacob's ladder of density functional approximations*, earth is the Hartree approximation ($E_{xc} = 0$), and heaven is the realm of high accuracy. The strategy behind the construction of the ladder is to try to include additional exact constraints into approximations beyond the LDA, in the hope that they will make the functional even more accurate. This figure has been extracted from [157].

This functional is given by

$$E_{xc}^{LDA}[n(\mathbf{r})] = \int \varepsilon_{xc}^{ug}[n(\mathbf{r})]\ n(\mathbf{r})\ d\mathbf{r} \tag{2.19}$$

where ε_{xc}^{ug} is the exchange-correlation energy functional for a uniform gas, which is well established [158].

Generalized Gradient Approximation (GGA)

The GGA [156] is a step towards a higher precision as it includes not only the density but also the gradient of the density contribution to the exchange correlation energy. The equation 2.19 becomes

$$E_{xc}^{GGA}[n(\mathbf{r})] = \int \varepsilon_{xc}[\nabla n(\mathbf{r}), n(\mathbf{r})]\ n(\mathbf{r})\ d\mathbf{r} \tag{2.20}$$

In comparison with LDA, the GGA functional tends to improve total energies, atomization energies, energy barriers and structural energy differences, although it systematically underestimates insulator characteristic gaps. It expands and softens atomic bonds, an effect that sometimes corrects and sometimes overcorrects the LDA prediction.

The most commonly used GGA functional is PBE, which was named after its creators: Perdew, Burke, and Ernzerhof [159]. It retains the correct features of LDA and combines them with the most energetically important features of gradient-corrected nonlocality. Among its improvements over previous GGA functionals it includes an accurate description of the

linear response of the uniform electron gas, correct behavior under uniform scaling, and a smoother potential.

Hybrid energy functionals

Hybrid functionals are approximations that incorporate a contribution of exact exchange from Hartree-Fock theory with exchange and correlation calculated *ab initio*. This hybrid approach was introduced by Becke[160]. Hybridization with the exact Hartree-Fock exchange provides a simple scheme for improving many molecular properties (such as atomization energies, bond lengths or vibration frequencies) which are usually poorly described with the previously discussed functionals. However, the description improvement comes with a high computational cost.

One of the simplest of these is the *PBE0* hybrid[161,162] which mixes a fraction of exact exchange with a complementary fraction of *PBE* exchange and full *PBE* correlation as follows

$$E_{xc}^{PBE0} = \frac{1}{4}E_x^{HF} + \frac{3}{4}E_x^{PBE} + E_c^{PBE}. \tag{2.21}$$

In the calculations that we will present in this thesis we have used the *HSE06*[163] variant of the Heyd-Scuseria-Ernzerhof (HSE) [164,165] screened hybrid functional family where only short-range exact-exchange is admixed, with the aid of an empirical range-separation parameter, such that it approaches PBE0 in the short-range and PBE in the long-range. This way, it retains only short-range Fock exchange and preserves the accuracy of PBE0 while avoiding the cost and pathologies of long-range Fock exchange. By construction of the HSE, the computational time needed for these calculations is within a factor of 2-4 of pure DFT calculations while previous hybrid calculations (as PBE0) needed significantly more memory and CPU time. As we were saying, the distinction between long range (*LR*) and short range (*SR*) contributions of the electron-electron interaction is only present in the exchange interactions. The electronic correlation is represented by the corresponding part of the PBE density functional. Thus, the exchange-correlation term can be written

$$E_{xc}^{HSE} = aE_x^{HF,SR}(\mu) + (1-a)E_x^{PBE,SR}(\mu) + E_x^{PBE,LR}(\mu) + E_c^{PBE} \tag{2.22}$$

where a is the Hartree-Fock mixing constant and μ is the parameter that defines the range-separation, and is related to a characteristic distance ($2/\mu$) at which the short-range interactions become negligible. For the specific case of the *HSE06* functional, these parameters take the values $a = 0.25$ and $\mu = 0.2$. Notice that for the same a value and $\mu = 0$ the *PBE0* expression is recovered.

Random Phase Approximation

The fifth-rung functionals in Fig. 2.1 are the functionals based on the random phase approximation (RPA) [166–168]. It is a many-body approximation that includes unoccupied Kohn–Sham orbitals, unlike the first four rungs, which use only the occupied orbitals. RPA is nearly exact for the long-range part of the exchange-correlation hole, but the short-range part is not so well described. RPA can actually be useful for materials science, even without a correction, due to a remarkable cancellation of errors. Traditionally, for molecules, the error cancellation has been some what imperfect [169], so by itself the RPA was not very useful. A non-empirical nonlocal correction to RPA was required to solve this problem. The main disadvantage of the RPA functionals is that they make the calculations very expensive in terms of computational resources. For this reason they were not considered as an option to deal with the problems that we have faced in this thesis.

2.2.2 Accounting for the van der Waals dispersion in the calculations

The so-called van de Waals (vdW) forces were firstly identified by Johannes Diderik van der Waals in 1873 [152]. In the chemistry community all intermolecular attractions are known collectively as van der Waals forces. According to this nomenclature, vdW forces account for both electrostatic interactions, dipole-dipole interactions –where the hydrogen bonds are a particular case considered separately because is more energetic– and for even weaker interactions between non-polar molecules –instantaneously induced dipoles–. London dispersion [170], also known as dispersion forces, are specifically limited to this weaker interactions between non-polar molecules. Dispersion forces, thus, are a particular case of vdW forces, although in the literature the two terms are used interchangeably to mean weak interactions between non-polar molecules. In this thesis we have also used these two terms, vdW or dispersion forces, to refer to the dispersion forces.

The vdW force is present everywhere, but its variation from one environment to another and its complex manifestations still pose challenging questions. They are relevant for a wide range of systems such as soft matter, surfaces, and DNA, and in phenomena as different as supramolecular binding, surface reactions, and the dynamic properties of water. However, a general theoretical framework that can describe small molecules as well as extended systems is still needed.

Like all non-relativistic electronic effects, the vdW interactions would be present in the exact DFT functional but, as it has been discussed in previous sections, the exchange-correlation term is often evaluated following different approximations that do not include

the full vdW interactions resulting from dynamical correlations between fluctuating charge distributions.

A suitable theory for atoms, molecules and, in general, condensed matter, should account for all forces at play, including covalent bonds, hydrogen bonds, and electrostatic interactions, because they are all relevant in typical materials and systems. Proper inclusion of vdW interactions in DFT calculations requires that the total energy functional depends on the electron density $n(\mathbf{r})$ in a manner that reflects both the long-ranged and medium-ranged nature of vdW interactions. By construction, standard exchange-correlation functionals –LDA, GGA or hybrid functionals– neglect the long-range, nonlocal correlations that give rise to the vdW forces. Although this is a long known problem, a definitive solution has not been found yet and, at present and mostly since recently, a lot of different researching groups are working on different implementations to include vdW interactions in standard functionals [147,171].

There are two separate groups of methods: (i) those which are based on calculating atom-based London dispersion forces [142,145,172–178], some of those also with the inclusion of advanced screening mechanisms [145,177,179,180]; and (ii) the implementations which follow a first-principles DFT treatment of the long-to-medium-ranged interactions between fragments across regions with low densities such as the one proposed by Dion *et al.* [181] which is a non-local correlation functional that approximately accounts for dispersion interactions.

Next we will describe some of those implementations, especially those that we have used in our work due to their suitability for our systems.

Atom-based vdW corrections

As we have already introduced, these energy corrections are atom-based London dispersion forces of the pairwise C_6/R^6 kind. The difference between them is how they calculate the C_6 coefficients. An advantage of these approaches is that the specific vdW contribution can be easily extracted from the total energy easing the analysis of its effect in the general behaviour of the studied systems. A lot of approaches belong to this group. We will now present the ones that we have used in our calculations for being the most widely used in some cases and specially indicated for graphene simulation.

Grimme's DFT-D A pragmatic method to work around this problem has been given by the DFT-D approach [172,173]. It consists in adding a semi-empirical dispersion energy to the conventional Kohn-Sham DFT energy. By semi-empirical, one typically refers to methods that rely on optimization to reference systems for which data from accurate, computation-

ally expensive methods are available. As we detail below, the dispersive energy is described by damped interatomic potentials of the form C_6/R^6 on which the vdW contribution is independent of the charge density. This family of implementations is probably the most widely applied (according to the number of cites of the main references [142,172,173], that add more than 10000 cites), partly due to its computational efficiency, and also because it is a very well tested method. The energy is calculated as follows

$$E_{DFT-D} = E_{DFT} + E_{disp}, \tag{2.23}$$

where

$$E_{disp} = -s_6 \sum_{i,j<i}^{N_{atoms}} f_{damp}\left(R_{ij}\right) \frac{C_6^{ij}}{R_{ij}^6}, \tag{2.24}$$

being N_{atoms} the total atom number, R_{ij} the distance between atoms i and j, s_6 is a scaling parameter depending on the choice of the DFT functional used and the C_6^{ij} denotes the dispersion coefficient for the atom pair ij. In order to avoid double counting in the energy for small R [1], a damping function f_{damp} must be used, which is given by

$$f_{damp}\left(R_{ij}\right) = \left(1 + e^{-d\left(R_{ij}/R_r - 1\right)}\right)^{-1}, \tag{2.25}$$

where R_r is the sum of atomic vdW radii [172] and d is a fitting parameter. The basic strategy in the development to restrict the density functional description to shorter electron correlation lengths scales and to describe situations with medium to large interatomic distances by damped $C_6 \cdot R^6$ terms seems to be very successful, as demonstrated for some notoriously difficult reactions.

- In the DFT-D2 variant [142], a second version of the DFT-D method refined regarding higher accuracy, the van der Waals interactions are described via a simple pair-wise force field, which is optimized for several popular DFT functionals. The C^{6ij} coefficients are usually optimized to nicely reproduce the results contained in big databases computed with the more advanced computational methods. In this particular case, a simple computational scheme was proposed to calculate the atomic C^{6ij} coefficients derived from the London formula for dispersion and based on DFT/PBE0 calculations of atomic ionization potentials and static dipole polarizabilities [142,162]. The simplicity and computational efficiency of this approach along with the fact that works very good with the systems that we have simulated made it a natural candidate to use in our calculations.

[1] Notice that standard DFT functionals already take into account corrections of this distance range

- In the DFT-D3 variant[173], unlike in the D2 case where they are fixed beforehand, the dispersion coefficients C^{6ij} are geometry dependent as they are adjusted on the basis of local geometry (coordination number) around atoms i and j. Thus, although the computation of the vdW contribution is still pairwise, the previous calculation of the C^{6ij} coefficients can involve more than two atoms. This represented a big improvement in the description of metal surfaces in particular, given that in the original D2 they were treated as if they were on a atomic configuration. This is fixed with the D3 scheme thank to its approach to calculate the C^{6ij} coefficients. This is an improvement over the DFT-D3 which slightly increases the computational cost of the simulation with respect to DFT-D2 but is still very promising and worth to be tested in our calculations.

Tkatchenko and Sheffler's TS+SCS The expression for the dispersion energy within the DFT-TS method[176] is formally identical to that of DFT-D2 method previously introduced. However, the important difference is that the dispersion coefficients and damping function are charge-density dependent. They are not tabulated or provided from the beginning of the calculation like in DFT-D2. The DFT-TS method is able to take into account variations on the contribution of the atoms due to their local chemical environment. The polarizability, dispersion coefficients, and atomic radii of each atom are computed from their free-atomic values. In other words, the vdW parameters are functionals of the electron density $n(\mathbf{r})$, hence they respond to changes in the electron density induced by hybridization, static charge transfer, and other electron redistribution processes.

A computationally efficient way to account for electrodynamic response effects, in particular the interaction of atoms with the dynamic electric field due to the surrounding polarizable atoms, was implemented in later developments[145] giving rise to the TS+SCS method. In this approach the frequency-dependent screened polarizabilities are obtained by solving the self-consistent screening equation. We have used this last implementation in our calculations in the aim of being as much accurate as possible.

Many-body dispersion (MBD) To move beyond the traditionally employed second-order pairwise additive approximations, Tkatchenko's group has recently (2014-2015) developed the so-called many-body dispersion (MBD) method[146,147]. The MBD is computed by considering a system of coupled quantum harmonic oscillators. The short-range part of the dipole interaction is used to self-consistently compute the screening –or long-range Coulomb response– that effectively modifies the polarizabilities of the species in the system which, in turn, are employed as the input in the MBD energy expression. The

resulting many-body dispersion energy contains two different contributions. The first one deals with this electrodynamic response screening and the other one arises from a non-additive many-body energy which is missing in simple pairwise dispersion approaches. We have used this approach for our calculations hoping that accounting for this polarizability effect in surfaces of graphene on metals would improve the description of our system.

DFT functional-based vdW corrections

These vdW *flavours* belong to the group of implementations on which the DFT kernel is modified to include the dispersion forces into the exchange-correlation term. The main representative of this group is the vdW-DF[181] family of approaches. In the line of what have just been said, the objective of vdW-DF –also referred to as vdW-DF1– is to provide within DFT an efficient method for calculations of vdW effects in all kinds of electron systems based on many-body physics and general physical laws. In this regard, the vdW-DF method differs from methods that use empirical, semi-empirical, and *ad hoc* assumptions for such calculations. The first versions of this implementation were very computationally demanding which made its use to be strongly restricted. This issue was solved by Román-Pérez *et al.*[182], which led the use of this method to become extended.

In general terms, in vdW-DF the non-local correlation is calculated so that the exchange–correlation energy takes the form

$$E_{xc} = E_x^{GGA} + E_c^{LDA} + E_c^{non-local} \tag{2.26}$$

where E_x^{GGA} is the GGA exchange energy, E_c^{LDA} accounts for the local correlation energy obtained within LDA and $E_c^{non-local}$ is the non-local correlation energy. The formula for $E_c^{non-local}$ is based on electron densities interacting via a model response function and the particular form is still a subject of research. A visualization of the problematic of this approach (which can be extended for the general vdW in DFT issue) is depicted in Fig. 2.2.

Klimeš's vdW-DF-opt functionals For some covalently-bound solids such as heavy transition metals, vdW-DF's account can even be inferior to that of standard GGAs. Motivated by this shortcoming, Klimeš and co-workers[184] designed two exchange functionals for vdW-DF called optB86b and optB88. These *opt* functionals arose, then, as a way to take advantage of the promising vdW-DF scheme for the efficient treatment of dispersion bonded systems but improving dramatically the accuracy both for dispersion and hydrogen bonded complexes through the judicious selection of its underlying exchange

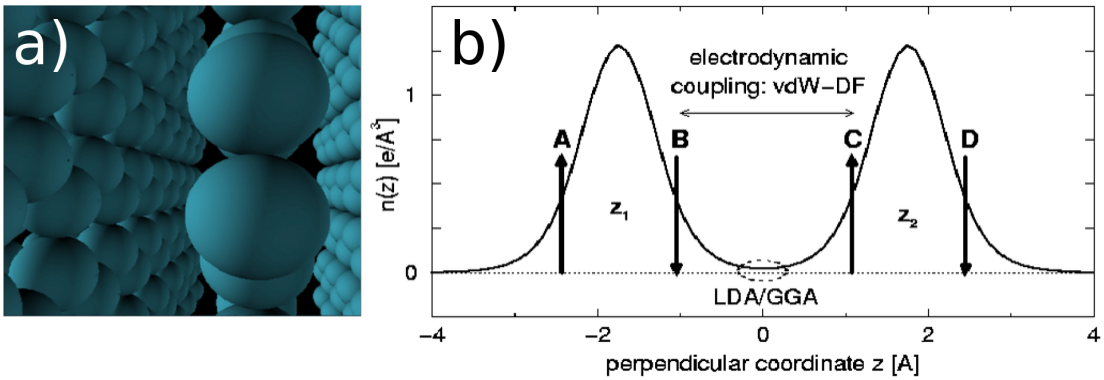

Figure 2.2 a) Ball-and-stick model of graphite. b) Schematic account of vdW forces in sparse, layered matter (two graphene sheets at equilibrium separation). Towards a background of laterally averaged electron density, the vertical arrows mark typical locations of charge fluctuations, the horizontal arrow the region of correlation between them and the dotted ellipse the very different region of relevance for GGA (and LDA). As vdW dispersion forces are characterized by charge fluctuations in one part of an atomic system electrodynamically correlated with charge fluctuations in another they are truely nonlocal. Common LDA/GGA DFT functionals depend on the density in local/semilocal ways and give no account of the nonlocal vdW interaction. Figure adapted from [183].

functional. In particular the vdW-DF-optB86 functional performs well for many other kinds of systems and, together with vdW-DF-optB88 [144], it has played an important role in showing that vdW-DF can handle systems characterized by weak chemisorption. For this reason, for our calculations we discarded the original vdW-DF implementation [181] and its next version vdW-DF2 [185] and tried the Klimeš functionals.

2.3 Periodic boundary conditions

In general terms, we are interested in solving the eigenvalues and eigenfunctions of the Hamiltonian of a crystal, meaning that our system will have a certain periodicity. To solve for such a problem, one must first consider the boundary conditions that the eigenfunctions must satisfy. Given that we will be interested in the characterization of extended systems, we will apply Bloch's theorem to write the wave function of a periodic system as follows

$$\psi_{\mathbf{k}}(\mathbf{r}) = e^{i\mathbf{k}\cdot\mathbf{r}}\, u_{\mathbf{k}}(\mathbf{r}) \tag{2.27}$$

on which the electronic eigen state, $\psi_{\mathbf{k}}(\mathbf{r})$, is written in terms of the plane wave, $e^{i\mathbf{k}\cdot\mathbf{r}}$, and a periodic function, $u_{\mathbf{k}}(\mathbf{r})$, called Bloch's function. In this equation, $\mathbf{k}$ are the wave vectors of the first Brillouin-zone (BZ) and the Bloch's function obeys the following periodicity

rule

$$\psi_{\mathbf{k}}(\mathbf{r}+\mathbf{R}) = e^{i\mathbf{k}\cdot\mathbf{R}}\,\psi_{\mathbf{k}}(\mathbf{r}) \tag{2.28}$$

where **R** is the periodicity of the system. Equations 2.27 and 2.28 are equivalent and both can be used to refer to Bloch's theorem.

To keep on with the description of our system we discretize the continuous variable **k** to computationally evaluate the integrals over the BZ needed to compute many properties such as energies and forces, the density of states, the charge density, matrix elements, response functions, etc. The number of **k**-points –and their weight– needed for your calculation can be optimized using an specific sampling for the BZ. There are several methods to choose the **k**-points meshes to use in a calculation.

Monkhorst-Pack

The most extended method is the scheme proposed by Monkhorst and Pack[186]. The idea is to create an equally spaced mesh in the BZ taking into account the symmetry of the system. When the mesh is selected you can choose to make it Γ-centered or not.

Chadi-Cohen

An alternative method for choosing k-point mesh was proposed by Chadi and Cohen[187]. In contrast to Monkhorst and Pack, the refinement of the k-point mesh to obtain higher sampling density is based on a recursive scheme. However, for cubic symmetry, the outcome of this algorithm can also be interpreted as a special Monkhorst-Pack grid.

2.4 Choosing the basis set

Another important ingredient in our computational method is the basis set type. A basis set is a set of functions which are combined in linear combinations to create atomic orbitals. In terms of computational efficiency one have to chose the minimal basis set which still reproduces well the properties of the system that are going to be analyzed. In order to build the effective wave functions in the periodic potential, there are two types of basis sets which are typically used: a set of localized orbitals centered on atoms[188] and the plane-wave (PW) basis sets[189,190]. Next, we will briefly introduce these two main methods and the corresponding codes for each of them that have used to perform the calculations presented in this thesis.

2.4.1 Plane-wave basis sets

DFT has been traditionally implemented using PW basis sets[190]. A PW basis set has the advantage of being mathematically simple and it completely spans the Hilbert space. PWs cover all space equally and are thus not biased to any particular region. This is particularly important when one does not have any *a priori* knowledge of the form of the electronic wavefunctions. Although in some cases this can be an advantage, it also results in regions with null electron density having equal quality of description as regions of high electron density. It is thus, in a sense, inefficient. Regardless of the presence of vacuum, PW DFT calculations show a cubic scale with system size[191]. Accordingly, most efforts at achieving methods that scale linearly with system size have concentrated upon localised basis sets[192–194]. The description of the Hilbert space can be improved continuously by increasing the number of PW of the basis, allowing to reach the required precision for each system as long as it is computationally possible. This makes this scheme the preferred on for medium-sized systems with high precision requirements. However, the use of this approach to study large systems is problematic due to the amount of computational resources (both CPU and memory) it requires. This is due to the large number of PWs needed to form a satisfactory basis set for the problem at hand (typically of the order 100 PWs per atom in the unit-cell).

Using the Bloch's functions that we have just introduced, the $u_{\mathbf{k}}(\mathbf{r})$ functions can easily be expanded on a plane-wave basis described by wave vectors belonging to the reciprocal lattice of the crystal. Being

$$u_{\mathbf{k}}(\mathbf{r}) = \sum_{\mathbf{G}} c_{\mathbf{k},\mathbf{G}}\, e^{i\mathbf{G}\cdot\mathbf{r}}, \tag{2.29}$$

we obtain that

$$\psi_{\mathbf{k}}(\mathbf{r}) = \sum_{\mathbf{G}} c_{\mathbf{k},\mathbf{G}}\, e^{i(\mathbf{k}+\mathbf{G})\cdot\mathbf{r}}. \tag{2.30}$$

This is an easy expansion and its main advantage is that its convergence is controlled by a single parameter which is the cutoff. The cutoff is the maximum value of $|\mathbf{G}|$ and although, for an exact description we would need an infinite number of these vectors, given that the most relevant contributions come from the wave functions with a small kinetic energy

$$E_k = \frac{\hbar^2 |\mathbf{k}+\mathbf{G}|^2}{2m}, \tag{2.31}$$

the expansion can be restricted to those terms with lower energy than the cutoff. The main advantages of this method, then, are the simplicity of the functions of the basis sets

and the easy control of the precision which can be adjusted with this cutoff –the higher the cutoff the larger the number of plane waves of the basis and the greater the accuracy–.

However, this expansion results to be inefficient when describing the inside of the atoms because wave functions of real materials have very different signatures in different regions of space: in the bonding region the wave function is fairly smooth, whereas close to the nucleus the wave function oscillates rapidly due to the orthogonality rule between the wave functions of valence electrons and the inner core electrons. This is the source of the difficulty of electronic structure methods to describe the bonding region to a high degree of accuracy while accounting for the large variations in the atom center.

In order to solve this problem, you can either use pseudopotentials to replace the ionic potential and the core electrons or use one of the augmented plane waves (APW) methods originally invented by Slater[195]. The strategy of the augmented-wave methods has been to divide the wave function into parts –*muffin-tin* approximation–, namely, a partial-wave expansion within an atom-centered sphere and envelope functions in the interstitial regions. The envelope function can be expanded into plane waves or some other convenient basis set (it can also be used for localized-orbital basis). Envelope function and partial-wave expansions are then matched with value and derivative at the sphere radius.

A more recent approach known as projector-augmented-wave (PAW) method[196] generalizes both the pseudopotential method and the linear APW (LAPW) method[197] in a natural way and allows for DFT calculations to be performed with greater computational efficiency. The augmentation procedure is generalized in a way that partial-wave expansions are not determined by the value and the derivative of the envelope function at some *muffin-tin* radius, but rather by the overlap with localized projector functions. The pseudopotential approach based on generalized separable pseudopotentials can be regained by a simple approximation.

For the thesis projects, when we have needed to work with PW basis, we have used the code that we describe below.

Vienna Ab initio Simulation Package (VASP)

The Vienna Ab initio Simulation Package (VASP)[153] is a computer program for atomic scale materials modelling from first principles. It computes an approximate solution to the many-body Schrödinger equation, either within DFT, solving the Kohn-Sham equations, or within the Hartree-Fock (HF) approximation. Hybrid functionals that mix the HF approach with DFT are implemented as well. In VASP, central quantities, like the one-electron orbitals, the electronic charge density, and the local potential are expressed in

plane wave basis sets. The interactions between the electrons and ions are described using norm-conserving or ultrasoft pseudopotentials, or the PAW method.

In the calculations performed for this thesis we have used the DFT operation mode of this code with PAW potentials. In this context, this code is well MPI-parallelized to run in 32-64 processors for calculations with a single k-point. It is also parallelized for k-points allowing a larger number of processors for larger k-point meshes. The system size limit for this code is around a few hundred atoms. The standard/default cutoff energies for the PW basis sets for PAW functionals are also around 100-300 eV depending on the chemical specie. Given the parallelization limitations of this code, for big system sizes the code has to be pushed to its limit when very higher accuracy is needed. The standard convergence criteria for the electronic and ionic relaxations are $1 \cdot 10^{-4}$ eV and $1 \cdot 10^{-2}$ eV/Å. In Chapter 5, the precision requirements have forced to go to the limits in terms of cutoffs and the convergence criteria which are finer than the standards in both cases (see the details in the methods section of the Chapter).

2.4.2 Localized-orbital basis

The alternative local-orbital DFT methodology is more similar to the standard quantum-chemical approaches and it describes the effective wave functions as a superposition of localized-orbitals centered in each unit cell. This method does not present the computational problem of PW since good basis sets can be obtained with a reduced number of orbitals. The wave functions, then, can be expressed in terms of the localized-orbitals, ϕ, as follows

$$\psi_{\mathbf{k}}(\mathbf{r}) = \frac{1}{\sqrt{N}} \sum_{k} \sum_{\mu} \sum_{\mathbf{R}} e^{i\mathbf{k}\cdot\mathbf{R}} \phi_{\mu}(\mathbf{r} - \mathbf{R}), \tag{2.32}$$

where μ is a combined index, $\mu \equiv (\alpha, l, m)$, that refers to the particular atom, α (at $\mathbf{R}_{\alpha}$), atomic subshell l (*e.g.* $3s, 4s, 3p, 3d$), and angular component m (*e.g.* p_x, p_y, p_z).

This equation verifies the Bloch's theorem and is called Bloch sum. This localized-orbitals ϕ can be expressed using Gaussian functions, Slaters[198] or numerical atomic orbitals (NAOs) such as *Fireball*[199] whose particularity is that they exactly vanish out of a cutoff radius. This way of building your wave functions is known as local combination of atomic orbitals (LCAO).

In the context of a localized-orbitals scheme, a very important point is the definition of a suitable optimized local-orbital basis set for the problem we wish to analyze. In the particular case of the *Fireball* orbitals, the cutoff radii of the functions are very sensible parameters. These NAOs are obtained by solving the atomic problem with the boundary condition that the orbitals go to zero at and beyond a given cutoff radius r_c. In other

words, in the definition of the *Fireball* NAOs the confining potential is zero for $r < r_c$ and is infinitely high for $r > r_c$. The *Fireball* NAOs are thus strictly short-ranged. Therefore, the r_c have to be carefully chosen in order to adjust the results to a good description of your system properties. Apart from the range or spatial extension of the orbitals fixed by r_c, other parameters to take into account are the size, related with the number of atomic orbitals per atom which depends on the required accuracy and available computational power, and the shape of the radial part. Once the minimal basis is built, the interactions between the orbitals have to be computed.

Localized orbitals methods usually use an uniform real-space grid representation of the electronic wave functions. This offers several advantages, most notably good computational scalability and systematic convergence properties. On the other hand, in real space it is possible to work entirely with local and semi-local operations which enables efficient parallelization with small communication overhead. The accuracy of a real-space representation can be increased systematically by decreasing the grid spacing, similar to increasing the kinetic energy cut-off in a PW calculation.

As plane waves codes are more trustworthy due to their asymptotic convergence with the cutoff, they are usually employed to get some benchmarks when working with localized orbitals codes. Apart from their performance advantages coming from the power of description of a system with a minimal basis, localized orbitals are connected in a natural way to the transport formalism that we will be using to perform scanning tunneling microscopy simulations discussed in next section. Moreover, order-N techniques [194,200,201], in which the computational load scales linearly with the system size N (N is the number of atoms in the unit-cell), have been developed, taking advantage of the localized nature of the basis orbitals.

Open source package for Material eXplorer (OpenMX)

The Open source package for Material eXplorer (OpenMX) [154,155] is a DFT software package under GNU license for nano-scale material simulations based on norm-conserving pseudopotentials, and numerical pseudo-atomic localized basis functions. The main advantage of this code is that it has been carefully designed to be a powerful tool in large-scale *ab initio* electronic and structural calculations. Its parallelization scheme is based on an MPI/OpenMP hybrid approach which optimizes not only the CPU time consumption and scalability of the calculations, but also the memory usage. Thus, systems with a few thousand atoms can be treated using the conventional diagonalization method running it in thousands of processors. This makes this code an ideal candidate to be run on machines of the *tier0* –fastest supercomputers available, typically in or close to the top 10 in the

world– kind. Moreover, this code presents a simple and practical method for variationally optimizing basis orbitals starting from the primitive basis orbitals which is based on the force theorem[155]. Using this approach, both the computational efficiency and accuracy are maximized.

Standard calculations use convergence criteria of $1 \cdot 10^{-6}$ Hartree for the electronic self-consistency cycle and $1 \cdot 10^{-4}$ Hartree/bohr as the maximum force tolerance. The default electronic temperature is 300 K and the energy cutoff –which control the density of the grid on which the cell is divided– is 150 Ry. For the calculations performed in this thesis with this code, the sensibility of the system studied has required to go to very low temperatures and to increase the energy cutoff to improve the precision of the results (see the details in Chapter 4).

2.5 Scanning Tunneling Microscopy theoretical simulations

The Scanning Tunneling Microscope (STM) has become a fundamental experimental tool in the field of nanotechnology and surface science. This microscopy technique is, in a nutshell, a scanning probe microscopy on which a very sharp tip scans a surface measuring the tunneling current –with an exponential behaviour with respect to the distance between tip and sample– generated between them (see Fig. 2.3a). Applying different voltages between tip an sample different parts of the electronic structure of the sample can be explored (see Fig. 2.3b). The proper description of the electronic transport between these electrodes requires solving a complex non-equilibrium problem.

From the point of view of the theory, methods following different approximations have been developed in order to explain the STM experimental images. However, most of the times, the approximations used to calculate it are too simple and, thus, unable to accurately reproduce the experimental images. One of the most used approaches to the problem is the perturbative approximation (Bardeen's tunneling theory[202] as applied to scanning tunneling microscopy) and its simplification called the Tersoff-Hamann (T-H) theory[203,204]. These approximations ignore the effect of the electronic structure of the tip in the image contrast simplifying –or even ignoring in the case of T-H– the transport calculation.

Due all the limitations of these approaches, in our group a specific homemade code has been developed to perform STM simulations[205], based on the non-equilibrium Green-Keldysh formalism to compute the current, which is able to include all these effects in the STM images. This formalism is able to account for inelastic electronic processes and

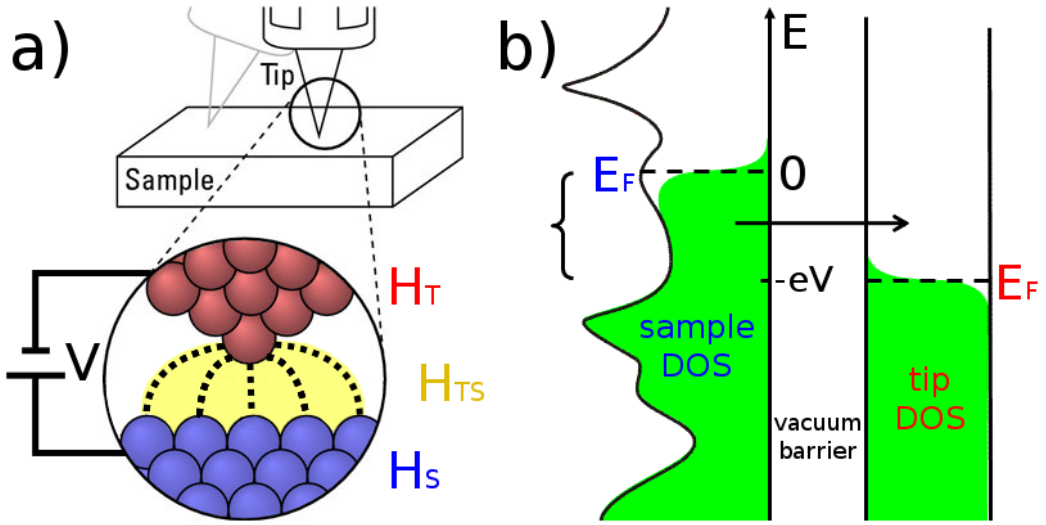

Figure 2.3 a) Simplified scheme of the STM set up where the three pieces needed for our method have been identified: the tip and sample hamiltonians (represented in red and blue) and the hoppings (yellow). b) Schematic of tip-sample tunneling. Energy is along the vertical axis, and density of states of the sample and tip are along the horizontal axes. Filled states are shown in green. In this case, a negative bias voltage -eV has been applied to the sample, which effectively raises its Fermi level by eV with respect to the Fermi level of the tip. This allows for filled electronic states on the left (sample) to tunnel into empty electronic states on the right (tip).

all order electronic multiple scattering –which account for processes of reflexion and propagation of electrons in both tip and sample– using a very compact formulation for the current calculation.

Next, we will briefly analyze the problems of the most commonly used approach, Tersoff-Hamman, and our STM simulation method, discussing for both of them their pros and cons.

2.5.1 Bardeen's theory and the Tersoff-Hamman approach

Bardeen's approximation to the tunneling current[202] considerates both the tip and the sample as isolated electrodes and a transference term is added to account for the electron tunneling probability. If we use time dependent perturbation theory then to describe the first order transition probability we obtain

$$P_{(k\to k')} = \frac{2\pi}{\hbar} |T_{kk'}|^2 \rho_f, \tag{2.33}$$

where $T_{kk'} = \langle \varphi_k | H | \varphi_{k'} \rangle$ is the matrix element between the tip electronic state (φ_k) and the sample electronic state ($\varphi_{k'}$), also known as hopping, and ρ_f is the final density of states (DOS).

If we assume that electrons can only be transferred from an occupied state to an empty state and that these are elastic processes where energy must be preserved we get the following equation for the current at first order

$$I = \frac{2\pi e}{\hbar} \sum_{k \in occupied}^{k' \in empty} |T_{kk'}|^2 \delta\left(\epsilon_{k'} - \epsilon_k - eV_{bias}\right). \tag{2.34}$$

Bardeen proved that that the hoppings could be written as

$$T_{kk'} = \frac{\hbar}{2m} \int_S d\mathbf{S} \left(\varphi_{k'} \bigtriangledown \varphi_k - \varphi_k \bigtriangledown \varphi_{k'}\right), \tag{2.35}$$

where the integral is calculated over the surface separating both electrodes.

Assuming that the tip structure is usually unknown, Tersoff and Hamann[203,204] went a step farther in this approximation considering the tip as a single spherical orbital with s symmetry assuming that it would be a good approach to describe a generic metallic tip. In that case, $|T_{kk'}|^2$ could be now written as

$$|T_{kk'}|^2 \propto \left|\varphi_k\right|^2 = \rho_{sample}\left(\mathbf{r}_{tip}, \epsilon_k\right) \tag{2.36}$$

and, therefore, the total current of equation 2.34 becomes

$$I \propto \int_{-\infty}^{\infty} \rho_{sample}\left(\mathbf{r}_{tip}, \epsilon_k\right) \left[f_T(\epsilon) - f_S(\epsilon)\right] d\epsilon, \tag{2.37}$$

where the summation over the states is now an energy integral and the Fermi functions restrict it to be from occupied states to empty states. At the conductance level the tunneling current, in this approximation, is proportional to the sample DOS at the tip's height at the Fermi level, meaning that the tip follows the lines of constant DOS

$$I \propto \rho_{sample}\left(\mathbf{r}_{tip}, \epsilon_k\right), \tag{2.38}$$

which can be directly computed with any DFT code.

This equation reveals one of the crucial features needed to understand STM imaging: the images are not showing topography, what we see is the electronic DOS. Topography and electronic structure could have the same behaviour, but this is not true for all systems.

At his point we can summarize the two main drawbacks of this method as follows:

1. The distance between tip and sample has to be large in order to be out of the range where the multiple scattering effects start to be relevant and, thus, the first order approximation is no longer valid.

2. The tip, which in this method is treated as a single point, must have a spherical symmetry –without a complex electronic structure or directionality– because there is no way to include in the calculations a specific structure. This can hide some tip-dependent behaviours such as changes in the image contrast. Treating the tip as a point can also lead to a wrong interpretation of the tip-sample current given that, what a real tip measures is the average current of the closer sample atoms.

These approximations sometimes get good qualitative agreement with the experimental data for measurements performed at large tip-sample distances, >5-7 Å depending on the system, where the multiple scattering effects are not important. In order to obtain a quantitative description for all distances and understand some fundamental behaviours a more advanced method is needed. It is crucial to include not only the tip electronic structure effect but also to account for the electronic transport between tip and sample.

2.5.2 Our approach to the STM: Electronic current with Keldysh formalism and the two-center approach

The difference of our homemade STM simulation tool with respect to the previous approach is, in simple words, that the electronic transport is properly described. This involves including in the calculation both the influence of the tip electronic structure in the image contrast and other effects that arise from tunneling features like the multiple scattering which is described below. For this purpose, you need to be able to separate the three pieces of your problem (see Fig. 2.3a): the hamiltonians for both the tip and the sample and the coupling between them (hoppings). It necessarily has to be dealt with a localized-orbitals scheme. On the contrary, PW are not appropriated for this job because the tip-sample coupling can not be separated from the rest of the system information.

An effective and smart way to solve the non-equilibrium problem beyond the previous approximations is using the formalism of non-equilibrium Green Functions[206]. It can be regarded as one of the most accurate methods used nowadays to perform this kind of simulations. In this formalism we can write the total current for $T \to 0K$ as

$$I = \frac{4\pi e}{\hbar} \int_0^{eV} dE \left[\rho_{SS}(E)\, D^r_{SS}(E)\, t_{ST} \rho_{TT}(E-eV)\, D^a_{TT}(E-eV)\, t_{TS} \right], \tag{2.39}$$

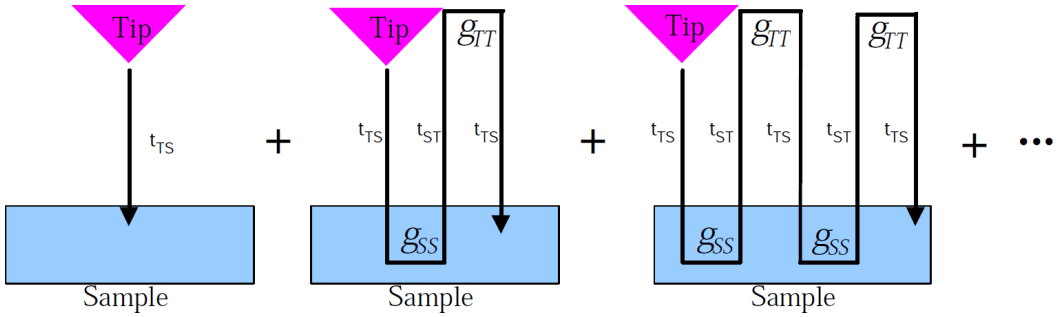

Figure 2.4 Scheme of the addition of the multiple processes of reflexion and propagation in both tip and sample (multiple scattering effects). This figure has been extracted from[205].

where $D^a_{TT}(E-eV)$ and $D^r_{SS}(E)$ (D for denominators) are the terms accounting for the multiple scattering effects (see Fig. 2.4) and are defined as

$$D^a_{TT}(E-eV) = \left[1 - t_{TS}\, g^a_{SS}(E)\, t_{ST}\, g^a_{TT}(E-eV)\right]^{-1}, \tag{2.40}$$

$$D^r_{SS}(E) = \left[1 - t_{ST}\, g^r_{TT}(E-eV)\, t_{TS}\, g^r_{SS}(E)\right]^{-1}. \tag{2.41}$$

On these equations ρ_{TT} and ρ_{SS} are the DOS from tip and sample, t_{ST} and t_{TS} are the *hopping* terms sample-tip and tip-sample and the $g^{a,r}_{TT}$ and $g^{a,r}_{SS}$ are the advanced or retarded green functions of the isolated electrodes (tip or sample).

Eq. 2.39 provides a method to compute the current at one tip position. The numerical treatment that the code does of this problem allows to compute full STM images based on these single point calculations computation. For that we just need to feed our code with a precise model describing the structure and electronic properties of both the tip and the sample. The Keldysh formalism that we use to describe the electronic transport is compatible with a localized orbitals basis. More details about this formalism applied to this STM code can be found in ref.[205].

Using this methodology we could compute the exact current, but the method is so CPU demanding that some approximations have been incorporated in the code to ease the calculations. The code is using two main ones

1. Two-center approximation for the correspondent tip-sample coupling calculation.

2. The hoppings between all the chemical species involved in the calculation are computed in advance and tabulated for a wide range of distances. This parametrization enables the code to quickly evaluate an interpolation of the hopping for a needed distance using this data.

These two approximations allow to simplify the computational scheme and the expressions written above allowing to get accurate STM images in a reasonable computing time. The main disadvantage of this method is that, as tip and sample are treated separately and their hamiltonians computed in advance, relaxation effects due to the tip-sample interactions are very costly to account for.

2.6 Main experimental techniques

The experimental characterization of graphene involves measurements based on various microscopic and spectroscopic techniques. In this section we make a quick review of the most relevant experimental tools with emphasis in those ones related with the work of this thesis.

In modern surface science a handful of different techniques can be used to characterize different features of the system under study. Most of them can be assigned to one of the two big groups of methods. On one hand, we find the experimental techniques using a *wave-like* probe –photons or electrons mainly– like Low-Energy Electron Diffraction (LEED), Auger Electron Spectroscopy (AES), X-ray Photoemission Spectroscopy (XPS), Transmission Electron Microscope (TEM), etc. On the other hand, we have the scanning probe techniques, whose probe is a sharp tip placed very close to the sample. This techniques provide truly local interaction information on the atomic scale rather than the spatially averaged properties, which allows the study of individual surface features at unprecedented resolution. The Scanning Tunneling Microscope (STM) and the Atomic Force Microscope (AFM) are the main representatives of this second group.

The theoretical analysis on this thesis mostly relies in measurements obtained with this last mentioned techniques, but we will also comment some others closely related with the experimental measurements on which this thesis is based.

Scanning Tunneling Microscope (STM)

The idea of using a scanning probe to visualize the roughness of a surface is actually quite old. As early as 1929, G. Schmaltz[207] developed an instrument that had much in common with the modern SPMs: the *stylus profilometer*. A probe is lightly pressed against the surface by a leaf spring and moved across it; a light beam is reflected off the probe and its projection on a photographic emulsion exposes a magnified profile of the surface. The fundamental difference between these instruments and the modern SPM techniques is the attainable resolution, which is limited by the relatively unsharpened stylus, the scanning and detection mechanism, and thermal and acoustical noise.

The STM in particular, has its roots in the *topographiner* advanced by Young in 1971 [208]. This non-contact profiler used the current between a conducting tip and sample to sense the proximity of the surface. It already used a feedback circuit to keep the working distance constant and piezoelectric positioners as modern SPMs. Unlike the STM, which places the tip close to the sample and measures direct tunnelling, it operates in the Fowler-Nordheim field emission regime [209]. Because of this and insufficient isolation from external noise it only achieves a resolution comparable to that of optical microscopes.

In 1981, the physicists H. Rohrer and G. Binnig from the IBM research center in Zurich, developed the STM [210], a new kind of surface analytical instrument which allowed to resolve individual atoms on material surfaces and observe physical and chemical properties related to the behavior of surface electrons in real space for the first time (see Fig. 2.5). For the first STM prototype, they improved the vibration isolation of an instrument similar to the topografiner such that they were able to monitor electron tunneling instead of field emission between the tip and the sample. From the beginning, the STM stood out for being able of resolving the surface structure at the atomic scale and it is now regarded as one of the fundamental experimental tools in surface science and one of the basic tools which originated the actual field of nanotechnology [211]. This invention deserved the Nobel Prize in Physics in 1986. H. Rohrer and G. Binnig shared this award with the German scientist E. Ruska, designer of the first electron microscope (EM) [212,213].

Until the STM was introduced, it still remained a dream to directly observe geometric and electronic surface structures on the atomic level. Compared with other surface analytical techniques there are several advantages of the STM that has made it a fundamental tool in surface science. Here we summarize its main features [214–216].

- It can achieve atomic-level resolution (typically around 0.1 nm of lateral resolution and 0.01 nm of depth resolution).

- It can be used not only in ultra-high vacuum but also in air, water, and various other liquid or gas ambients, and at temperatures ranging from near zero kelvin to a few hundred degrees Celsius. However, although the STM itself does not need vacuum to operate (it works in air as well as under liquids), ultra-high vacuum is required to avoid contamination of the samples from the surrounding medium.

- Local surface electronic properties (measured with resolutions of down to a meV) such as charge-density waves, or the energy gap as well as spectroscopic images can be provided by the STM.

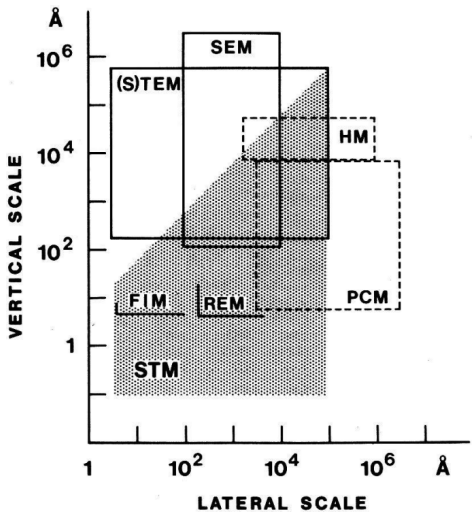

Figure 2.5 Comparison of resolutions of different devices at the time when the first STM was developed[210]. Scanning Tunneling Microscope (STM) resolution corresponds to the shaded area. The resolutions of the high-resolution optical microscope (HM), phase-contrast microscope (PCM), (scanning) transmission electron microscope ((S)TEM), scanning electron microscope (SEM), reflection electron microscope (REM) and field ion microscope (FIM) resolutions are also shown. This figure has been extracted from[210].

- STM can be employed for the modification of a surface and for the manipulation of atoms and molecules through tip-sample interactions –via current, voltage or mechanical interaction–, allowing the manipulation of matter at atomic scale.

To characterize the sample area, the tip scans all it surface through a number of parallel profile scans which conform the full STM image. In order to do this, the STM has two main operation modes: the constant height mode, on which the tip-sample distance is fixed and the current variations are recorded; and the constant current mode, on which a constant tunneling current is maintained during scanning and is the tip-sample distance at each point what is registered. The latter one is most common in STM. In addition to scanning across the sample, information on the electronic structure at a given location in the sample can be obtained by sweeping voltage and measuring current at a specific location[216]. This type of measurement is called scanning tunneling spectroscopy (STS) and typically results in a plot of the relation $\frac{dI/dV}{I/V}$ –which is proportional to the local DOS– as a function of energy. The advantage of STM over other measurements of the DOS lies in its ability to make extremely local measurements: for example, the DOS at an impurity site on a surface can be compared to the DOS far from impurities[217–219].

Regarding the specific systems to be studied in this thesis, it was recognized at an early stage that atomic resolution on HOPG could be achieved with the STM, in vacuum[220], air[221] or under liquids[222]. Graphite became a standard surface with which to calibrate an

STM, since it provided the unit cell spacing with good signal-to-noise on the corrugations. STM also provides high-resolution images of graphene[223,224], graphene nanoribbons (GNRs)[225] and even of molecular orbitals of simple molecules[118,119,226].

Atomic Force Microscope (AFM)

The same year when H. Rohrer and G. Binnig were awarded with the Nobel Prize, G. Binnig and his coworkers presented the first AFM[227]. The AFM, like the STM, consists on a sharp tip –which in certain models can be attached at the end of a cantilever– that is used to scan the sample surface. The difference with the STM is that, when the tip is brought into proximity of a sample surface, what it measures is the forces between the tip and the sample.

This new experimental technique immediately showed a tremendous potential to achieve exceptional results in both the *micro-* and *nano-* scale. However, an extra full decade of development and research was needed to achieve atomic resolution. It was in 1995 when F. J. Giessibl[228] and S. Kitamura *et al.*[229] simultaneously showed results of AFM operated in dynamic mode with atomic resolution of the Si(111)7×7 surface in UHV and at room temperature. Since that moment, dynamic operative modes of the AFM have become the standard approach providing a huge number of achievements in nanoscience including chemical identification of different species on a sample[230] or results with intramolecular resolution[231,232].

Some of its main features are[233–237]:

- It can achieve atomic-level resolution, good AFMs offering height resolution below 0.01 nm.
- It can be operated at different environments not only in ultra-high vacuum but also in air and liquids. This is specially useful for imaging biological samples that are commonly found in solution.
- AFM, like the STM, can be used for atomic manipulation. Changes in physical properties arising from changes in an atomic arrangement can be studied through it[238,239].
- It allows for chemical recognition of the different species in the sample[230].

The AFM can be operated in a number of modes (see Fig. 2.6), depending on the property under study of the analyzed system. In general, possible imaging modes are divided, according to the cantilever movement, into static modes (also called *contact*) and a variety

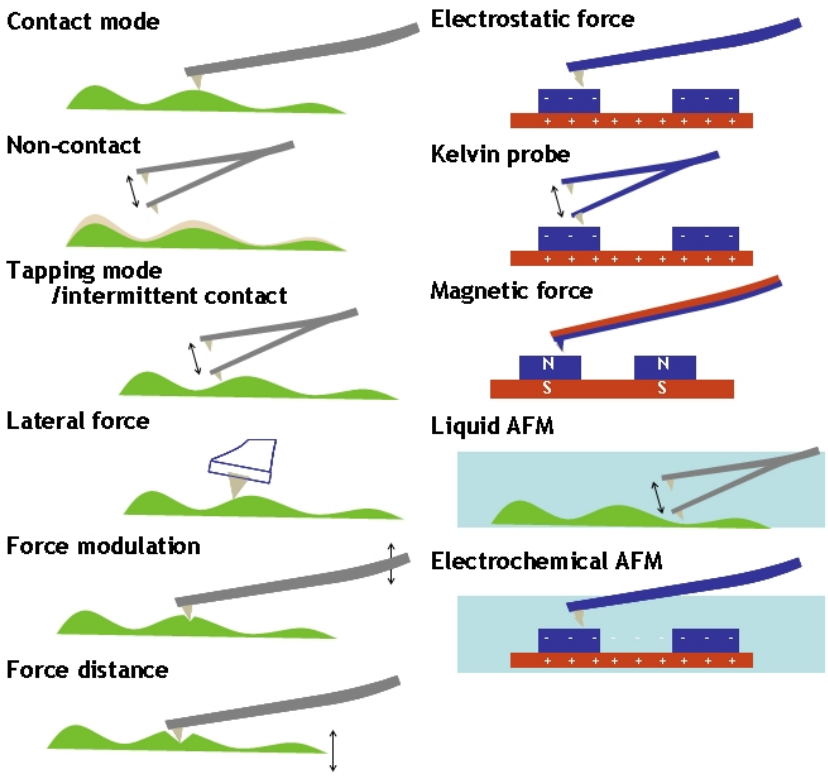

Figure 2.6 Schematic overview of the different AFM operation modes on which both static and dynamic modes are shown based on measuring different force sources such as the ones originated by electrostatic and magnetic interactions.

of dynamic modes (*non-contact* or *tapping*) where the cantilever is vibrated or oscillated at a given frequency. In this last group[234], the most used are the amplitude modulation (AM), where the actual value of the oscillation amplitude is employed as a measure of the tip-sample distance; and the frequency modulation (FM) operation modes, which uses the cantilever deflection as drive signal, thus ensuring that the cantilever instantaneously adapts to changes in the resonance oscillation frequency. In the context of graphene, the AFM has been used to image its topography[224,240] as well as its edges[231,241,242] and defects on top of it[243].

The AFM also provide a way to study the mechanical properties of the samples through indentation experiments (see Fig. 2.7). In particular, there have been several groups measuring the elastic properties and intrinsic breaking strength of free-standing monolayer graphene membranes by nanoindentation using AFM[22,127].

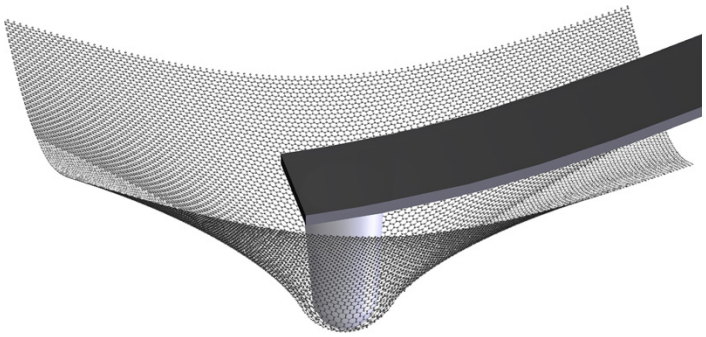

Figure 2.7 A representation of a diamond tip with a two nanometer radius indenting into a single atomic sheet of graphene. Figure extracted from[22].

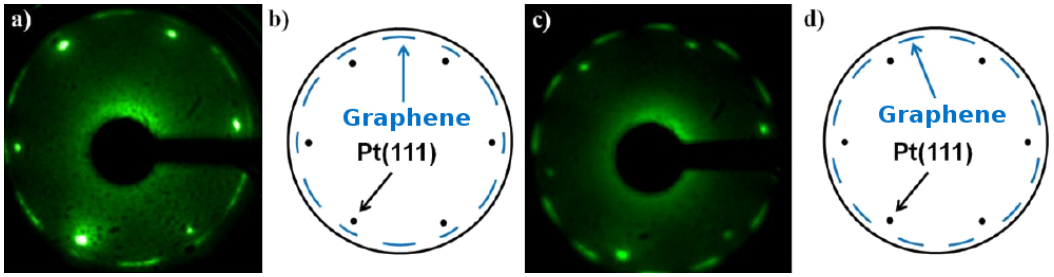

Figure 2.8 LEED patterns obtained from G/Pt(111) samples. In the experimental images a) and c), the points show the periodicity of the Pt(111) substrate and the arcs are related with the graphene. In a) half of the graphene arcs are aligned with the Pt(111) points while in c) they are all alternated. This denotes a different graphene-metal orientation –meaning different Moiré patterns– in the two samples reveling a weak interaction between the two materials. b) and d) are schemes of the experimental LEED patterns in a) and c) respectively. This figure has been extracted from[247].

Low energy electron diffraction (LEED)

This technique was discovered in 1927 at Bell Labs[244] confirming the L. de Broglie hypothesis[245] –the wavelike nature of all particles– experimentally by showing the appearance of diffraction patterns of backscattered electrons fired at a nickel target. However, it did not become a popular tool for surface analysis until the early 1960s. The main reasons were that monitoring directions and intensities of diffracted beams was a difficult experimental process –due to inadequate vacuum techniques and slow detection methods– and also that it requires well-ordered surface structures – the cleaning techniques for metal surfaces first became available much later–[246].

The usual LEED device consists of an electron gun firing a collimated electron beam onto a crystalline sample. Some of the electrons incident on the sample surface are backscattered elastically, and diffraction can be detected if sufficient order exists on the surface. This typically requires a region of single crystal surface as wide as the electron beam, although sometimes polycrystalline surfaces such as highly oriented pyrolytic

graphite (HOPG) are sufficient. It is very useful for identifying surface structures and reconstructions as it is directly related to the 2D reciprocal lattice of the surface crystal symmetry. The extreme selectivity to the surface terminations together with its simplicity, makes LEED an ideal technique for surface characterization prior to measurements through more complex methods. In Fig. 2.8 we show an example of the LEED characterization of a G/Pt(111) surface –which will be important for our theoretical studies– taken by one of our experimental collaborators[247].

Transmission Electron Microscopy (TEM)

This is another important subnanometer-resolved technique also based, as in the LEED, on characterizing a sample using an electron beam. When an electron beam interacts with the samples there are many types of signals that are produced by secondary electrons, backscattered electrons, X-rays or diffracted electrons (in crystalline samples) among others. These signals can all be studied using similar instruments with different detector attachments, but each one yields different information/insights about the sample. In the TEM case what is collected is the information of the transmitted electrons. An image is formed from the interaction of the electrons transmitted through a sufficiently thin specimen. It was the first of the electron microscopy family invented by M. Knoll and E. Ruska in 1931[212,213]. Time after the first working version, thank to the development of new aberration correction techniques[248,249], the resolution of these tools could be dramatically increased giving rise to a new TEM imaging mode, the High-resolution TEM (HRTEM). The HRTEM is a powerful tool to study properties of materials on the atomic scale, such as semiconductors, metals, nanoparticles and sp^2-bonded carbon such as graphene or carbon nanotubes. It has also been used to study defects on graphene such as vacancy defects, edges or grain boundaries[250]. The main disadvantage of this technique is that it only works with ultra-thin samples.

CHAPTER 3

SUBLATTICE LOCALIZED ELECTRONIC STATES IN ATOMICALLY RESOLVED GRAPHENE-PLATINUM EDGE-BOUNDARIES

3.1 Introduction

The breaking of the perfect 2D periodicity of graphene in the presence of topological defects or in strain relief structures modifies significantly its electronic properties[58,59]. In particular, graphene nanobubbles have been suggested to present pseudomagnetic associated Landau-levels[60], and electronic one-dimensional edge states have been revealed to be localized in graphene nanoribbons[251]. These recently developed nanoarchitectures could open the door to tune the electronic transport of graphene-based electronic devices by ribbon or boundary engineering.

1D extended structures in graphene are central to this effort[241,252]. The electronic structures of grain boundaries of polycrystalline graphene[253], graphene nanoribbons (GNRs)[128,254], or edges have been extensively studied[123,255]. Theory predicts that the electronic properties of the edges can be tuned by the orientation of their ending (zigzag, armchair, mixed), possible reconstructions (pentagonal, heptagonal and higher order rings), and their chemical functionalization (normally H passivation)[123,128,255–257]. Electron microscopy experiments were the first to provide a structural characterization of graphene edges with atomic resolution using either aberration-corrected TEM images[258] or scanning transmission electron microscope (STEM)[259]. Recent dynamic atomic force microscopy (AFM) studies have presented this technique as an ideal tool to the study of atomically precise carbon nanostructures[231,241,242]. Scanning tunneling microscope (STM) measurements performed on graphene patches deposited on different substrates[251,260,261] added the possibility to correlate the structure with the local electronic properties. Even

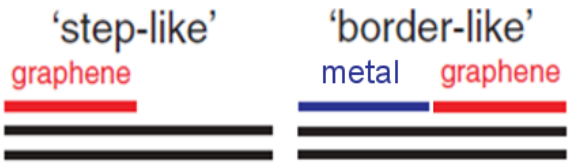

Figure 3.1 Scheme for visualization of the difference between border-like and step-like edges. Figure adapted from[263].

though atomic resolution was achieved in those experiments, STM was unable to reveal the details of the edge termination due to the interaction with the substrate. STM experiments based on graphene islands grown directly on a metallic substrate[255,262] offer the possibility to study not only the edges "flying freely" on the lower substrate terrace (*step-like* edges) but also those bound to the upper terrace of the substrate (*border-like* edges) –both are depicted in Fig. 3.1–. Although these studies were able to show a correlation between the atomic corrugation at the graphene edges and the Moiré pattern of G/Ir, where the absence of electronic G-edge states has been reported[256], an atomically precise description of graphene contacts with metallic substrates is still missing.

In this chapter we provide the first combined experimental and theoretical atomistic description of the in-plane contact region formed along the 1D interface in a graphene-metal heterostructure and unveil its electronic properties. Our collaborators from the group of J. A. Martín-Gago at the Instituto de Ciencia de Materiales de Madrid (CSIC) have been able to obtain high-resolution room temperature STM images of atomically resolved *border-like* edges of graphene on Pt(111) steps. We have combined these detailed experimental results with DFT simulations to fully characterize the atomic structure of the Pt-graphene edges, which allow us to understand their electronic properties. Our results contrast with the ones obtained for the G/Ir edges system[256], as we reveal the presence of 1D electronic states that are highly localized exclusively in one of the graphene sublattices. Theory predicts, and STM images confirm, that this state is mainly confined on the first lines of carbon atoms of the edge. This state is very robust and despite the thermal broadening it is possible to observe it even using a room temperature STM instrument. This combination of sublattice and edge localization would make possible the design of a dual-channel device based on a graphene nanoribbon contacted with two different *border-like* edges.

Moreover, our results also shed light on the role of the substrate steps in the nucleation and formation of different Moiré patterns on metal surfaces. The characterization of the particular periodicities found in these superstructures and their possible origin have been subjected to numerous studies (see[59,101,264] and references therein). Here we present an

atomic-scale description of the bonding arrangements at the interface between a Pt(111) step and a graphene island that brings a deeper understanding of this point. Our results show that graphene nucleates on the Pt steps inducing a 1D reconstruction on the Pt atoms, which are coupled to graphene ending in a zigzag configuration. We exploit these observations to show that the precise structure of these edges is responsible for originating the particular orientation of the formed Moiré patterns.

3.2 Experimental methods and theoretical details

3.2.1 Experiments

Experiments performed by our experimental collaborators were carried out in an ultrahigh vacuum (UHV) chamber with base pressure of $1 \cdot 10^{-10}$ mbar. The Pt(111) single crystal sample was cleaned by repeated cycles of Ar^+ sputtering and subsequent annealing at 1200 K. After several cycles, the sample purity was checked with LEED and STM. Once the sample was free of contaminants, they proceeded to graphene growth. For that purpose they exposed the clean Pt(111) to a partial pressure of propane (C_3H_8) of $1.1 \cdot 10^{-8}$ mbar during 15 min keeping the sample at 900 K and subsequent annealing at 1050 K during 20 min. Submonolayer coverage of graphene islands was observed in the STM sessions with an estimated coverage of >0.1 ML.

STM images were acquired using a room temperature (RT) microscope. They used both topographic and quasi-constant height modes with typical biases of -250 mV to 250 mV and currents between 0.1 nA and 4 nA. WSxM software was used for data acquisition and image analysis[265]. The thermal drift was corrected with a homemade program, which resized the images for a given hexagonal unit cell by keeping the fast scan axis as the reference distance.

Quasi-constant height images were acquired tuning the scanning conditions to constant-height but with feedback parameters reacting more slowly than usual conditions while recording the current map. This way, STM images are showing the difference between the current set-point and the actual current measured in each point recorded during the conventional STM operation with the feedback on. With these measurement conditions they were successful in simultaneously resolving the Pt atoms within the Pt(111) regions and the C atoms within the graphene islands. These exceptional resolving conditions could not be achieved under any other working mode explored. However, obtaining these high-resolution STM images is very demanding and tip crashes are relatively common. Notice that the information obtained by topography and quasi-constant

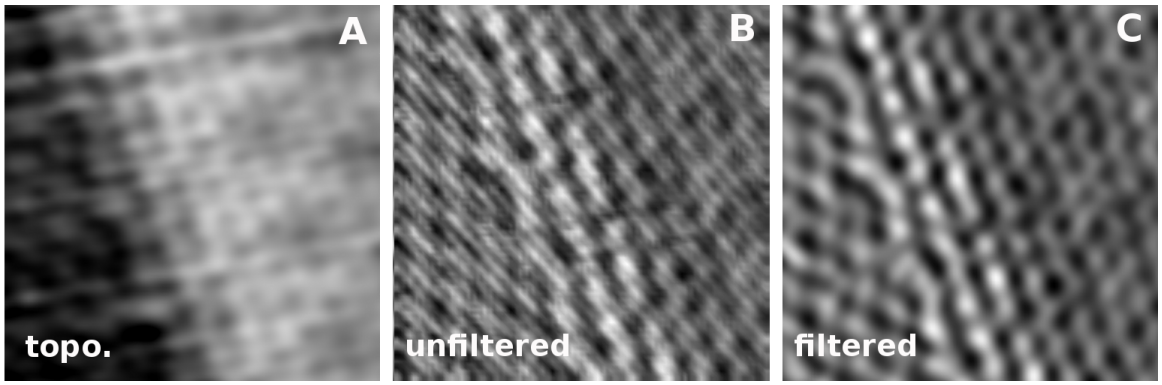

Figure 3.2 STM images of one of the scanned edges with a zigzag graphene ending (2.5 × 2.5 nm^2). a) Filtered image recorded in constant current mode. b) Unfiltered image recorded in quasi-constant height mode. c) FFT-Filtered image of b).

height images is exactly the same, and that the only difference between both modes is an increased atomic resolution, as the step jump is not followed properly by the scanning tip inducing poor imaging resolution in regular feedback loops. This is evidenced in Fig. 3.2, where the topographic and the quasi-constant height images are presented. They have also presented for the quasi-constant height the process of Fast Fourier Transform (FFT) filtering. This process eliminates noise coming from the experiment without altering the atomic features of the measurement.

3.2.2 Theory

DFT Calculations

We have calculated all the structural and electronic properties using DFT as implemented in the VASP code[153]. For these calculations, we employed the PBE[159] functional empirically corrected to include van der Waals interactions (using the D2 Grimme approach[142]) projector augmented wave (PAW) pseudopotentials[196], and a plane-wave cutoff of 400 eV.

Designing a cell with a reasonable size to simulate an extended system like this one with a wierd symmetry is not an easy task. The system had to be chosen in such a way that with a minimum atom number and cell size all the important properties are still represented in this system. To avoid the simulation of an infinite G/Pt(111) step edge we played with the Pt layer stacking in order to reduce the system size in an ingenious way that we describe below.

We have exploited the intrinsic periodic nature of the calculations, considering a unit cell where we cut the Pt surface and enforce a shift in the z coordinate of the cell (see Fig. 3.3) to recover the periodicity (the *ABC* stacking of the metal). In this way, we have still

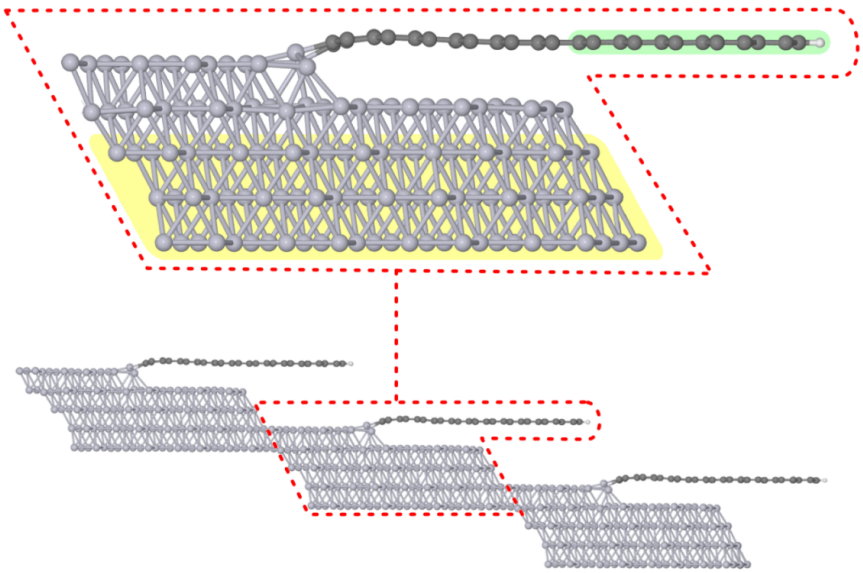

Figure 3.3 Scheme of the theoretical simulation of the step. The unit cell, shown on top, is repeated to create the step, as illustrated below. The atoms that are highlighted in green were fixed in the z direction during the relaxation while the ones highlighted in yellow were fixed in all directions.

a quite realistic description of the system without the need to include the other half of the Pt slab, reducing significantly the computational effort. Nevertheless, we have kept the longer G ribbon (including a free standing region) to ensure that both G edges (the one in contact with the Pt and the one saturated with H atoms) are effectively decoupled. The cell includes a slab of 5 layers of Pt at which a single sheet of graphene (a 3×12 cell with 72 atoms) has been attached. The 4 lower Pt layers contain 28 atoms each, while the one on top has half the area of the others (14 atoms) and the graphene layer is bonded to its free edge. The reason why we have imposed in our model the $3\times$ periodicity along the edge is, as we will see later, that is the most common and best characterized in the STM measurements. To make the electronic properties of the flake more realistic, we have saturated the other border with 3 H atoms. This edge does not pretend to mimic any border of the simulated experiments. Calculations with a flake half the length of the one in Fig. 3.3, confirm that the structural properties of the G-Pt boundary are not significantly affected by the flake length. The lattice constant of the Pt crystal was optimized for both PBE (to have this value as a reference) and PBE-D2, obtaining a value of 3.98 Å for the first and 3.95 Å for the latter. However, the mismatch between the C and Pt lattices in the 3×3 Moiré of G/Pt(111) is small (0.6%), and in our calculations we decided to fix the size of the supercell to match the relaxed graphene lattice ($a_0 = 2.46$ Å) calculated with PBE-D2.

We have constructed several different initial configurations with slightly different positions for the atoms in the G-Pt contact. For these structural relaxations, we have

only fixed the positions of the Pt atoms of the three lowest layers and the z coordinate of the C atoms of the half sheet next to the free edge (H-terminated) as to simulate the G-Pt distance that we would expect in a G-flake over a Pt terrace[266]. The final structures correspond to energies converged better than 10^{-4} eV/atom and forces smaller than 0.02 eV/Å. We have used a 2×6 $\Gamma-$centered Monkhorst-Pack grid to make the relaxation of the structures. For the DOS calculations, we first evaluated the electronic charge over a 2×21 $\Gamma-$centered Monkhorst-Pack grid, and then we calculated the DOS over a 4×75 $\Gamma-$centered Monkhorst-Pack. Together with this very fine k-points mesh we have chosen a small value for the broadening ($\sigma = 0.05$eV) which make us very confident about the convergence of the calculations.

We have included the vdW interaction using the Grimme-D2 approach[142] approach. In order to apply it to our system, we have had to provide the parameters for platinum as they are not automatically included in the implementation. We have calculated them ourselves as $C_6(Pt) = 20$ J·nm^6/mol and $R_0(Pt) = 1.9$ ÅṪhey have proven to be suitable to describe the G/Pt(111) surface successfully in previous works[266] and the results compare very well with those obtained with other vdW schemes that work well with metals (Grime-D3[173] and optB86b[144]). We used the default values given in ref.[142] for the rest of the chemical species. The results shown on this chapter are calculated without including spin polarization but we have also explored the possible magnetic solution of the system allowing it. We found that the interesting border was not magnetic while we recovered the expected magnetization in the H-terminated graphene end. As we focused our study in the G-Pt boundary edge we stuck to the non-polarized scheme.

STM profiles

The experimental STM images can be deeper understood with the help of theory. In our approach, introduced in Chapter 2, we use a nonequilibrium Green's function formalism to evaluate the currents[267], using the OpenMX code[154] to map the Hamiltonian into a local orbital basis, and an idealized Pt apex with a single dz^2 orbital to represent the microscope tip. Besides, all the simulations include the contribution to the current of multiple scattering processes, that are mandatory when exploring the short tip-sample distance range[267]. This model produces atomically resolved profiles, which is important for the understanding of the experimental images.

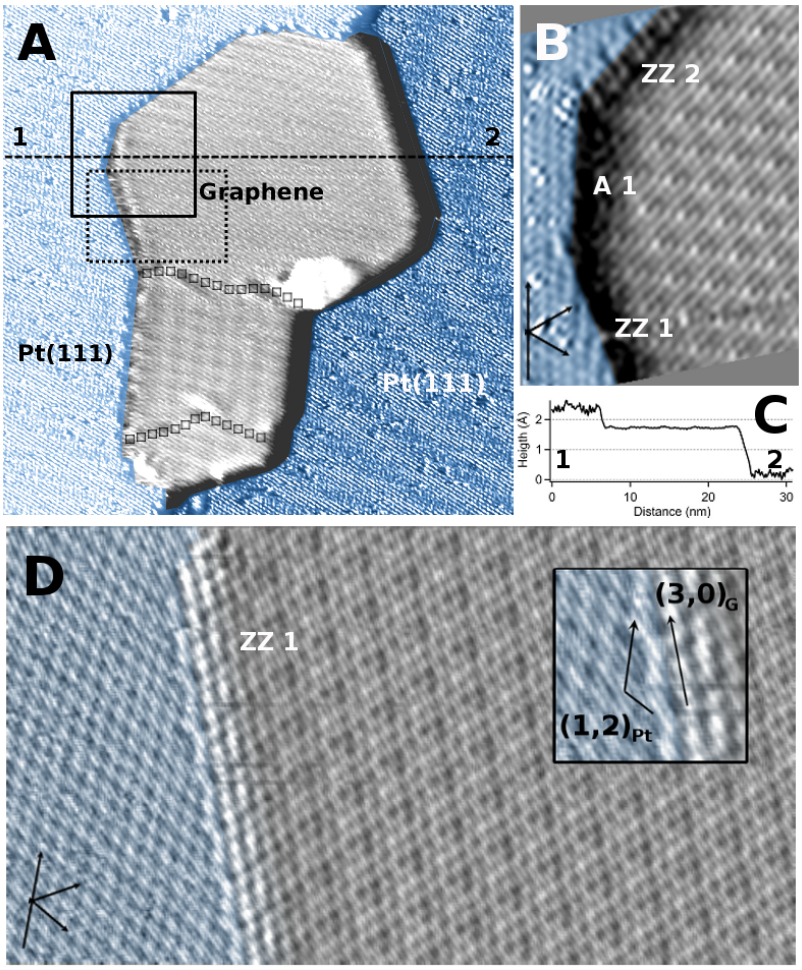

Figure 3.4 a) Constant current STM image (31×31 nm^2 , sample voltage $V_s = 100$ mV, tunneling current $I_t = 3.9$ nA) showing a graphene island embedded in a Pt(111) terrace exhibiting three different Moirés; the graphene-graphene edges between Moirés are represented with squared lines overimposed. b) Drift corrected quasi-constant height STM image (6×8 nm^2 , $V_s = 42$ mV, $I_t = 2.5$ nA) displaying a detailed view of three *border-like* edges of the solid black squared region in a). Black arrows indicate the $[1\bar{1}0]$ and equivalent Pt crystallographic directions. c) Profile recorded in topographic mode corresponding to the dashed line marked in a). d) High-resolution, unfiltered, atomically resolved, quasi-constant current STM image of the *ZZ1* edge corresponding to the pointed line rectangle marked in a) (12.6×6.8 nm^2 , $V = 40.2$ mV, $I = 5.2$ nA). The inset shows the surface crystallographic vectors of the edge and graphene structures with respect to the surface vectors of the Pt(111) (suffix Pt), and respect to the surface vectors of graphene (suffix G). All images have the same scanning direction, which is parallel to the horizontal.

3.3 Experimental STM results

The constant current STM image on Fig. 3.4a shows a graphene island (represented in gray color) which grows attached to the upper part of a Pt(111) step. The usually straight Pt step-edge has been altered from its original shape during the graphene growth. In this image, approximately half of the graphene island is embedded in the upper terrace (with respect to the Pt steps), adjusting itself to the crystallographic directions of the substrate. This morphology indicates significant mass transport of Pt atoms during graphene growth and differs from the structures reported for graphitization on other metal surfaces, such as Ir(111)[98,261] or Ru(0001)[93], where graphene normally grows over the metal steps without altering the metal substrate.

Three different rotational domains of graphene separated by nonperiodic grain boundaries can be clearly identified in the island of Fig. 3.4a (see squared lines). The upper domain is rotated 19.1° with respect to the surface $[1\bar{1}0]$ crystallographic surface direction, which in the image runs parallel to the vertical direction, and it exhibits a superstructure periodicity of 7.38 Å. This graphene superstructure is usually denoted as $(\sqrt{7}\times\sqrt{7})R19°$, with respect to the Pt(111) surface, $G(3\times3)$, with respect to the graphene surface vectors, or βG/Pt(111), according to the notation introduced in reference[101]. The middle domain is rotated 8° and presents a periodicity of 13 Å; it most likely corresponds to $(\sqrt{31}\times\sqrt{31})R9°$ or εG/Pt(111). Finally, the lowest domain is small in size and our collaborators were not able to attain Moiré resolution to deduce the graphene orientation.

The upper $(\sqrt{7}\times\sqrt{7})R19°$ domain of Fig. 3.4a exhibits a polygonal shape with four *border-like* and three *step-like* edges[262]. STM topographic profiles (see Fig. 3.4c) confirm the existence of both G-metal boundaries, showing different height jump decay for *border-like* and *step-like* edges. The atomic resolution at the *border-like* edge strongly depends on the tip termination. Although in some cases, as the one shown in Fig. 3.4d (corresponding to the pointed-line rectangle in the Fig. 3.4a), the resolution is very good, this is not a usual case. As we have said before, to routinely enhance the resolution at the G-Pt boundaries, we have recorded quasi-constant height STM images. As was advanced in Fig. 3.2, both STM topographic and quasi-constant height images show the same atomic features on the same positions, but the atomic resolution at both sides of the step is strongly enhanced, as it is shown in Fig. 3.4d. The improved resolution at the edge is also clearly illustrated in Fig. 3.4b where the quasi-constant height STM images exhibit atomic resolution not only on the Pt(111) terrace and the island but also at the interface.

Interestingly, some of these edges maintain a crystallographic relationship with the Pt substrate. This is the case of the edge shown in the constant-current image of Fig. 3.4d,

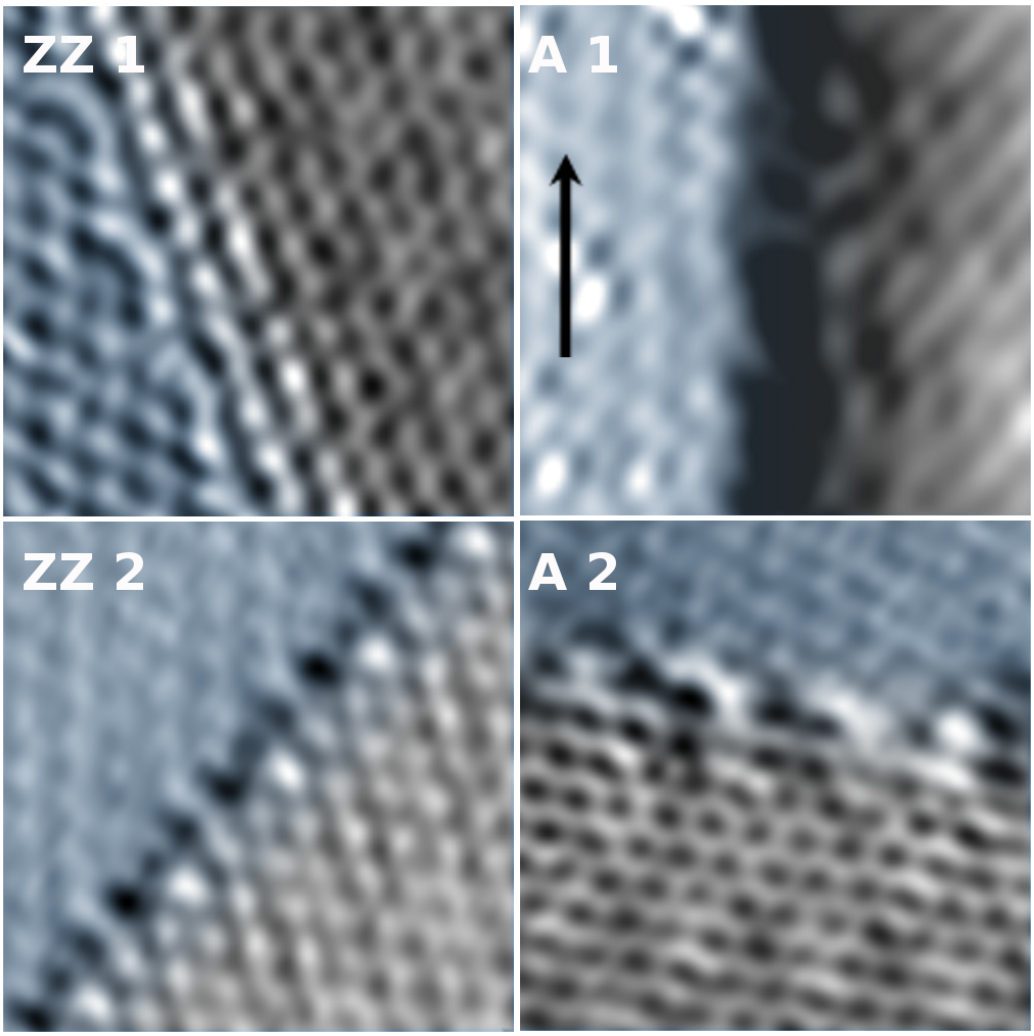

Figure 3.5 Atomically resolved quasi-constant height STM images (2.5×2.5 nm^2) of the zigzag edge number 1 (*ZZ1*), $I_t = 5.2$ nA, $V_s = 38$ mV; the amorphous edge number 1 (*A1*), $I_t = 2.4$ nA, $V_s = 42$ mV, the arrow indicates the Pt $[1\bar{1}0]$ direction; the zigzag edge number 2 (*ZZ2*), $I_t = 3.8$ nA, $V_s = 47$ mV; and the amorphous edge number 2 (*A2*), $I_t = 5.2$ nA, $V_s = 38$ mV. Blue/gray regions are identified by the lattice symmetry to be Pt/G, respectively. A boundary region of 3 to 4 atomic rows is also clearly observed with atomic resolution. These images have been drift corrected and FFT filtered.

where long-range order is appreciated at the interface between Pt and graphene. The inset shows the crystallographic vectors with respect to the surface unit cell of Pt(111). High-resolution STM images allow a systematic characterization of all of the different *border-like* edges on the $(\sqrt{7}\times\sqrt{7})R19^\circ$ graphene Moiré shown in Fig. 3.4. These results are shown in Fig. 3.5, where edges have been labeled as *ZZ* (for a zigzag graphene ending) and *A* (for an amorphous or armchair configuration). Border *A1* is parallel to the $[1\bar{1}0]$ Pt crystallographic direction, while borders *ZZ1* and *ZZ2* run along the $[32\bar{1}]$ and $[1\bar{3}2]$ directions, respectively, forming 19° and 41° with the $[1\bar{1}0]$ direction. *A1* and *A2* edges present a disordered structure with two different independent atomic structures (for example, *A2* border presents a mixture of armchair and zigzag termination), whereas the other two edges, *ZZ1* and *ZZ2*, are crystalline.

3.4 Theoretical interpretation of the experiments

Most atomically resolved edges show regions that can be unambiguously assigned to Pt and G (blue and gray colored areas on Fig. 3.5, respectively) and a boundary area of 3 to 4 atomic rows, where the atoms although clearly visible cannot be directly ascribed to a particular chemical element (gradient colored area). As a result of *ab initio* simulations based on DFT for a graphene flake attached to a Pt step, a much deeper understanding of these edges can be achieved.

3.4.1 Unveiling the structure of the G-Pt step boundary

Fig. 3.6 shows the main results of these calculations. Starting from different initial structures for the G-Pt interface, we have obtained a stable configuration where the stress induced in the G-Pt junction has been relaxed with a rearrangement of the outermost Pt atoms of the single-atom step (see Fig. 3.6a,b). The unit cell of our system involves three nonequivalent Pt atoms directly bonded to graphene. To ease the visualization, we have marked them with blue, red, and green colors in the figure. These Pt atoms undergo both out-of and in-plane displacements. The red Pt atom on Fig. 3.6 protrudes 0.65 Å out of the Pt terrace plane and it moves in plane from its original position ~ 1 Å toward the graphene forming a bond with an unsaturated C edge atom. As a result, a hole is created on the Pt side. This can be visualized in Fig. 3.6a as the vacant region beneath the red Pt atom. The blue and green Pt atoms also passivate one outermost C atom each, but they show lower strains and displacements, and the more significant is the -0.15 Å out-of-plane displacement (inward relaxation) of the blue atom on Fig. 3.6.

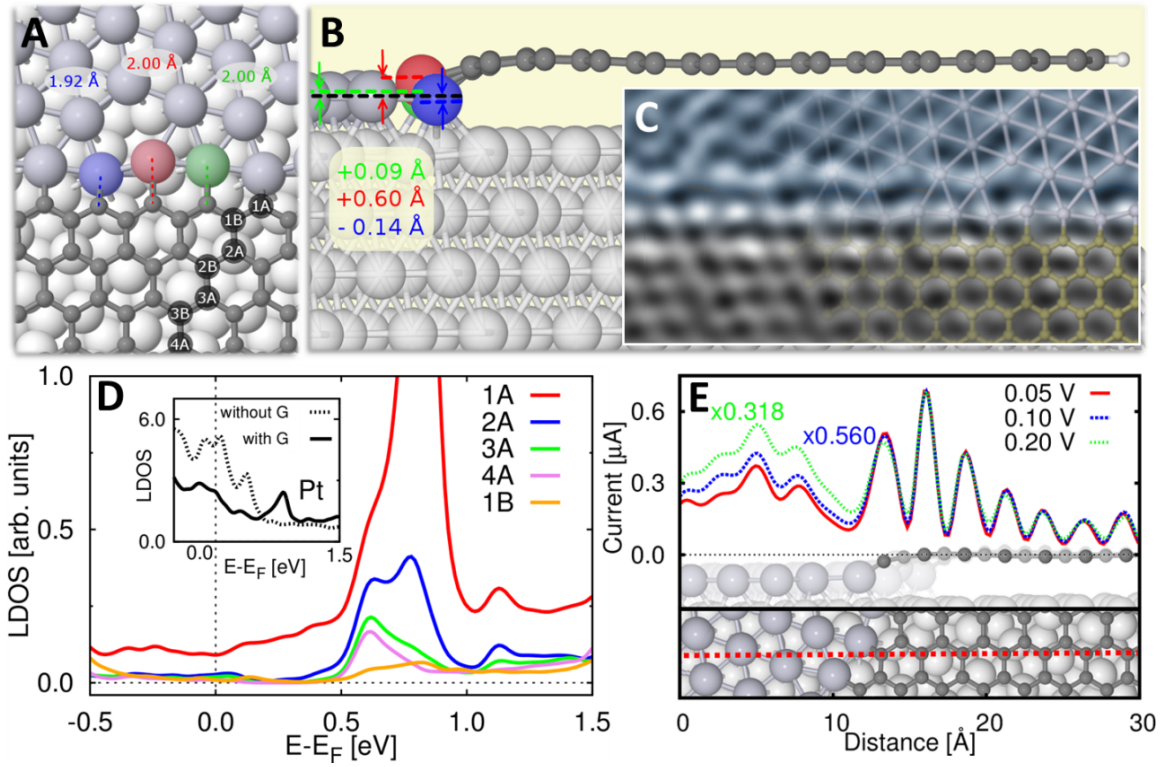

Figure 3.6 (a and b) Ball-and-stick model of the atomic configuration of graphene on the Pt(111) step edge calculated with DFT. Bond distance (a) and out of plane displacement (b) of the Pt edge atoms are indicated. c) Quasi-constant height STM image (3.5×1.6 nm^2) and overlay of the calculated structure for edge *ZZ1*. d) Local density of states (LDOS) for the 1^{st} (red), 2^{nd} (blue), 3^{rd} (green), and 4^{th} (pink) rows of C atoms belonging to the same sublattice and for the 1st (orange) one of the other sublattice. An electronic state at approximately +0.8 eV above E_F is clearly observed only in one sublattice and is mainly localized on the edge row. This state extends into the Pt row in direct contact with the graphene, as shown in the inset, where the theoretical LDOS of this Pt row is shown with and without the graphene flake. The electronic state at approximately +0.8 eV appears in the case of the complete system while it is missing in the isolated metal. e) Theoretical constant-height STM simulations of a profile through one of the A-sublattice lines depicted below in both side view and top view where the line profile is highlighted by a dashed red line. Currents at a tip-sample distance of 2.75 Å with respect to the uppermost atom in the cell including multiple scattering contributions for 0.05 V (red), 0.10 V (green), and 0.20 V (blue) bias voltages are shown. The rescaling of the profiles for 0.10 and 0.20 V allow us to check that the behavior is not affected by the voltage used.

This atomic structure mimics with great accuracy the atomically resolved experimental STM images (see Fig. 3.6c) for the *ZZ* edge. The strain induced on the Pt side is localized mainly on the outermost Pt atoms and only slightly propagate to the second Pt row. While free-standing zigzag edges should undergo reconstruction, no relevant rearrangement is observed on the graphene side in our results. The external C atoms of the zigzag edge are covalently bonded to the metal step, keeping their graphene-like positions. This covalent interaction between graphene and Pt, already theoretically proposed for Cu, Co, and Ni(111) surfaces[268,269] and observed with STM on G/Ir[262], passivates the graphene dangling bonds and stabilizes the zigzag structure[270].

Our calculations have found another stable configuration. The match between this theoretical structure and the STM experimental images for *ZZ1* and *ZZ2* edges is clearly worse. However, for the shake of completeness, we next analyze this other structure and compare it with the one already described.

3.4.2 An alternative configuration for the boundary

When relaxing the system from different initial configurations of the G-Pt interface, two stable structures were found in the calculations. The main difference between them is the position of the atoms in the edge: while in Fig. 3.6b the Pt atoms move towards the graphene flake and the C atoms are close to the typical graphene sheet ones, in Fig. 3.7b the Pt atoms remain almost in bulk positions and the C atoms are the ones moving towards the Pt. Besides, in the first case we have just three Pt atoms bounding with the three C atoms (see Fig. 3.6a), while, in the second one, we have one C-Pt bond and another Pt atom passivating the other two C atoms (see Fig. 3.7a). The match between this alternative theoretical structure and the STM experimental images for the *ZZ1* and *ZZ2* edges is clearly worse (see Fig. 3.7c) than for the structure previously proposed. The energy of the two models is very similar although the configuration that has a better agreement with the experiments has lower energy. The energy difference between both models is ~ 75 meV.

3.4.3 Details of the electronic structure of the G-Pt step boundary

The good match between the calculated atomic structure and the experimental STM images also motivates us to characterize the electronic structure at the edges by calculating the local density of states (LDOS) associated to this nanostructure. The boundary configuration showed in the Fig. 3.6, presents a clear electronic edge state at ~ 0.8 eV above the Fermi level with a FWHM of 0.2 eV. It derives from the graphene π-band. Freestanding

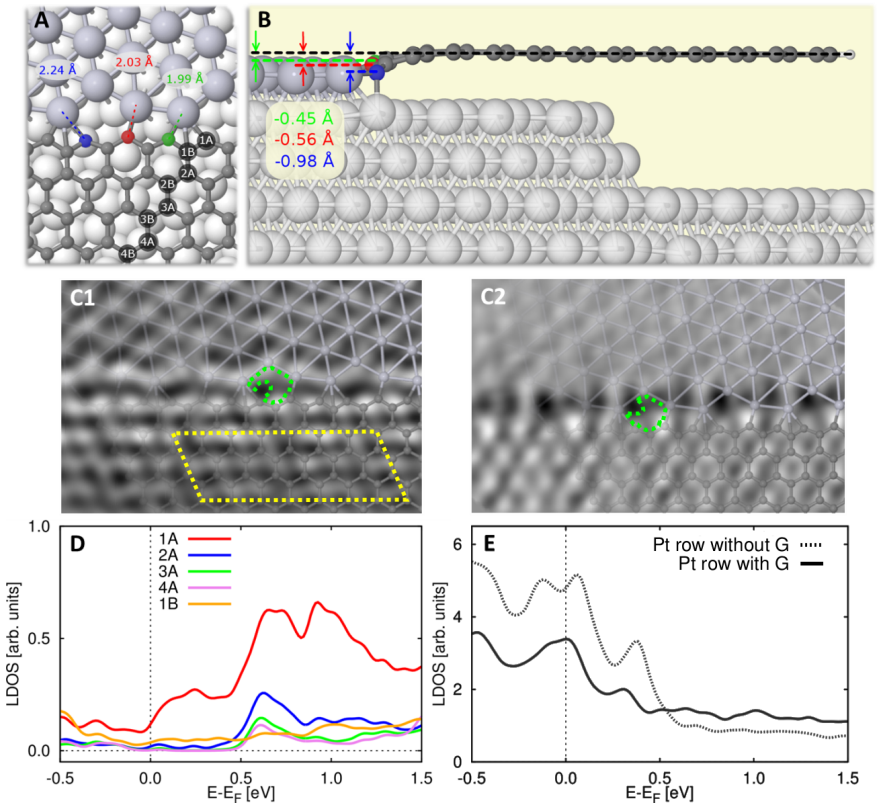

Figure 3.7 a) and b) Ball-and-stick model of another stable atomic configuration for the contact between graphene and a Pt(111) step edge calculated with DFT. Distance bonds, a), and out of plane displacement, b), of the carbon edge atoms are indicated (in this case the Pt atoms remain close to bulk positions). c1) and c2) overlay of the relaxed structure with the best-fit STM images. It can be seen that the fit is worse than in the other configuration. Areas where there is a clear conflict between the image and the structure are highlighted. Circled in green there are some areas showing electronic density in the experimental STM image while regarding the theoretical model there should be no atoms or bonds there. The carbon rings bordered by the yellow dashed line show a considerable mismatch between the theory and the experimental data. d) Local density of states (LDOS) of the graphene atoms for the 1^{st} (red), 2^{nd} (blue), 3^{rd} (green) and 4^{th} (pink) row of carbon atoms belonging to the same sublattice and for the 1^{st} (orange) one of the other sublattice. A localized electronic state at an energy of ~ +0.8 eV (above E_F) can be observed only in one sublattice, although is not compared to the other step model. e) Local density of states (LDOS) of the Pt atoms at the edge of the step that are bond to the carbon atoms (solid red) versus the same atoms in a step without a graphene flake attached (dashed red). We can no longer see the localized electronic state in the Pt LDOS.

graphene edges are characterized by the presence of a localized state at the Fermi level. In our case, both the charge transfer between the flake and the metal and the strong G-Pt interaction broaden this peak and shift it toward positive energies resulting in the peak that we observe at about +0.8 eV. The contribution to the DOS of each one of the C edge atoms (see Fig. 3.8a) is very similar as the chemical environment is mostly the same for the three atoms. This peak extends only over one of the sublattices, A, and it rapidly decays going inside the flake but is uniform parallel to the edge (see Fig. 3.8a). Its position with respect to the Fermi level and its decay length –that we analyze later– are similar to the ones associated with a single atom vacancy on graphene on Pt[266]. As in this case, the magnetic moments associated with the G-edge in free-standing graphene are quenched due to the interaction with the metal. This result contrast with that of ref.[256] where the authors show that the edge states at Ir(111) are quenched by the strong interaction between the metal and the graphene. In this case, the graphene edges are hybridized with the substrate. The graphene-metal interaction is much stronger than that in Pt, and therefore, it is able to modify the sp^2 hybridization of the edge-G/Ir atoms and to block the edge-state.

Interestingly, we have also study how the edge state of the G-Pt boundary extends into the Pt due to strong C-Pt interaction. Fig. 3.8c shows the LDOS projected on the Pt atoms bound to G. Clear traces of the G state at ~ 0.8 eV are observed on the three Pt atoms, indicating a good metal contact between Pt and G. For reference we also show in Fig. 3.8d the LDOS of the total Pt and the total C contributions. In the latter we can appreciate both peaks: the one of the step edge and the H-terminated one.

If we look at the total graphene contribution to the DOS of the system in Fig. 3.8d, another peak at the Fermi level can be clearly observed. This one is associated with the H-terminated edge: the peak of the LDOS corresponds in this case to the contribution of the atoms of the sublattice B (the LDOS of the nearby atoms of the sublattice A is suppressed) and it decreases as you get away from the first row (see Fig. 3.8b). The Pt is too far (in all directions) to have any influence on the LDOS of these atoms and thus the peak is centered at ~ 0 eV[58,252]. The peak is narrower than the other in which the interaction with Pt has result also in broadening[123].

The LDOS shows other peaks, like those at ~ +0.6 eV and ~ +1.1 eV, that can be explained by the finite size of our model graphene nanoribbon[58].

The presence of the G-edge has a profound influence not only for energies around the edge state at ~ +0.8 eV but also in a wider energy range including the Fermi level. Our calculated LDOS at zero energy shows the same spatial decay found for the main peak (see Fig. 3.9).

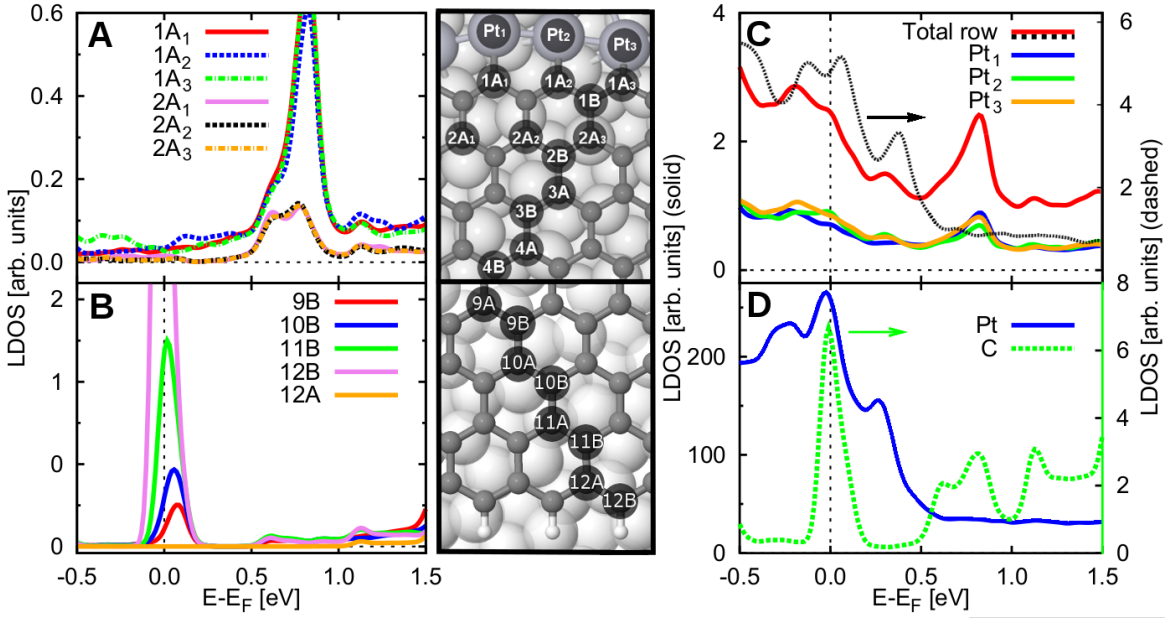

Figure 3.8 a), b) and c) LDOS of the atoms depicted in the ball-and-stick model corresponding to the atomic configuration shown in Fig. 3.6. In a) we can see that the LDOS of the C atoms in sublattice A (the sublattice to which the C atoms bonded to the Pt atoms belong) decreases as we get away from the step. As the chemical environment of the 3 C atoms of the step edge ($1A_1$, $1A_2$ and $1A_3$) is very similar, the LDOS of each of them is almost the same. On the other hand, we can see that in the opposite end of the graphene flake simulated (saturated with H atoms) is the other sublattice b) the one that has a peak in the LDOS that decreases as we move away from this end. The C atoms of the sublattice A at that end (orange) have a very small LDOS. In c) we can see the LDOS of the Pt atoms bonded to the C atoms. As it happens in the case of the first row of C atoms the LDOS of the 3 Pt atoms (Pt_1 in blue, Pt_2 in green and Pt_3 in yellow) are very similar. We can see the same localized electronic state at ~ +0.8 eV appearing in the LDOS of the entire row in our system (black solid line) compared to the LDOS of the system without the graphene flake (black dashed line) that does not show any peak at this voltage. d) The addition of the LDOS of all the Pt atoms (left scale) and all the C atoms (right scale).

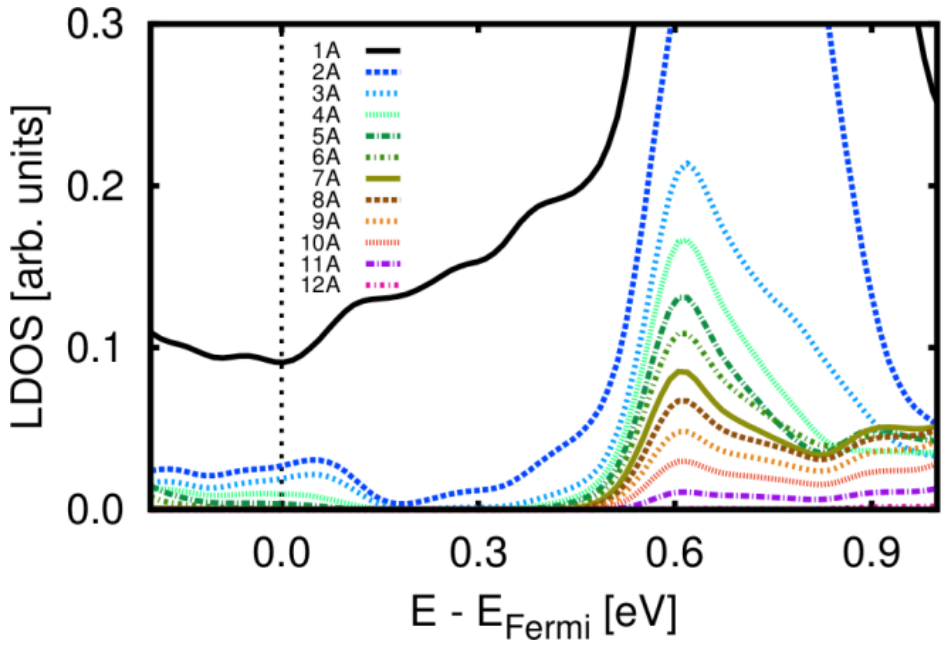

Figure 3.9 Zoom in the LDOS of the different rows of the A sublattice of the graphene flake as they are named in Fig. 3.8. The decay of the LDOS while you go away from the edge that can be seen in the main peak is also present at the surroundings of the Fermi level.

Low bias simulated STM images should display this behavior and this is indeed what we observe. In Fig. 3.6e, we show the results of different constant height STM simulations of a line profile scanning the A-graphene sublattice, the one whose atoms are in direct contact with the metal. There, the decay of the electronic states associated to the G-edge for energies close to the Fermi level (see Fig. 3.6e) can be seen along with its dependency with the voltage. The periodic protrusions decaying in intensity as we move into the graphene layer are the most characteristic attributes.

On the other hand, in Fig. 3.10 the decay of the state in the two sublattices can be compared. In this case the simulations are performed at 0.05 V at different tip-sample distances, being one of them the same used in Fig. 3.6 (2.75 Å with respect to the uppermost atom in the cell). In this case the decay length of sublattice A is 5.9 Å while the value for the other sublattice is more than double, 13.7 Å.

Another feature can be observed in Fig. 3.10: the dependency of the relative height between Pt and C atoms with the tip-sample distance. In Fig. 3.4 it can be clearly seen that in the experiments the Pt is brighter than the C. However, in the theory this relative brightness totally depends on the tip-sample distance. The larger it is, the brighter the Pt with respect to the C. For small distances, the C atoms are even brighter than the Pt ones. Of course the first rows of C are always quite bright because of the localized state but,

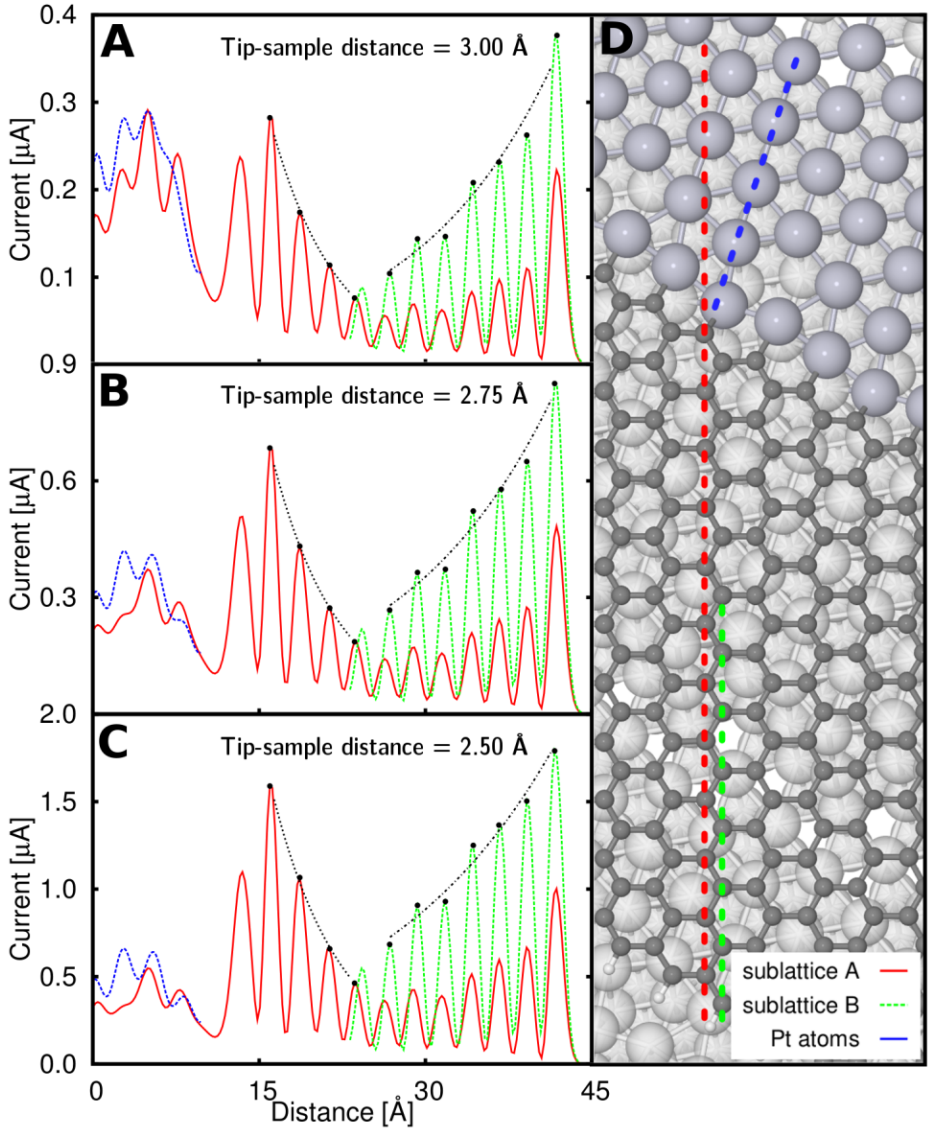

Figure 3.10 STM constant height profile simulations at a bias voltage of 0.05 V. Results for tip-surface distances (measured with respect to the uppermost atom in the cell) of 3.00 Å a), 2.75 Å b) and 2.50 Å c) are shown. The different profiles are depicted in d) being in red the profile through the sublattice A atoms of the graphene, in green the profile through the sublattice B atoms and in blue the sublattice through the Pt atoms. The values of the blue profile are similar to the red profile in the Pt region even though the latter does not goes through top Pt sites. Decay lengths are calculated for the states localized in each of the sublattices. From a) to c) the decay lengths for the sublattice A are 5.9 Å, 5.9 Å and 6.1 Å while for sublattice B we have 12.6 Å 13.7 Å and 16.2 Å. These decay lengths are calculated by fitting to an exponential decay function (black dashed lines) the maxima of the current oscillations (black dots) for each case.

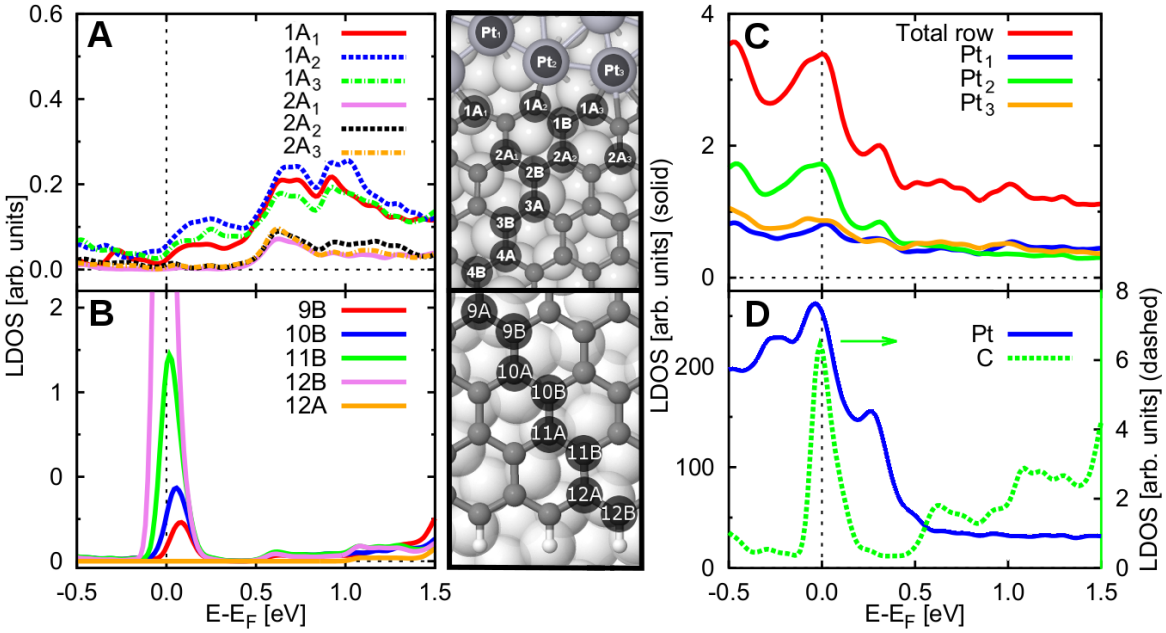

Figure 3.11 a), b) and c) LDOS of the atoms depicted in the ball-and-stick model corresponding to the alternative atomic configuration shown in Fig. 3.8. In a) we can see that the LDOS of the C atoms in sublattice A (the sublattice to which the C atoms bonded to the Pt atoms belong) decreases as we get away from the step. As the chemical environment of the 3 carbon atoms of the step edge ($1A_1$, $1A_2$ and $1A_3$) is different, the LDOS of each atom varies. On the other hand we can see that in the opposite end of the graphene flake simulated (saturated with H atoms) is the other sublattice c) the one that has a peak in the LDOS that decreases as we move away from this end. The C atoms of the other sublattice at that end (orange) have a very small LDOS. In c) we can see the LDOS of the 3 Pt atoms bonded to the C atoms (Pt_1, Pt_2 and Pt_3) the LDOS of the full row (Pt_1+Pt_2+Pt_3) in solid black and the comparison with the calculation of the same Pt configuration without the G flake. d) shows addition of the LDOS of all the Pt atoms (left scale) and all the carbon atoms (right scale) compared to the total DOS (left scale) of the system.

after the first rows, the isolated-graphene-like profile arises. After that, the current starts increasing again even in the sublattice A atoms. That is not because the state is located there, but an effect of the presence of the tip in the calculation which is seeing the wider DOS peaks located in the sublattice B atoms. That is why the peaks in both profiles (red and green of Fig. 3.10) are in the same spatial position, the position of the sublattice B atoms, and not slightly shifted from each other as should be if the peaks coincide with the position of the atoms of each sublattice.

3.4.4 Electronic structure of the alternative configuration

The structural differences between the two configurations presented reflect in changes in the electronic properties (Figs. 3.7d, 3.7e and 3.11). Due to the stronger C-Pt interaction

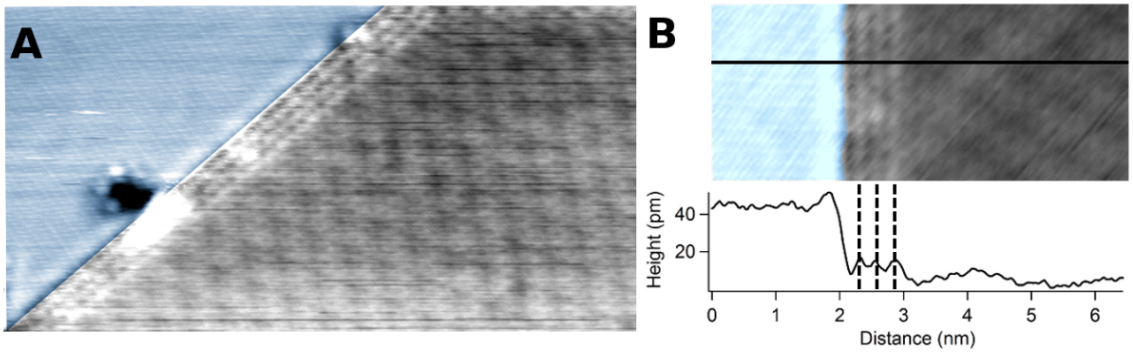

Figure 3.12 a) Constant current STM image (13.4×6.9 nm^2) of a *border-like* edge where an excess of charge is visualized parallel to the interface in the first three rows of graphene, $V_s = 51mV$, $I_t = 4nA$. b) Detail of such 1D states and height profile.

in this alternative structure, the peak in the LDOS projected on the C atoms at the step edge (see Fig. 3.7d) is wider and lower in energy. We can no longer see a clear trace of this state in the LDOS projected on the Pt edge atoms (Figs. 3.7e and 3.11c). Differences in the bonding configuration of the carbon atoms show up in the corresponding LDOS (Fig. 3.11a), at variance with the identical behavior found for the other structure discussed (Fig. 3.8a). As expected, the behavior of the other border of the flake saturated with H atoms (see Fig. 3.11b) is very similar in both models. Fig. 3.11d compares the total LDOS of the Pt with the total C LDOS (in a different scale). In spite of the quantitative differences described above, the electronic states associated with the two structures for the G-Pt edge share the same spatial localization properties: they are confined in one of the graphene sublattices and decay very rapidly when moving away from the edge.

3.5 Experimental characterization of the localized state predicted by theory

In Figs. 3.4d and 3.12a, we show experimental STM images where a modulation of the signal parallel to the *border-like* edge is clearly visualized. The distance between the maxima of the atomic lines is 2.4 Å (see the height profile in Fig. 3.12). This value corresponds to the distance of equivalent atoms in the graphene network and indicates that the edge state is mainly confined in one of the two sublattices.

This state, decaying away from the interface and localized in one of the sublattices, is also visible in the STM image of the *ZZ1* edge in Fig. 3.5 and Fig. 3.10. STM images of different edges show that, typically, after 4 atomic lines the state fully disappears.

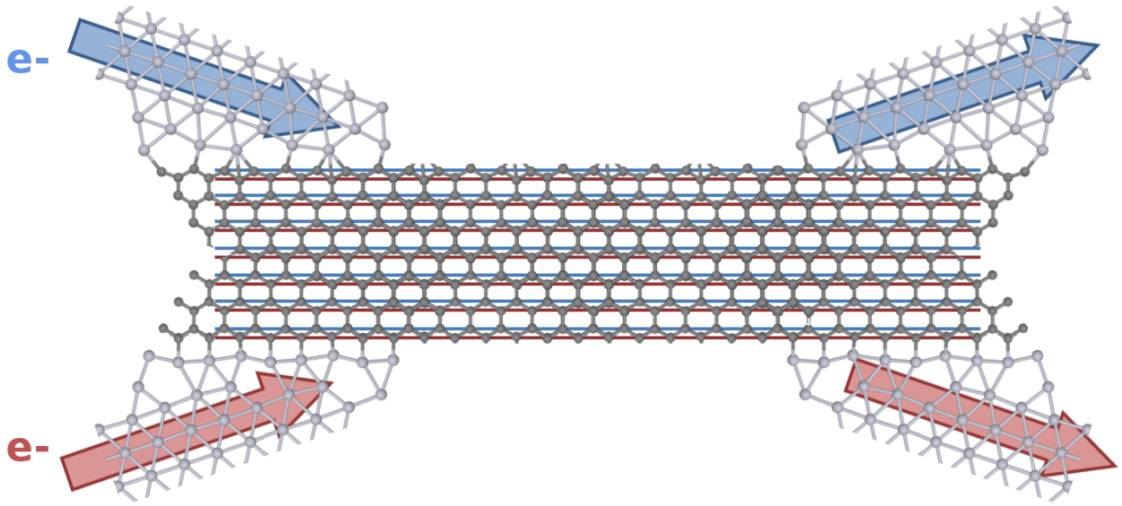

Figure 3.13 Sketch showing a possible two-channel conductor. This proposal takes profit of the sublattice states that appear at the G-Pt interface through the contact of two independent electrodes exciting the different channels.

Interestingly, this state is localized both in energy and real space. It vanishes as we move out of the interface. Therefore, they can be considered as 1D electronic states associated to each of the graphene sublattices. These electronic states confined in specific sublattices of the graphene structure open new opportunities to future atomically precise graphene based electronics and valleytronics[271,272].

3.5.1 Possible design of an hypothetical dual channel nanoribbon

Taking into account that we have shown that there are electronic states confined in every one of the graphene sublattices, we can take advantage of this to transport independently current trough out the edges without mixing both signals.

For instance, new multichannel nanowires could be built by contacting the opposite sides of a graphene flake with two different *border-like* edges as indicated in Fig. 3.13. We speculate that these atomically precise nanoleads will excite, respectively, each one of the two graphene sublattices, allowing two-ways atomically controlled transport via these independent electronic states.

The possibility of combining the spin, valley, and sublattice quantum numbers in the same device opens new paradigms in the electronic design of graphene-based nanoeletronics.

3.6 Crystalline borders and their relation with Moiré patterns

The precise determination of the atomic structure of the G-Pt boundaries sheds light on the geometry of the stable Moiré patterns reported for G/Pt(111) [101]. Our results show that these superstructures can be correlated with the crystallographic edges of the graphene islands formed during their growth. Rotational domains nucleate on the Pt step, binding the graphene island with the metal substrate with one of the particular orientations that produce energetically favorable *border-like ZZ* boundaries, and then continuing its growth with that angle. The link between the stability of the Moiré and the energetic of the edge boundary is supported by the STM analysis of different graphene islands. The observed Moiré patterns have grown following particular orientations that maximize the number of zigzag graphene terminations and the G-Pt edges tend to be parallel to the apparent angle of the Moiré superstructure.

Analogously to the standard notation used for nanotubes, we can assign the crystallographic stable interfaces with a couple of chiral vectors (defining a chiral vector as for nanotubes: two integers, n and m, denoting the number of unit vectors along two directions in the surface crystal lattice) one for Pt and other for the graphene (edge). With this notation, the *ZZ1* step can be denoted as $(1,2)_{Pt}(3,0)_G$ and *ZZ2* as $(-2,3)_{Pt}(0,3)_G$. Every one of those pairs of vectors represent a possible Moiré, however, only a few of all the possible combinations of these pairs will be stable. The phenomenological model presented in ref. [101] indicates that, in a first approximation, the existing Moirés are those that minimize the strain. However, not only strain plays a role. In the case of *border-like* edges the energetic of the interface is also important.

The study of the crystallographic parameters of the Moiré superstructures by STM images is a difficult task, because simultaneous atomic resolution in both graphene and metal surface is required. It is important to notice that, usually, STM images of graphene Moirés lack of any information about the commensurability of the superstructures. Thus, even though we could say that near the graphene-Pt border the structure is commensurated, nothing can be said about zones far apart from the edges, as the accumulation of mismatch will either disrupt the long range order of the Moiré superstructure or generate defects, such as ripples, vacancies, or domes. Fig. 3.14a shows a small epitaxial graphene island grown attached to a Pt step. As usual, it appears with part of its area inside the upper Pt terrace, indicating mass transport. Looking carefully to the lower left part of the image we see a 6×3 nm^2 graphene nanobubble.

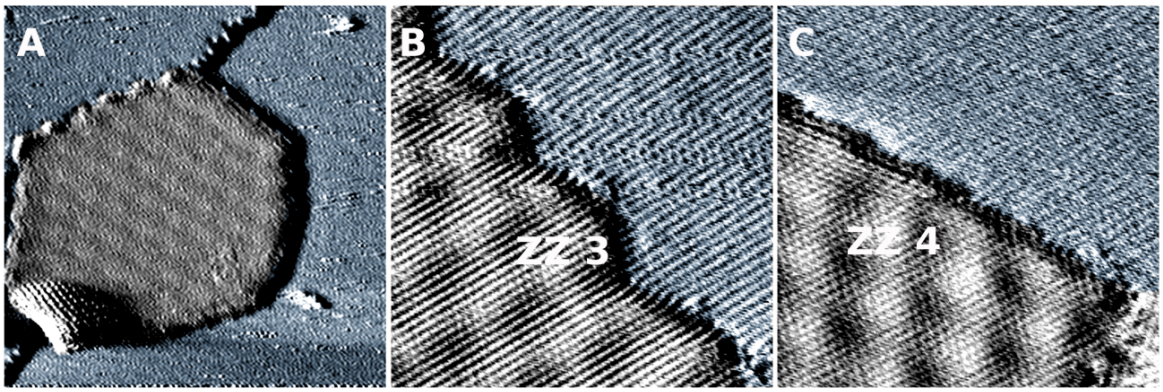

Figure 3.14 a) STM image showing a graphene island, a nanobubble can be seen in the lower part. 17×17 nm^2, 1.9 nA, 100 mV. b) Detail of a crystalline edge with a graphene zigzag termination (*ZZ3*), 10×10 nm^2, 3.94 nA, 10 mV. c) Detail of a crystalline edge with a graphene zigzag termination (*ZZ4*), 10×10 nm^2, 3.94 nA, 10 mV.

Fig. 3.14 shows STM images of 3 *border-like* atomically resolved crystalline edges giving rise to different Moirés superstructures. Figs. 3.14bc correspond to Moiré patches of ζG/Pt(111) for *ZZ3* and μG/Pt(111) for *ZZ4*[101]. Using the vector notation, these edges correspond to these pairs of chiral vectors: $(8,0)_{Pt}(9,0)_G$ for *ZZ3* and $(7,1)_{Pt}(8,1)_G$ for *ZZ4*. They both involve a large number of atoms, and escape the capabilities of regular DFT calculations. However, a visual inspection of these edges (and others not shown) provides us with some general ideas about their atomic structures. At first sight, it seems that in all crystallographic *border-like* edges, the graphene islands end up in a zigzag configuration. Hence, the Pt atoms at the edge absorb the largest part of the strain and reconstruct to adopt the structure that yields the maximum possible graphene ending in a zigzag arrangement.

Fig. 3.15 illustrates this point. In this figure we have schematically reproduced edges similar to *ZZ3* and *ZZ4* of Fig. 3.14, another hypothetical *ZZ* edge (called *ZZX*) and an amorphous edge (*A*). Graphene prefers to stabilize its edges by maximizing the number of the –energetically favored– zigzag edges. The amount of the armchair regions needed in the interface (marked in the figure by red ovals) depends on the angle between G and Pt (and, therefore, the angle between the Moiré and the Pt). We observe that the more often found graphene edges are those which have maximized the number of zigzag unit cells versus the armchair ones, thus, in Fig. 3.15, *ZZ4* will be preferred versus the *A* edge, although both are rotated 6°. The *A* termination is exclusively observed in defective regions of the G-Pt edge, like *A2* in Fig. 3.5.

The fact that the system tends to maximize the number of straight regions of zigzag termination intercalating single armchair unit cells leads to an interesting secondary

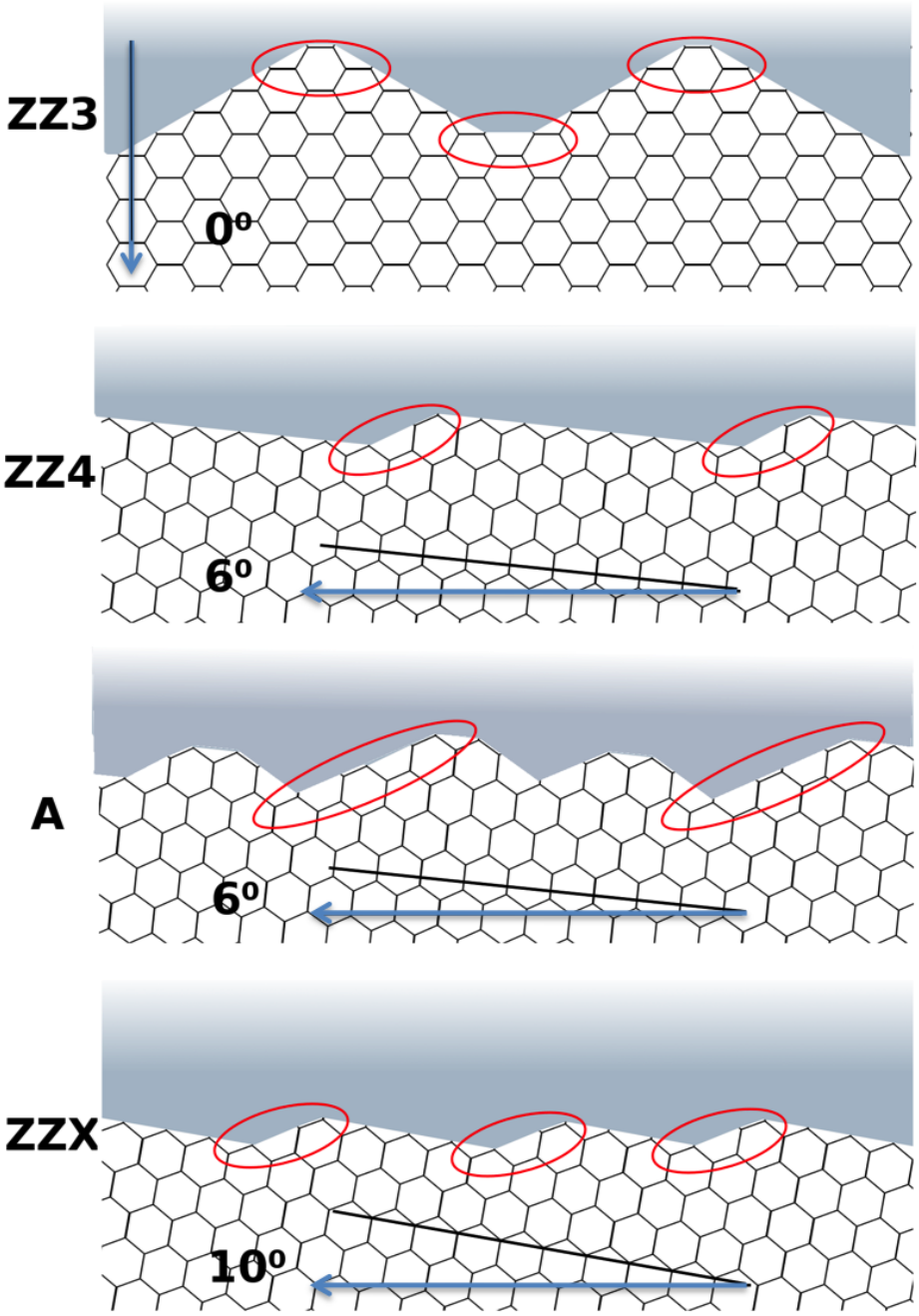

Figure 3.15 Schematic model of the preferred graphene termination of *border-like* at the G-metal interface. The bluish side corresponds to the Pt region, with crystallographic direction, indicated by a blue arrow, along the horizontal (except for *ZZ3*, where it is along the vertical). The graphene tends to adopt zigzag configurations by minimizing the number of armchair unit cells for a given crystallographic angle with respect to the Pt surface. Armchair configurations are marked with red ovals.

effect. The Pt edge directions are normally parallel to the apparent angle of the Moiré[101] (see Fig. 3.16). This means that if we ignore the local relaxation of individual Pt atoms, the G-Pt edge is not parallel to the crystallographic directions of the substrate, but to the direction of the Moiré superstructure. This can be very useful for determination and assignment of the structure of unknown rotational domains with large scale STM or AFM images, even when the periodicity of the Moiré is not resolved. However, one has to be very careful if using this method for Moiré determination, as there are normally more than one Moiré with a similar apparent angle, i.e. there are more than one rotational domains with different crystallographic angles yielding Moirés with different atomic structure but the same apparent angle[101].

The case of the edges between $(\sqrt{7} \times \sqrt{7})R19°$ graphene and Pt described in this chapter (*ZZ1* and *ZZ2*) present the –rather rare– particularity that the crystallographic directions of Moiré and graphene are the same, i.e. 19°, and thus it wrongly seems that the edges are parallel to the crystallographic directions of graphene. The case of *ZZ4* (Fig. 3.14c), or the island shown in Fig. 3.14a, are the rule. The edges run parallel to the Moiré crystallographic directions. In Fig. 3.16 we see more examples of these behavior: zigzag G-Pt edges in which the Pt crystallographic border runs parallel to the Moiré apparent angle.

ZZ3 seems to be different, as the Moiré runs perpendicular to the edge. However, this Moiré corresponds to the case where the angle between the graphene and the Pt is 0 degrees, and then the normal edge would be exclusively formed by armchair termination, which is energetically unfavorable. This edge adopts the structure shown in Fig. 3.15 *ZZ3* diagram. It maximizes the zigzag graphene unit cells at the metal interface by creating the corner-like structures that can be observed in the experiments (see Fig. 3.14b).

In conclusion, we have shown that a relationship exists between the Moiré and the crystallographic *border-like* edges that may be an important factor in the determination of the orientations of graphene epitaxially grown on Pt(111). Although other kinetic effects, such as the formation of defects or folds due to the shrinking occurring during the cooling-down after the growth annealing (due to the difference between the thermal coefficients of graphene and the substrate) can also play a role.

We usually observe graphene domains embedded within the upper Pt terrace, indicating mass transport within the upper terraces, see for instance Fig. 3.14a. However, we do not know which is the real growth mechanism as we only are able to study the final stage of the graphene CVD growth process. In principle, two possibilities can be envisaged. First, graphene nucleation on the upper terrace undergoes etching of some Pt atoms within this terrace. Thus, the graphene domains would grow "going into" the Pt step. The second

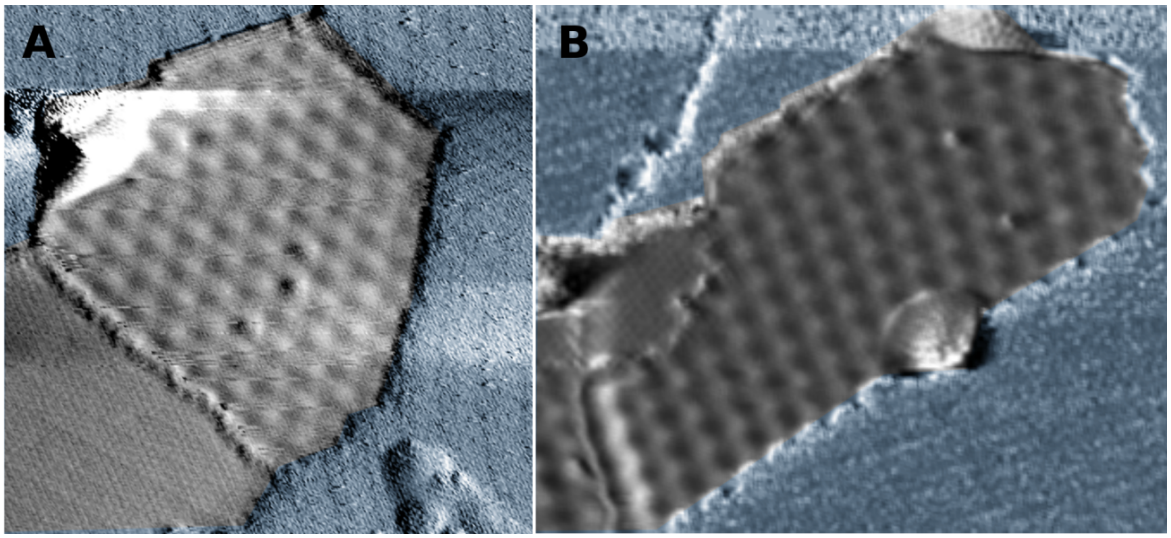

Figure 3.16 STM images showing graphene edges running parallel to their Moiré apparent angles. Nanobubble or graphene folds can be seen in the islands a) 30×30 nm^2, 2 nA, -100 mV. b) 30×25 nm^2, 1 nA, 50 mV.

possible explanation implies severe mass transport on the substrate surface due to the high temperatures needed during growth. The diffusion of Pt atoms might occur both along the step-edges and on within the terraces. In this case the graphene would nucleate into the described G-Pt edge boundaries and the diffusing Pt atoms would embrace the graphene seed, as can be seen in Fig. 3.4a.

3.7 Conclusions

We present a combined STM and DFT study of edge heterostuctures of graphene grown on Pt(111) in which we disclose the atomic structure of the G-Pt boundary. The unsaturated C atoms strongly interact with the Pt step, preserving a zigzag structure quite close to the ideal configuration. However, on the other side, Pt edge atoms experience a 3-fold reconstruction that stabilizes the structure. The tendency to form passivated zigzag graphene terminations plays a relevant role in the formation and orientation of the stable Moiré patterns. Our combined approach reveals the interesting electronic properties of this nanoscopic system including, as stated by the simulations, the preservation of the G–edge state shifted to energies at about ~0.8 eV above Fermi level, highly localized in one of the graphene sublattices and confined to the G-Pt interface. This state spreads out inside the first Pt row resulting in a high quality G–metal electric contact that could be relevant for designing future atomically precise graphene metal leads.

CHAPTER 4

GRAPHENE MONOVACANCIES: ELECTRONIC AND MECHANICAL PROPERTIES FROM LARGE SCALE AB INITIO SIMULATIONS

4.1 Introduction

Graphene is a promising material due to its outstanding electronic and mechanical properties[42]. Real materials have defects which, instead of being a drawback, can be regarded as an opportunity to tune their properties. Defect engineering in graphene is nowadays an active and crucial research area[38,95,122,243,273–275]. Of particular interest is the influence of defects on both the mechanical properties and the tuning of electronic and magnetic properties of this material. Spintronics represents one of the most exciting fields for possible applications of graphene[38]. Monovacancies (V_1), one of the most common defects on graphene[122], have been proposed to induce local magnetic moments in this carbon-based material[63,138,139]. Furthermore, recent measurements show that the mechanical properties are modified in an unexpected way: instead of contributing to a softness of the material, low concentrations of vacancies increase the graphene stiffness[127].

The removal of an atom from the graphene lattice leaves three equivalent C atoms with unsaturated σ bonds and the structure of the V_1 could remain in a symmetric arrangement ($s-V_1$). However, density functional theory (DFT) simulations[63,122,138,139] predict a Jahn-Teller distortion by the formation of a soft σ bond between two of the C atoms which leads the V_1 to an asymmetric 5-9 reconstruction ($a-V_1$) with a formation energy in the range of 7.3−8.58 eV[122]. On the other hand, classical force fields[122,276] yield to a symmetric structure and no soft bond is formed due to the electronic nature of this reconstruction, which this computational scheme cannot account for.

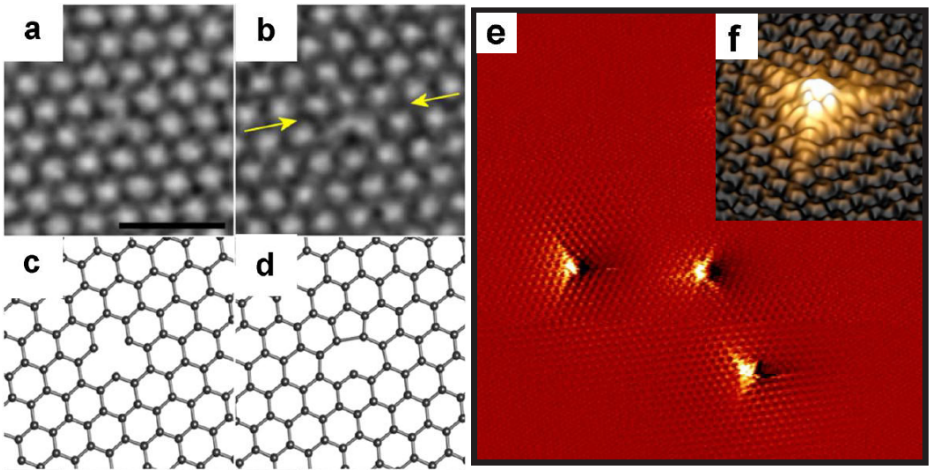

Figure 4.1 a) and b) are smoothed AC-TEM images of the symmetric and asymmetric monovacancies respectively, with their corresponding ball-and-stick models shown in c) and d). In the asymmetric structure image yellow arrows indicate the zigzag axis containing the reconstruction. e) STM topography showing a graphite surface after Ar^+ ion irradiation. Monovacancies occupy sites at both sublattices of the graphite honeycomb lattice. f) 3D view of the STM topography one a single isolated vacancy. Figure adapted from[278] (TEM images) and[279] (STM images).

The V_1 have been observed by transmission electron microscope (TEM) studies[250,273,274,277,278]. Both $a-V_1$ and $s-V_1$ vacancy structures have been reported[278] (see Fig. 4.1a-d). Scanning tunneling microscope (STM) experiments have also measured V_1 on graphite and graphene on metals[266,279,280] where the atomic structure is distorted by the electronic effects but comparison with DFT simulations[266] support the presence of the $a-V_1$ reconstruction (see Fig. 4.1e,f).

According to previous works (see ref.[38] and references therein), there are experimental evidences of magnetism in defected graphene sheets. Supporting these experimental results, DFT calculations on clusters or small cells (high V_1 concentration)[63,122,138,139] predict the V_1 to be magnetic. The explanation for this phenomena is straightforward in terms of the electron redistribution. Among the 3 σ electrons that are now unpaired, 2 form a soft bond and the other one remains unpaired. There is a semilocalized π state associated with the V_1 which is close to the Fermi level that, in the case of an isolated V_1, could be either unoccupied, occupied by one electron –ferro or antiferromagnetically coupled with the σ electron– or double occupied. Therefore, the local magnetic moment, adding up the possible contributions from the σ and π states, could be 0 μ_B –σ and π single occupied and antiferromagnetically coupled–, 1 μ_B –with an unoccupied or double occupied π state which would not contribute to the magnetic moment– or 2 μ_B –σ and π single occupied and ferromagnetically coupled–.

However, simulations of point defects in extended systems computed imposing periodic boundary conditions (PBC), have a problem with the size of the cell[281]. In the case of graphene, small unit cells do not provide a proper description of the charge transfer from the π states of bulk graphene to the π states of V_1. When using small cells, the limited number of bulk states that contribute to the charge transfer results in an artificial over-doping, reflected in the displacement of the Fermi level with respect to the extended states that shifts the Dirac point towards higher energies. Moreover, small cells allow the semilocalized π states of the vacancies to interact with each other. This spurious interaction contributes to the displacement and broadening of those defect states. Due to these effects, previous calculations have predicted the magnetic moment of a V_1 to be $< 2\ \mu_B$[63,64,66,282,283]. Several works have reported results showing a reduction of the local magnetic moments upon cell size increasing[64,66]: they reach cell sizes up to 2.5 nm and it has been argued that the magnetism due to π orbitals should be quenched for low V_1 concentrations[66]. On the other hand, calculations based on clusters show that the magnetic moment increases upon cluster size, pointing out to a 2 μ_B moment[64,65]. Therefore, calculations including periodicity seem to produce the opposite result of cluster based simulations.

We should also highlight that previous theoretical results have been calculated assuming ideal conditions with isolated and balanced graphene layers. However, the graphene layers are usually under strain due to the effect of the substrate or, in general, the environment. This effect could modify the properties induced by defects[284].

Regarding the mechanical properties of graphene, it has been reported that the Young's modulus of pristine graphene is around 1 TPa with an intrinsic breaking strength of 42 N/m[22] and it also presents a negative thermal expansion coefficient (TEC)[285,286]. Theoretical descriptions[122,287–289] predict a softness of the layer with the appearance of V_1. However, experiments based on atomic force microscopy (AFM) indentation have shown an increase of effective Young's modulus up to almost double the value for ideal graphene when the V_1 content is $\sim 0.2\%$[127] (see Fig. 4.2).

In this work we have performed a complete set of large scale DFT simulations, with cell sizes in the range of 1.5−7.4 nm, in order to shed some light on: i) the magnetism of an isolated V_1, ii) the influence of the strain on the magnetic properties of V_1, and iii) the effect of the V_1 on the mechanical properties of graphene. We have respectively found: i) a clear tendency of the local magnetization of a V_1 towards a value of 2 μ_B for the diluted limit, ii) a structural and electronic transition of the V_1 state when it is under an external in-plane tensile strain beyond the 2% and iii) a correlation between the strain field generated by the presence of the V_1 and the partial suppression of out-of-plane

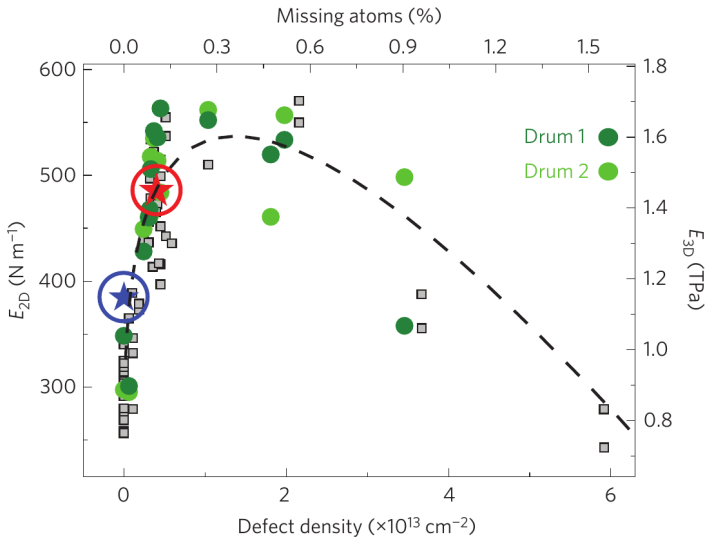

Figure 4.2 Measurements by AFM indentation of E_{2D} as a function of defect concentration. The different sets of experimental measurements (green circles and grey squares) correspond to experiments of AFM indentation on graphene drumheads prepared by mechanical exfoliation of natural graphite on Si(300 nm)/SiO_2 substrates with predefined circular wells with diameters ranging from 0.5 to 3 μm. This figure has been extracted form the original work by López-Polín *et al.*[127].

fluctuations which leads to an increasing of the effective stiffness of the material for a low concentration of these defects.

With that purpose, we first present the methodology used on the simulations (see Sect. 4.2), of great importance given the crucial good scaling of the code used which enables us to work with large system sizes. We then tackle the problem of the magnetism of V_1 on graphene (see Sect. 4.3). Next, we show the results of the study of the V_1 local magnetization dependency with an external in-plane strain (see Sect. 4.4). We finally show the strain field induced by the reconstruction of the V_1, which is consistent regardless of the cell size (see Sect. 4.5). We study how this can affect to the mechanical properties of the sheet analyzing both the in-plane and out-of-plane deformations to correctly address the source of the stiffness increasing.

4.2 Methods

The calculations whose results are shown in this chapter were done using the DFT OpenMX (Open source package for Material eXplorer) code[154,155]. The main advantage of this code it has been carefully designed to be a powerful tool in large-scale ab initio electronic and structural calculations (see Chapter 2 for details). Our largest simulation performed in the Curie supercomputer[290], a *tier0* machine, was a $G(30 \times 30)$ cell (1800 atoms) with a

maximum k-point mesh of $19 \times 19 \times 1$ for what 368 MPI and a threading of 8 were used (2944 processors in total).

We employed the generalized gradient approximation exchange-correlation density functional of Perdew, Burke, and Ernzerhof (PBE) [159] for the calculations. In order to be able to reach very large system sizes we restricted our basis to a DZ ($s2p2$) after checking with some tests in the smaller systems that there were no big differences in the results performed with a DZP ($s2p2d1$) basis or those computed with a plane waves code [153]. For both basis we used a cutoff radius of 6.0 a.u. The calculations were performed including spin polarization to be able to study the magnetization of the system, using an electronic temperature of 6 K. For the cell construction we used a lattice parameter obtained for the ideal graphene system of 248 pm.

For the first part of the study of the magnetization induced by the V_1 for different cell sizes a real space grid equivalent to an energy cutoff of 200 Ry was used with a criteria for both electronic and ionic relaxations of $1 \cdot 10^{-6}$ Hartree and $1 \cdot 10^{-4}$ Hartree/Bohr respectively. In order to study the evolution of the reconstruction of the V_1 with the size of the cell, the structures of the $G(6 \times 6)$, $G(12 \times 12)$ and $G(18 \times 18)$ were optimized using equivalent $\Gamma-$centered k-point meshes of $13 \times 13 \times 1$, $7 \times 7 \times 1$ and $5 \times 5 \times 1$ respectively. In the latter we stopped the structural optimization at a slightly larger criterion ($2 \cdot 10^{-4}$ Hartree/Bohr) due to extremely long convergence times. For this same reason, no larger cells were structurally explored. For the study of the magnetization dependency with the cell and k-point mesh sizes, the $G(6 \times 6)$ reconstruction was fixed for all of them and more atoms were added up to the specific cell size. These calculations were static.

For very large k-point meshes in the larger cells, some calculations were stopped with an electronic convergence criterion of $\sim 5 \cdot 10^{-5}$ Hartree always ensuring that the magnetization had converged up to $1 \cdot 10^{-4} \mu_B$.

Under typical experimental conditions, the interaction with the substrate where the graphene is grown or supported induces a finite strain. We have applied an external isotropic tensile strain to the system to analyze the possible influence of different experimental conditions in the properties of the graphene sheet. For the exhaustive study of the magnetization evolution with strain, a system consisting on two monovacancies ($2V_1$) on a $G(12 \times 12)$ cell was used. As the convergence of a single V_1 per cell was very demanding, another V_1 was added to the system and located in the other sublattice in such a way that the two vacancies were as far as possible to minimize interaction. This new system is easier to deal with in terms of structural and energy convergence. A $5 \times 5 \times 1$ k-point mesh was used for the structure optimization while a larger $11 \times 11 \times 1$ mesh was employed to get the electronic results; both calculations employed finer electronic and ionic relaxation

criteria than in the previous part ($1 \cdot 10^{-7}$ Hartree and $5 \cdot 10^{-5}$ Hartree/Bohr respectively). The study of the effect of the strain applied to the system requires changing the cell size. For this reason, we chose to fix the real space grid at (300, 300, 225) which corresponds to an energy cutoff of 350 Ry for a $G(12 \times 12)$ with a strain of 5% (~370 Ry for the non-strained cell). In this study, we have considered the local magnetization of the vacancies as the average of the absolute values of magnetic moment for each of the two vacancies. This average cancels out the effect of a small asymmetry in the filling of the four states (taking into account the k/-k symmetry) associated with the up-π_1 (majority spin for vacancy 1) and down-π_2 (majority spin for vacancy 2) bands close to the Fermi level. This asymmetry –that appears due to numerical errors that break the energy degeneracy of these two bands, and to the use of a k-sampling that includes the Γ point– induces a difference between the local magnetizations that scales as 1/(# of k points).

4.3 The magnetism of a single monovacancy on graphene

We start our study characterizing a small cell size, $G(6 \times 6)$, on which the vacancies are separated ~1.5 nm, and their interaction is strong. We get the $a - V_1$ reconstruction (see Fig. 4.3) where the soft bond distance is 209 pm and the formation energy 7.98 eV, in good agreement with previous results[122]. The graphene layer is not completely flat, it shows a topographic corrugation of 9 pm (see Fig. 4.3). With a k-point mesh of $3 \times 3 \times 1$, the V_1 induces a magnetic moment of 1.55 μ_B, again in good agreement with previous results[63].

Its band structure and DOS are shown in Fig. 4.4. Both the localized σ bands, filled with one electron, and the semi-localized π states associated with the V_1 are clearly identified. The π band, although very flat in some areas of the Brillouin zone, shows a broadening of ~75 meV due to the interaction. The high V_1 concentration has also modified the Dirac point (see the blue circle in Fig. 4.4a): i) it has been shifted towards positive energies (~0.25 eV) and ii) a small gap is opened between the two Dirac cones. Since the Dirac point is shifted towards positive energies, the extended states of graphene transfer charge to the π state of the V_1. However, due to the broadening of this band, the up-π state is not able to accommodate all this transferred charge, so the rest of the electronic charge has to fill the next band which is the vacancy down-π state. As a consequence, the magnetic moment is less than 2 μ_B and the Fermi level is pinned in the down-π state. The precise value of the magnetic moment is, therefore, related with the Fermi wave vector (k_F) –the k vector of the last occupied state– associated with the extended band and the semi-localized V_1 up-π band. Both features depend on i) the k-mesh used in the calculation and ii) the size of the unit cell.

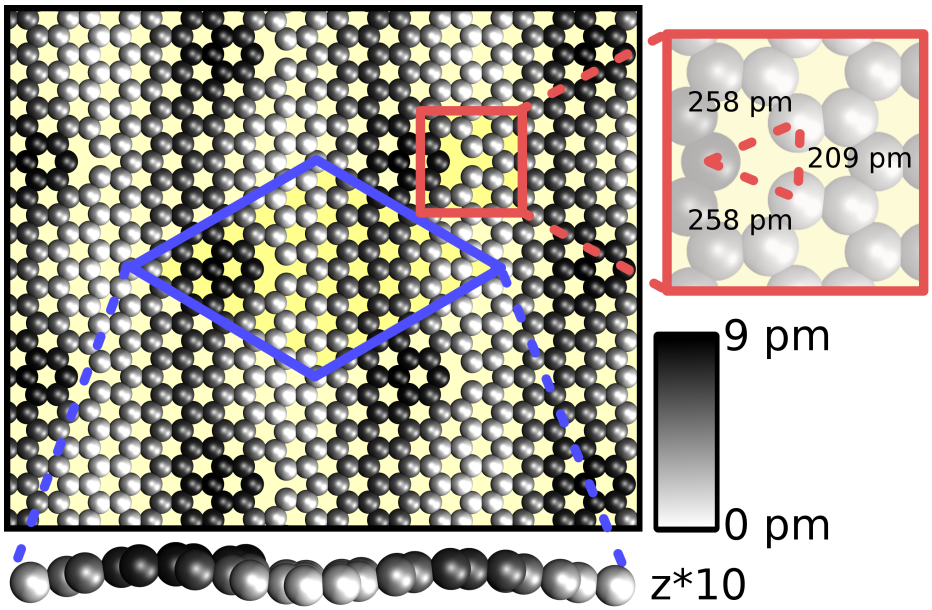

Figure 4.3 Ball-and-stick scheme of the $G(6\times6)$ cell structure (unit cell highlighted in blue) where the asymmetric reconstruction of the V_1 can be seen ($a-V_1$). The relevant distances between atoms of the V_1 are shown in the zoom of the top view of the cell (red square). They can be compared to the reference ideal graphene distance which according to our calculations is 248 pm. In the side view the z coordinates have been multiplied by 10 to ease the visualization of the corrugation of the system which is around 9 pm.

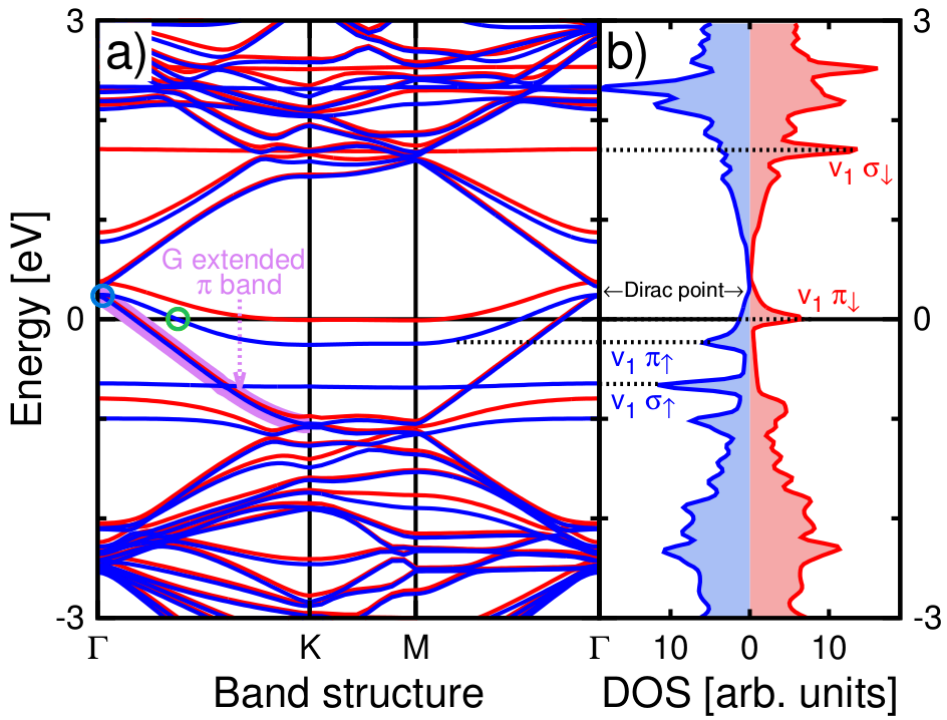

Figure 4.4 a) Bands and b) DOS (calculated with a Γ−centered 100 × 100 × 1 k-point mesh) of the $G(6\times6)+V_1$ cell as shown in Fig. 4.3. In a) the graphene extended π band is highlighted in purple. The blue circle shows the point where this band reaches the Γ point of the Brillouin zone, which denotes a shift of the Dirac point, and the green circle shows the Fermi wave vector (k_F) of the V_1 up-π band. In both a) and b) the main states corresponding to the V_1 are identified.

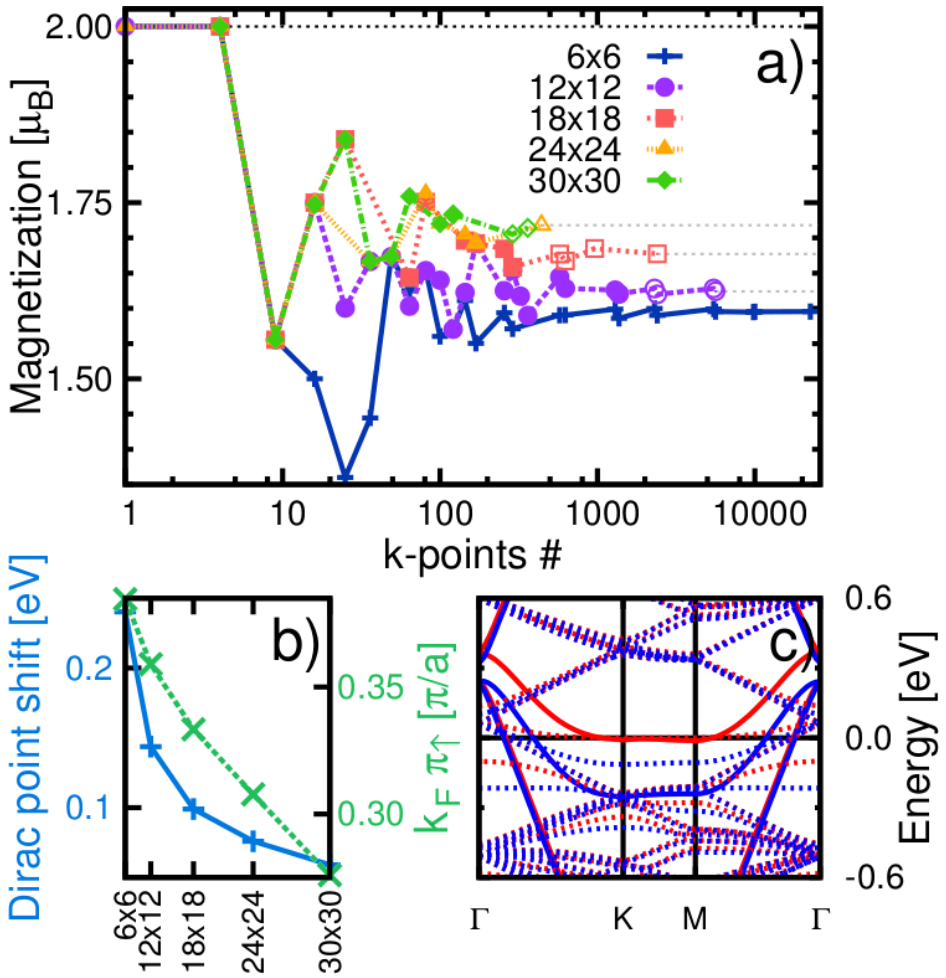

Figure 4.5 a) Total magnetization for different cell sizes versus the number of k-points used to converge the calculations. The solid points have been calculated with an electronic convergence criterion of $1 \cdot 10^{-6}$ Hartree while the open points have been calculated with $5 \cdot 10^{-5}$ Hartree, however, the magnetization is always converged up to $1 \cdot 10^{-4} \mu_B$. b) Shift of the Dirac point (blue) and Fermi wave vector (k_F) of the V_1 up-π band (green), both points highlighted in Fig. 4.4 for the $G(6 \times 6) + V_1$ case. The best converged results for each of the cell sizes studied in a) are shown. c) Comparison of the bands –for the same energy range– of the smaller and bigger of all systems: $G(6 \times 6) + V_1$ (solid lines) vs $G(30 \times 30) + V_1$ (in dashed lines).

In Fig. 4.5 we show the values of the local magnetic moment as a function of the number of k-points used in the calculation for different cell sizes. We observed that the convergence with the k-point mesh is very slow, and it requires ~1000 k-points to reach converged values, much larger meshes than have previously been reported[63,65,66,122]. More importantly, as the π state associated with the V_1 is semi-localized, its correct description requires a large number of k-points independently of the size of the cell. Our results show that, in the converged limit, the local magnetic moment increases with the cell size. Previous works have obtained the opposite result probably due to the k-mesh used in their calculations[66].

Fig. 4.5b shows the Dirac point shift as a function of the cell size. It tends to the Fermi level position for large sizes. The Fermi wave vector (k_F) –the k vector of the last occupied state– of the V_1 up-π band is also displaced towards the Γ point (see Fig. 4.5b), reducing the electron charge transferred from the up-π to the down-π band. Fig. 4.5c shows a comparison between the band structure of the $G(6\times6)+V_1$ and $G(30\times30)+V_1$ systems close to the Fermi level. The reduction of both the Dirac point shift and the broadening of V_1 π bands can be clearly observed. The exchange interaction between the π bands and the single-occupied σ state, i.e. the Hund's rule, breaks the spin symmetry and splits the two bands. Our results indicate that, in the limit of an isolated V_1, the splitting between the V_1 up-π and down-π bands is complete, leading to a completely filled V_1 up-π band and an empty V_1 down-π band, and, thus, a local magnetic moment of 2 μ_B (1 μ_B from the flat σ band plus 1 μ_B from this completely filled up-π band), as pointed out by the calculations carried out with large clusters[64,65]. This solves the discrepancy between the predictions based on DFT+PBC and DFT calculations using clusters[64–66].

We have to emphasize that our assignment of a local magnetic moment of 2 μ_B for the isolated vacancy limit requires the combination of two results: (i) the increasing values of the magnetization for larger unit cells shown in Fig. 4.5a, and (ii) the evolution with cell size of the Dirac point and the k_F of the V_1 up-π band illustrated in Figs. 4.5b and 4.5c, that points towards a complete filling in the limit of a single vacancy.

This very gradual evolution of the band is related with the slow spatial decay of the semilocalized state associated with the monovacancy. Even for our larger cell sizes, the semilocalized states from defects belonging to different cells are still interacting with each other. This effect is unavoidable in the type of calculation we are performing –DFT with periodic boundary conditions (PBC)– and produces a partial band filling. In the diluted limit –where these states do not interact with each other– they are either totally empty or totally filled, making the total magnetic moment to be either 1 μ_B or 2 μ_B respectively. In spite of their limitations, DFT-PBC calculations do allow us to determine

	K-points	Mag. mom. [μ_B]	Dimer [pm]	Corrugation [pm]
$G(6\times6)$ Pol.	$13\times13\times1$	-1.69	209	9
$G(12\times12)$ Pol.	$5\times5\times1$	-1.61 (-1.60)	201 (209)	13 (9)
	$7\times7\times1$	-1.67 (-1.67)	201 (209)	13 (9)
$G(18\times18)$ Pol.	$4\times4\times1$	-1.75 (-1.75)	200 (209)	13 (9)
	$5\times5\times1$	-1.84 (-1.84)	200 (209)	13 (9)
$G(6\times6)$ Non Pol.	$13\times13\times1$	0	219	59
$G(12\times12)$ Non Pol.	$7\times7\times1$	0	209	62

Table 4.1 Magnetic moment, soft-bond dimer distance and sample corrugation for different systems studied with different k-point meshes. We show results for calculations including spin polarization and also non-polarized. The corrugation of the sample in the latter cases is referred to the displacement of this atom. The results in brackets are referred to calculations where the $G(6\times6)$ structure is fixed for the V_1 vicinity and they can be compared to the results provided for fully relaxed calculations.

the evolution of the filling of that band. Our results reveal a clear trend, slow but steady, in the magnetization and the evolution of the up-π band that suggests that this band is going to be completely filled in the limit of low defect concentration, leading to a magnetic moment of 2 μ_B.

These calculations for the evolution of the magnetic moment have been carried out by fixing the vacancy structure relaxed for the $G(6\times6)$ cell, but the possible influence of the changes in the relaxation for larger cells has also been considered. Our analysis shows that the main features of the structure, in particular the length of the soft bond, converge quite rapidly: this bond length is 209 pm in the $G(6\times6)$, decreases for the $G(12\times12)$ down to 201 pm, and keeps a very similar value, 200 pm, for the $G(18\times18)$ (see Table 4.1). The small corrugation which appears upon relaxation is also converged to a value of 13 pm for $G(12\times12)$ cell sizes.

Moreover, we have checked that the local magnetic moments obtained from fully relaxed calculations on these larger cells are almost identical to the ones determined from static calculations using the V_1 structure relaxed for the smaller $G(6\times6)$ unit cell. Thus, we have confirmed that, even for the cases where the soft bond distance is not totally converged, the local magnetic moment is not affected.

Notice that non-polarized calculations yield to different structures, with a formation energy higher in ~+170 meV for the $G(12\times12)+V_1$, where there is a strong out-of-plane relaxation of ~60 pm of the V_1 atom that is not forming the soft bond (see Table 4.1).

Stability of the 5-9 asymmetric reconstruction

We have studied the stability of the $a-V_1$ reconstruction versus the $s-V_1$ structure of the V_1 as experiments have reported both reconstructions[273,277,278,291]. The $s-V_1$ reconstruction is not stable according to our calculations. Anyway, we have optimized the interatomic distances of the 3 atoms performing constrained calculations of this symmetric V_1. We found that the V_1 is slightly expanded with respect to the ideal graphene lattice distances (250 pm vs 248 pm for the reference) and in this case there is no corrugation induced on the sheet. The energetic difference between this $s-V_1$ configuration and the $a-V_1$ stable reconstruction is around 350 meV for the $G(6\times 6)$ cell.

Up to this point we have calculated the ground state of the system, but the stability of the $a-V_1$ structure could be affected by thermal fluctuations. To analyzed this we have performed, also with the OpenMX code, some *ab initio* NVT molecular dynamics simulations by the Nosé-Hoover method[292–294] for a temperature of 300 K and time steps of 2 fs. Our DFT-MD simulations at room temperature show that the $a-V_1$ reconstruction is maintained also at finite temperatures. In Fig. 4.6 we show the results for the variation with time of the distances between the three atoms of the V_1 for two different systems: a $G(4\times 4)+V1$ and a $G(12\times 12)+2V1$ systems. We have used the small size system as a first test and then we have checked the consistency of the results in a bigger one on which we can also analyze the effect of the interaction between two V_1 in this larger system. The V_1 structures in both cases oscillate around the 5-9 ground-state reconstruction with 2 larger distances and a short one corresponding to the soft bond and the fluctuations of the soft bond distance are larger than the other two. In the smaller system several orientation switches –soft bond jumps among the three atoms– can be observed during the simulation every ~400 fs in average. Most importantly, right after every rotation, the V_1 recovers an asymmetric reconstruction as was observed at ground-state calculations (see Fig. 4.6). In the $G(12\times 12)+2V1$ case there is only one switch per V_1 in the time range that we have analyzed, what makes sense because the system size is larger and the interaction between the V_1 is weaker. Notice that when the first V_1 rotates (~1250 fs), the other defect rotates shortly after (~350 fs later) too in the same direction (highlighted with a yellow background in Fig. 4.6). The change of the orientation of one V_1, thus, seems to induce a rotation in the other in the same direction.

These facts support the interpretation of the experimental evidence for a $s-V_1$ reconstruction found with different experimental techniques (including STM[138] and TEM[250]) as a result of the overlap of the three possible $a-V_1$ structure orientations of the V_1.

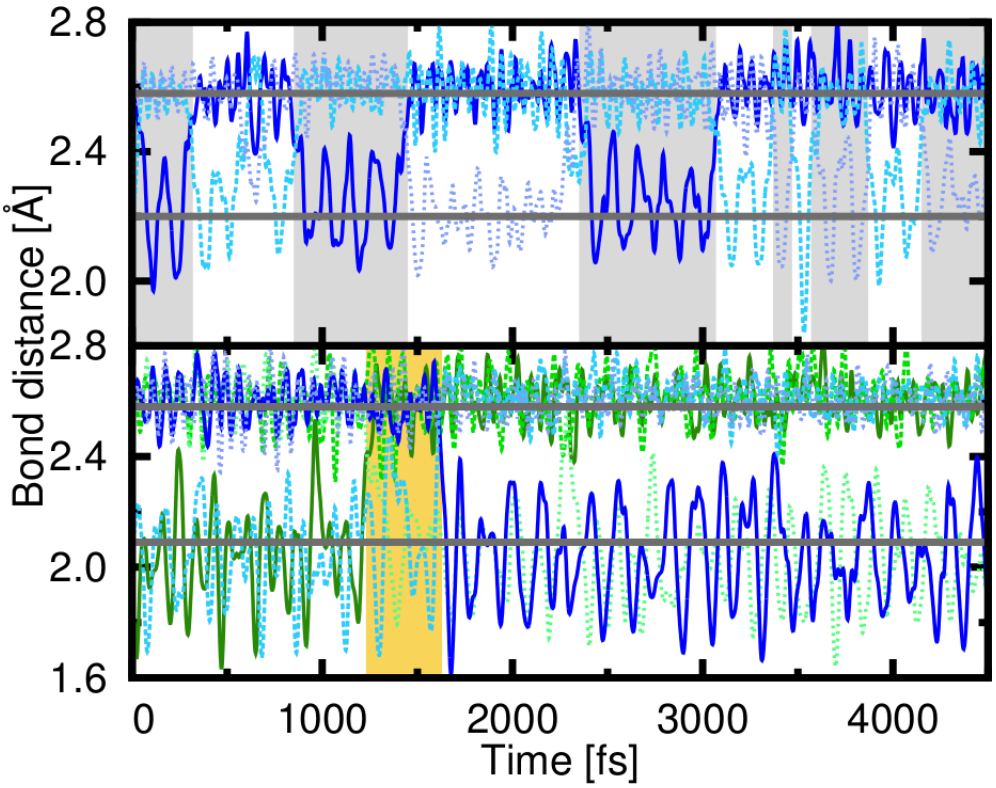

Figure 4.6 *Ab initio* molecular dynamics simulations at 300K for different cells ($G(4\times4)+V1$ in the upper panel and $G(12\times12)+2V1$ in the lower panel) showing the evolution of the 3 distances between the atoms that characterize the V_1. The dark grey solid lines are the corresponding ground-state distances of the 5-9 reconstruction. In the upper panel every switch of the orientation in the structure of the only V_1 is highlighted with a change in the background color of the plot (white/grey). In the lower panel, there is only one switch per V_1 and the time range from the switch of one of the V_1 (green lines) until the other V_1 rotates too (blue lines) is highlighted in yellow.

4.4 Effects of isotropic in-plane strain in the magnetism of monovacancies

Real graphene sheets are not in their equilibrium state. The substrate, the boundary conditions, the temperature or the environment induce a strain field on the graphene layers. Moreover, strain engineering in graphene has been proposed to tune their electronic properties, in particular the magnetism[60,284]. Therefore, we have also studied the stability and the variation of the magnetic moments induced by the V_1 as a function of an external isotropic strain applied to the layer. We have fixed our attention in the stretching as previous works focused on other regimes[284].

The large computational cost required to converge the previous calculations prohibited this characterization in the systems (a single V_1 per unit cell) showed above. We have realized that the electronic convergence is faster for V_1 coupled antiferromagnetically, this occurs when the V_1 are located in different graphene sublattices. Also, the size of the unit cell cannot be very large. Therefore, due to these limitations, we have carried out the study of strain in a $G(12 \times 12)$ cell with two V_1 in opposite sublattices (see Fig. 4.7).

We have applied an in-plane strain, relaxing all the atoms and calculating the local magnetic moment associated with each V_1. As the vacancies interact with each other, we have obtained their local magnetic moment as the addition of the moments of the atoms inside a region around each V_1. These regions, highlighted in yellow and magenta in the ball-and-stick model inside the bottom panel of Fig. 4.7, have been chosen to treat both vacancies on an equal footing and maximize the number of atoms that contribute to the calculation, avoiding any overlap between the areas associated to each defect.

In Fig. 4.7 we also show the absolute value of the average local magnetic moment of a V_1 as a function of the applied strains. The higher panels show the spin density map around the vacancies, as well as the moments associated with the atoms. The gray area in Fig. 4.7 emphasizes the region (strains <2%) where the same 5-9 $a-V_1$ solution[63] found in the equilibrium state (strain of 0%) is preserved. The V_1 of this system at a strain of 0% present a soft-bond distance of 201 pm and as higher strains are applied the soft dimer bond is elongated but still exists (see green lines in Fig. 4.7). In this region the local magnetic moment of the V_1 increases ~9% with respect to the equilibrium upon extension (~2%) and abruptly decreases upon compression in agreement with previous results[284].

Around a stretching strain of 2% we can see a transition into a different solution. This new state is mainly characterized by a change in the reconstruction of the vacancies which turns into a structure close to the $s-V_1$ configuration, where the soft bond has effectively disappeared, and the distances among the three atoms in the V_1 are very similar (e.g. 294

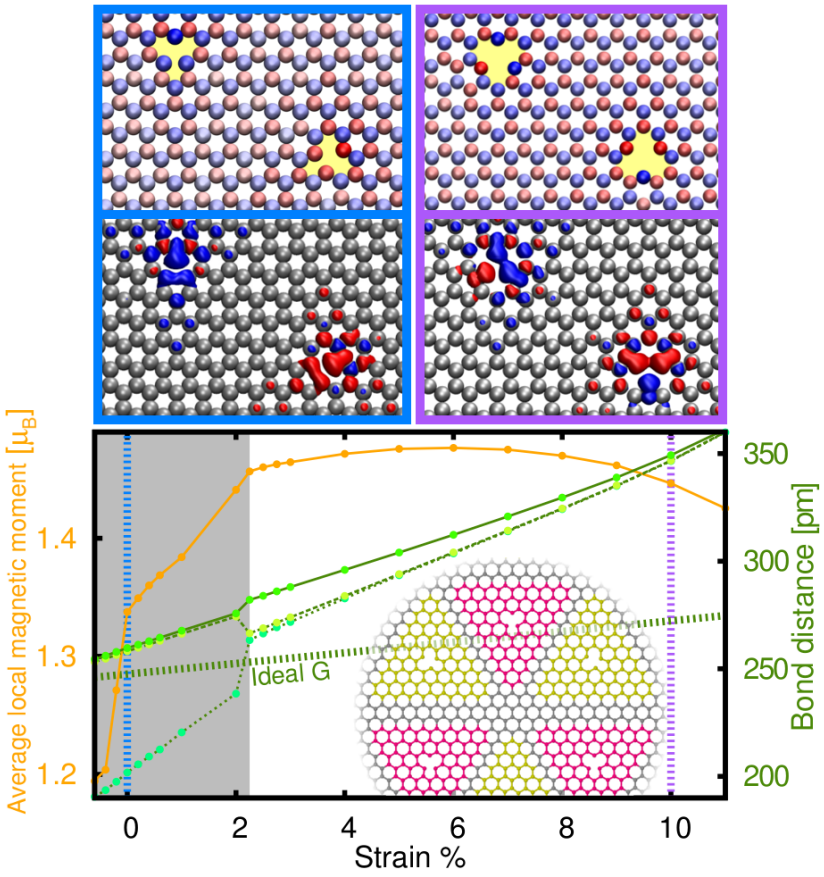

Figure 4.7 (bottom) Local magnetization (orange) and evolution of the distances between the three atoms of the V_1 (green) for the $G(12\times12)+2V_1$ system. We have included a reference dashed line (also in green) with distances corresponding to a pristine graphene layer under strain. The atoms of the equivalent regions used to calculate the local magnetization of each V_1 are shown in the ball-and-stick scheme inside the plot (highlighted in yellow and magenta). In the gray area, the $a-V_1$ (asymmetric) structure found at the equilibrium is preserved while for the rest of the plot the most favourable solution is the $qs-V_1$. Atomic magnetic moments (upper panel) and spin density (lower panel) for the $a-V_1$ structure at 0% strain (framed in blue) and the $qs-V_1$ configuration at 10% strain (framed in purple) are shown. In the upper panels, each atom is painted in blue or red depending on its total magnetic polarization according to the Mulliken spin populations. The darker the color of the atom (either blue or red) the higher the magnetic moment for this atom. The location of the V_1 is highlighted in yellow. Below each magnetization map we show the spin density of the same region. Maps for strain values corresponding to the same V_1 structure are alike.

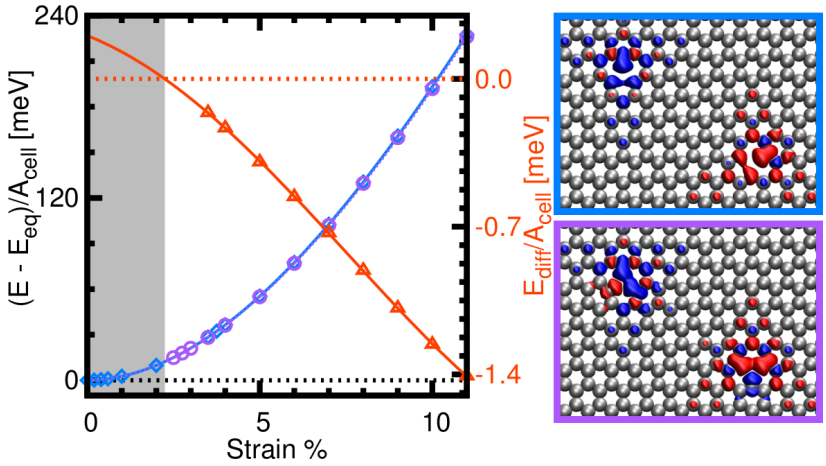

Figure 4.8 Energy difference for the two different spin distributions studied for the $G(12\times12)+2V_1$ system: the $a-V_1$ and the $qs-V_1$. The points represented have been computed for cases on which we have managed to converge both solutions. The solid line has been calculated through the subtraction of the fitting curves of the energy data for each solution. This curve not only reproduces remarkably well the calculated points but also predicts quite accurately the transition state and the behavior in the low-strain side. According to this curve the $a-V_1$ solution is stable up to a ~2% strain (range highlighted with a grey shadow).

pm, 294 pm and 304 pm for a 5% strain). Thus, we will denominate it as quasi-symmetric reconstruction ($qs-V_1$). The higher the strain the closer the reconstruction is to a $s-V_1$. Fig. 4.7 shows the structural evolution of the V_1 through the bond distances between the three atoms surrounding it which can be compared. The plot also shows a comparison against the corresponding values for pristine graphene.

While the new $qs-V_1$ structure is geometrically more symmetric, the opposite happens with the magnetic distribution. The local spin density shows two atoms of the V_1 occupied by the majority spin and the other by the minority spin. In spite of this change in the magnetic distribution, the total magnetic moment remains fairly constant, reaching a saturation value ~10% larger than the value in the equilibrium. This high-strain solution is stable up to strains of 12% where the structure of the full sheet is broken with the cracks starting in the vacancy.

The transition between solutions takes place due to the competition between the magnetic and mechanical contributions to the energy depending on the strain. Beyond the 2% strain the Jahn-Teller distortion that created the 5-9 reconstruction becomes unstable since the double occupied σ state associated with the soft dimer bond increases its energy upon stretching. Then, a new magnetic solution[284] –associated with a new way to fill the states created by the V_1– becomes comparable in energy with the previous solution. This new configuration is characterized by the filling of the three σ states

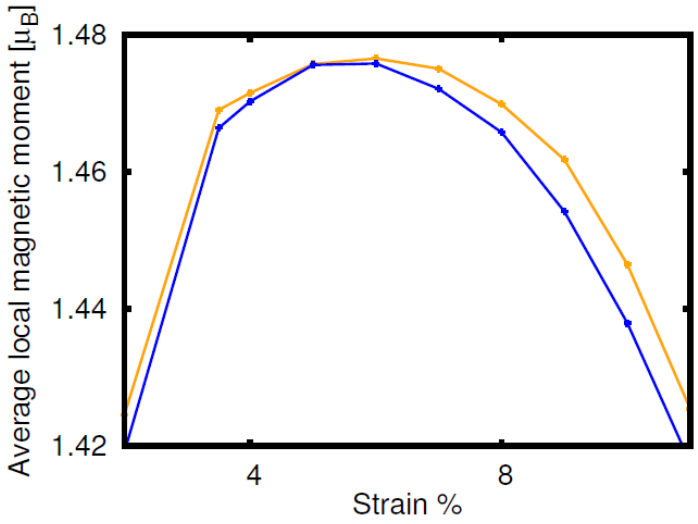

Figure 4.9 Average local magnetic moment of the $a-V_1$ (blue) and the $qs-V_1$ (orange) solutions for the large strain range. The variations are very small between them.

associated with each atom of the V_1 with just one electron –2 of them with majority spin and the other with the minority one– leaving the total magnetism associated with the σ states equal to 1 μ_B as in the previous solution. On the other hand, the semi-localized pi state is mainly occupied with the majority spin. As a result, the spin behaviour is as showed in the spin maps in Fig. 4.7. For strains larger than 3%, this new solution becomes the most stable as can be seen in Fig. 4.8 where energy differences between solutions are shown.

According to our calculations, the $qs-V_1$ solution is unstable for strains below 2% even when we start the simulations with a spin distribution of this kind. However, following this method for the $a-V_1$ solution in strains larger than 2%, we have get to keep this spin symmetry for these strain values and, thus, calculate the energies for this strain range. Therefore, we can only directly compare their energy difference only in the large strain range as it can be clearly seen in Fig.4.8. For this reason, we are not able to exactly address the point were one energy overcomes the other –as for lower strains we just have the energy values of only one of the solutions– but it is notable that the difference of the energy curves (fitted in each case through a 4^{th} order polynom) changes its sign (stabilizing a different solution) at the same strain value where the transition happens according to what we showed in Fig.4.7.

Fig.4.8 also shows the charge densities for both magnetic distribution solutions at the same strain (4%) and they are comparable to what we obtained for each solution at Fig.4.7. Despite the differences in the atom-by-atom magnetic distribution between the

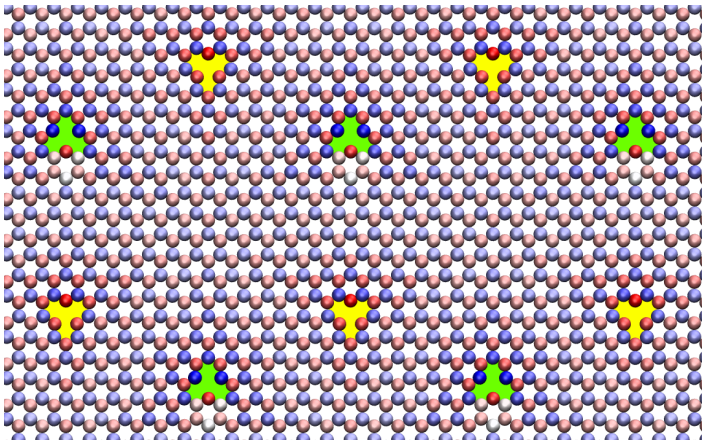

Figure 4.10 Spin charge map for the $G(12\times12)+2V_1$ system converged for an external strain of 2% starting the optimization with both V_1 in a $qs-V_1$ reconstruction. One of the V_1 (yellow background) changes to an $a-V_1$ structure while the other remains as a $qs-V_1$.

two solutions, the local magnetic moments are similar for the strain range where they coexist (see Fig. 4.9) and the structure evolves in both cases towards a $s-V_1$ reconstruction.

Another evidence of the structural transition induced by an external isotropic strain is that in the surroundings of the 2% of strain applied we had difficulties converging the calculations and we even obtained mixed states (with one $a-V_1$ and one $qs-V_1$) as the one showed in Fig. 4.10. Reaching this kind of mixed states with a geometric optimization totally depends on the starting structure used for the process when dealing with strains close to the transition ($\approx 2\%$). In the case of Fig. 4.10 both V_1 started on a $qs-V_1$ reconstruction for an applied strain of 2% –which is slightly below of the stable regime for the $qs-V_1$ solution–. Even though one of the V_1 of the system remained in a $qs-V_1$ reconstruction.

Notice that there is a disagreement between the magnetization values obtained in the previous section and those obtained in the strain effect analysis. If we go back to the result for the same cell size ($G(12\times12)+V_1$) in the unstrained case and with the same $5\times5\times1$ k-point mesh (see Fig. 4.5), we notice a conflict with the magnetization values obtained for the $G(12\times12)+2V_1$ system, being 1.60 and 1.34 respectively (also in Table 4.2). We can explain this in terms of the method used to compute it in the $2V_1$ coupled system. If we calculate the magnetization of the $G(12\times12)+V_1$ following the same scheme used in Fig. 4.7 we find a better agreement because using this scheme (to which we are forced to in the case of the $2V_1$) we are missing a residual contribution of the atoms that we are not computing. However, still there is not a perfect match between the two results. This is due to a combination of two factors: (i) we are comparing the same cell size, but the V_1 concentration is not the same so a difference between those two cases must expected and

System	Method	Magnetization/V_1 [μ_B]
$G(12\times12)+V_1$	Total magnetic moment	1.60
	Partial magnetic moment	1.43
$G(12\times12)+2V_1$	Partial magnetic moment	1.34

Table 4.2 List of computed V_1 magnetization values comparing the results obtained for different calculation schemes. In the case of the single V_1 is possible to compute the magnetization induced by the defect as the total magnetization of the system, but in the $2V_1$ case, due to the AF coupling between the vacancies, this is not possible and, thus, we compute it using the scheme explained in Fig. 4.7.

(ii) in the $G(12\times12)+2V_1$ system, the interaction between the two V_1 is larger than in the single defected cell (by reasons of proximity) and, due to the antiferromagnetic coupling, each one contributes to lower the magnetization of the other (while in the $G(12\times12)+V_1$ case they are ferromagnetically coupled).

In summary, we have seen how the magnetization of graphene with V_1 defects changes by applying an external in-plane strain to the system. The magnetism is stable and does not disappear with the strain. We mainly see a decrease upon compression and an increase upon extension of the layer. Apart from the known $a-V_1$ solution for lower strains, we have found a transition to a $qs-V_1$ structure around strains of 2% that is characterised by a new magnetic distribution with the three σ states associated with the V_1 single electronically occupied. Moreover, we have explored a different arrangement of V_1 to analyse the influence of the relative location on these defects obtaining very similar results.

4.5 Mechanical properties of graphene tailored with monovacancies

Monovacancies, besides inducing magnetism in graphene, can also tune its mechanical properties even at low concentrations[127]. AFM microscopy indentation experiments have concluded that a low concentration of V_1 in graphene increases its effective stiffness and reduces its fracture strength[127].

The latter is an expected behaviour for defected covalent solids and it can be explained by classical mechanics[122,288]. However, the modifications observed in the effective Young's modulus are unexpected and its origin is still unclear (see Fig. 4.2). It has been suggested that this behaviour is due to the dependency of the mechanical properties of 2D membranes on the flexural modes and thermal fluctuations. However, a fundamental, atomistic

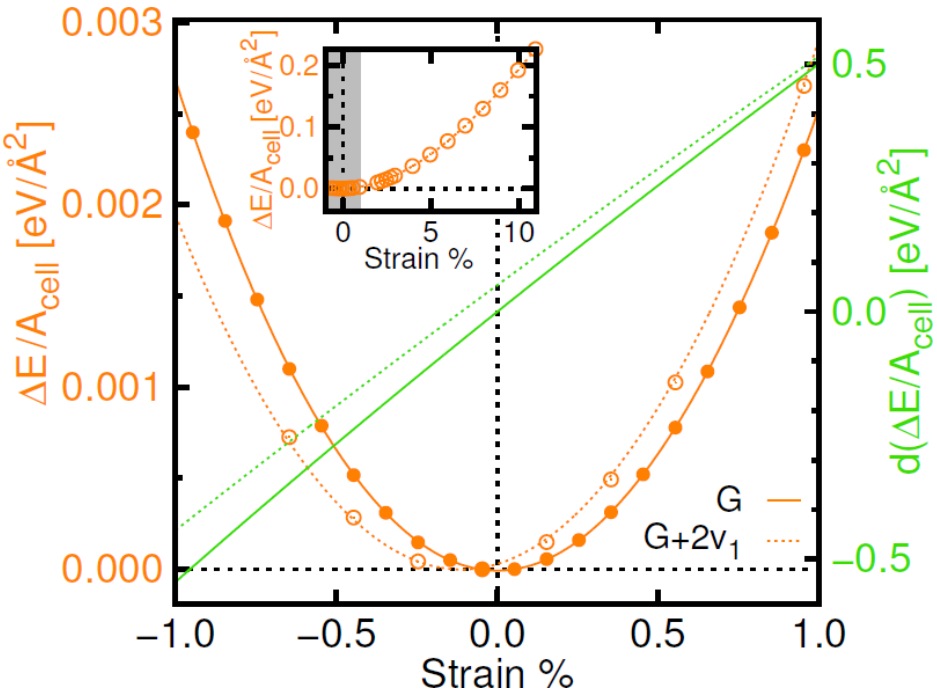

Figure 4.11 Comparison between the energy response to an isotropic in-plane strain of the $G(12\times12)$ and the $G(12\times12)+2V_1$ systems. The energy variation curve is shown in orange and the derivative of this energy with respect to the strain is depicted in green (solid/open circles are the calculated data for $G(12\times12)/G(12\times12)+2V_1$, solid/dashed lines are the respective 4^{th} order polynomial fits). In the inset, we show the energy variation curve for the full range on which calculations for the $G(12\times12)+2V_1$ were performed. A grey shade marks the strain region shown in the main plot.

explanation is still missing. Our large scale simulations of V_1 in graphene allow us to compute the real 2D Young's modulus, the strain fields generated by the V_1 and their effect in the out-of-plane modes. The analysis of these results sheds light on the origin of the experimental observations.

Effect of the monovacancies in the graphene mechanical in-plane response.

The calculated energy variations per unit cell of both the pristine layer and the $G(12\times12)+2V_1$ system as a function of an isotropic in-plane strain applied to the layer are shown in Fig. 4.11. The defect has slightly shifted the minimum towards negative strains. The inset of Fig. 4.11 shows the energy variation when stretching the layer up to the rupture. The failure strain is ~12%, smaller than in pristine graphene (>20%) and in agreement with previous results[79,82,295]. The green curve is the derivative of the energy variation with

respect to the strain. Total-energy calculations of graphene give access to the 2D bulk modulus, B, through the relation

$$\frac{\Delta E}{A_{cell}} = \frac{B}{1}\left(\frac{\Delta A_{cell}}{A_{cell}}\right)^2. \tag{4.1}$$

ΔE corresponds to the energy differences and ΔA_{cell} to the change of the unit-cell area A_{cell} obtained by an assumed tension. The 2D bulk modulus can be written in terms of the Young's modulus for 2D samples, E_{2D}, and the in-plane Poisson coefficient, ν (taken here as 0.165, the Poisson's ratio for graphite in the basal plane[296]), as follows

$$B = \frac{E_{2D}}{2\,(1-\nu)} \tag{4.2}$$

In turn, E_{2D}, can be expressed in terms of the elastic constants C_{11} , C_{12} and an arbitrary thickness of the graphene monolayer h (usually taken as the graphite interlayer distance, $h = 335$ pm[297])

$$E_{2D} = h\frac{C_{11}^2 - C_{12}^2}{C_{11}} \tag{4.3}$$

As expected, but contrary to the experimental results, the pristine graphene ($E_{2D} = 349$ N/m, $B = 209$ N/m) is stiffer than the defective graphene ($E_{2D} = 321$ N/m, $B = 192$ N/m).

The results that we present are simulations that can be compared with an ideal system at zero or very low temperature. However, experiments are done at room temperature and, in membranes and 2D materials, thermal fluctuations play a relevant role in the mechanical properties[27,74,75]. The energy dispersion of the flexural modes induces important out-of-plane corrugations with large wave lengths in the layers. Moreover, the out-of-plane modes depend on the in-plane strain field[27,298,299]. So the question that arises is: could the V_1 induce a strain field able to modify the out-of-plane modes and, therefore, the mechanical properties of graphene layers at finite temperatures?

The strain field induced by monovacancies in graphene.

We have calculated, as a representation of the strain field, the average bond distance map for different V_1 concentrations and external strains. We have defined the average bond distance as the mean nearest-neighbour distance of each atom referred to the ideal graphene nearest-neighbour distance for each of the external strains applied. In Fig. 4.12a, we show the result for the $G(6\times 6)+V_1$ system. Blue atoms have larger average bond distances than in pristine graphene whereas red atoms have shorter average bond distances. The Jahn-Teller distortion induces the formation of the soft bond and, as a

consequence, the graphene lattice at both sides of the bond is stretched. On the contrary, in the perpendicular direction of the soft bond the atoms around the V_1 (in red) are compressed in a figure-of-8-like structure.

Upon reduction of V_1 concentration (simulated by increasing the unit cell size), a similar strain field appears. However, while the compressed 8-shaped area remains localized around the V_1 and does not significantly depend on V_1 concentration, the stretched area spreads in a larger region around the V_1 as the cell size is increased (see Fig. 4.12a-e for the $G(6\times6)+V_1$, the two $G(12\times12)+2V_1$ with V_1 in different arrangements, the $G(12\times12)+V_1$ and the $G(18\times18)+V_1$ cells). Most importantly, in all cases, the stretching of the lattice is always predominant over the compression. Fig. 4.12 shows the histograms for the relative average bond distance respect to pristine graphene. It can be clearly seen that most of the atoms are stretched rather than compressed and that most of them are in the range $(-0.5, 0.5)$% of strain. This total effect is also confirmed by the displacement of the energy minimum, with respect to the clean graphene case, towards negative strain values as shown in Fig. 4.11.

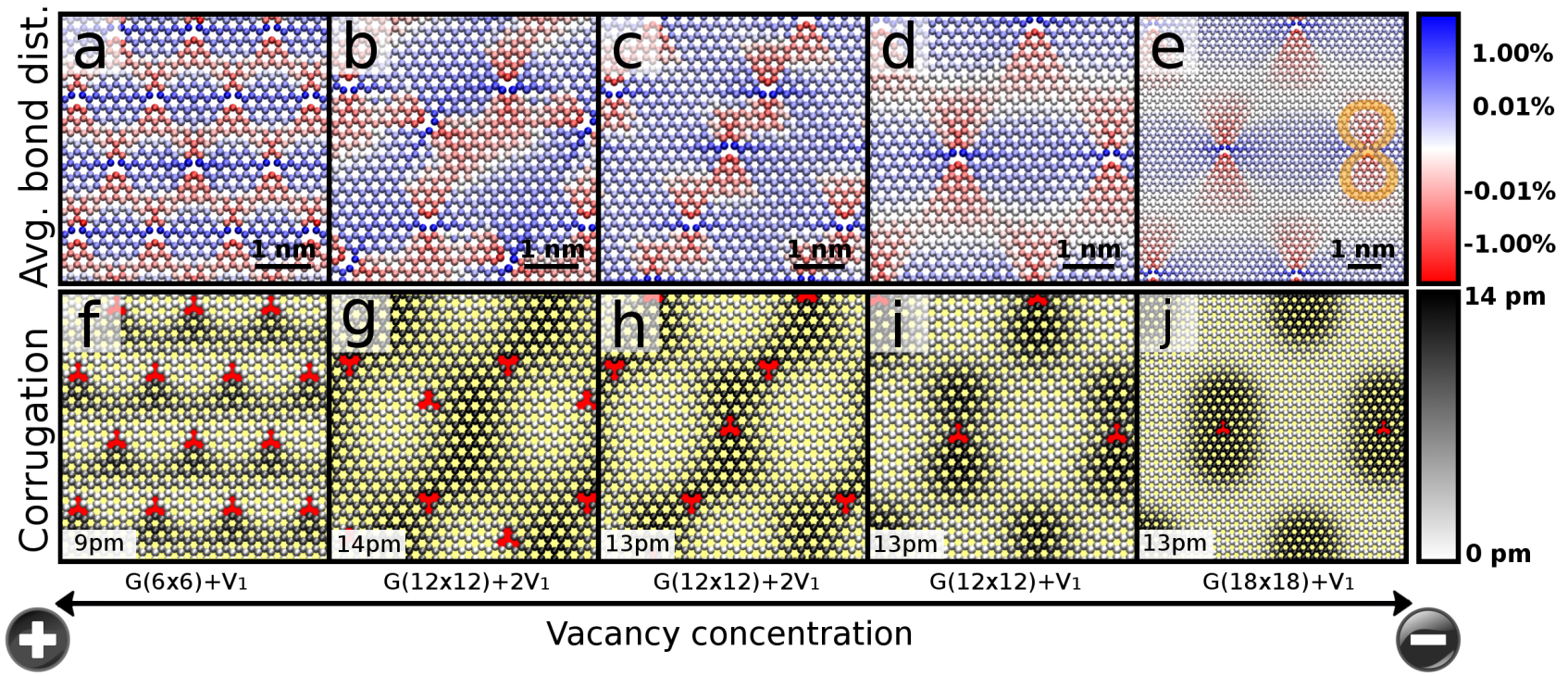

Figure 4.12 Comparison between the average bond distance map (top panels) and corrugation (bottom panels) for different V_1 concentrations ($G(6\times6)+V1$, $G(12\times12)+2V1$, $G(12\times12)+V1$ and $G(18\times18)+V1$) and different vacancies arrangements (two different ones for the $G(12\times12)+2V1$ case). In the average bond distance maps, the red color corresponds to compressed atoms (closer to their nearest neighbours than in pristine graphene) and the stretched atoms (farther than in the perfect surface) are depicted in blue, being most of the atoms around a ±0.5%. The 8 shape of the compressed region is highlighted in orange for the lowest concentration case. In the corrugation maps the locations of the V_1 are highlighted in red and the corrugation value (represented by the difference between the black and white atoms in the color scale) for each case is provided.

We have also studied the effect of the V_1 arrangement in the induced strain fields. In the $G(12\times12)+2V_1$ system we have tested two different arrangements (see Fig. 4.12b,c). The main results explained above related with the stretched/compressed areas still hold for both distributions. However, the results point out that the induced strain fields are controlling the atomic structure of the ground state: after careful optimization of the structures, the soft bond is formed between the two atoms of each V_1 such that the overlap of both compressed areas and each stretched area with the compressed area of the other V_1 are minimized. Therefore, the V_1 are interacting through their induced strain fields.

In Fig. 4.12f-j we also show the corrugation map for each case. The creation of the reconstructed vacancy induces a stress in the graphene layer. This stress is relaxed by inducing both an in-plane strain field and a small out-of-plane deformation of the layer. This corrugation pattern does not follow the in-plane strain field but is mostly controlled by the boundary conditions, i.e. the cell shape. This is clearly seen comparing the two $G(12\times12)+2V_1$ cases (Figs. 4.12b,c,g and h): the corrugation maps are very similar whereas the strain field is significantly affected by the V_1 location and orientation. The induced corrugation converges to ~13 pm for unit cells larger than the $G(12\times12)$ case.

Furthermore, we have also checked that an applied external strain does not substantially modify the average bond distance maps in the range where the 5-9 reconstruction is preserved. In our calculations on the $G(12\times12)+2V_1$ system, the bond stands the extra stretching of the lattice up to an external strain of 2%. Then, it breaks and the reconstruction changes to the $qs-V_1$ structure inducing changes in the strain field generated by the V_1. However, even with the broken soft bond, in terms of strain field the transition is not abrupt but progressive between the two extreme average bond distance maps (for 0% and 10%) shown in Fig. 4.14. As it can be seen in Fig. 4.7, the $qs-V_1$ gradually changes towards a $s-V_1$ as smoothly as the strain field map changes reducing the stretched area to become mostly compressive (see Fig. 4.14). However, for most cases, in particular for thermal fluctuations and AFM indentation experiments[22,127,298] strains suffered by a graphene layer in a realistic environment are much smaller than 2%.

In conclusion, our results show that the V_1 are effectively stretching the layer. Next, we show how this V_1-induced strain field modifies the strength of the out-of-plane modes.

Monovacancy-induced strain field effect on out-of-plane deformations

The effect of the V_1 in the out-of-plane modes can be seen in Fig. 4.15. The energy curves for small out-of-plane displacements are calculated for atoms located in the compressed, stretched and neutral areas of the $G(12\times12)+2V_1$ strain field map (the strain field color code is included in the ball-and-stick scheme of Fig. 4.15). The pristine graphene energy

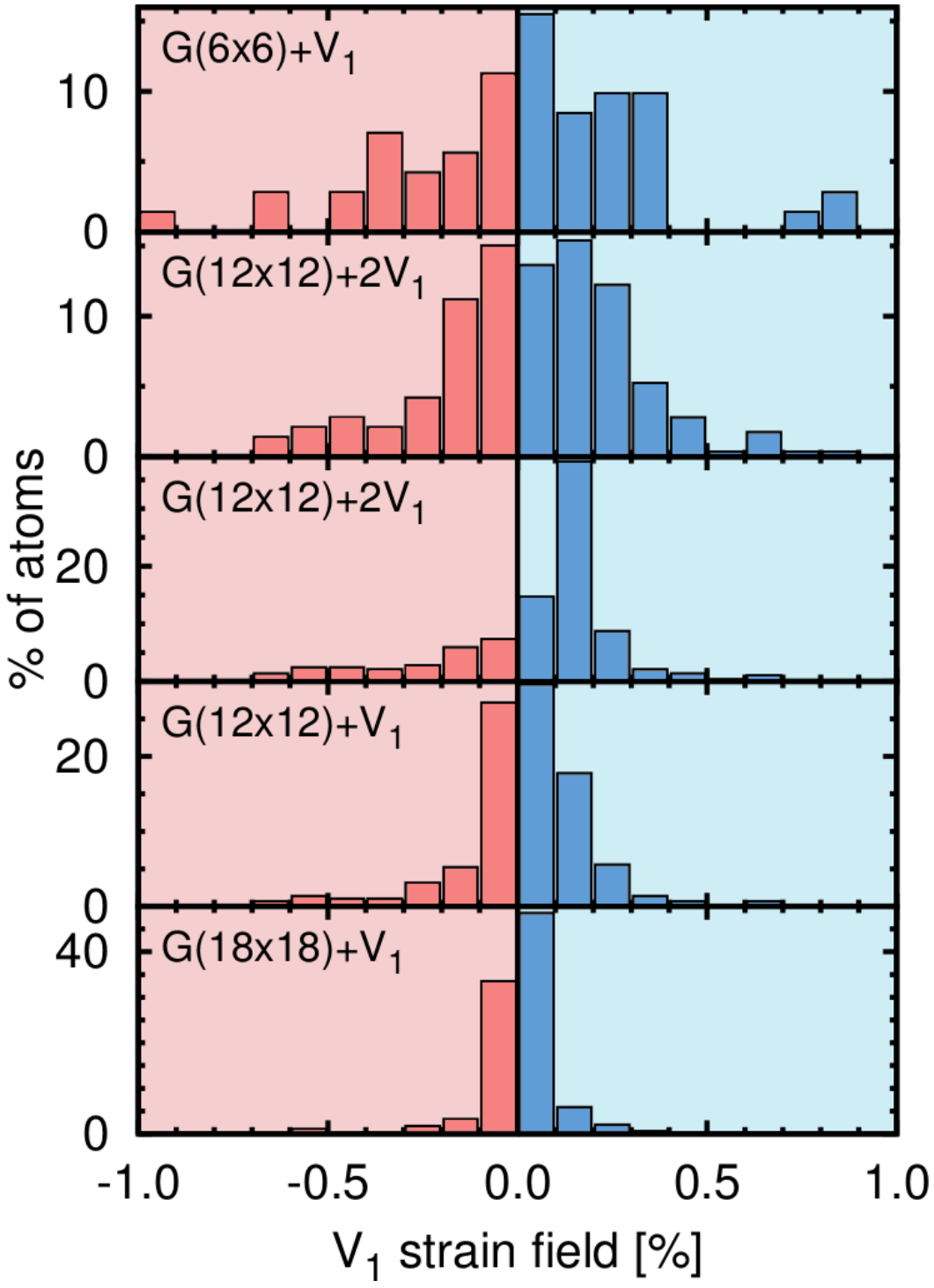

Figure 4.13 Histogram showing the distribution of atoms according to the strain field generated by the presence of the V_1 for different V_1 concentrations ($G(6\times6)+V1$, $G(12\times12)+2V1$, $G(12\times12)+V1$ and $G(18\times18)+V1$) and different vacancies distributions (two different for the $G(12\times12)+2V1$ case). We are only showing the most populated strain range to ease the visualization.

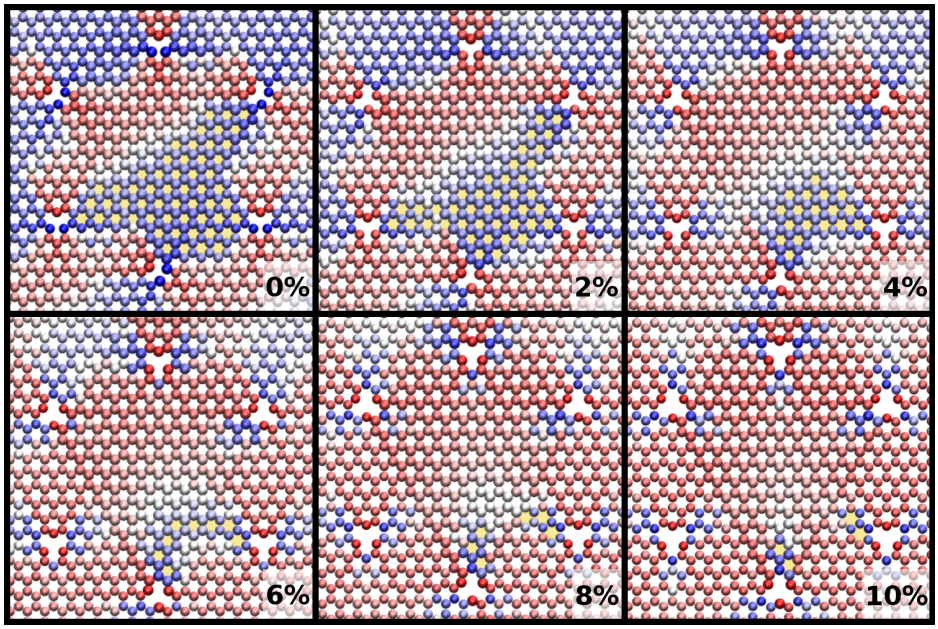

Figure 4.14 Evolution of the average bond distance map generated by the V_1 as an externally applied isotropic strain is increased. For each frame the corresponding strain applied is shown.In the average bond distance maps, bonds shorter than the distance of the strained ideal graphene are coloured in red while the stretched bonds are painted in blue. In the case of the equilibrium solution the dimer is regarded as a bonded pair of atoms, that is the reason why is depicted in blue (stretched). The yellow shadow helps to notice the decreasing of the blue areas (stretched) and progression of the red ones (compressed).

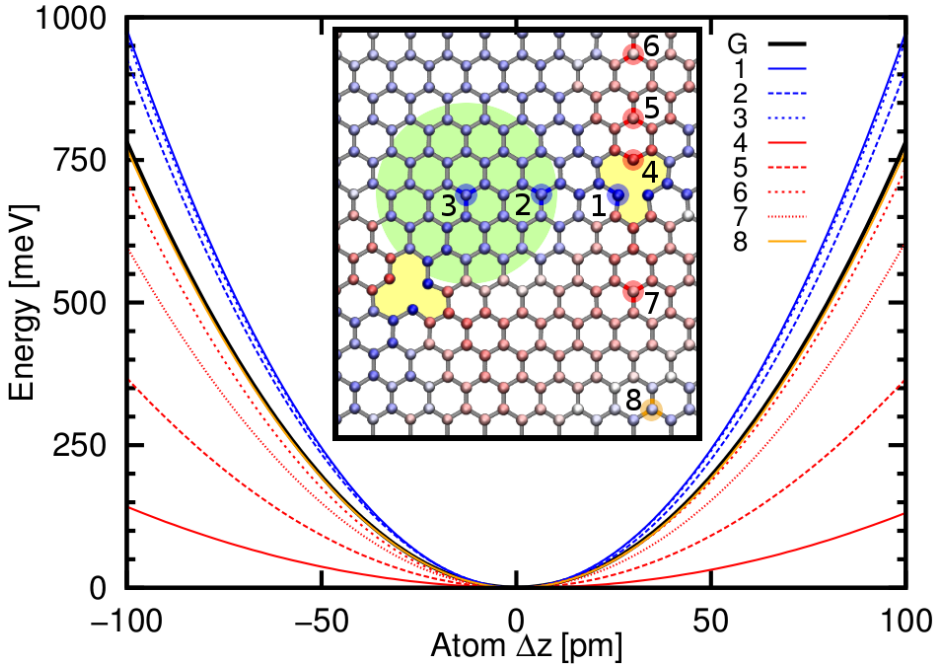

Figure 4.15 Out-of-plane energy curves for atoms in different regions of the V_1-induced strain field. The ball-and-stick scheme shows the location of the atoms analyzed which are depicted in the same color as its corresponding energy curve. In the calculations we fix the given atom at a certain δz displacement with respect to its equilibrium height and optimize the structure within a radius of 573 pm. The rest of the atoms of the sheet are also fixed during the optimization. As an example, a circle containing all the atoms that have been relaxed in the calculations around the atom 3 has been highlighted in green. The location of the V_1 is painted in yellow. The color code (red for compressed bond atoms and blue for stretched bond atoms) used for the average bond distance maps is preserved to ease visualization and comparison.

curve is shown also as a reference (black curve in Fig. 4.15). For an atom in the neutral area we exactly recover what we had for the ideal system (see orange line in Fig. 4.15). For atoms in the stretched areas (which take up most of the sheet surface), we clearly see an increasing of the stiffness while the compressed areas present a softer behaviour. Therefore, our calculations point out that the extra strain induced by the presence of the V_1 in the sheet makes the system stiffer for out-of-plane displacements than the ideal system. As a consequence, this could quench some of the fluctuations of the graphene layer and tune the mechanical properties related with the thermal fluctuations as the effective stiffness [127] or the negative thermal expansion coefficient [27,300].

4.6 Conclusions

We have analyzed the magnetic and mechanical properties induced by V_1 in graphene. We have concluded that the magnetization of the system for low V_1 concentrations tends to a value of 2 μ_B, contrary to previous works in extended systems calculated with PBC, and supporting the results of cluster calculations. This discrepancy can be explained in terms of the huge cell size and fine k-point meshes required to converge the magnetism of the system in calculations with extended systems. Moreover, we have seen that the magnetism of a V_1 can be tuned by applying an external in-plane strain getting an increasing of a 10% on the magnetization upon stretching. We have found a transition around a strain of 2% between the well-known $a-V_1$ solution and a $qs-V_1$, one on which the soft dimer bond of the $a-V_1$ reconstruction is broken, leading to an almost symmetric configuration with a different electronic structure.

We have also shown that the V_1 affect the mechanical properties through the strain field induced by the soft bond that stretches the graphene lattice around the V_1. Our results show that this stretching stiffens the out-of-plane modes of the layer. This extra energy cost quenches these fluctuations, possibly leading to an increase of the effective stiffness of the graphene and to the reduction of the absolute value of the negative thermal expansion coefficient in defective graphene samples.

CHAPTER 5

STUDY OF SELF-ASSEMBLED MOLECULAR LAYERS FORMATION ON WEAKLY INTERACTING SYSTEMS: AZABENZENE 1,3,5-TRIAZINE ON GRAPHENE–TERMINATED SUBSTRATES

5.1 Introduction

The ability of some molecules to self assemble on ordered networks is a remarkable property that allows bottom-up fabrication of functional structures in a size range of 1–100 nm[301,302]. Self-assembled molecular layers (SAMs) represent an versatile and cheap source of surface coatings useful for several applications, such as wetting and adhesion tuning, biocompatibility, molecular recognition for sensor applications, chemical resistance and sensitization for photon harvesting[301–304].

The formation of SAMs on different substrates is controlled by a delicate balance between the intermolecular and the molecule-substrate interactions. The strength of this last interaction is highly dependent upon the chemical nature of both molecule and substrate. For very weak molecule–substrate interaction, the SAM structure is practically the same as the isolated monolayer, while if it is very strong, each molecule will be adsorbed on a substrate preferential site regardless of the intermolecular interaction. There are multiple studies of SAMs on reactive surfaces[301–304]. On the other hand, the formation of SAMs of organic molecules on non–reactive surfaces –the very weakly interacting limit– is still not well understood.

Here we fill this gap and present a comprehensive study of the SAMs formed by the small molecule 1,3,4-triazine (hereafter referred as triazine, see Fig. 5.2a)on different graphene–terminated substrates: single layer graphene (G), graphite and G/Pt(111). Triazine (C3N3H3) is essentially a benzene ring where three of the carbon atoms (and the corresponding Hs attached) have been replaced by nitrogen (N) atoms. This makes it an

ideal candidate for this study: it is small, planar, highly symmetric, and, at variance with benzene, it supports strong intermolecular interactions through N–H hydrogen bonds that give rise to stable SAMs. The low reactivity and flatness of G makes it an ideal substrate to understand SAMs formation on a weakly interacting substrate. Moreover, adsorption of molecules on G has been proposed as one of the most promising and effective methods to tune the properties of G sheets[105,305,306].

There are numerous previous experimental and theoretical studies on the adsorption of single molecules –particularly benzene and other polycyclic aromatic hydrocarbons (PAHs)– on G (see refs.[105,305,306] and references therein). Most of them are focused on the molecule–substrate binding interaction, with very few works addressing the properties that control the formation of SAMs. The absorption of triazine on G has already been studied theoretically[307–310], but none of these works has specifically tried to unveil the mechanisms of the SAMs formation. Further motivation comes from recent STM experiments on the formation of triazine SAMs on highly ordered pyrolytic graphite (HOPG)[140], G/Pt(111)[141]. These experiments revealed the formation of different large Moiré patterns –the superperiodicity patterns due to the mismatch between the SAM and the substrate– on the different substrates, opening the way to explore not only the competition between intermolecular and molecular–G interactions but also the subtle changes induced in the graphene by the support. The influence of the support has been recently confirmed by experiments that show that the binding energy of a naphthalene molecule on G on Ir changes by the intercalation of atoms between the G sheet and the metal[311].

The adsorption of PAHs, in particular triazine, on G is controlled by the π-π interplay, one of the most intriguing noncovalent interactions[105], on which attraction is driven by van der Waals (vdW) dispersion forces while repulsion is controlled by the electronic overlap between the π wave functions of the molecules and G. Thermal desorption spectroscopy shows that the adsorption energy of PAHs on HOPG has a contribution of ~52±5 meV per C atom and ~ 31 meV per H atom (i.e. adsorption energy for benzene is ~500 meV/molecule[312]. The theoretical determination of these small binding energies, resulting from the balance between vdW forces and subtle short–range electron–electron interactions, is a challenge. Recent calculations show that the most accurate approaches for vdW interactions are needed in order to achieve an accuracy better than 2 meV per C atom[146,171,313,314] when comparing adsorption energies for PAHs on graphite to experiments.

In this work, we have characterized by state-of-the-art DFT approaches the formation of triazine SAMS on G, graphite and G/Pt(111). We have used the most recent developments to include the relevant interactions: gradient corrected (GGA) and hybrid

exchange–correlation (XC) functionals to describe the short range chemical forces, and a battery of different methodologies –from semiempirical to the many-body dispersion (MBD) framework– to account for the long–range electronic correlations that are responsible for vdW interactions. In the case of triazine/ on graphite and G/Pt(111), on top of these methodological issues and the tight convergence parameters needed to determine energy differences of the order of few meV, we have to cope with the large unit cells needed to represent the observed Moire patterns. To tackle this problem, we have developed a methodology to extract, from two different sets of manageable calculations, the necessary information to characterize separately the molecule-substrate and intermolecular interactions.

The rest of the chapter is organized as follows. Firstly, we summarize (section 5.2) the relevant experimental information on the triazine SAMs on graphite and G/Pt(111). Then, we describe our methodological approach to characterize the two interactions separately (section 5.3) and the computational methods chosen to perform the calculations (section 5.4). Section 5.5 presents a thorough study of the simplest case: a free standing G sheet as substrate. Next, we deal with the realistic substrates characterized in the experiments: graphite and G/Pt(111) (section 5.6). Based on these results, in section 5.7, we will (i) compare our theoretical predictions with the experimental evidence, (ii) characterize the role played by the different interactions on the SAM formation, and (iii) address the accuracy of the theoretical approaches that we have used. Section 5.8 presents our conclusions.

5.2 Experimental evidence on the adsorption of triazine on graphite and G/Pt.

Triazine on different G–based substrates systems have been characterized experimentally with variable temperature scanning tunneling microscopy at ultra–high–vacuum (UHV) conditions and low temperatures [140,141,315]. The molecules were deposited on different substrates: highly ordered pyrolytic graphite (HOPG) [140], G/Pt(111) [141] and G/Rh(111) [315]. They observed the formation of SAMs on these materials. These studies account for both the diffusion energies and the intermolecular distances of the adsorbed monolayer. They have also characterized the growth mechanisms of the SAMs depending on the substrate.

The expected triangular molecular lattice due to the three-fold symmetry of the triazine can be observed in the experiments but, more importantly, different Moiré patterns can be clearly identified on HOPG and G/Pt(111) [140,141] (see Fig. 5.1). Both moires have large lattice parameters (~4.0 nm and ~4.4 nm for graphite and G/Pt respectively) and

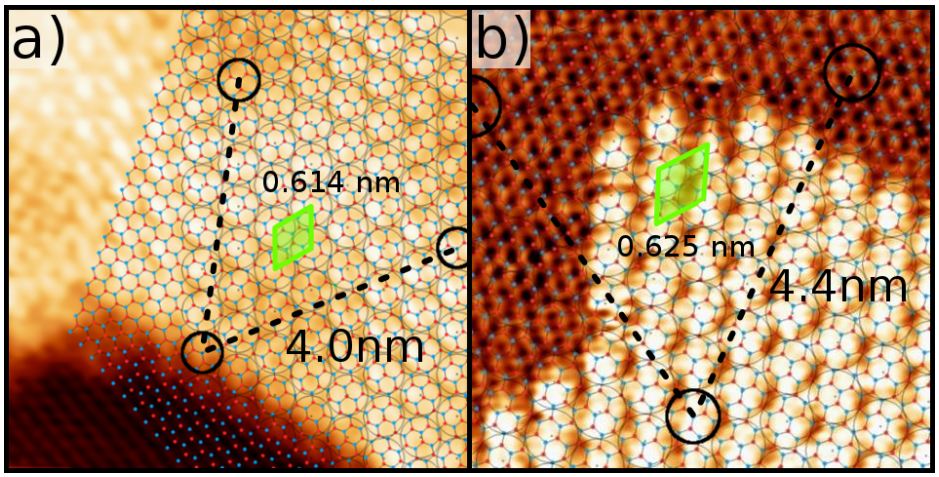

Figure 5.1 Experimental STM images [140,141] for the triazine on the HOPG (a) and on the G/Pt(111) (b) substrate. Both the full system Moiré (black dashed line) and the intermolecular (light green solid line) cells are depicted.

form large domains that extend several tens of nm. For G/Rh(111), they observe at least 3 different rotational domains of the triazine with respect to the G/Rh(111) but they are unable to identify their periodicity due to the high corrugation of the G/Rh(111). The intermolecular distance is different for each substrate, 2.39 Å, 2.49 Å and 2.54 Å for HOPG, G/Pt(111) and G/Rh(111) respectively, even though, in all cases, the uppermost layer of the substrate is G. Another significant difference among the substrates is the molecular diffusion energy: 55±8 meV for the HOPG case, 68±9 meV for G/Pt(111), and 80±9 meV for the G/Rh(111) system. These differences are presumably responsible for alternative growth mechanisms that result on the observation of triazine islands with different morphologies during growth: in HOPG, the boundary of the islands shows a very irregular, fractal–like shape while, for G/Pt(111), the islands present a much more regular, round shape. This smooth boundary suggests a smaller intermolecular interaction than in the HOPG case, that is also consistent with the larger lattice parameter observed in G/Pt(111).

5.3 Methodological approach

A direct calculation of the large Moires found on the experiments for the triazine SAMs on graphite and G/Pt(111) is out of the capabilities of current DFT methods. This section describes our methodological approach to characterize the two interactions separately: (1) an study of the molecule-substrate interaction (section 5.3.1), and (2) a characterization of the molecule–molecule interaction (section 5.3.2). We have applied the general procedure

outlined below to characterize the intermolecular interaction and binding to the case of a single G sheet acting as substrate. This study identifies the atomistic mechanisms controlling the triazine SAM formation. Based on these results, we extend our study to the cases of graphite and G/Pt(111) in order to understand the role played by the G support.

5.3.1 Adsorption of a single molecule: molecule-substrate interaction characterized through the binding energy

For this study, a single molecule of triazine is adsorbed on a $G(3 \times 3)$ cell (see Fig. 5.2b). This cell corresponds to the smallest Moire pattern observed on G/Pt(111). It allows an intermolecular distance larger than the equilibrium distance in isolated layers of triazine molecules, but not enough to completely eliminate the intermolecular interaction. In order to remove this contribution and retain just the molecule-substrate interaction, we will focus on the binding energy, E_{bind}, defined as

$$E_{bind} = E_{mol+sub} - (E_{mol} + E_{sub}), \tag{5.1}$$

where $E_{mol+sub}$ is the energy of the full system in the $G(3\times3)$ cell and E_{mol} and E_{sub} are the energies of the molecular layer and the substrate calculated separately on the $G(3 \times 3)$ cell using the geometry obtained during the relaxation of the whole system. Subtracting E_{mol}, that includes the residual intermolecular interaction, E_{bind} just provides information about the molecule-substrate interaction.

We have also calculated the standard adsorption energy, E_{ads}, that takes into account both the binding energy and the intermolecular interaction. The latter obviously depends on the relative orientation between molecules. It is given by

$$E_{ads} = E_{mol+sub} - (E^0_{mol} + E^0_{sub}), \tag{5.2}$$

where the new energy references, E^0_{mol} and E^0_{sub}, are the energies for a molecule in the gas phase and the isolated substrate respectively, both relaxed to their equilibrium configuration. The single molecule energy, E^0_{mol}, is computed in a much larger cell ($30 \times 30 \times 30$ Å^3) to minimize any intermolecular interaction.

We have characterized the potential energy surface (PES) profile by calculating these energies and adsorption distances for several high symmetry adsorption sites of the molecule on the G layer. Apart from the analysis on the plane parallel to the surface (the xy-plane), we have also studied the energy variation upon changes in the adsorption distance. Starting from the geometry of the ground state of the system we have modified

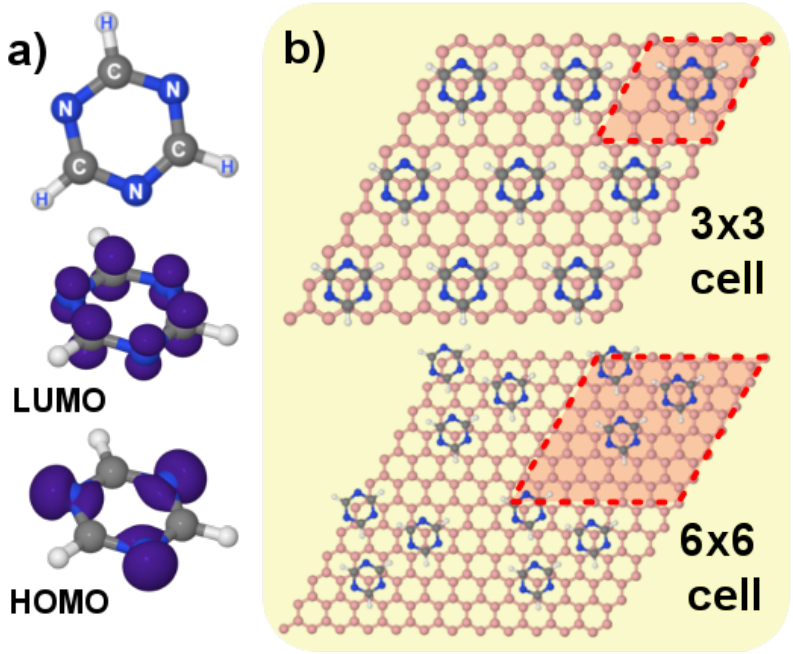

Figure 5.2 a) Scheme of the triazine molecule and its LUMO and HOMO orbital geometries. b) Ball-and-stick models for the $G(3\times3)$ and $G(6\times6)$ cells of G used for the study of the molecule-substrate and molecule-molecule interactions respectively. The G C atoms are colored in pink while for the triazine molecule the same color code in a) has been used. The unit cell is highlighted in red.

homogeneously the adsorption distance of the molecule letting the atoms relax but freezing the z coordinate of all atoms in the molecule. This procedure allows us to unveil the PES as a function of the molecule-substrate separation as well as to disclose the different contributions (short range, vdW or intramolecular energy changes) in both the binding energy and the energy barriers.

5.3.2 SAM characterization: intermolecular interaction

The study of the intermolecular interaction in an isolated layer of triazine molecules can be easily performed by a simulation with a small unit cell including just one molecule. However, the large sizes of the Moiré patterns found in the experiments are out of the possibilities of the current implementations of the DFT codes. Our characterization of the intermolecular interaction among triazine molecules adsorbed on different G–terminated substrates is based on simulations of islands formed by three triazine molecules, the smallest combination needed to preserve the triangular symmetry of the SAM lattice. Our calculations have been carried out with a $G(6\times6)$ cell (see Fig. 5.2b). With this cell size, there is still a residual interaction between neighbouring islands, but it is very small

compared to the interaction among molecules inside the island. The validity of this approach is confirmed by the comparison of the energetics and structure of a triazine monolayer with our three–molecule island: the H–bond distances are identical (2.35 Å) for both cases, and the interaction energy per H-bond are very similar (127 meV and 131 meV respectively), with just an expected small change due to the different coordination number (see inset of Fig. 5.5b).

Our goal is to determine the intermolecular energy as a function of the H–bond distance between the molecules in the island. Our starting point is a full relaxation of the island on top of each of the different substrates to determine the equilibrium structure. Then, we use this optimized geometry to prepare a set of configurations where we displace the molecules from their equilibrium positions in the xy plane while preserving the symmetry of the island and its orientation with respect to the substrate. Each of these configurations is subsequently relaxed, keeping fixed the xy position of C and a N atom from each molecule (to enforce the constraint on the H–bond distance) and allowing the rest of the atoms in the molecule and substrate to move freely.

For each configuration, we determine the intermolecular interaction among the molecules on the island, $E_{intermol}$, using the equation:

$$E_{intermol} = E_{interac} - E_{bind}, \tag{5.3}$$

where we subtract the molecule–substrate interaction, E_{bind}, from the total interaction energy, $E_{interac}$. The total interaction energy is calculated by subtracting from the total energy of the system, $E_{island+sub}$, the energy of the isolated substrate, E_{sub}, and the energy of the isolated molecules, E_{mol_i}:

$$E_{interac} = E_{island+sub} - \left(\sum_{i=1}^{3} E_{mol_i} + E_{sub} \right), \tag{5.4}$$

where the reference energies E_{sub} and E_{mol_i} are calculated using the geometries corresponding to the equilibrium configuration of the whole system.

As the chemical environment of each molecule in the island is different, we have to perform three independent simulations to determine the binding energy of each molecule. Each of these simulations includes only one of the molecules of the island interacting with the substrate. Its contribution to the binding energy is obtained from the total energy E_{mol_i+sub} by subtracting the total energies of the substrate, E_{sub}, and the isolated molecule E_{mol_i}

$$E_{bind} = \sum_{i=1}^{3} \left(E_{mol_i+sub} - E_{sub} - E_{mol_i} \right). \tag{5.5}$$

Combining the two equations, we can calculate the intermolecular energy for one particular configuration from:

$$E_{intermol} = E_{island+sub} - \sum_{i=1}^{3} E_{mol_i+sub} + 2 \cdot E_{sub}. \tag{5.6}$$

5.4 Computational methods

We have characterized these systems with first principle calculations based in DFT as implemented in the *VASP*[153] and *Crystal*[316,317] codes. We have used very fine convergence criteria to reach an accuracy of 1 meV per molecule. In our *VASP* calculations, we have used the 5.3 version with projector augmented wave (PAW) pseudopotentials[318] and a plane-wave cutoff of 600 eV. The energy convergence is better than 10^{-7} eV/atom and residual forces smaller than 0.007 eV/Å. We have used a $6 \times 6 \times 1$ Γ-centered Monkhorst-Pack grid for the calculations in the $G(3 \times 3)$ cell and an equivalent grid $(3 \times 3 \times 1)$ for the bigger $G(6 \times 6)$ cell.

We have also employed *Crystal14*, an all-electron linear combination of atomic orbital code[316,317]. We have used consistent gaussian basis sets of triple-zeta valence with polarization. Integration was carried out over reciprocal space using a shrinking factor of 24 to form a Monkhorst-Pack mesh of k points. This grid converges the integrated charge density to an accuracy of about 10^{-6} electrons per unit cell. The Coulomb and exchange series are summed directly and truncated using overlap criteria with thresholds of [7,7,7,7,14]. The self-consistent field algorithm was set to converge at the point at which the change in energy was less than 10^{-7} Hartree.

In order to find the best description of the electron-electron interaction, we have used various implementations to incorporate the contribution of dispersive (vdW) interactions and test different exchange-correlation (XC) functionals to describe the chemical interaction.

Chemical interaction description. For most of our calculations, we have used the PBE functional supplemented by different vdW approaches. Some calculations have been done with XC functionals like optB86b (see below) that include a different exchange contribution and a kernel to account for vdW interactions. We have also explored the possible role of an improved description of the short range contributions using hybrid functionals, in particular HSE06[163]. These last calculations were performed using *Crystal14* as the convergence with hybrid functionals is more optimized in this code. For these simulations,

	A_0 [Å]	d_{nn} [Å]	$< d_{GPt} >$ [Å]	$< d_{GG} >$ [Å]
	Bulk Pt	Graphene	G/Pt(111)	Graphite
Exp	3.913 [320]	2.46 [321]	3.30 [322]	3.35 [102]
PBE-D2	3.953	2.458	3.345	3.227
PBE-D3	3.927	2.470	3.296	3.489
optB86b	3.958	2.468	3.361	3.310
PBE-TS+SCS	3.951	2.466	3.325	3.453
PBE-MBD	3.968	2.466	3.427	3.462

Table 5.1 Values of characteristic parameters to describe the substrates that we have simulated for different functionals and vdW flavours. The first two columns correspond to the values for Pt and G lattice parameters and the third an fourth are the G-metal distance and graphite interlayer distance respectively.

we carried out only static calculations using the geometry from the PBE+vdW result but optimizing the adsorption distance.

Van der Waals approaches. There are two ways to include this interaction in the calculations: either as a correction to the final energy or through a kernel in the electronic exchange-correlation functional that includes these effects in the self–consistency process.

From the first group of vdW implementations we have used the simplest Grimme approach (PBE-D2) [142] and also an advanced implementation by the same authors (PBE-D3) [143]. For the PBE-D2 calculations, we have used the default values given in [142] for all the chemical species except for the Pt, which is not tabulated. For this metal, we have used the parameters $C_6(Pt) = 20\text{J}\cdot\text{nm}^6/\text{mol}$ and $R_0(Pt) = 1.9$Å which successfully reproduce the G-Pt distance [266]. In the case of the PBE-D3 implementation, the vdW C_6 parameter takes into account the local environment of the atom through its coordination number –which means that it may change during the simulation– and is determined by the program. We have also performed calculations with the TS+SCS [145] –similar to D2, apart from the fact that in this approach the parameters are charge–density dependent, accounting in this way for screening effects–, and the many–body dispersive (MBD) approach [146,147] –which contains both the many-body energy and the screening which are missing in simple pairwise approaches–, which are the more sophisticated methods to date.

From the second group –the so–called DFT-DF fucntionals– we have used the Klimes optB86b functional [144] which is able to partially account for screening effects and has proven to work very well for G systems [319]. Table 5.1 shows the variation on the characteristic distances of our systems depending on the vdW approach used.

The mismatch between the C and Pt lattices in the $G(3\times3)$ Moiré of G/Pt(111) is small (0.6%) (see Table 5.1) and we decided to fix the size of the supercell to match the relaxed G lattice calculated with each functional-vdW scheme.

We performed the calculations in three different substrates and for the different cells. For the smaller $G(3\times3)$ cells the G sheet is composed by 18 C atoms, the graphite substrate is a 4-layer slab of G sheets with the AB stacking corresponding to this material and finally the G/Pt(111) consists on a G layer with a slab of Pt(111) underneath formed by 4 layers with 7 atoms each. Building the $G(6\times6)$ cells is trivial from these smaller $G(3\times3)$ ones. For all full structural relaxations only the two lower layers of the slab were fixed to their bulk-like positions (except for the simplest case of the single sheet of G on which all the atoms of the substrate were free to move).

5.5 SAMs formation in graphene

We start the study of the SAMs formation with the simplest case –the substrate being a single sheet of G–. We first show our characterization of the relevant adsorption sites, the PES profile and the diffusion energy of the molecules. After that, we analyze the intermolecular energy per H-bond and the equilibrium length of the triazines on the G layer.

5.5.1 Molecule-substrate interaction

Triazine adsorption sites

In order to study the energetic dependence of the SAM formation properties with the substrate we first characterize the preferential adsorption sites. In Fig. 5.3 we can see all the high symmetry adsorption sites studied. Most of them have the same relative angle between the G sheet and the molecule, except for the Cross(R) and Bridge(R) geometries which, in this $G(3\times3)$ cell, are rotated to a more attractive orientation in terms of intermolecular interaction with respect to molecules in neighbour cells.

All the energies and distances associated with these high symmetry adsorption sites appear in Table 5.2 where we can see that, in terms of the binding energy, the minimum is the C top adsorption geometry followed by the N top. However, adsorption energies, that include the intramolecular interaction, yield the Cross(R), following by the Bridge(R), as the most stable configurations. This is a consequence of the larger intramolecular energy found in this orientation and it could induce wrong conclusions respect to the preferential adsorption sites in terms of the molecule-substrate interactions for which the binding

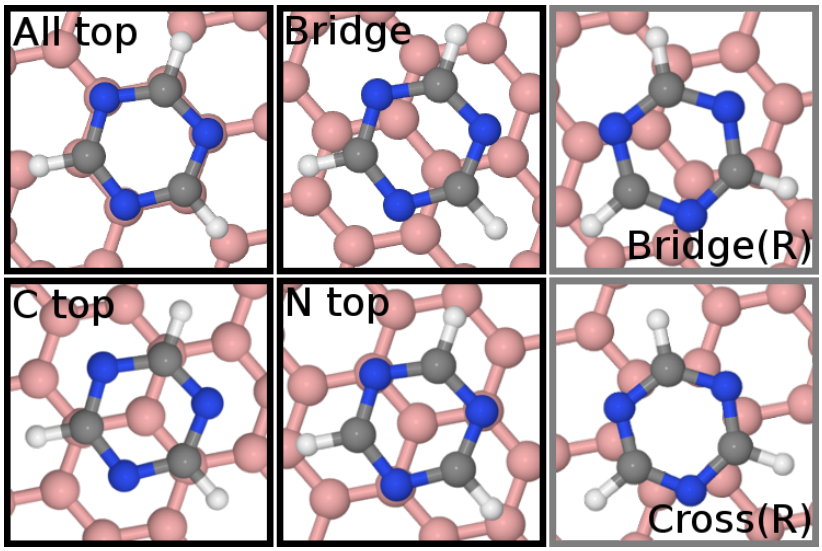

Figure 5.3 Ball-and-stick models for the high symmetry adsorption sites studied. All top, C top, Bridge and N top adsorption sites share the same molecule-G orientation, while Cross(R) and Bridge(R) (labeled with a grey border) are rotated 30° respected the other sites.

energy should be taken as reference. The values for the binding energies are similar, ~400 meV/molecule at an absorption distance of 3.15 Å, to the cohesive energy measured for a benzene on HOPG, ~500 meV/molecule[312], which points out that both adsorptions are ruled by the same mechanism: the π-π interaction. We have checked this value with different vdW flavours as well as with the HSE06 hybrid functional. Important differences are found in the binding properties between different approaches: while PBE-D2 and PBE-D3 yields similar energies, 404 meV vs 391 meV, the adsorption distances differs on near 20 pm. In the other hand the use of DFT-DF based approach for the vdW with the optB86b functional significantly increase the energy to 562 meV but with similar distances, 3.19 Å. Similar energies as this latter case, 574 meV, are obtained for the PBE-TS+SCS scheme but at significantly lager distances, 3.43 Å. The scheme including manybody effects and the proper screening (PBE-MBD) reduces both the binding energy and distance –360 meV and 3.30 Å respectively– which are very similar values to those provided by the DFT-D2/3 approaches. The use of the hybrid functional HSE06 including the dispersion interaction as in the D2 approach remarkably reduces the binding energy (explicar por qué son tan bajas), 289 meV, but keeping similar –slightly larger– distances, 3.28 Å. After this discussion about the results obtained by different theoretical approaches, we now compare them with the experimental data for the diffusion energy barriers allowing our argument to be based in some references.

Functional	Site	$E_{binding}$ [meV]		E_{ads} [meV]		d_{ads} [Å]
PBE-D2	All top	-344	(60)	-327	(61)	3.28
	C top	-404	(0)	-388	(0)	3.15
	N top	-377	(27)	-361	**(27)**	3.20
	Bridge(R)	-367	(37)	-494	(-106)	3.21
	Cross(R)	-339	(65)	-464	(-76)	3.29
PBE-D3	C top	-391	(0)	-384	(0)	3.33
	N top	-376	(15)	-369	**(15)**	3.37
optB86b	C top	-562	(0)	-563	(0)	3.19
	N top	-537	(26)	-538	**(25)**	3.25
PBE-TS+SCS	C top	-574	(0)	-559	(0)	3.43
	N top	-551	(22)	-536	**(23)**	3.49
PBE-MBD	C top	-360	(0)	-345	(0)	3.30
	N top	-342	(17)	-327	**(17)**	3.35
HSE06-D2	C top	-289	(0)	-267	(0)	3.28
	N top	-262	(27)	-241	**(26)**	3.39

Table 5.2 Characteristic binding energies, adsorption energies and mean adsorption distances calculated for different adsorption sites of triazine on G using different exchange correlation functionals including PBE[159], HSE06[163] and different vdW flavours (DFT-D2[142], DFT-D3[143], DFT-DF(optB86b)[144], TS+SCS[145], and MBD[146,147]) (see section 5.4). The full set of adsorption sites studied (see Fig. 5.3) has only been calculated with PBE-D2. The values of the adsorption energies agree with previous works[309]. For the other functionals only the C top –energy minimum– and N top sites are presented. The energy differences respect to C top for each site are shown in brackets next to the absolute energies.

Energy barrier calculation

The calculation of the diffusion energy of the molecule on G requires to characterize the PES and to disclose the minimum energy path (MEP). The results of this study can be seen in Fig. 5.4 on which a triangular path is explored going through all the high symmetry adsorption positions framed in black in Fig. 5.3. It seems clear from this study that a C top–N top path yields the lower energy barrier. We have confirmed it performing some calculations using the nudged elastic band method[323,324]. For PBE-D2 we obtain a barrier of 27 meV, around one half smaller than those determined experimentally for the triazine on HOPG or G/Pt(111), 55±8 meV and 68±9 meV respectively. Surprisingly and contrary to the differences in behaviour found for the binding energy and distances, all of the vdW flavours used yield similar results (see Table 5.2), from the slightly reduced 15 meV of the PBE-D3 to the 26 meV of the DFT-DF(optB86b). Neither including self-consistently screening effects as approached by the TS+SCS method[145] which produce a diffusion energy of 22 meV, nor even introducing the manybody effects in the dispersion interaction with PBE-MBD with an obtained value of 17 meV, produce relevant changes in the barrier. Furthermore, the use of the hybrid functional HSE06+D2, which significantly reduces the binding energies, also results on a very similar energy diffusion barrier of 28 meV.

We find, then, that the diffusion energies are always underestimated by the calculations regardless of the method used, similarly to what was found in benzene on G. For this case, some DFT approaches predict a barrier of less than 10 meV[314], which is small compared to the experimental measurements performed in benzene on graphite systems (17±12 meV)[325]. However, it is worth noting that for this system the experimental values to compare have very large errors.

After this study of the energy landscape in the xy plane we also study the effects on the z direction. Fig. 5.4b shows the adsorption energy, and short range and vdW contributions, as a function of the adsorption distance for the triazine on the C top and N top sites using the PBE-D2 functional. The molecule adsorbs at a distance of 3.15 Å (3.20 Å) with respect to the G on the C top (N top) configuration. We can see the typical behaviour of the π-π interacting systems: the driving attractive force is the vdW –which is very similar in the two cases– while it is the short range contribution the interaction that originates the PES corrugation and makes the equilibrium adsorption distance change a little ($\sim$ 0.05 Å) between the two sites. Notice that the minimum of both curves is located in the repulsive region of the short range thank to the effect of the vdW which pushes the molecule closer to the surface.

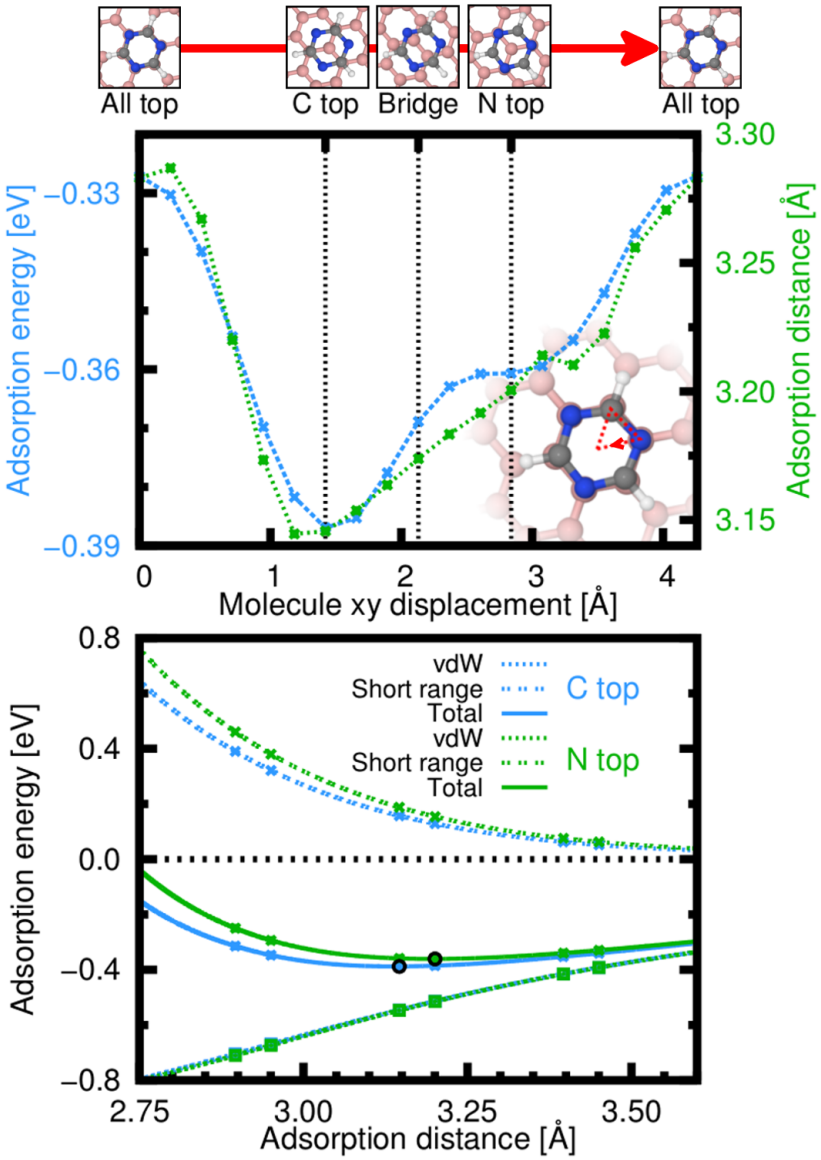

Figure 5.4 Energy landscape calculated for triazine molecules on G with PBE-D2 for in-plane (top image) and out-of-plane (bottom plot) displacements of the molecule. In the top image the PES is shown for an All top–C top–N top–All top trajectory. Both the adsorption energy (blue) and distance (green) are shown for each point of the path. The graph on the bottom shows the energy behaviour with the variation of the adsorption distance for the two geometries that define the diffusion energy of the molecule (C top in blue and N top in green). In the total energy curves (solid color), the minima, whose difference is the energy barrier, are circled in black. The short range and vdW contributions are also plotted. The points shown in this graph correspond to actual calculations and the lines are spline interpolations calculated from those points.

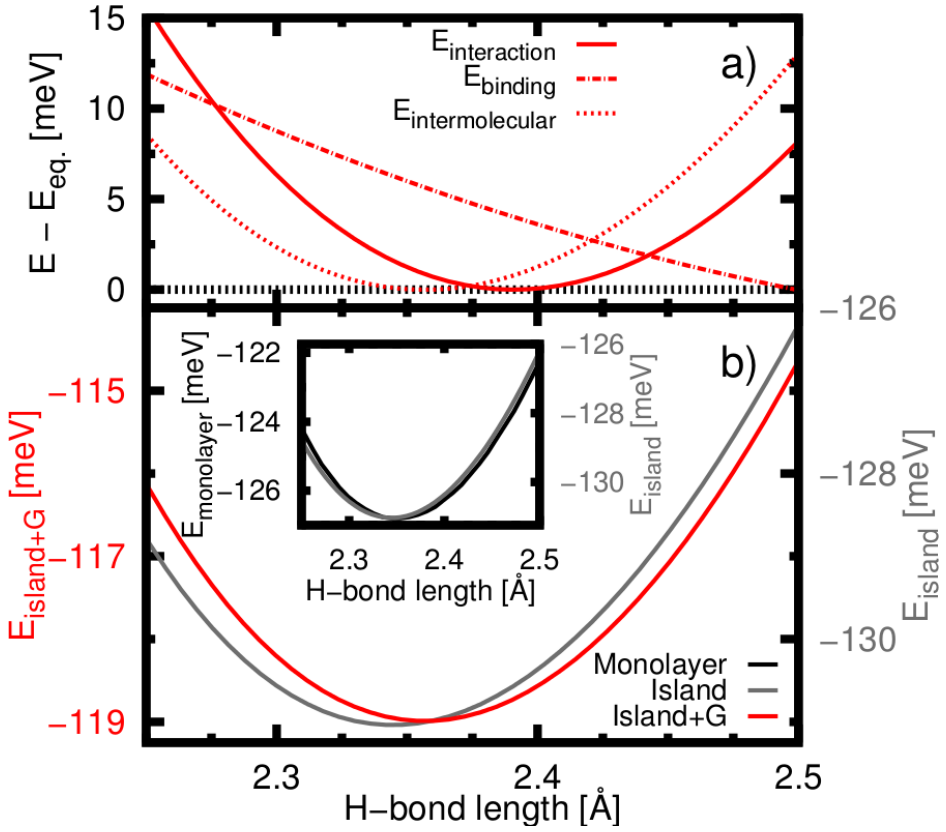

Figure 5.5 Intermolecular interaction. a) Decomposition of the interaction energy per H-bond for the G vs the H-bond distance. All the energies are referred to its minimum value in the represented range to make it easier to visualize. b) Comparison of the intermolecular energy per H-bond between the G (red) and the isolated island (grey). The minimum of the case with substrate (2.36 Å) is slightly displaced with respect to the isolated island (2.35 Å) and there is a energy shift of ~ 11 meV between both cases being the H-bond softer in the G case. In the inset we compare the isolated monolayer (black) and the isolated island (grey). The behaviour is very similar except for a shift of ~ 4 meV in the energy per H-bond being stronger for the case of the island.

5.5.2 Intermolecular interaction

To analyze the role of the intermolecular interaction in the SAM formation, we first optimize the structure of the system including both the 3-molecule island and the G substrate. The resultant equilibrium geometry is depicted in Fig. 5.2b. Notice that the molecules are not exactly on the most stable absorption configuration of a single adsorbed triazine, C top site. The interaction with other molecules induces a small rotation and displacement on each molecule from the C top configuration.

We have calculated the energy of the interaction between molecules following the procedure described in the section 5.3.2. Figure 5.5 shows the energies as a function of the separation between the three molecules of the island. The total interaction energy,

$E_{interaction}$, is showed in Fig. 5.5a, as well as the binding energy –the sum of the interaction energies of each molecule with the substrate, as defined by equation 5.5–. The difference between both energies yields the intermolecular energy also plotted. Figure 5.5b compares the intermolecular energy per H-bond of the isolated island with the energy of the island in the G. Although both interactions are very similar, it can be seen that the H-bond distance is slightly increased from 2.35 Å to 2.36 Å and the H-bond energy reduced from ~-131 meV to ~-119 meV. It seems, then, that the substrate has the effect of slightly weakening the intermolecular interaction.

5.6 Realistic graphene growth environments: graphite and G/Pt(111)

The properties of G layers are modified by its underneath substrate. In the following section we will show how these substrate-induced changes on the G properties affect the formation of SAMs of triazines.

In the case of the graphite it is well known that, in the uppermost layer a gap is opened in one of the sublattices due to the Bernal stacking . This loss of symmetry converts the mass-less fermion behaviour of the G in massive fermions. This effect can be already seen in the bilayer G and, thus, is present in our 4-layer slab [42].

In the case of the G/Pt(111), a weakly G-metal interacting system, there are two main substrate induced changes on the G[84]. First, the difference between the G and metal work functions and the their interaction induce a dipole in the interface with its positive pole at the G layer (see Fig. 5.6 and[84]). Second, it dopes the G causing a shift of the Dirac point of ~0.6 eV above the Fermi level. In terms of geometry there is another fundamental difference with respect to the free standing G and the graphite. The relative orientation between the G layer and the metal surface induces Moiré patterns, being the most common in the G/Pt(111) the $G(3\times3)$ [101]. C atoms inside the Moiré see different local arrangements of surface metal atoms which induces differences on its relative heights as well as in their local electronic properties. As in the G/Pt(111) the interaction is very week, these effects are subtle (for example height differences of ~2 pm, see Fig. 5.7), however, they can be observed with the STM[266]. The Moiré pattern modulation makes the adsorption of molecules on the different G-equivalent adsorption sites (C top, N top, etc.) of its supercell nonequivalent.

The two main differences on the SAMs growth for the different substrates that we have studied deal with the diffusion energies, 55 meV for HOPG and 68 meV for G/Pt(111), and the equilibrium intermolecular distances, 3.39 Å for HOPG and 3.49 Å for G/Pt(111).

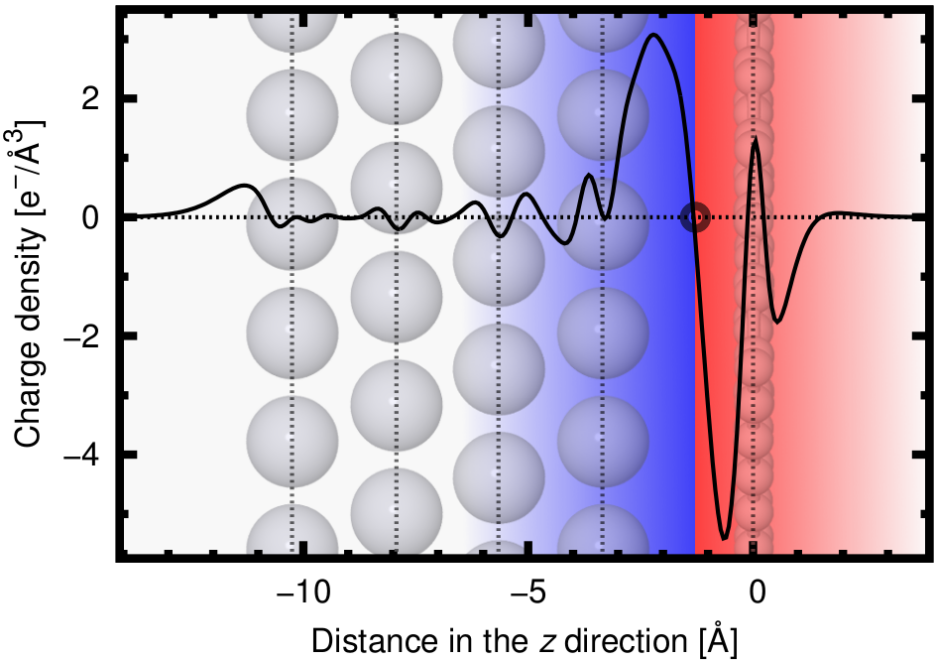

Figure 5.6 Dipole induced between the G layer and the Pt(111) substrate.

These differences could be addressed to a difference on the charge transfer between the molecule and the substrate. As the work functions of graphite and G/Pt(111) differ, this charge transfer could be different producing an enhancement or a weakness in the H-bonds and in the coupling with the substrate. However, we have calculated the charge transfer of the triazine on G, graphite and G/Pt(111) (see the xy-integrated charge density difference, $\rho_{triazine+substrate} - \rho_{triazine} - \rho_{substrate}$, in Fig. 5.8) and we do not find any relevant charge transfer in any case. However, we observe a small charge redistribution with the formation of a small dipole in the area between the molecules and the G sheet that is slightly different for each substrate. This small dipole is also reflected in a small decrease of the work function of 183 meV and 159 meV for graphite and G/Pt(111) respectively. Nevertheless, in the following sections we will show that these variations do not modify neither the molecule-substrate coupling nor the H-bonds.

5.6.1 Molecule-substrate interaction

Triazine adsorption sites

We follow the same procedure used for the case of the freestanding G as substrate. We first characterize the relevant adsorption sites of the triazine by the study of the molecule-substrate binding energy. The results, with the PBE-D2 functional, for both graphite and

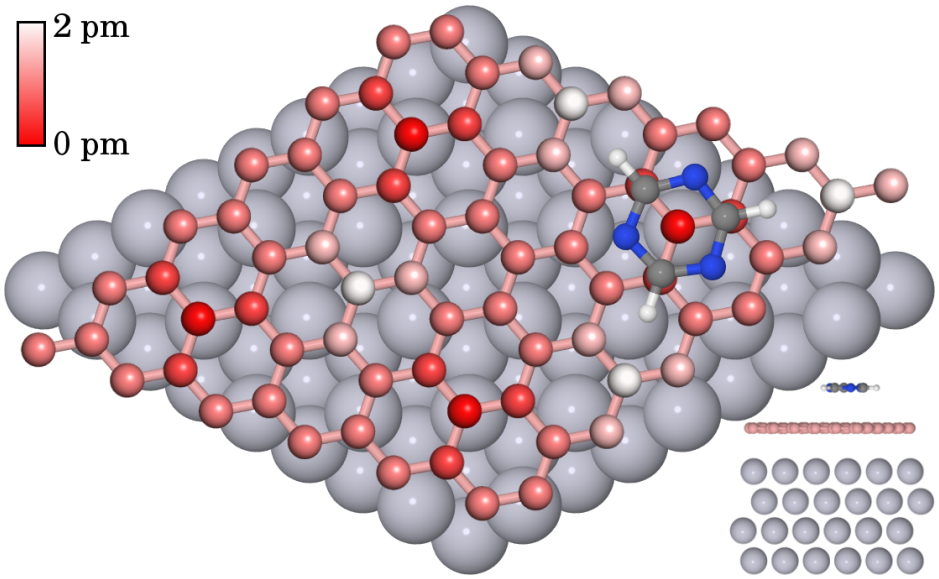

Figure 5.7 Ball-and-stick scheme of the G/Pt(111) Moiré cell simulated. It corresponds to the $G(3\times3)$ Moiré pattern, the one seen in our reference experiments [140,141], which is the more common in G/Pt(111) according to previous literature [101]). In the top sight an extra color range varying from red (for the lower) to white (for the highest) represent the relative height of the corrugated G sheet. The molecule depicted corresponds to the lower energy –among all the G-equivalent positions in the $G(3\times3)$ Moiré– C top adsorption geometry. In the side view (bottom right corner) the slab structure and the relative distances between the metal, the G and the triazine are shown.

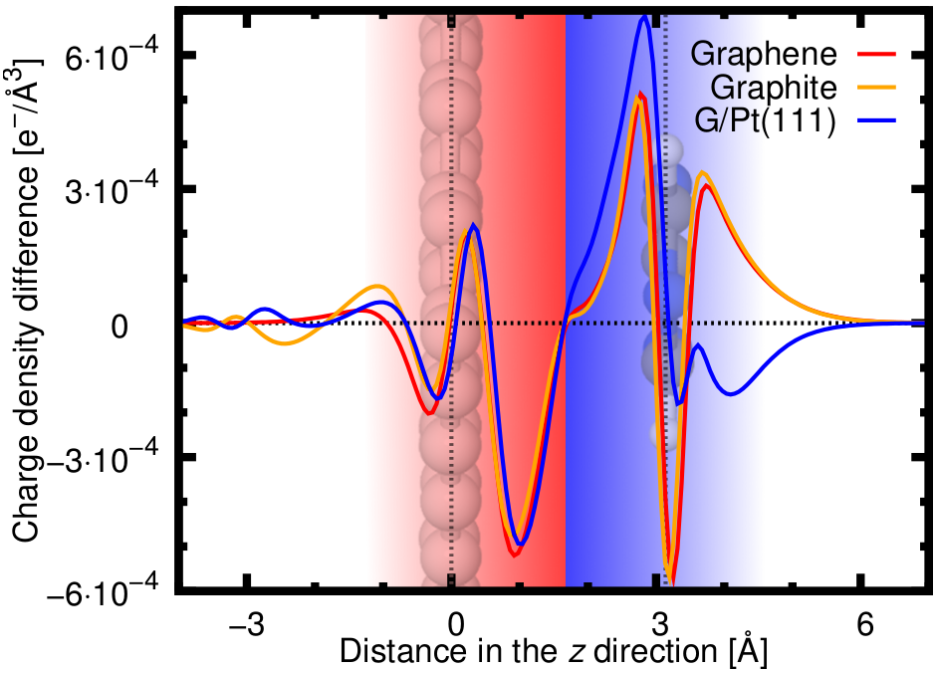

Figure 5.8 Integrated charge density difference along the z axis for the three systems that we have studied. The vertical dashed lines represent the position of the G sheet (left) and the triazine monolayer (right). The change of sign of the dipole that appears between the substrate and the molecule is highlighted with a change in the background color from blue to red.

	Graphene			Graphite			G/Pt(111)		
	meV		Å	meV		Å	meV		Å
All top	-344	(60)	3.28	-382	(63)	3.28	-402	(64)	3.28
C top	-404	(0)	3.15	-445	(0)	3.13	-466	(0)	3.11
N top	-377	**(27)**	3.20	-417	**(27)**	3.20	-440	**(25)**	3.17
Bridge(R)	-367	(37)	3.21	-407	(38)	3.20	-428	(38)	3.20
Cross(R)	-339	(65)	3.29	-377	(68)	3.28	-398	(67)	3.26

Table 5.3 Molecule-substrate binding energy and mean adsorption distance for the different high symmetry adsorption sites studied for the three different substrates we are characterizing.

G/Pt(111) are similar to what we have found in the G case (see Table 5.3). We just can see a small rigid shift of the binding energies, around -40 meV for the graphite and -60 meV for the G/Pt(111), and variations of the adsorption distances less than 5 pm.

The data shown in Table 5.3 is for a chosen area of the G/Pt(111) Moiré cell but we have also characterized the rest of the possibilities. The maximum difference among all the Moiré possibilities on G-equivalent adsorption sites is ~2 meV corresponding to variations on the adsorption distance of ~0.02 Å.

In the other hand, our results do show that the total binding energy is modified by the material underneath the G sheet, in agreement with experiments[311] that show how the binding energy of naphthalene molecules on G/Ir(111) changes by intercalation of either oxygen or europium atoms between a G layer and the underlying metal surface. In that work[311] was claimed that this binding energies change is a consequence of the modification on the vdW attractive interaction due to different screening effects induced on the top G layer by the underlying substrate which changes the doping of the sheet from n-doped with O intercalation to p-doped with Eu. However, in our case, we cannot attribute the change to that screening effects on the vdW interaction as our results are calculated with the PBE-D2 approach that does not include any of these effects (the C_6 parameters of the G are always the same). There are changes on the vdW interaction but these are due to the different vdW interaction of the molecules with either the Pt or the second G layer on the graphite case. Results with other vdW flavours are very similar.

Energy barrier calculation

Contrary to the experimental evidence we have not found with the PBE-D2 functional any difference in the diffusion energy barriers by changing the substrate. This lack of substrate dependency on our results could be related with a non-accurate description of the vdW interaction as D2 approach is very basic and do not account for the charge density distribution of the particular system, that is changing between the G, graphite and

	Graphene	Graphite	G/Pt(111)
	meV	meV	meV
EXP [140,141]		55±8	68±9
PBE-D2	27	27	27
PBE-D3	15	17	17
optB86b	25	25	26
PBE-TS+SCS	22	19	21
PBE-MBD	17	17	18

Table 5.4 Energy barriers calculated for the three different substrates we are characterizing compared to the experimental values.

G/Pt(111). In order to check these effects we have also calculated the barrier with others vdW flavours that take into account, effects of the neighbouring atoms (PBE-D3) [143], the actual charge density of the system (DFT-DF (optB86b)) [144], screening effects (DFT-TS-SCS) [145], and manybody effects on the dispersion interaction (DFT-MBD) [147]. However, in any of the flavours, significant differences are observed (see Table 5.4). Even considering energy variation among C-top and N-top sites inside the G/Pt(111) Moiré cell, a maximum of ~4 meV of increasing on the G/Pt(111) barrier, would not be enough to reach the experimental values. Therefore, respect to the energy barriers although our simulations provide the correct order of magnitude, they yield smaller values (about half) than in the experiments. Moreover, no differences with substrate are found.

5.6.2 Intermolecular interaction

Next, we analyze the effect of the substrate in the intermolecular interaction. The experiments show a change on the intermolecular distance of ~0.1 Å between the triazines adsorbed on graphite and on G/Pt(111). Our calculations of a 3-triazine island on G showed that the presence of the layer shifted the energy per H-bond, ~11 meV, respect to the isolated island but it had an effect of just 1 pm on the distance. In Fig. 5.9 we show our analysis of the energy per H-bond, as calculated following the procedure explained above, for all the substrates studied and compared to the isolated island. However, again we cannot observe differences among the substrates (<1 meV per H-bond in energies and <1 pm in distances). Therefore, although the presence of the G is inducing some –small– differences in the intermolecular interaction, the influence of the underneath substrate, even although it modifies the electronic properties of the G sheet, does not affect to the interaction between the triazines.

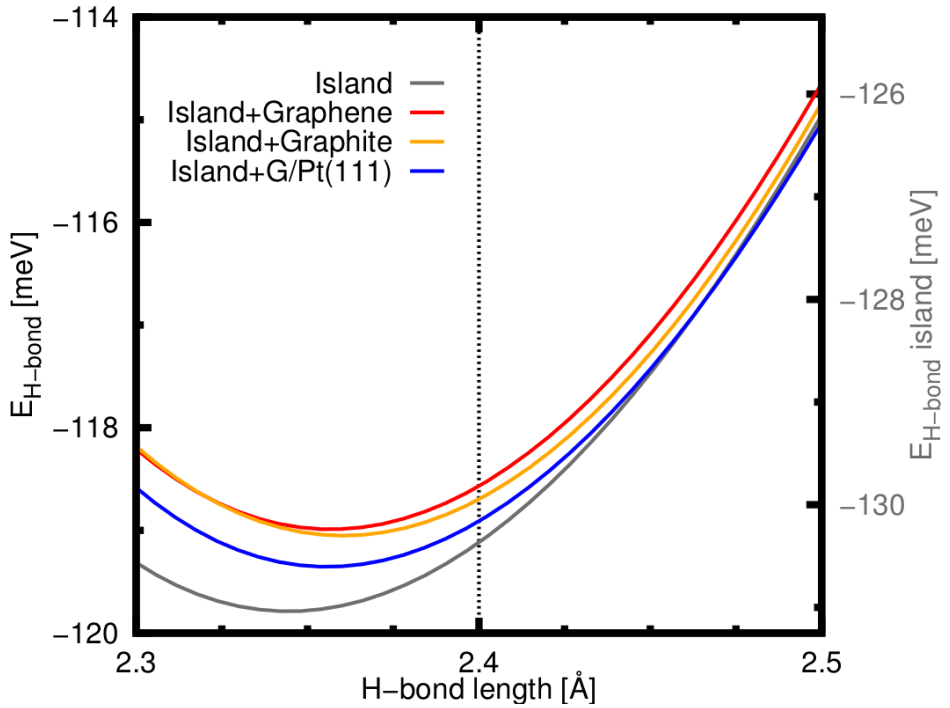

Figure 5.9 Intermolecular energy per H-bond vs the H-bond distance for simulations with the isolated 3-molecule island of triazines (grey), the island on top of G (red), the island on top of graphite (orange) and the island on top of G/Pt(111) (blue). Note that the energy axis for the three substrates (left) is different from the energy axis of the isolated island (right) but both axis represent the same energy increment. The minimum for the case of the isolated island is at a H-bond distance of ~2.35 Å while for the three substrates it slightly increases up to ~2.36 Å.

5.7 Discussion

All this exhaustive theoretical study of the adsorption of the triazine molecule over different G-based substrates, having the experimental evidence as a reference, allows us to unveil some of the basic properties driven the SAM formation on G layers. However, we are still unable to address the influence on the SAM formation –found in the experiments– of the material on which the G has been grown. Despite this, we have learnt relevant notions on the SAMs formation and we have also been able to point out the possible origins of the discrepancies with the experiments.

In both the graphite and the G/Pt(111) systems, the preferred configuration of the adsorption a single molecule is the C top position. The orientation of the triazines respect to G observed on the experiments, both on the HOPG and G/Pt(111), agrees, among all the possible ones (for example that one on the Cross(R) configuration), with the orientation defined by the C top configuration. This means that the molecule-substrate interaction, even being weak, is the driven force that fixes the SAM orientation respect to the G. It can be observed in Fig. 5.10 where we show a ball-and-stick scheme of the $G(\sqrt{7}\times\sqrt{7})$ cell. It can be clearly seen that the system accommodates the molecules close to C top positions in order to maximize the substrate-molecule interaction. Nevertheless, the molecules are slightly rotated from the perfect C top positions so as to favour the H-bonds alignment.

In the other hand, the large Morié patterns found in the experiments point out to a relatively stronger intermolecular interaction respect to the molecule-substrate interaction. If this last interaction were strong enough, the Moiré cell size should have been smaller. Other adsorption configurations of smaller size, as the $G(\sqrt{7}\times\sqrt{7})$ cell, where the intermolecular distance is ~2.7 Å and all the molecules would be adsorbed in a favourable C top configuration, should be the candidates to be the most stable SAM Moiré. However, our calculations show that the strength of both molecule-substrate and intermolecular interactions are similar. For the G case, for example, we find that the binding energy in the C top position (-404 meV with PBE-D2) is similar to the H-bond energy corresponding to a whole molecule (6/2 H-bonds/molecule × -119 meV/H-bond = -357 meV/molecule). This explains why, even when the molecule-substrate interaction is relevant, the Moiré cell has a big size. The SAM formation is ruled by the subtle balance between the changes on the binding energy and the changes on the intermolecular interaction. Thus, the Moiré patterns that favours the molecule-substrate interaction should paid energy on the intermolecular interaction (for the $G(\sqrt{7}\times\sqrt{7})$ the binding energy is optimized but the intermolecular energy is increased 3 H-bonds/molecule × ~23 meV/H-bond = 69 meV/molecule). On the contrary, for the larger Moiré patterns, as the observed in the

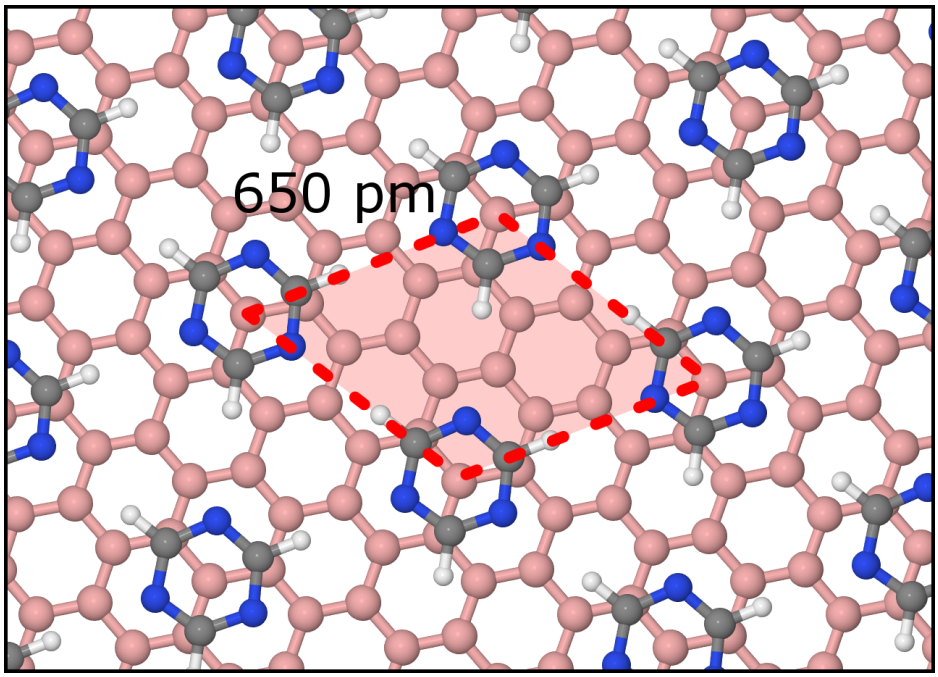

Figure 5.10 Ball-and-stick scheme of the $G(\sqrt{7}\times\sqrt{7})$ cell obtained from DFT (PBE-D2) simulations. The intermolecular distance is shown and the triazine network is commensurated to the G lattice.

experiments in the HOPG case, the intermolecular distance is kept close to its optimum value with an intermolecular energy loss of less than 3 meV per molecule (see Fig. 5.9) but the molecules are not placed on the optimum adsorption configurations but distributed along the PES whose corrugation is around 60 meV (see Fig. 5.4). Assuming a uniform distribution as a first approach, this would result on an average binding energy loss of ~30 meV/molecule. Therefore, this explains why this large Moiré patterns are more stable than the smaller ones. As a matter of fact, on these Moiré patterns a variation of the molecule absorption distances of ~15 pm inside the Moiré should be expected (see Fig. 5.4) and molecules on non-highly-symmetric configurations should be slightly tilted.

Finally, we now address the possible reasons behind the discrepancy found between our calculations and the experimental evidence about the influence of the substrate on the SAM formation. The reason why in the experiments we have different Moiré patterns for HOPG and G/Pt(111) can be explained phenomenologically in terms of the mismatch between the lattices involved[101]. Attending to the experimental STM images, in the graphite case the mismatch of the monolayer with respect to the G lattice is very small (-0.02%). When the platinum is introduced a new lattice parameter has to be taken into account. If the Moiré pattern G-triazine is preserved there would be a mismatch of more than 2% of the metal with respect to the G-triazine system. That is why the Moiré changes

into a cell which slightly increases the mismatch of the triazine monolayer with the G (0.05%) but reduces considerably the mismatch with the platinum (0.2%).

This implies that the effect of the platinum does exist and it is related to the interaction of the molecules with the Pt atoms (either directly or through the modulation created in the G by the metal surface). The SAM is paying some intermolecular energy to accommodate the adsorption positions to the Pt lattice, or to the $G(3\times3)$/Pt(111) Moiré. Our calculations should see this effect, but if we estimate the energy balance between a cell as the Moiré on the graphite and the observed Moiré on G/Pt(111) we cannot explain the preference of this last one: the increase on the intermolecular distances would result on an increase of the energy of ~2 meV/H-bond×3 H-bond/molecule~6 meV/molecule (see Fig. 5.9), that cannot be compensated by the ~ 2 meV/molecule of difference found between the G-equivalent adsorption positions inside the $G(3\times3)$/Pt(111) Moiré. This discrepancy is supported by the underestimation of the diffusion barriers obtained in our calculations.

The question is, then, why are we unable to reproduce the influence of the substrate on the Moiré pattern sizes and the experimental diffusion energies? As we said in the introduction, there are two main interactions that play an important role in these systems whose incorrect description could be causing the discrepancies with the experimental evidences: the vdW and the short range chemical interaction.

From the point of view of the chemical interaction description we have mostly used the standard PBE functional but we have also performed some calculations with more accurate hybrid functionals obtaining similar results. We have also tried the state-of-the-art implementations regarding the dispersion energy. With different methods we have reached similar conclusions: we do not see any difference in energy barriers between substrates. For both discrepancies, the value of the energy barriers and the energy differences inside the absorption position induced by the presence of the Pt, our calculations show a lack of interaction in order to explain the experimental evidence.

We can see that if we push the triazine towards the G layer the energy barriers are increased (see Fig. 5.11). We would need a decrease on the adsorption distance of ~0.2 Å and ~0.3 Å for graphite and G/Pt(111) respectively to reach the experimental values of diffusion barriers.

What we have presented in Fig. 5.11 is a qualitative estimation of how the energy barriers would change if the substrate-molecule interaction is modified by rigidly changing the adsorption distances of the C top and N top geometries. However, for a quantitative evaluation, we need to go a step farther in our analysis. In this case, we are going to include a new parameter in the calculation which allows for tuning the relative weight of the vdW contribution to the total energy. In this new approach we are homogeneously shifting the

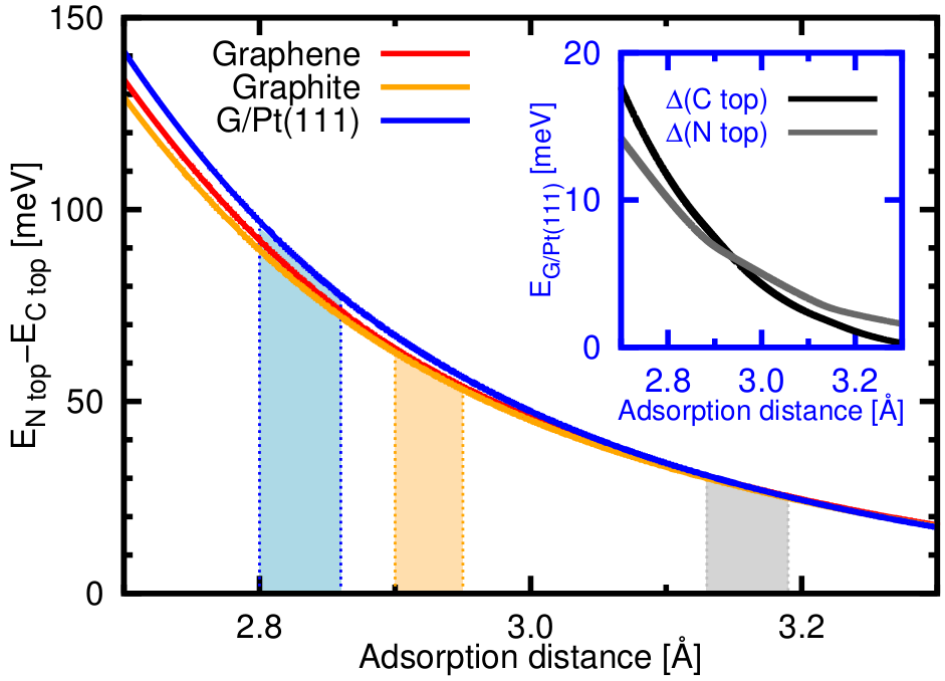

Figure 5.11 The difference of energies between the C top and N top adsorption positions is plotted for different adsorption distances. The results for the three substrates (G in red, graphite in orange and G/Pt(111) in blue) are shown. The interval of adsorption distances that was got in the calculations is highlighted in grey. The regions colored with light orange and light blue are those on which the adsorption distances should reproduce the experimental barrier for the graphite and G/Pt(111) respectively. The inset shows the increasing in energy difference when the adsorption distance decreases between the most repulsive and most attractive Moiré sites for the same geometry (C top in black and N top y grey) in the G/Pt(111) substrate.

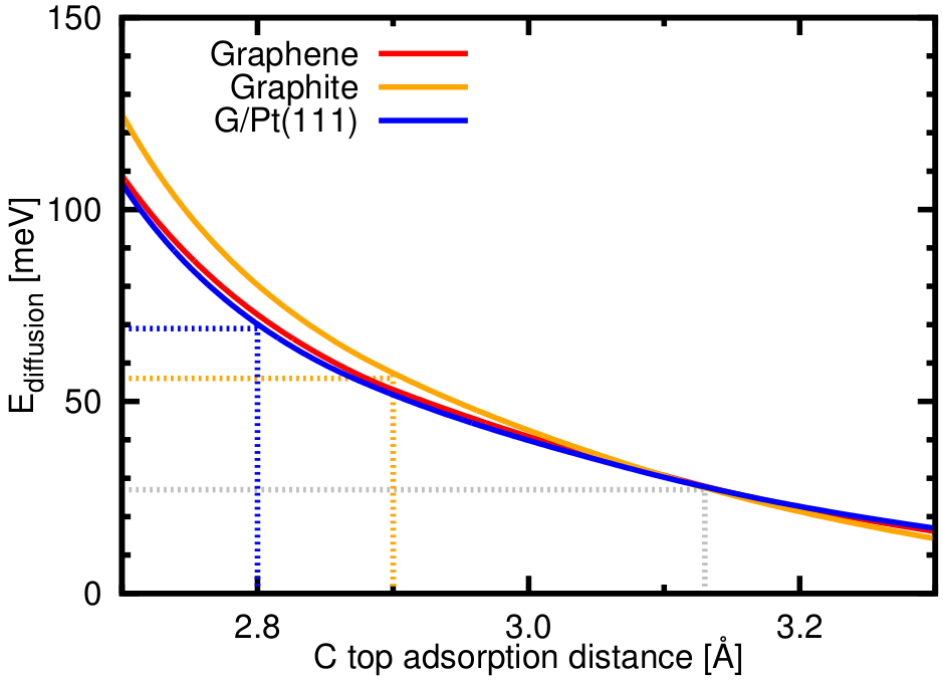

Figure 5.12 Diffusion energy estimation with respect to the C top equilibrium adsorption, tuned by a parameter that changes the weight of the vdW contribution to the total energy. The barrier for the original DFT calculation is indicated with a grey dashed line. The orange and blue dashed lines show the points where the experimental values for the case of graphite and G/Pt(111), respectively, are recovered. These new barriers are acquired with a multiplicative vdW factor of ~2 for the case of the graphite and a factor of ~3 for the G/Pt(111) one.

weight of the vdW contribution to the total energy for both adsorption sites instead of homogeneously changing their adsorption distances as we did in Fig. 5.11. This enables a more realistic estimation of the energy barrier and this results are shown in Fig. 5.12.

Moreover, for the G/Pt(111) case, at that distance the variation of the binding energy between G-equivalent adsorption positions within the $G(3 \times 3)$ cell would be of ~10 meV/molecule (see inset on Fig. 5.11) and could compensate the intermolecular energy loss, ~6 meV (see above), required to accommodate the triazine SAM to the Pt lattice. This hypothesis addresses the correct energy barriers, the source of the intermolecular distance change between substrates and, therefore, the reason why the Moiré observed is different in HOPG to what is observed in G/Pt(111).

5.8 Conclusions

We have studied the SAMs formation of triazine on G, graphite and G/Pt(111) substrates with the more advanced DFT techniques. In the three cases, we have characterized both

the molecule-substrate and the intermolecular interactions. Our results show that the SAM formation in these weakly interacting systems is ruled by a subtle balance between both interactions which are of the same order. Thus, the theory shows that the molecular orientation found in the experiments, the same that characterizes the minimum energy adsorption site for a single molecule, is driven by the molecule-substrate interaction. However, the intermolecular contribution leads to a big Moiré pattern instead of letting the system fall into smaller cells as would be preferred by the molecule-substrate interaction. The intermolecular interaction is only slightly affected by the presence of the G layer: there is a change of ~11 meV in the H-bond energy but no differences on the equilibrium intermolecular distances.

The experiments show that the SAMs of triazine form Moiré patterns which try to minimize the mismatch with not only the G layer but also with the underneath substrate. However, our calculations cannot see this effect nor the differences between substrates on the diffusion energies. The reason why we cannot see any difference between substrates could be related with a lack of interaction. If we push the molecules toward the substrate we would (i) get the correct experimental diffusion energies and (ii) explain the subtle energy balance that determine the most stable Moiré pattern in the substrates.

Moreover, our study shows that these molecule-G like systems are a paradigmatic example to the study of the accuracy of the new functionals for the electron-electron interaction developed for weakly interacting systems. Not only binding energies but also diffusion barriers and the balance between intermolecular and molecule-substrate interactions would remarkably help to benchmark this accuracy. The actual state-of-the-art DFT-based methods are not accurate enough to reproduce experimental results on these systems.

CONCLUSIONS

After the excitement of the first graphene characterization experiments, the scientific community realized that it is not the Holy Grail of materials. It has, indeed, extraordinary properties, but also some drawbacks which prevent it to be directly used in a wide range of devices. The interaction of graphene with other materials or lattice defects modify its properties which is regarded as an opportunity to tune them. In this thesis we have explored, using first principles simulations based in density functional theory (DFT) methods, some of this proposed graphene modifications. For that purpose we have had to push the available simulation methods to their limits in terms of precision, system sizes and supercell designs.

We have first presented in chapter 3 a combined STM and DFT study of the interaction between graphene edges and Pt(111) steps in which we disclose the atomic structure of the G–Pt boundary. The unsaturated C atoms strongly interact with the Pt step, preserving a zigzag structure quite close to the ideal configuration. However, Pt edge atoms experience a reconstruction of 3× periodicity that stabilizes the structure. The tendency to form passivated zigzag graphene terminations plays a relevant role in the formation and orientation of the stable Moiré patterns. Our combined approach reveals the interesting electronic properties of this nanoscopic system including, as stated by the simulations, the preservation of the G–edge state shifted to energies at ~0.8 eV above Fermi level, highly localized in one of the graphene sublattices and confined to the G–Pt interface. This state spreads out inside the first Pt row resulting in a high quality G–metal electric contact that could be relevant for designing future atomically precise graphene metal leads.

Later on in this thesis (see chapter 4), we have analyzed the magnetic and mechanical properties induced by monovacancies (V_1) in graphene. We have concluded that the magnetization of the system for low V_1 concentrations tends to a value of 2 μ_B, contrary to previous works in extended systems calculated with periodic boundary conditions, and supporting the results of cluster calculations. This discrepancy can be explained in terms of the huge cell size and fine k-point meshes required to converge the magnetism of the system in calculations with extended systems. Moreover, we have seen that the magnetism

of a V_1 can be tuned by applying an external in-plane strain getting an increasing of a 10% on the magnetization upon stretching. We have found a transition around a strain of 2% between the well-known asymmetric solution ($a-V_1$) and a quasi-symmetric ($qs-V_1$) structure, on which the soft dimer bond of the $a-V_1$ reconstruction is broken, leading to an almost symmetric configuration with a different electronic structure.

We have also shown that the V_1 affect the mechanical properties through the strain field induced by the soft bond that stretches the graphene lattice around the V_1. Our results show that this stretching stiffens the out-of-plane modes of the layer which are easily excited with temperature. This extra energy cost quenches the thermal fluctuations due to the excitation of these out-of-plane modes, leading to an increase of the effective stiffness of the graphene and to the reduction of the absolute value of the negative thermal expansion coefficient in defective graphene samples and, in general, to the modification of all the mechanical properties which are related with these fluctuations.

In the last chapter (see chapter 5) we have studied the SAMs formation of triazine on graphene, graphite and G/Pt(111) substrates with the more advanced vdW implementations. In the three cases, we have characterized both the molecule-substrate and the intermolecular interactions. Our results show that the SAM formation in these weakly interacting systems is ruled by a subtle balance between both interactions which are of the same order. The molecule-substrate interaction seems to be fixing the monolayer orientation –the same found in the experiments– with respect to the graphene while the intermolecular contribution leads to a big Moiré pattern instead of letting the system fall into smaller cells preferred by the molecule-substrate interaction.

The experiments show that the SAMs of triazine form Moiré patterns which try to minimize the mismatch with not only the graphene layer but also with the underneath substrate. However, our calculations cannot see this effect nor the differences between substrates on the diffusion energies. The reason why we cannot see any difference between substrates could be related with a lack of interaction. If we push the molecules toward the substrate we would (i) get the correct experimental diffusion energies and (ii) explain the subtle energy balance that determine the most stable Moiré pattern in the substrates.

In summary, these studies represent a contribution in the search of understanding the basic properties of graphene taking into account the interaction with its surroundings which will enable us to tune its properties. We have not only characterized electronic and mechanical modifications of its properties performed via the interaction with other materials or the deformation of its ideal 2D lattice. We have also tested the state-of-the-art simulation methods, whose capacity of describing intricated systems grows everyday. We

think that the analysis of our results, along with that of many others, serve as a benchmark to find the right path to continue their development.

CONCLUSIONES

Trás la emoción de su descubrimiento, la comunidad científica se dio cuenta de que el grafeno no era el Santo Grial de los materiales. Es cierto que tiene propiedades extraordinarias, pero también algunos inconvenientes que impiden que pueda ser directamente aplicado en una amplia variedad de dispositivos. Para ser capaces de aprovechar al máximo las sobresalientes propiedades del grafeno todavía necesitamos esquivar esos obstáculos, principalmente mediante la interacción con otros materiales pero también rompiendo su red bidimensional ideal.

En esta tesis hemos explorado, sobre todo desde el punto de vista teórico, algunos de estos caminos propuestos de modificación de las propiedades del grafeno. Con este propósito hemos llevado al límite los métodos de simulación disponibles en cuanto a precisión, tamaño de los sistemas estudiados y diseño de las superceldas adecuadas para cada problema.

Hemos presentado primero, en el capítulo 3, un estudio en el que hemos combinado experimentos con microscopía de efecto túnel y cálculos basados en la teoría del funcional de la densidad para caracterizar las heteroestructuras de los bordes de grafeno crecido sobre Pt(111) en el que revelamos la estructura atómica de la frontera entre el grafeno y el platino. Los átomos de carbono insaturados interaccionan fuertemente con el escalón de platino, manteniendo una estructura en zigzag muy cercana a la de la configuración ideal. Sin embargo, por otra parte, los átomos del borde de platino sufren una reconstrucción de periodicidad 3 que estabiliza la estructura. Esta tendencia a formar terminaciones de grafeno en zigzag pasivadas juega un importante papel en la formación y orientación de los patrones de Moiré estables. Nuestro procedimiento combinado de teoría y experimento revela las interesantes propiedades de este sistema nanoscópico incluyendo, según se deduce de las simulaciones, la conservación del estado de borde del grafeno, desplazado en energía unos ~0.8 eV sobre el nivel de Fermi, altamente localizado en una de las subredes del grafeno y que está confinado en la interfase entre el grafeno y el platino. Este estado se extiende hasta la primera fila de átomos de platino lo que da como resultado un

contacto eléctrico entre el grafeno y el metal de una alta calidad que podría ser relevante a la hora de diseñar futuros electrodos grafeno-metal con precisión atómica.

A continuación hemos analizado las propiedades magnéticas y mecánicas inducidas por la presencia de monovacantes (V_1) en grafeno (ver capítulo 4). Concluimos que la magnetización del sistema para una baja concentración de V_1 tiende a un valor de 2 μ_B, que es contrario a lo predicho en anteriores trabajos sobre este tema en sistemas extendidos con condiciones periódicas de contorno pero refuerza los resultados obtenidos cálculos en *clusters*. Esta discrepancia se explica por el hecho de que en nuestros cálculos en sistemas extendidos hemos necesitado tamaños enormes de celda y mallas muy finas de puntos k para converger el magnetismo del sistema. Además hemos visto que el magnetismo inducido por las V_1 puede ser modificado aplicando una tensión externa paralela al plano obteniendo un aumento de hasta un 10% al estirar la lámina. Al estirar se encuentra una transición alrededor de un 2% entre la conocida reconstrucción asimétrica ($a-V_1$) y una quasi-simétrica ($qs-V_1$), en la que el enlace débil del dímero característico de la solución $a-V_1$ se rompe, dando lugar a una configuración casi simétrica con una estuctura electrónica diferente.

También mostramos que las V_1 afectan a las propiedades mecánicas a través del campo de tensiones inducido por la formación del enlace débil que estira la red del grafeno alrededor de las V_1. De nuestros resultados se deduce que este estiramiento endurece los modos de vibración que tienen lugar fuera del plano de la lámina. Este coste energético extra atenua estas fluctuaciones, y son presumiblemente las responsables del incremento de la rigidez efectiva del grafeno y de la redución del valor absoluto –es negativo– del coeficiente de expansión térmica en muestras de grafeno con defectos.

En el último capítulo (ver capítulo 5) hemos estudiado la formación de monocapas de moléculas autoensambladas (*SAMs*) de triacina sobre sustratos de grafeno, grafito y G/Pt(111) haciendo uso de las técnicas más avanzadas de la teoría del funcional de la densidad. En los tres casos hemos caracterizado tanto la interacción molécula-sustrato como la intermolecular. Nuestros resultados muestran que la formación de *SAMs* en esta clase de sistemas de interacción débil está gobernada por un sutil balance entre ambas interacciones que resultan ser del mismo orden. La interacción molécula-sustrato es responsable de fijar la orientación de la monocapa con respecto al grafeno –la misma que se encuentra en los experimentos– mientras que la contribución intermolecular conduce a un patrón de Moiré mucho más grande de lo que hubiera dictado la interacción molécula-sustrato.

Los experimentos muestran que las *SAMs* de triacina forman los patrones de Moiré de manera que se minimice la diferencia de tamaño con respecto no sólo a la red del grafeno

sino también a la del sustrato que se encuentra debajo de este. Nuestros cálculos no son capaces de ver este efecto como tampoco reproducen las diferencias que dependiendo del sustrato aparecen en la energía de difusión. La razón por la cual teóricamente no se ven estas diferencias puede estar relacionada con una falta de interacción. Si empujáramos las moléculas hacia el sustrato podríamos (i) recuperar las energías de difusión experimentales correctas y (ii) explicar el sutil balance energético que determina el Moiré más estable para cada sustrato.

En resumen, este conjunto de estudios son una contribución en la búsqueda de los métodos que nos permitirán controlar y modificar las propiedades del grafeno. No sólo hemos caracterizado cómo cambian sus propiedades tanto electrónicas como mecánicas a través de la interacción con otros materiales o la deformación de su red bidimensional ideal. También hemos puesto a prueba los últimos avances en métodos de simulación cuya capacidad de describir sistemas complejos crece día a día. Creemos que análisis de este tipo servirán como evaluación y referencia a los desarrolladores de estos métodos para avanzar en el camino correcto hacia programas cada vez más certeros al simular fenómenos reales.

PUBLICATIONS

Publications on which this thesis is based:

1. **L. Rodrigo**, P. Pou, R. Martínez, A. J. Martínez-Galera, J. M. Gómez-Rodríguez, R. Pérez. *Study of self-assembled molecular layers formation on weakly interacting systems.* Submitted.

2. **L. Rodrigo**, P. Pou, R. Pérez. *Graphene monovacancies: electronic and mechanical properties from large scale ab initio simulations.* Carbon, 2016. DOI: 10.1016/j.carbon.2016.02.064.

3. P. Merino^{+}, **L. Rodrigo**$^{+}$, A. L. Pinardi, J. Méndez, M. F. López, P. Pou, R. Pérez and J. A. Martín-Gago. *Sublattice Localized Electronic States in Atomically Resolved Graphene-Pt(111) Edge-Boundaries.* ACS Nano, 2014, 8 (4), pp 3590–3596. DOI: 10.1021/nn500105a. ($^{+}$ both authors contributed equally).

Other publications during the thesis period:

1. M. M. Ugeda, A. J. Bradley, **L. Rodrigo**, M. Yu, W. Liu, P. Doak, A. Riss, S. Wickenburg, J. Neaton, D. Tilley, R. Pérez and M. F. Crommie. *Covalent Functionalization of GaP(110) Surfaces via Staudinger–type Reaction.* Submitted.

2. S. Yamazaki, K. Maeda, Y. Sugimoto, M. Abe, V. Zobač, P. Pou, **L. Rodrigo**, P. Mutombo, R. Pérez, P. Jelínek and S. Morita. *Interplay between Switching Driven by the Tunneling Current and Atomic Force of a Bistable Four-Atom Si Quantum Dot.* Nano Lett., 2015, 15 (7), pp 4356–4363. DOI: 10.1021/acs.nanolett.5b00448

3. M. Z. Baykara, M. Todorović, H. Mönig, T. C. Schwendemann, **L. Rodrigo**, E. I. Altman, R. Pérez and U. D. Schwarz. *Simultaneous Measurement of Multiple Independent Atomic-Scale Interactions Using Scanning Probe Microscopy: Data Interpretation and the Effect of Cross-Talk.* J. Phys. Chem. C, 2015, 119 (12), pp 6670–6677. DOI: 10.1021/acs.jpcc.5b00594.

4. H. Mönig, M. Todorović, M. Z. Baykara, T. C. Schwendemann, **L. Rodrigo**, E. I. Altman, R. Pérez, and U. D. Schwarz. *Understanding Scanning Tunneling Microscopy Contrast Mechanisms on Metal Oxides: A Case Study.* ACS Nano, 2013, 7 (11), pp 10233–10244. DOI: 10.1021/nn4045358.

5. M. Z. Baykara, M. Todorović, H. Mönig, T. C. Schwendemann, O. Ünverdi, **L. Rodrigo**, E. I. Altman, R. Pérez, and U. D. Schwarz. *Atom-specific forces and defect identification on surface-oxidized Cu(100) with combined 3D-AFM and STM measurements.* Phys. Rev. B, 2013, 87, 155414. DOI: 10.1103/PhysRevB.87.155414

REFERENCES

[1] K. S. Novoselov, A. K. Geim, S. V. Morozov, D. Jiang, Y. Zhang, S. V. Dubonos, I. V. Grigorieva, and A. A. Firsov. Electric Field Effect in Atomically Thin Carbon Films. *Science*, 306(5696):666–669, 2004. doi: 10.1126/science.1102896.

[2] A. C. Ferrari, F. Bonaccorso, V. Fal'ko, K. S. Novoselov, S. Roche, P. Boggild, S. Borini, F. H. L. Koppens, V. Palermo, N. Pugno, J. A. Garrido, R. Sordan, A. Bianco, L. Ballerini, M. Prato, E. Lidorikis, J. Kivioja, C. Marinelli, T. Ryhanen, A. Morpurgo, J. N. Coleman, V. Nicolosi, L. Colombo, A. Fert, M. García-Hernández, A. Bachtold, G. F. Schneider, F. Guinea, C. Dekker, M. Barbone, Z. Sun, C. Galiotis, A. N. Grigorenko, G. Konstantatos, A. Kis, M. Katsnelson, L. Vandersypen, A. Loiseau, V. Morandi, D. Neumaier, E. Treossi, V. Pellegrini, M. Polini, A. Tredicucci, G. M. Williams, Byung Hee H., J.-H. Ahn, J. Min Kim, H. Zirath, B. J. van Wees, H. van der Zant, L. Occhipinti, A. Di Matteo, I. A. Kinloch, T. Seyller, E. Quesnel, X. Feng, K. Teo, N. Rupesinghe, P. Hakonen, S. R. T. Neil, Q. Tannock, T. Lofwander, and J. Kinaret. Science and technology roadmap for graphene, related two-dimensional crystals, and hybrid systems. *Nanoscale*, 7:4598–4810, 2015. doi: 10.1039/C4NR01600A.

[3] K. S. Novoselov, A. K. Geim, S. V. Morozov, D. Jiang, M. I. Katsnelson, I. V. Grigorieva, S. V. Dubonos, and A. A. Firsov. Two-dimensional Gas of Massless Dirac Fermions in Graphene. *Nature*, 438:197–200, 2005. doi: 10.1038/nature04233.

[4] B. C. Brodie. On the Atomic Weight of Graphite. *Phil. Trans. R. Soc.*, 149, 1859. doi: 10.1098/rstl.1859.0013.

[5] G Ruess and F. Vogt. Höchstlamellarer Kohlenstoff aus Graphitoxyhydroxyd. *Monatshefte für Chemie und verwandte Teile anderer Wissenschaften*, 78:222–242, 1948. doi: 10.1007/BF01141527.

[6] H. P. Boehm, A. Clauss, and U. Hoffmann. Graphite oxide and its membrane properties. *Journal de Chimie Physique*, 58:110–117, 1960.

[7] H. P. Boehm, A. Clauss, G. O. Fischer, and U. Hofmann. Das Adsorptionsverhalten sehr dünner Kohlenstoff-Folien. *ZAAC*, 316:119–127, 1962. doi: 10.1002/zaac.19623160303.

[8] R. Setton H. P. Boehm and E. Stumpp. Nomenclature and Terminology of Graphite Intercalation Compounds. *Carbon*, 24:241–245, 1986. doi: 10.1016/0008-6223(86)90126-0.

[9] H. Shioyama. Cleavage of Graphite to Graphene. *J. Mater. Sci. Lett.*, 20:499–500, 2001. doi: 10.1023/A:1010907928709.

[10] L. M. Viculis, J. J. Mack, and R. B. Kaner. A Chemical Route to Carbon Nanoscrolls. *Science*, 299:1361, 2003. doi: 10.1126/science.1078842.

[11] S. Horiuchi, T. Gotou, M. Fujiwara, T. Asaka, T. Yokosawa, and Y. Matsui. Single Graphene Sheet Detected in a Carbon Nanofilm. *Appl. Phys. Lett.*, 84:2403, 2004. doi: 10.1063/1.1689746.

[12] K. S. Novoselov, E. McCann, S. V. Morozov, V. I. Fal'ko, M. I. Katsnelson, U. Zeitler, D. Jiang, F. Schedin, and A. K. Geim. Unconventional Quantum Hall Effect and Berry's Phase of 2π in Bilayer Graphene. *Nat. Phys.*, 2:177–180, 2006. doi: 10.1038/nphys245.

[13] K. S. Novoselov, Z. Jiang, Y. Zhang, S. V. Morozov, H. L. Stormer, U. Zeitler, J. C. Maan, G. S. Boebinger, P. Kim, and A. K. Geim. Room-Temperature Quantum Hall Effect in Graphene. *Science*, 315:1379, 2007. doi: 10.1126/science.1137201.

[14] K. S. Novoselov, V. I. Fal'ko, L. Colombo, P. R. Gellert, M. G. Schwab, and K. Kim. A Roadmap for Graphene. *Nature*, 490:192–200, 2012. doi: 10.1038/nature11458.

[15] A. A. Balandin, S. Ghosh, W. Bao, I. Calizo, D. Teweldebrahn, F. Miao, and C.N. Lau. Superior Thermal Conductivity of Single-Layer Graphene. *Nano Lett.*, 8:902–907, 2008. doi: 10.1021/nl0731872.

[16] R. Murali, Y. Yang, K. Brenner, T. Beck, and J. D. Meindl. Breakdown Current Density of Graphene Nanoribbons. *Appl. Phys. Lett.*, 94:243114, 2009. doi: 10.1063/1.3147183.

[17] N. Tombros, C. Jozsa, M. Popinciuc, H. T. Jonkman, and B.J. van Wees. Electronic spin transport and spin precession in single graphene layers at room temperature. *Nature*, 448:571–574, 2007. doi: 10.1038/nature06037.

[18] Y.-F. Cho, S. Chen and M. S. Fuhrer. Gate-tunable Graphene Spin Valve. *Appl. Phys. Lett.*, 91:123105, 2007. doi: 10.1063/1.2784934.

[19] H. Min, G. Borghi, M. Polini, and A.H. MacDonald. Pseudospin Magnetism in Graphene. *Phys. Rev. B*, 77:041407, 2008. doi: 10.1103/PhysRevB.77.041407.

[20] P. Blake, P. D. Brimicombe, R. R. Nair, T. J. Booth, D. Jiang, F. Schedin, L. A. Ponomarenko, S. V. Morozov, H. F. Gleeson, E. W. Hill, A. K. Geim, and K. S. Novoselov. Graphene-based Liquid Crystal Device. *Nano Lett.*, 8(6):1704–1708, 2008. doi: 10.1021/nl080649i.

[21] J.-H. Lee, P. E. Loya, J. Lou, and E. L. Thomas. Dynamic Mechanical Behavior of Multilayer Graphene via Supersonic Projectile Penetration. *Science*, 346(6213):1092–1096, 2014. doi: 10.1126/science.1258544.

[22] C. Lee, X. Wei, J. W. Kysar, and J. Hone. Measurement of the elastic properties and intrinsic strength of monolayer graphene. *Science*, 321(5887), 2008. doi: {10.1126/science.1157996}.

[23] W. Mehr, J. Dabrowski, J. Christoph Scheytt, G. Lippert, Ya-Hong Xie, Max C. Lemme, M. Ostling, and G. Lupina. Vertical Graphene Base Transistor. *Electron Device Letters, IEEE*, 33(5):691–693, 2012. doi: 10.1109/LED.2012.2189193.

[24] P. Goswami, X. Jia, and S. Chakravarty. Quantum Oscillations in Graphene in the Presence of Disorder and Interactions. *Phys. Rev. B*, 78:245406, 2008. doi: 10.1103/PhysRevB.78.245406.

[25] E. J. Siochi. Graphene in the Sky and Beyond. *Nat. Nanotechnol.*, 9:745–747, 2014. doi: 10.1038/nnano.2014.231.

[26] J. Meyer, P. R. Kidambi, B. C. Bayer, C. Weijtens, A. Kuhn, A. Centeno, A. Pesquera, A. Zurutuza, J. Robertson, and S. Hofmann. Metal Oxide Induced Charge Transfer Doping and Band Alignment of Graphene Electrodes for Efficient Organic Light Emitting Diodes. *Sci. Rep.*, 4(5380), 2012. doi: 10.1038/srep05380.

[27] M. I. Katsnelson and A. Fasolino. Graphene as a prototype crystalline membrane. *Acc. Chem. Res.*, 46:97, 2013. doi: 10.1021/ar300117m.

[28] R. R. Nair, H. A. Wu, P. N. Jayaram, I. V. Grigorieva, and A. K. Geim. Unimpeded Permeation of Water Through Helium-Leak-Tight Graphene-Based Membranes. *Science*, 335:442–444, 2012. doi: 10.1126/science.1211694.

[29] J. S. Bunch, S. S. Verbridge, J. S. Alden, A. M. van der Zande, J. M. Parpia, H. G. Craighead, and P. L. McEuen. Impermeable Atomic Membranes from Graphene Sheets. *Nano Lett.*, 8:2458–2462, 2008. doi: 10.1021/nl801457b.

[30] F. Yavari, Z. Chen, A. V. Thomas, W. Ren, H.-M. Cheng, and N. Koratkar. High Sensitivity Gas Detection Using a Macroscopic Three-Dimensional Graphene Foam Network. *Sci. Rep*, 1(166), 2011. doi: 10.1038/srep00166.

[31] S. Chun, Y. Kim, H.-S. Oh, G. Bae, and W. Park. A highly sensitive pressure sensor using a double-layered graphene structure for tactile sensing. *Nanoscale*, 7:11652–11659, 2015. doi: 10.1039/C5NR00076A.

[32] H. Tian, Y. Shu, X.-F. Wang, M. A. Mohammad, Z. Bie, Q.-Y. Xie, C. Li, W.-T. Mi, Y. Yang, and T.-L. Ren. A Graphene-Based Resistive Pressure Sensor with Record-High Sensitivity in a Wide Pressure Range. *Sci. Rep.*, 5:8603, 2015. doi: 10.1038/srep08603.

[33] Y. Li, K. Yan, H.-W. Lee, Z. Lu, N. Liu, and Y. Cui. Growth of Conformal Graphene Cages on Micrometre-sized Silicon Particles as Stable Battery Anodes. *Nat. Energy*, 1(15029), 2016. doi: 10.1038/nenergy.2015.29.

[34] P. You, Z. Liu, Q. Tai, S. Liu, and F. Yan. Efficient Semitransparent Perovskite Solar Cells with Graphene Electrodes. *Adv. Mater.*, 27(24):3632–3638, 2015. doi: 10.1002/adma.201501145.

[35] V. Tozzini and V. Pellegrini. Reversible Hydrogen Storage by Controlled Buckling of Graphene Layers. *J. Phys. Chem. C*, 115(51):25523–25528, 2011. doi: 10.1021/jp208262r.

[36] S. Goler, C. Coletti, V. Tozzini, V. Piazza, T. Mashoff, F. Beltram, V. Pellegrini, and S. Heun. Influence of Graphene Curvature on Hydrogen Adsorption: Toward Hydrogen Storage Devices. *J. Phys. Chem. C*, 117(22):11506–11513, 2013. doi: 10.1021/jp4017536.

[37] L. Gao, P. P. Pal, T. Seideman, N. P. Guisinger, and J. R. Guest. Current-driven hydrogen desorption from graphene: Experiment and theory. *J. Phys. Chem. Lett.*, 7 (3):486–494, 2016. doi: 10.1021/acs.jpclett.5b02471.

[38] S.-J. Han, A. Valdés-García, S. Oida, K. A. Jenkins, and W. Haensch. Graphene Radio Frequency Receiver Integrated Circuit. *Nat. Commun.*, 5(3086), 2014. doi: 10.1038/ncomms4086.

[39] S. Y. Zhou, G.-H. Gweon, A. V. Fedorov, P. N. First, W. A. de Heer, D.-H. Lee, F. Guinea, A. H. Castro Neto, and A. Lanzara. Substrate-induced Bandgap Opening in Epitaxial Graphene. *Nat. Mater.*, 6(10):770–775, 2007. doi: 10.1038/nmat2003.

[40] Y. Shao, S. Zhang, C. Wang, Z. Nie, J. Liu, Y. Wang, and Y. Lin. Highly Durable Graphene Nanoplatelets Supported Pt Nanocatalysts for Oxygen Reduction. *J. Power Sources*, 195(15):4600–4605, 2010. doi: 10.1016/j.jpowsour.2010.02.044.

[41] C. Chung, Y.-K. Kim, D. Shin, S.-R. Ryoo, B. H. Hong, and D.-H. Min. Biomedical Applications of Graphene and Graphene Oxide. *Acc. Chem. Res.*, 46(10):2211–2224, 2013. doi: 10.1021/ar300159f.

[42] A. H. Castro Neto, F. Guinea, N. M. R. Peres, K. S. Novoselov, and A. K. Geim. The electronic properties of graphene. *Rev. Mod. Phys.*, 81, 2009. doi: 910.1103/RevModPhys.81.109.

[43] A. K. Geim and K. S. Novoselov. The Rise of Graphene. *Nat. Mater.*, 6(3):183–191, 2007. doi: 10.1038/nmat1849.

[44] W. Norimatsu and M. Kusunoki. Epitaxial Graphene on SiC0001: Advances and Perspectives. *Phys. Chem. Chem. Phys.*, 16:3501, 2014. doi: 10.1039/C3CP54523G.

[45] W. S. Hummers Jr. and R. E. Offeman. Preparation of Graphitic Oxide. *J. Am. Chem. Soc.*, 80(6):1339–1339, 1958. doi: 10.1021/ja01539a017.

[46] S. Niyogi, E. Bekyarova, M. E. Itkis, J. L. McWilliams, M. A. Hamon, and R. C. Haddon. Solution Properties of Graphite and Graphene. *J. Am. Chem. Soc.*, 128:7720, 2006. doi: 10.1021/ja060680r.

[47] D. A. C. Brownson and C. E. Banks. The Electrochemistry of CVD Graphene: Progress and Prospects. *Phys. Chem. Chem. Phys.*, 14:8264–8281, 2012. doi: 10.1039/c2cp40225d.

[48] E. Voloshina and Y. Dedkov. Graphene on Metallic Surfaces: Problems and Perspectives. *Phys. Chem. Chem. Phys.*, 14:13502, 2012. doi: 10.1039/c2cp42171b.

[49] M. Eizenberg and J. M. Blakely. Carbon Monolayer Phase Condensation on Ni(111). *Surf. Sci.*, 82:228, 1979. doi: 10.1016/0039-6028(79)90330-3.

[50] X. Li, W. Cai, J. An, S. Kim, J. Nah, D. Yang, R. Piner, A. Velamakanni, I. Jung, E. Tutuc, S. K. Banerjee, L. Colombo, and R. S. Ruoff. Large-Area Synthesis of High-Quality and Uniform Graphene Films on Copper Foils. *Science*, 324:1312, 2009. doi: 10.1126/science.1171245.

[51] T. Yoon, W. C. Shin, T. Y. Kim, J. H. Mun, T.-S. Kim, and B. J. Cho. Direct measurement of adhesion energy of monolayer graphene as-grown on copper and its application to renewable transfer process. *Nano Lett.*, 12(3):1448–1452, 2012. doi: 10.1021/nl204123h.

[52] J. Kang, D. Shin, S. Bae, and B. H. Hong. Graphene transfer: Key for applications. *Nanoscale*, 4:5527–5537, 2012. doi: 10.1039/C2NR31317K.

[53] J.S. Bunch and M.L. Dunn. Adhesion mechanics of graphene membranes. *Solid State Communications*, 152(15):1359–1364, 2012. doi: 10.1016/j.ssc.2012.04.029.

[54] P. Miró, M. Audiffred, and T. Heine. An Atlas of Two-dimensional Materials. *Chem. Soc. Rev.*, 43:6537–6554, 2014. doi: 10.1039/C4CS00102H.

[55] P. R. Wallace. The Band Theory of Graphite. *Phys. Rev.*, 71:622, 1947. doi: 10.1103/PhysRev.71.622.

[56] P. A. M. Dirac. The quantum theory of the electron. *Proc. R. Soc. Lond. A*, 117(778):610–624, 1928. doi: 10.1098/rspa.1928.0023.

[57] L. Van Hove. The Occurrence of Singularities in the Elastic Frequency Distribution of a Crystal. *Phys. Rev.*, 89:1189, 1953. doi: 10.1103/PhysRev.89.1189.

[58] K. Nakada, M. Fujita, G. Dresselhaus, and M. S. Dresselhaus. Edge State in Graphene Ribbons: Nanometer Size Effect and Edge Shape Dependence. *Phys. Rev. B*, 54:17954–17961, 1996. doi: 10.1103/PhysRevB.54.17954.

[59] M. Batzill. The Surface Science of Graphene: Metal Interfaces,CVD Synthesis, Nanoribbons, Chemical Modifications, and Defects. *Surface Science Reports*, 67(3-4):83–115, 2012. ISSN 0167-5729. doi: 10.1016/j.surfrep.2011.12.001.

[60] N. Levy, S. A. Burke, K. L. Meaker, M. Panlasigui, A. Zettl, F. Guinea, A. H. C. Neto, and M. F. Crommie. Strain-Induced Pseudo-Magnetic Fields Greater Than 300 Tesla in Graphene Nanobubbles. *Science*, 329:544–547, 2010. doi: 10.1126/science.1191700.

[61] S. Bhowmick and V. B. Shenoy. Edge state magnetism of single layer graphene nanostructures. *J. Chem. Phys.*, 128:244717, 2008. doi: 10.1063/1.2943678.

[62] C. N. R. Rao and A. K. Sood. *Graphene: Synthesis, Properties, and Phenomena*. Wiley, 2012.

[63] O. V. Yazyev and L. Helm. Defect-induced magnetism in graphene. *Phys. Rev. B*, 75(12), 2007. doi: 10.1103/PhysRevB.75.125408.

[64] M. Casartelli, S. Casolo, G. F. Tantardini, and R. Martinazzo. Spin coupling around a carbon atom vacancy in graphene. *Phys. Rev. B*, 88:195424, 2013. doi: 10.1103/PhysRevB.88.195424.

[65] B. Wang and S. T. Pantelides. Magnetic moment of a single vacancy in graphene and semiconducting nanoribbons. *Phys. Rev. B*, 86:165438, 2012. doi: 10.1103/PhysRevB.86.165438.

[66] J. J. Palacios and F. Ynduráin. Critical analysis of vacancy-induced magnetism in monolayer and bilayer graphene. *Phys. Rev. B*, 85:245443, 2012. doi: 10.1103/PhysRevB.85.245443.

[67] R. J. Young, I. A. Kinloch, L. Gong, and K. S. Novoselov. The Mechanics of Graphene Nanocomposites: a Review. *Compos. Sci. Technol.*, 72:1459–1476, 2012. doi: 10.1016/j.compscitech.2012.05.005.

[68] Y. Kim, J. Lee, M. S. Yeom, J. W. Shin, H. Kim, Y. Cui, J. W. Kysar, J. Hone, Y. Jung, S. Jeon, and S. M. Han. Strengthening Effect of Single-atomic-layer Graphene in Metal-graphene Nanolayered Composites. *Nat. Commun.*, 4(2114), 2013. doi: 10.1038/ncomms3114.

[69] Y. C. Yang, W. Rigdon, X. Y. Huang, and X. D. Li. Enhancing Graphene Reinforcing Potential in Composites by Hydrogen Passivation Induced Dispersion. *Sci. Rep*, 3 (2086), 2013. doi: 10.1038/srep02086.

[70] K. S. Kim, Y. Zhao, H. Jang, S. Y. ALee, J. M. Kim, K. S. Kim, J.-H. Ahn, P. Kim, J.-Y. Choi, and B. H. Hong. Large-scale pattern growth of graphene films for stretchable transparent electrodes. *Nature*, 457:706–710, 2009. doi: 10.1038/nature07719.

[71] T. Zhu and J. Li. Ultra-strength Materials. *Prog. Mater. Sci.*, 55:710–757, 2010. doi: 10.1016/j.pmatsci.2010.04.001.

[72] J. S. Bunch, A. M. van der Zande, S. S. Verbridge, I. W. Frank, D. M. Tanenbaum, J. M. Parpia, H. G. Craighead, and P. L. McEuen. Electromechanical Resonators from Graphene Sheets. *Science*, 315(5811):490–493, 2007. doi: 10.1126/science.1136836.

[73] V. Sorkin and Y. W. Zhang. Graphene-based Pressure Nano-sensors. *J. Mol. Model.*, 17(11):2825–2830, 2011. doi: 10.1007/s00894-011-0972-0.

[74] J. A. Aronovitz and T. C. Lubensky. Fluctuations of solid membranes. *Phys. Rev. Lett.*, 60:2634, 1988. doi: 10.1103/PhysRevLett.60.2634.

[75] D. Nelson, T. Piran, and S. Weinberg. Statistical Mechanics of Membranes and Surfaces. *World Scientific Singapore*, 2004. doi: 10.1002/actp.1990.010410813.

[76] L.D. Landau and E.M. Lifshitz. *Theory of Elasticity*. Pergamon Press, 1970.

[77] J.-W. Jiang, Wang B.-S., J.-S. Wang, and H. S. Park. A Review on the Flexural Mode of Graphene: Lattice Dynamics, Thermal Conduction, Thermal Expansion, Elasticity and Nanomechanical Resonance. *J. Phys. Condens. Matter*, 27(8):083001, 2015.

[78] H. Ochoa, F. Guinea, and V. I. Fal'ko. Spin Memory and Spin-lattice Relaxation in Two-dimensional Hexagonal Crystals. *Phys. Rev. B*, 88:195417, 2013. doi: 10.1103/PhysRevB.88.195417.

[79] F. Liu, P. Ming, and J. Li. *Ab initio* calculation of ideal strength and phonon instability of graphene under tension. *Phys. Rev. B*, 76:064120, 2007. doi: 10.1103/PhysRevB.76.064120.

[80] A. A. Griffith. The phenomena of rupture and flow in solids. *Phil. Trans. R. Soc. London A*, 221:163–198, 1921. doi: 10.1098/rsta.1921.0006.

[81] B. Lawn. *Fracture of Brittle Solids*. Cambridge Univ. Press, 1993.

[82] P. Zhang, L. Ma, F. Fan, Z. Zeng, C. Peng, P. E. Loya, Z. Liu, Y. Gong, J. Zhang, X. Zhang, P. M. Ajayan, T. Zhu, and J. Lou. Fracture toughness of graphene. *Nat. Commun.*, 5, 2014. doi: 10.1038/ncomms4782.

[83] Y. Hwangbo, C.-K. Lee, S.-M. Kim, J.-H. Kim, K.-S. Kim, B. Jang, H.-J. Lee, S.-K. Lee, S.-S. Kim, J.-H. Ahn, and S.-M. Lee. Fracture Characteristics of Monolayer CVD-Graphene. *Sci. Rep.*, 4(4439), 2014. doi: 10.1038/srep04439.

[84] G. Giovannetti, P. A. Khomyakov, G. Brocks, V. M. Karpan, J. van den Brink, and P. J. Kelly. Doping graphene with metal contacts. *Phys. Rev. Lett.*, 101(2), 2008. doi: {10.1103/PhysRevLett.101.026803}.

[85] K. S. Mali, J. Greenwood, J. J. Adisoejoso, R. Phillipson, and S. De Feyter. Nanostructuring graphene for controlled and reproducible functionalization. *Nanoscale*, 7: 1566–1585, 2015. doi: 10.1039/C4NR06470D.

[86] S. Bae, H. Kim, Y. Lee, X. Xu, J. S. Park, Y. Zheng, J. Balakrishnan, T. Lei, H. R. Kim, Y. I. Song, Y. J. Kim, K. S. Kim, B. Ozyilmaz, J. H. Ahn, B. H. Hong, and S. Iijima. Roll-to-roll Production of 30-inch Graphene Films for Transparent Electrodes. *Nat. Nanotechnol.*, 5(8):574–578, 2010. doi: 10.1038/nnano.2010.132.

[87] A. J. Martínez-Galera, I. Brihuega, and J. M. Gómez-Rodríguez. Ethylene irradiation: A new route to grow graphene on low reactivity metals. *Nano Lett.*, 11(9):3576–3580, 2011. doi: 10.1021/nl201281m.

[88] B. Kiraly, E. V. Iski, A. J. Mannix, B. L. Fisher, M. C. Hersam, and N. P. Guisinger. Solid-source Growth and Atomic-scale Characterization of Graphene on Ag(111). *Nat. Commun.*, 4(2804), 2013. doi: 10.1038/ncomms3804.

[89] B. Lang. A LEED Study of the Deposition of Carbon on Platinum Crystal Surfaces. *Surf. Sci.*, 53(1):317–329, 1975. doi: 10.1016/0039-6028(75)90132-6.

[90] T. A. Land, T. Michely, R. J. Behm, J. C. Hemminger, and G. Comsa. STM Investigation of Single Layer Graphite Structures Produced on Pt(111) by Hydrocarbon Decomposition. *Surf. Sci.*, 263(3):261–270, 1992. doi: 10.1016/0039-6028(92)90183-7.

[91] E. Soy, Z. Liang, and M. Trenary. Formation of Pt and Rh Nanoclusters on a Graphene Moiré Pattern on Cu(111). *J. Phys. Chem. C*, 119(44):24796–24803, 2015. doi: 10.1021/acs.jpcc.5b06472.

[92] E. Miniussi, M. Pozzo, A. Baraldi, E. Vesselli, R. R. Zhan, G. Comelli, T. O. Menteş, M. A. Niño, A. Locatelli, S. Lizzit, and D. Alfè. Thermal Stability of Corrugated Epitaxial Graphene Grown on Re(0001). *Phys. Rev. Lett.*, 106:216101, 2011. doi: 10.1103/PhysRevLett.106.216101.

[93] S. Marchini, S. Günther, and J. Wintterlin. Scanning tunneling microscopy of graphene on Ru(0001). *Phys. Rev. B*, 76(7):075429, 2007. doi: 10.1103/PhysRevB.76.075429.

[94] D. Eom, D. Prezzi, K. T. Rim, H. Zhou, M. Lefenfeld, S. Xiao, C. Nuckolls, M. S. Hybertsen, T. F. Heinz, and G. W. Flynn. Structure and Electronic Properties of Graphene Nanoislands on Co(0001). *Nano Lett.*, 9(8):2844–2848, 2009. doi: 10.1021/nl900927f.

[95] J. Lahiri, Y. Lin, P. Bozkurt, II Oleynik, and M. Batzill. An Extended Defect in Graphene as a Metallic Wire. *Nat. Nanotechnol.*, 5:326–329, 2010. doi: 10.1038/nnano.2010.53.

[96] A. Martín-Recio, C. Romero-Muñiz, A. J. Mart'inez-Galera, P. Pou, R. Pérez, and J. M. Gómez-Rodríguez. Tug-of-war between Corrugation and Binding Energy: Revealing the Formation of Multiple Moiré Patterns on a Strongly Interacting Graphene-metal System. *Nanoscale*, 7:11300–11309, 2015. doi: 10.1039/C5NR00825E.

[97] A. T. N'Diaye, J. Coraux, T. N. Plasa, C. Busse, and T. Michely. Structure of Epitaxial Graphene on Ir(111). *New J. Phys.*, 10(4):043033, 2008. doi: 10.1088/1367-2630/10/4/043033.

[98] J. Coraux, A. T. N'Diaye, M. Engler, C. Busse, D. Wall, N. Buckanie, F.-J. Meyer zu Heringdorf, R. van Gastel, B. Poelsema, and T. Michely. Growth of graphene on Ir(111). *New J. Phys.*, 11(2):023006, 2009. doi: 10.1088/1367-2630/11/2/023006.

[99] E. Loginova, S. Nie, K. Thürmer, N. C. Bartelt, and K. F. McCarty. Defects of Graphene on Ir(111): Rotational Domains and Ridges. *Phys. Rev. B*, 80:085430, 2009. doi: 10.1103/PhysRevB.80.085430.

[100] S.-Y. Kwon, C. V. Ciobanu, V. Petrova, V. B. Shenoy, J. Bareño, V. Gambin, I. Petrov, and S. Kodambaka. Growth of Semiconducting Graphene on Palladium. *Nano Lett.*, 9(12):3985–3990, 2009. doi: 10.1021/nl902140j.

[101] P. Merino, M. Švec, A. L. Pinardi, G. Otero, and J. A. Martín-Gago. Strain-driven moiré superstructures of epitaxial graphene on transition metal surfaces. *ACS Nano*, 5(7):5627–5634, 2011. doi: 10.1021/nn201200j.

[102] Y. Baskin and L. Meyer. Lattice Constants of Graphite at Low Temperatures. *Phys. Rev.*, 100:544–544, 1955. doi: 10.1103/PhysRev.100.544.

[103] J. D. Bernal. The structure of graphite. *Proc. Roy. Soc. A*, 106(740):749–773, 1924. doi: 10.1098/rspa.1924.0101.

[104] M. Terrones, A. R. Botello-Méndez, J. Campos-Delgado, F. L'opez-Urías, Y. I. Vega-Cantúd, F. J. Rodríguez-Macías, A. L. Elías, E. Muñoz Sandoval, A. G. Cano-Márquez, J.-C. Charlier, and Terrones H. Graphene and Graphite Nanoribbons: Morphology, Properties, Synthesis, Defects and Applications. *Nano Today*, 5:351–372, 2010. doi: 10.1016/j.nantod.2010.06.010.

[105] V. Georgakilas, M. Otyepka, A. B. Bourlinos, V. Chandra, N. Kim, K. C. Kemp, P. Hobza, R. Zboril, and K. S. Kim. Functionalization of graphene: Covalent and non-covalent approaches, derivatives and applications. *Chem. Rev.*, 112(11):6156–6214, 2012. doi: 10.1021/cr3000412.

[106] J. M. MacLeod and F. Rosei. Molecular Self-Assembly on Graphene. *Small*, 10(6): 1038–1049, 2014. doi: 10.1002/smll.201301982.

[107] A. K. Geim. Graphene: Status and Prospects. *Science*, 324(5934):1530–1534, 2009. doi: 10.1126/science.1158877.

[108] S. Yu. Davydov. On charge transfer in the adsorbed molecules-graphene monolayer-sic substrate system. *Semiconductors*, 45(5):618–622, 2011. doi: 10.1134/S1063782611050083.

[109] T. Hu and I. C. Gerber. Theoretical Study of the Interaction of Electron Donor and Acceptor Molecules with Graphene. *J. Phys. Chem. C*, 117(5):2411–2420, 2013. doi: 10.1021/jp311584r.

[110] J. O. Sofo, A. S. Chaudhari, and G. D. Barber. Graphane: A two-dimensional hydrocarbon. *Phys. Rev. B*, 75:153401, 2007. doi: 10.1103/PhysRevB.75.153401.

[111] H. J. Xiang, Su-Huai Wei, and X. G. Gong. Structural motifs in oxidized graphene: A genetic algorithm study based on density functional theory. *Phys. Rev. B*, 82:035416, 2010. doi: 10.1103/PhysRevB.82.035416.

[112] J. Zhou, M. M. Wu, X. Zhou, and Q. Sun. Tuning electronic and magnetic properties of graphene by surface modification. *Applied Physics Letters*, 95(10), 2009. doi: 10.1063/1.3225154.

[113] G. Profeta, M. Calandra, and F. Mauri. Phonon-mediated Superconductivity in Graphene by Lithium Deposition. *Nat. Phys.*, 8:131–134, 2012. doi: 10.1038/nphys2181.

[114] K.-H. Jin, S.-M. Choi, and S.-H. Jhi. Crossover in the adsorption properties of alkali metals on graphene. *Phys. Rev. B*, 82:033414, 2010. doi: 10.1103/PhysRevB.82.033414.

[115] S.-M. Choi and S.-H. Jhi. Self-assembled metal atom chains on graphene nanoribbons. *Phys. Rev. Lett.*, 101:266105, 2008. doi: 10.1103/PhysRevLett.101.266105.

[116] Y. Liu, Y. M. Wang, B. I. Yakobson, and B. C. Wood. Assessing carbon-based anodes for lithium-ion batteries: A universal description of charge-transfer binding. *Phys. Rev. Lett.*, 113:028304, 2014. doi: 10.1103/PhysRevLett.113.028304.

[117] J. Zhou, S. Zhang, Q. Wang, Y. Kawazoed, and P. Jena. Self-assembly of Metal Atoms (Na, K, Ca) on Graphene. *Nanoscale*, 2:2352, 2015. doi: 10.1039/c4nr05990e.

[118] M. Garnica, D. Stradi, S. Barja, F. Calleja, C Díaz, M. Alcamí, N. Martín, A. L. Vázquez de Parga, F. Martín, and R. Miranda. Long-range Magnetic Order in a Purely Organic 2D Layer Adsorbed on Epitaxial Graphene. *Nat. Phys.*, 9:368–374, 2013. doi: 10.1038/nphys2610.

[119] A. J. Martínez-Galera, N. Nicoara, J. I. Martínez, Y. J. Dappe, J. Ortega, and J. M. Gómez-Rodríguez. Imaging Molecular Orbitals of PTCDA on Graphene on Pt(111): Electronic Structure by STM and First-principles Calculations. *J. Phys. Chem. C*, 118 (24):12782–12788, 2014. doi: 10.1021/jp500768y.

[120] P. Song, C. S. S. Sangeeth, D. Thompson, W. Du, K. P. Loh, and C. A. Nijhuis. Molecular Electronics: Noncovalent Self-Assembled Monolayers on Graphene as a Highly Stable Platform for Molecular Tunnel Junctions. *Adv. Mater.*, 28(4):784–784, 2016. doi: 10.1002/adma.201670028.

[121] A. L. Vázquez de Parga, F. Calleja, B. Borca, M. C. G. Passeggi, J. J. Hinarejos, F. Guinea, and R. Miranda. Periodically Rippled Graphene: Growth and Spatially Resolved Electronic Structure. *Phys. Rev. Lett.*, 100:056807, 2008. doi: 10.1103/PhysRevLett.100.056807.

[122] S. T. Skowron, I. V. Lebedeva, A. M. Popov, and E. Bichoutskaia. Energetics of atomic scale structure changes in graphene. *Chem. Soc. Rev.*, 44:3143, 2015. doi: 10.1039/C4CS00499J.

[123] M. Acik and Y. J. Chabal. Nature of Graphene Edges: A Review. *Jpn. J. App. Phys.*, 50: 070101, 2011. doi: 10.1143/JJAP.50.070101.

[124] B. C. Wood, T. Ogitsu, M. Otani, and J. Biener. First-Principles-Inspired Design Strategies for Graphene-Based Supercapacitor Electrodes. *J. Phys. Chem. C*, 118(1): 4–15, 2014. doi: 10.1021/jp4044013.

[125] Z. E. Hughes and T. R. Walsh. Computational Chemistry for Graphene-based Energy Applications: Progress and Challenges. *Nanoscale*, 7:6883–6908, 2015. doi: 10.1039/C5NR00690B.

[126] A. W. Robertson, C. S. Allen, Y. A. Wu, K. He, J. Olivier, J. Neethling, A. I. Kirkland, and J. H. Warner. Spatial control of defect creation in graphene at the nanoscale. *Nat. Commun.*, 3:1144, 2012. doi: 10.1038/ncomms2141.

[127] G. López-Polín, C. Gómez-Navarro, V. Parente, F. Guinea, M. I. Katsnelson, F. Pérez-Murano, and J. Gómez-Herrero. Increasing the elastic modulus of graphene by controlled defect creation. *Nat. Phys.*, 11(1):2631, 2015. doi: {10.1038/NPHYS3183}.

[128] O. V. Yazyev. A Guide to the Design of Electronic Properties of Graphene Nanoribbons. *Acc. Chem. Res.*, 46:2319–2328, 2013. doi: 10.1021/ar3001487.

[129] P. Koskinen, S. Malola, and H. Häkkinen. Evidence for Graphene Edges Beyond Zigzag and Armchair. *Phys. Rev. B*, 80:073401, 2009. doi: 10.1103/PhysRevB.80.073401.

[130] M. Fujita, K. Wakabayashi, K. Nakada, and K. Kusakabe. Peculiar Localized State at Zigzag Graphite Edge. *P. J. Phys. Soc. Jpn.*, 65:1920–1923, 1996. doi: 10.1143/jpsj.65.1920.

[131] K. Wakabayashi, M. Fujita, H. Ajiki, and M. Sigrist. Electronic and Magnetic Properties of Nanographite Ribbons. *Phys. Rev. B*, 59:8271–8282, 1999. doi: 10.1103/PhysRevB.59.8271.

[132] Y. Miyamoto, K. Nakada, and M. Fujita. First-principles study of edge states of H-terminated graphitic ribbons. *F. Phys. Rev. B*, 59:9858–9861, 1999. doi: 10.1103/PhysRevB.59.9858.

[133] Y. Kobayashi, K. Fukui, T. Enoki, K. Kusakabe, and Y. Kaburagi. Observation of zigzag and armchair edges of graphite using scanning tunneling microscopy and spectroscopy. *Phys. Rev. B*, 71:193406, 2005. doi: 10.1103/PhysRevB.71.193406.

[134] Y. Niimi, T. Matsui, H. Kambara, K. Tagami, M. Tsukada, and H. Fukuyama. Scanning Tunneling Microscopy and Spectroscopy of the Electronic Local Density of States of Graphite Surfaces Near Monoatomic Step Edges. *Phys. Rev. B*, 73:085421, 2006. doi: 10.1103/PhysRevB.73.085421.

[135] Y. W. Son, M. L. Cohen, and S. G. Louie. Half-metallic Graphene Nanoribbons. *Nature*, 444:347, 2006. doi: 10.1038/nature05180.

[136] D. Jiang, B. G. Sumpter, and Dai S. Unique Chemical Reactivity of a Graphene Nanoribbon's Zigzag Edge. *J. Chem. Phys.*, 126:134701, 2007. doi: 10.1063/1.2715558.

[137] M. Gmitra, S. Konschuh, C. Ertler, C. Ambrosch-Draxl, and J. Fabian. Band-structure Topologies of Graphene: Spin-orbit Coupling Effects from First Principles. *Phys. Rev. B*, 80:235431, 2009. doi: 10.1103/PhysRevB.80.235431.

[138] A. A. El-Barbary, R. H. Telling, C. P. Ewels, M. I. Heggie, and P. R. Briddon. Structure and energetics of the vacancy in graphite. *Phys. Rev. B*, 68:144107, 2003. doi: 10.1103/PhysRevB.68.144107.

[139] Y. Ma, P. O. Lehtinen, A. S. Foster, and R. M. Nieminen. Magnetic properties of vacancies in graphene and single-walled carbon nanotubes. *New Journal of Physics*, 6:68, 2004. doi: 10.1088/1367-2630/6/1/068.

[140] A. J. Martínez-galera and J. M. Gómez-Rodríguez. Nucleation and Growth of the Prototype Azabenzene 1, 3, 5-Triazine on Graphite Surfaces at Low Temperatures. *J. Phys. Chem. C*, 115:11089–11094, 2011. doi: 10.1021/jp200613c.

[141] A. J. Martínez-Galera and J. M. Gómez-Rodríguez. Surface Diffusion of Simple Organic Molecules on Graphene on Pt(111). *J. Phys. Chem. C*, 115(46):23036–23042, 2011. doi: 10.1021/jp208026u.

[142] S. Grimme. Semiempirical GGA-Type Density Functional Constructed with a Long-Range Dispersion Correction. *J. Comput. Chem.*, 27:1787–1799, 2006. doi: 10.1002/jcc.20495.

[143] S. Grimme, S. Ehrlich, and L. Goerigk. Effect of the damping function in dispersion corrected density functional theory. *J. Comput. Chem.*, 32:1456–1465, 2011. doi: 10.1002/jcc.21759.

[144] J. Klimeš, D. R. Bowler, and A. Michaelides. Chemical Accuracy for the Van der Waals Density Functional. *J. Phys.: Condens. Matter*, 22:022201, 2010. doi: 10.1088/0953-8984/22/2/022201.

[145] A. Tkatchenko, R. A. DiStasio, R. Car, and M. Scheffler. Accurate and Efficient Method for Many-Body Van der Waals Interactions. *Phys. Rev. Lett.*, 108:236402, 2012. doi: 10.1103/PhysRevLett.108.236402.

[146] A. Ambrosetti, A. M. Reilly, R. A. DiStasio, and A. Tkatchenko. Long-Range Correlation Energy Calculated from Coupled Atomic Response Functions. *J. Chem. Phys.*, 140:18A508, 2014. doi: 10.1063/1.4865104.

[147] A. Tkatchenko. Current Understanding of Van der Waals Effects in Realistic Materials. *Adv. Funct. Mater.*, 25:2054–2061, 2015. doi: 10.1002/adfm.201403029.

[148] E. Schrödinger. An undulatory theory of the mechanics of atoms and molecules. *Phys. Rev.*, 28:1049–1070, 1926. doi: 10.1103/PhysRev.28.1049.

[149] M. Born and R. Oppenheimer. Zur Quantentheorie de Molekeln. *Annalen der Physik*, 398:457–484, 1927. doi: 10.1002/andp.19273892002.

[150] P. Hohenberg and W. Kohn. Inhomogeneous Electron Gas. *Phys. Rev.*, 136, 1964. doi: 10.1103/PhysRev.136.B864.

[151] W. Kohn and L. J. Sham. Self Consistent Equations Including Exchange and Correlation Effects. *Phys. Rev.*, 140:A1133, 1965. doi: 10.1103/PhysRev.140.A1133.

[152] Y. Kipnis, B. E. Yavelov, and J. S. Rowlinson. *Van der Waals and Molecular Sciences*. Clarendon Press/Oxford University Press, Oxford, 1996.

[153] G. Kresse and J. Furthmüller. Efficient Iterative Schemes for ab Initio Total-Energy Calculations Using a Plane-Wave Basis Set. *Phys. Rev. B*, 54:11169, 1996. doi: 10.1103/PhysRevB.54.11169.

[154] T. Ozaki. Variationally Optimized Atomic Orbitals for Large-Scale Electronic Structures. *Phys. Rev. B*, 67:155108, 2003. doi: 10.1103/PhysRevB.67.155108.

[155] T. Ozaki and H. Kino. Numerical atomic oasis orbitals from h to kr. *Phys. Rev. B*, 69:195113, 2004. doi: 10.1103/PhysRevB.69.195113.

[156] D. C. Langreth and J. P. Perdew. Theory of Nonuniform Electronic Systems I. Analysis of the Gradient Approximation and a Generalization that Works. *Phys. Rev. B*, 21, 1979. doi: 10.1103/PhysRevB.21.5469.

[157] J. P. Perdew and K. Schmidt. Jacob's Ladder of Density Functional Approximations for the Exchange-Correlation Energy. *AIP Conf. Proc.*, 577, 2001. doi: 10.1063/1.1390175.

[158] J. P. Perdew and Y. Wang. Accurate and Simple Analytic Representation of the Electron-Gas Correlation Energy. *Phys. Rev. B*, 45:13244, 1992. doi: 10.1103/PhysRevB.45.13244.

[159] J. P. Perdew, K. Burke, and M. Ernzerhof. Generalized Gradient Approximation Made Simple. *Phys. Rev. Lett.*, 77:3865, 1996. doi: 10.1103/PhysRevLett.77.3865.

[160] Axel D. Becke. A New Mixing of Hartree-Fock and Local Density Functional Theories. *J. Chem. Phys.*, 98:1372, 1993. doi: 10.1063/1.464304.

[161] J. P. Perdew, M. Ernzerhof, and K. Burke. Rationale for Mixing Exact Exchange with Density Functional Approximations. *J. Chem. Phys.*, 105:9982, 1996. doi: 10.1063/1.472933.

[162] C. Adamo and V. Barone. Toward Reliable Density Functional Methods without Adjustable Parameters: The PBE0 Model. *J. Chem. Phys.*, 110:6158, 1999. doi: 10.1063/1.478522.

[163] A. V. Krukau, O. A. Vydrov, A. F. Izmaylov, and G. E. Scuseria. Influence of the Exchange Screening Parameter on the Performance of Screened Hybrid Functionals. *J. Chem. Phys.*, 125:224106, 2006. doi: 10.1063/1.2404663.

[164] J. Heyd and G. E. Scuseria. Assessment and Validation of a Screened Coulomb Hybrid Density Functional. *J. Chem. Phys.*, 120, 2004. doi: 10.1063/1.1668634.

[165] J. Heyd and G. E. Scuseria. Efficient Hybrid Density Functional Calculations in Solids: Assessment of the Heyd-Scuseria-Ernzerhof Screened Coulomb Hybrid Functional. *J. Chem. Phys.*, 121, 2004. doi: 10.1063/1.1760074.

[166] D. Bohm and D. Pines. A Collective Description of Electron Interactions I. Magnetic Interactions. *Phys. Rev.*, 82:625–634, 1951. doi: 10.1103/PhysRev.82.625.

[167] D. Bohm and D. Pines. A Collective Description of Electron Interactions II. Collective vs Individual Particle Aspects of the Interactions. *Phys. Rev.*, 85:338–353, 1952. doi: 10.1103/PhysRev.85.338.

[168] D. Bohm and D. Pines. A Collective Description of Electron Interactions III. Coulomb Interactions in a Degenerate Electron Gas. *Phys. Rev.*, 92:609–625, 1953. doi: 10.1103/PhysRev.92.609.

[169] F. Furche. Molecular Tests of the Random Phase Approximation to the Exchange-Correlation Energy Functional. *Phys. Rev. B*, 64:195120, 2001. doi: 10.1103/PhysRevB.64.195120.

[170] R. Eisenschitz and F. London. Über das Verhältnis der van der Waalsschen Kräfte zu den homöopolaren Bindungskräften. *Zeitschrift für Physik*, 60:491–527, 1930. doi: 10.1007/BF01341258.

[171] K. Berland, V. R. Cooper, K. Lee, E. Schröder, T. Thonhauser, P. Hyldgaard, and B. I. Lundqvist. Van der waals forces in density functional theory: a review of the vdw-df method. *Rep. Prog. Phys.*, 78(6):066501, 2015. doi: 10.1088/0034-4885/78/6/066501.

[172] S. Grimme. Accurate Description of Van der Waals Complexes by Density Functional Theory Including Empirical Corrections. *J. Comput. Chem.*, 25:1463–1473, 2004. doi: 10.1002/jcc.20078.

[173] S. Grimme, J. Antony, S. Ehrlich, and H. Krieg. A Consistent and Accurate *Ab Initio* Parametrization of Density Functional Dispersion Correction (DFT-D) for the 94 Elements H-Pu. *J. Chem. Phys.*, 132:154104, 2010. doi: 10.1063/1.3382344.

[174] Y. Andersson, D. C. Langreth, and B. I. Lundqvist. Van der Waals Interactions in Density-Functional Theory. *Phys. Rev. Lett.*, 76:102, 1996. doi: 10.1103/PhysRevLett.76.102.

[175] K. Rapcewicz and N. Ashcroft. Fluctuation Attraction in Condensed Matter: A Nonlocal Functional Approach. *Phys. Rev. B*, 44:4032–4035, 1991. doi: 10.1103/PhysRevB.44.4032.

[176] A. Tkatchenko and M. Scheffler. Accurate Molecular Van Der Waals Interactions from Ground-State Electron Density and Free-Atom Reference Data. *Phys. Rev. Lett.*, 102:073005, 2009. doi: 10.1103/PhysRevLett.102.073005.

[177] V. G. Ruiz, W. Liu, E. Zojer, M. Scheffler, and A. Tkatchenko. Density-Functional Theory with Screened Van der Waals Interactions for the Modeling of Hybrid Inorganic-Organic Systems. *Phys. Rev. Lett.*, 108:146103, 2012. doi: 10.1103/PhysRevLett.108.146103.

[178] X. Wu, M. C. Vargas, S. Nayak, V. Lotrich, and G. Scoles. Towards Extending the Applicability of Density Functional Theory to Weakly Bound Systems. *J. Chem. Phys.*, 115:8748, 2001. doi: 10.1063/1.1412004.

[179] E. Hult, Y. Andersson, B. I. Lundqvist, and D. C. Langreth. Density Functional for Van der Waals Forces at Surfaces. *Phys. Rev. Lett.*, 77:2029, 1996. doi: 10.1103/PhysRevB.64.195414.

[180] E. Hult, H. Rydberg, and B. I. Lundqvist. Unified Treatment of Asymptotic Van der Waals Forces. *Phys. Rev. B*, 59:4708, 1999. doi: 10.1103/PhysRevB.59.4708.

[181] M. Dion, H. Rydberg, E. Schröder, D. C. Langreth, and B. I. Lundqvist. Van der Waals Density Functional for General Geometries. *Phys. Rev. Lett.*, 92:246401, 2004. doi: 10.1103/PhysRevLett.92.246401.

[182] G. Román-Pérez and J. M. Soler. Efficient implementation of a van der waals density functional: Application to double-wall carbon nanotubes. *Phys. Rev. Lett.*, 103:096102, 2009. doi: 10.1103/PhysRevLett.103.096102.

[183] D. C. Langreth, B. I. Lundqvist, S. D. Chakarova-Käck, V. R. Cooper, M. Dion, P. Hyldgaard, A. Kelkkanen, J. Kleis, L. Kong, S. Li, P. G. Moses, E. Murray, A. Puzder, H. Rydberg, E. Schröder, and T. Thonhauser. A density functional for sparse matter. *J. Phys.: Condens. Matter*, 21(8):084203, 2009. doi: 10.1088/0953-8984/21/8/084203.

[184] J. Klimeš, D. R. Bowler, and A. Michaelides. Van der waals density functionals applied to solids. *Phys. Rev. B*, 83:195131, 2011. doi: 10.1103/PhysRevB.83.195131.

[185] K. Lee, É. D. Murray, L. Kong, B. I. Lundqvist, and D. C. Langreth. Higher-Accuracy Van der Waals Density Functional. *Phys. Rev. B*, 82:081101, 2010. doi: 10.1103/PhysRevB.82.081101.

[186] H. J. Monkhorst and J. D. Pack. Special Points for Brillouin-Zone Integrations. *Phys. Rev. B*, 13:5188, 1976. doi: 10.1103/PhysRevB.13.5188.

[187] D. J. Chadi and M. L. Cohen. Special Points in the Brillouin Zone. *Phys. Rev. B*, 8: 5747, 1973. doi: 10.1103/PhysRevB.13.5188.

[188] D. R. Hartree. The wave mechanics of an atom with a non-coulomb central field. part i. theory and methods. *Mathematical Proceedings of the Cambridge Philosophical Society*, 24:89–110, 1928. doi: 10.1017/S0305004100011919.

[189] C. Herring. A new method for calculating wave functions in crystals. *Phys. Rev.*, 57: 1169–1177, 1940. doi: 10.1103/PhysRev.57.1169.

[190] J. Ihm, A. Zunger, and M. L. Cohen. Momentum-space formalism for the total energy of solids. *J. Phys. C: Solid State Phys.*, 12(21):4409, 1979. doi: 10.1088/0022-3719/12/21/009.

[191] M. D. Segall, P. J. D. Lindan, M. J. Probert, C. J. Pickard, P. J. Hasnip, S. J. Clark, and M. C. Payne. First-principles Simulation: Ideas, Illustrations and the CASTEP Code. *J. Phys.: Condens. Matter*, 14(11):2717, 2002. doi: 10.1088/0953-8984/14/11/301.

[192] J. M. Soler, E. Artacho, J. D. Gale, A. García, J. Junquera, P. Ordejón, and D. Sánchez-Portal. The SIESTA Method for *ab initio* Order-N Materials Simulation. *J. Phys.: Condens. Matter*, 14(11):2745, 2002. doi: 10.1088/0953-8984/14/11/302.

[193] D. R. Bowler, T. Miyazaki, and M. J. Gillan. Recent Progress in Linear Scaling *ab initio* Electronic Structure Techniques. *J. Phys.: Condens. Matter*, 14(11):2781, 2002. doi: 10.1088/0953-8984/14/11/303.

[194] S. Goedecker. Linear scaling electronic structure methods. *Rev. Mod. Phys.*, 71: 1085–1123, 1999. doi: 10.1103/RevModPhys.71.1085.

[195] J. C. Slater. Wave Functions in a Periodic Potential. *Phys. Rev.*, 51:846, 1937. doi: 10.1103/PhysRev.51.846.

[196] P. E. Blöchl. Projector Augmented-Wave Method. *Phys. Rev. B*, 50:17953, 1994. doi: 10.1103/PhysRevB.50.17953.

[197] O. K. Andersen. Linear Methods in Band Theory. *Phys. Rev. B*, 12:3060, 1975. doi: 10.1103/PhysRevB.12.3060.

[198] E. Clementi and C. Roetti. Roothaan-hartree-fock atomic wavefunctions. In *Atomic Data and Nuclear Data Tables*, volume 14. Academic Press, New York, 1974.

[199] O. F. Sankey and D. J. Niklewski. *Ab initio* multicenter tight-binding model for molecular-dynamics simulations and other applications in covalent systems. *Phys. Rev. B*, 40:3979–3995, 1989. doi: 10.1103/PhysRevB.40.3979.

[200] P. Ordejón. Order-N Tight-binding Methods for Electronic-structure and Molecular Dynamics. *Comput. Mater. Sci.*, 12(3):157–191, 1998. doi: 10.1016/S0927-0256(98)00027-5.

[201] S. D. Shellman, , J. P. Lewis, K. R. Glaesemann, K. Sikorski, and G. A. Voth. Massively parallel linear-scaling algorithm in an *ab initio* local-orbital total-energy method. *J. Comp. Phys.*, 188(1):1–15, 2003. doi: 10.1016/S0021-9991(03)00069-X.

[202] J. Bardeen. Tunneling from a Many-Particle Point of View. *Phys. Rev. Lett.*, 6:57, 1961. doi: 10.1103/PhysRevLett.6.57.

[203] J. Tersoff and D. R. Hamann. Theory and Application for the Scanning Tunneling Microscope. *Phys. Rev. Lett.*, 102:073005, 1983. doi: 10.1103/PhysRevLett.50.1998.

[204] J. Tersoff and D. R. Hamann. Theory of the Scanning Tunneling Microscope. *Phys. Rev. B*, 31:805, 1985. doi: 10.1016/j.sna.2005.02.036.

[205] J. M. Blanco Ramos. *Estudio teórico del Microscopio de Efecto Túnel con métodos de primeros principios*. PhD thesis, Universidad Autónoma de Madrid, 2004.

[206] L. V. Keldysh. Diagram Technique for Nonequilibrium Processes. *Sov. Phys. JETP*, 20:1018, 1965.

[207] G. Schmaltz. Über Glätte und Ebenheit als physikalisches und physiologisches Problem. *Zeitschrift des Vereins Deutscher Ingenieure*, 12:1461–1467, 1929.

[208] R. Young, J. Ward, and F. Scire. The topografiner: an instrument for measuring surface micro-topography. *Review of Scientific Instruments*, 43:999–1011, 1972. doi: 10.1063/1.1685846.

[209] R. H. Fowler and L. Nordheim. Electron Emission in Intense Electric Fields. *Proc. R. Soc. Lond. A*, 119(781):173–181, 1928. doi: 10.1098/rspa.1928.0091.

[210] G. Binning and H. Rohrer. Scanning Tunneling Microscopy. *Helv. Phys. Acta*, 55: 726–735, 1982. doi: 10.1147/rd.441.0279.

[211] R. P. Feynman. Feynman and computation. chapter There's Plenty of Room at the Bottom, pages 63–76. Perseus Books, Cambridge, MA, USA, 1999. ISBN 0-7382-0057-3.

[212] E. Ruska. *Ernst Ruska Autobiography*. Nobel Foundation. Retrieved 2010-01-31, 1986.

[213] M. M. Freundlich. Origin of the Electron Microscope. *Science*, 142:185–188, 1963. doi: 10.1126/science.142.3589.185.

[214] G. Binnig and H. Rohrer. In Touch with Atoms. *Rev. Mod. Phys.*, 71:S324–S330, 1999. doi: 10.1103/RevModPhys.71.S324.

[215] C. J. Chen. *Introduction to Scanning Tunneling Microscopy*. Oxford University Press, 1993.

[216] C. Bai. *Scanning Tunneling Microscopy and its Applications*. New York: Springer Verlag, 2000.

[217] S. H. Pan, E. W. Hudson, K. M. Lang, H. Eisaki, S. Uchida, and J. C. Davis. Imaging the Effects of Individual Zinc Impurity Atoms on Superconductivity in $Bi_2Sr_2CaCu_2O_{8+\delta}$. *Nature*, 403:746–750, 2000. doi: 10.1038/35001534.

[218] J.-M. Jancu, J.-Ch. Girard, M. O. Nestoklon, A. Lemaître, F. Glas, Z. Z. Wang, and P. Voisin. STM Images of Subsurface Mn Atoms in GaAs: Evidence of Hybridization of Surface and Impurity States. *Phys. Rev. Lett.*, 101:196801, 2008. doi: 10.1103/PhysRevLett.101.196801.

[219] Zhanybek Alpichshev, Rudro R. Biswas, Alexander V. Balatsky, J. G. Analytis, J.-H. Chu, I. R. Fisher, and A. Kapitulnik. STM Imaging of Impurity Resonances on Bi_2Se_3. *Phys. Rev. Lett.*, 108:206402, 2012. doi: 10.1103/PhysRevLett.108.206402.

[220] G. Binnig, H. Fuchs, Ch. Gerber, E. Stoll, and E. Tosatti. Energy-Dependent State-Density Corrugation of a Graphite Surface as Seen by Scanning Tunneling Microscopy. *Europhys. Lett.*, 1:31–36, 1986. doi: 10.1209/0295-5075/1/1/005.

[221] S.-I. Park and C.F. Quate. Tunneling Microscopy of Graphite in Air. *Appl. Phys. Lett.*, 48:112, 1986. doi: 10.1103/PhysRevB.34.4979.

[222] R. Sonnenfeld and P.K. Hansma. Atomic-Resolution Microscopy in Water. *Science*, 232:211, 1986. doi: 10.1126/science.232.4747.211.

[223] G. M. Rutter, N. P. Guisinger, J. N. Crain, E. A. A. Jarvis, M. D. Stiles, T. Li, P. N. First, and J. A. Stroscio. Imaging the Interface of Epitaxial Graphene with Silicon Carbide via Scanning Tunneling Microscopy. *Phys. Rev. B*, 76:235416, 2007. doi: 10.1103/PhysRevB.76.235416.

[224] M. Ishigami, J. H. Chen, W. G. Cullen, M. S. Fuhrer, and E. D. Williams. Atomic Structure of Graphene on SiO_2. *Nano Lett.*, 7(6):1643–1648, 2007. doi: 10.1021/nl070613a.

[225] L. Tapasztó, G. Dobrik, P. Lambin, and L. P. Biró. Tailoring the Atomic Structure of Graphene Nanoribbons by Scanning Tunnelling Microscope Lithography. *Nature Nanotechnology*, 3:397–401, 2008. doi: 10.1038/nnano.2008.149.

[226] J. I. Pascual, J. Gómez-Herrero, C. Rogero, A. M. Baró, D. Sánchez-Portal, E. Artacho, P. Ordejón, and J. M. Soler. Seeing Molecular Orbitals. *Chem. Phys. Lett.*, 321(1-2):78–82, 2000. doi: 10.1016/S0009-2614(00)00337-7.

[227] G. Binning, C. F. Quate, and C. Gerber. Atomic Force Microscope. *Phys. Rev. Lett.*, 56:930, 1986. doi: 10.1103/PhysRevLett.56.930.

[228] F. J. Giessibl. Atomic Resolution of the Silicon (111)-(7×7) Surface by Atomic Force Microscopy. *Science*, 267:68–71, 1995. doi: 10.1126/science.267.5194.68.

[229] S. Kitamura and M. Iwatsuki. Observation of 7×7 Reconstructed Structure on the Silicon (111) Surface using Ultrahigh Vacuum Noncontact Atomic Force Microscopy. *Jpn. J. Appl. Phys.*, 34:145–148, 1995. doi: 10.1143/JJAP.34.L145.

[230] Y. Sugimoto, P. Pou, M. Abe, P. Jelínek, R. Pérez, S. Morita, and O. Custance. Chemical Identification of Individual Surface Atoms by Atomic Force Microscopy. *Nature*, 446(7131):64–67, 2007. doi: 10.1038/nature05530.

[231] L. Gross, F. Mohn, N. Moll, P. Liljeroth, and G. Meyer. The Chemical Structure of a Molecule Resolved by Atomic Force Microscopy. *Science*, 325:1110–1114, 2009. doi: 10.1126/science.267.5194.68.

[232] D. G. de Oteyza, P. Gorman, Y.-C. Chen, S. Wickenburg, A. Riss, D. J. Mowbray, G. Etkin, Z. Pedramrazi, H.-Z. Tsai, A. Rubio, M. F. Crommie, and F. R. Fischer. Direct Imaging of Covalent Bond Structure in Single-Molecule Chemical Reactions. *Science*, 340:1434–1437, 2013. doi: 10.1126/science.1238187.

[233] T. Sakurai and Y. Watanabe. *Advances in Scanning Probe Microscopy*. Springer-Verlag Berlin Heidelberg, 2000.

[234] R. Garcıía and R. Pérez. Dynamic Atomic Force Microscopy Methods. *Surface Science Reports*, 47(6–8):197–301, 2002. doi: 10.1016/S0167-5729(02)00077-8.

[235] F. J. Giessibl. Advances in Atomic Force Microscopy. *Rev. Mod. Phys.*, 75:949–983, 2003. doi: 10.1103/RevModPhys.75.949.

[236] R. Pérez, R. García, and U. Schwarz. High-resolution Noncontact Atomic Force Microscopy. *Nanotechnology*, 20(26):260201, 2009. doi: 10.1088/0957-4484/20/26/260201.

[237] P. Eaton and P. West. *Atomic Force Microscopy*. Oxford University Press, Oxford, 2010.

[238] Y. Sugimoto, P. Pou, O. Custance, P. Jelínek, M. Abe, R. Pérez, and S. Morita. Complex Patterning by Vertical Interchange Atom Manipulation Using Atomic Force Microscopy. *Science*, 322(5900):413–417, 2008. doi: 10.1126/science.1160601.

[239] O. Custance, R. Pérez, and S. Morita. Atomic Force Microscopy as a Tool for Atom Manipulation. *Nat. Nano.*, 4(12):803–810, 2009. doi: 10.1038/nnano.2009.347.

[240] C. H. Lui, L. Liu, K. F. Mak, G. W. Flynn, and T. F. Heinz. Ultraflat Graphene. *Nature*, 462(7271):339–341, 2009. doi: 10.1038/nature08569.

[241] M. P. Boneschanscher, J. Van der Lit, Z. Sun, I. Swart, P. Liljeroth, and D. Vanmaekelbergh. Quantitative Atomic Resolution Force Imaging on Epitaxial Graphene with Reactive and Nonreactive AFM Probes. *ACS Nano*, 6:10216–10221, 2012. doi: 10.1021/nn3040155.

[242] J. van der Lit, M. P. Boneschanscher, D. Vanmaekelbergh, M. Ijäs, A. Uppstu, M. Ervasti, A. Harju, P. Liljeroth, and I. Swart. Suppression of Electron-Vibron Coupling in Graphene Nanoribbons Contacted via a Single Atom. *Nat. Commun.*, 4, 2013. doi: 10.1038/ncomms3023.

[243] L. Liu, M. Qing, Y. Wang, and S. Chen. Defects in Graphene: Generation, Healing, and Their Effects on the Properties of Graphene: A Review. *J. Mater. Sci. Technol.*, 31 (6):599–606, 2015. doi: 10.1016/j.jmst.2014.11.019.

[244] C. Davisson and L. H. Germer. Diffraction of Electrons by a Crystal of Nickel. *Phys. Rev.*, 30:705, 1927. doi: 10.1103/PhysRev.30.705.

[245] L. de Broglie. Recherches sur la théorie des quanta. *Annales de Physique*, 10:22–128, 1925. doi: 10.1119/1.1986821.

[246] M. A. Van Hove, W. H. Weinberg, and C.-M. Chan. *Low-Energy Electron Diffraction: Experiment, Theory and Surface Structure Determination*. Springer Berlin Heidelberg, 1986.

[247] A. J. Martínez Galera. *Nucleación, crecimiento y nanoestructuración en grafeno epitaxial sobre metales*. PhD thesis, Universidad Autónoma de Madrid, 2012.

[248] Aberration correction for tem.

[249] D. J. Smith. Development of Aberration-Corrected Electron Microscopy. *Microscopy and Microanalysis*, 14:2–15, 2 2008. doi: 10.1017/S1431927608080124.

[250] A. W. Robertson and J. H. Warner. Atomic resolution imaging of graphene by transmission electron microscopy. *Nanoscale*, 5:4079–4093, 2013. doi: 10.1039/c3nr00934c.

[251] C. Tao, L. Jiao, O. V. Yazyev, Y.-C. Chen, J. Feng, X. Zhang, R. B. Capaz, J. M. Tour, A. Zettl, S. G. Louie, Hongjie D., and M. F. Crommie. Spatially Resolving Edge States of Chiral Graphene Nanoribbons. *Nat. Phys.*, 7:616–620, 2011. doi: 10.1038/nphys1991.

[252] L. Wang, I. Meric, P. Huang, Q. Gao, Y. Gao, H. Tran, T. Taniguchi, K. Watanabe, L. Campos, and D. Muller. One-Dimensional Electrical Contact to a Two-Dimensional Material. *Science*, 342:614–617, 2013. doi: 10.1126/science.1244358.

[253] O. V. Yazyev and S. G. Louie. Electronic Transport in Polycrystalline Graphene. *Nat. Mater.*, 9:806–809, 2010. doi: 10.1038/nmat2830.

[254] P. Ruffieux, J. Cai, N. C. Plumb, L. Patthey, D. Prezzi, A. Ferretti, E. Molinari, X. Feng, K. Mullen, and C. A. et al. Pignedoli. Electronic Structure of Atomically Precise Graphene Nanoribbons. *ACS Nano*, 6:6930–6935, 2012. doi: 10.1021/nn3021376.

[255] M. Yamamoto, S. Obata, and K. Saiki. Structure and Properties of Chemically Prepared Nanographene Islands Characterized by Scanning Tunneling Microscopy. *Surf. Interface Anal.*, 42:1637–1641, 2010. doi: 10.1002/sia.3583.

[256] Y. Li, D. Subramaniam, N. Atodiresei, P. Lazić, V. Caciuc, C. Pauly, A. Georgi, C. Busse, M. Liebmann, and S. et al. Blügel. Absence of Edge States in Covalently Bonded Zigzag Edges of Graphene on Ir(111). *Adv. Mater.*, 25:1967–1972, 2013. doi: 10.1002/adma.201204539.

[257] C.-I. Chia and V. H. Crespi. Stabilizing the zigzag edge: Graphene nanoribbons with sterically constrained terminations. *Phys. Rev. Lett.*, 109:076802, 2012. doi: 10.1103/PhysRevLett.109.076802.

[258] C. O. Girit, J. C. Meyer, R. Erni, M. D. Rossell, C. Kisielowski, L. Yang, C. H. Park, M. F. Crommie, M. L. Cohen, and S. G. et al. Louie. Graphene at the Edge: Stability and Dynamics. *Science*, 323:1705–1708, 2009.

[259] K. Suenaga and M. Koshino. Atom-by-Atom Spectroscopy at Graphene Edge. *Nature*, 468:1088–1090, 2010. doi: 10.1038/nature09664.

[260] K. A. Ritter and J. W. Lyding. The Influence of Edge Structure on the Electronic Properties of Graphene Quantum Dots and Nanoribbons. *Nat. Mater.*, 8:235–242, 2009. doi: 10.1038/nmat2378.

[261] M. Ridene, J. C. Girard, L. Travers, C. David, and A. Ouerghi. STM/STS Investigation of Edge Structure in Epitaxial Graphene. *Surf. Sci.*, 606:1289–1292, 2012. doi: 10.1016/j.susc.2012.04.006.

[262] S.-H. Phark, J. Borme, A. L. Vanegas, M. Corbetta, D. Sander, and J. Kirschner. Atomic Structure and Spectroscopy of Graphene Edges on Ir(111). *Phys. Rev. B*, 86:045442, 2012. doi: 10.1103/PhysRevB.86.045442.

[263] S.-H. Phark, J. Borme, A. L. Vanegas, M. Corbetta, D. Sander, and J. Kirschner. Atomic structure and spectroscopy of graphene edges on ir(111). *Phys. Rev. B*, 86:045442, 2012. doi: 10.1103/PhysRevB.86.045442.

[264] J. Wintterlin and M. L. Bocquet. Graphene on Metal Surfaces. *Surf. Sci.*, 603:1841–1852, 2009. doi: 10.1016/j.susc.2008.08.037.

[265] I. Horcas, R. Fernandez, J. M. Gomez-Rodriguez, J. Colchero, J. Gomez-Herrero, and A. M. Baro. WSXM: a Software for Scanning Probe Microscopy and a Tool for Nanotechnology. *Rev. Sci. Instrum.*, 78:013705, 2007. doi: 10.1063/1.2432410.

[266] M. M. Ugeda, D. Fernandez-Torre, I. Brihuega, P. Pou, A. J. Martinez-Galera, Ruben Perez, and J. M. Gomez-Rodriguez. Point Defects on Graphene on Metals. *Phys. Rev. Lett.*, 107(11), 2011. doi: 10.1103/PhysRevLett.107.116803.

[267] J. M. Blanco, F. Flores, and R. Pérez. STM-Theory: Image Potential, Chemistry and Surface Relaxation. *Prog. Surf. Sci*, 81:403, 2006. doi: 10.1016/j.progsurf.2006.07.004.

[268] J. Gao, J. Yip, J. Zhao, B. I. Yakobson, and F. Ding. Graphene Nucleation on Transition Metal Surface: Structure Transformation and Role of the Metal Step Edge. *J. Am. Chem. Soc.*, 133:5009–5015, 2011. doi: 10.1021/ja110927p.

[269] K. Stokbro, M. Engelund, and A. Blom. Atomic-Scale Model for the Contact Resistance of the Nickel-Graphene Interface. *Phys. Rev. B*, 85:165442, 2012. doi: 10.1103/PhysRevB.85.165442.

[270] J. Gao, J. Zhao, and F. Ding. Transition Metal Surface Passivation Induced Graphene Edge Reconstruction. *J. Am. Chem. Soc.*, 134:6204–6209, 2012. doi: 10.1021/ja2104119.

[271] D. Gunlycke and C. T. White. Graphene Valley Filter Using a Line Defect. *Phys. Rev. Lett.*, 106:136806, 2011. doi: 10.1103/PhysRevLett.106.136806.

[272] A. Rycerz, J. Tworzydlo, and C. W. J. Beenakker. Valley Filter and Valley Valve in Graphene. *Nat. Phys.*, 3:172–175, 2007. doi: 10.1038/nphys547.

[273] A. Hashimoto, K. Suenaga, A. Gloter, K. Urita, and S. Iijima. Direct evidence for atomic defects in graphene layers. *Nature*, 430:870, 2004. doi: 10.1038/nature02817.

[274] H. Terrones, R. Lv, M. Terrones, and M. S. Dresselhaus. The role of defects and doping in 2d graphene sheets and 1d nanoribbons. *Rep. Prog. Phys.*, 75:062501, 2012. doi: 10.1088/0034-4885/75/6/062501.

[275] F. Banhart, J. Kotakoski, and A. V. Krasheninnikov. Structural defects in graphene. *ACS Nano*, 5, 2010. doi: 10.1021/nn102598m.

[276] M. Neek-Amal, , and F. M. Peeters. Linear reduction of stiffness and vibration frequencies in defected circular monolayer graphene. *Phys. Rev. B*, 81:235437, 2010. doi: 10.1103/PhysRevB.81.235437.

[277] J. C. Meyer, C. Kisielowski, R. Erni, M. D. Rossell, M. F. Crommie, and A. Zettl. Direct imaging of lattice atoms and topological defects in graphene membranes. *Nano Lett.*, 8:3582–3586, 2008. doi: 10.1021/nl801386m.

[278] A. W. Robertson, B. Montanari, K. He, C. S. Allen, Y. A. Wu, N. M. Harrison, A. I. Kirkland, and J. H. Warner. Structural reconstruction of the graphene monovacancy. *ACS Nano*, 7:4495–4502, 2013. doi: 10.1021/nn401113r.

[279] M. M. Ugeda, I. Brihuega, F. Guinea, and J. M. Gómez-Rodríguez. Missing atom as a source of carbon magnetism. *Phys. Rev. Lett.*, 104:096804, 2010. doi: {10.1103/PhysRevLett.104.096804}.

[280] T. Kondo, Y. Honma, J. Oh, T. Machida, and J. Nakamura. Edge states propagating from a defect of graphite: Scanning tunneling spectroscopy measurements. *Phys. Rev. B*, 82(153414), 2010. doi: {10.1103/PhysRevB.82.153414}.

[281] Christoph Freysoldt, Blazej Grabowski, Tilmann Hickel, Jörg Neugebauer, Georg Kresse, Anderson Janotti, and Chris G. Van de Walle. First-principles calculations for point defects in solids. *Rev. Mod. Phys.*, 86, 2014. doi: 10.1103/RevModPhys.86.253.

[282] C.-C. Lee, Y. Yamada-Takamura, and T. Ozaki. Competing magnetism in pi-electrons in graphene with a single carbon vacancy. *Phys. Rev. B*, 90(1), 2014. doi: 10.1103/PhysRevB.90.014401.

[283] J.-J. Chen, H.-C. Wu, D.-P. Yuab, and Z.-M. Liao. Magnetic moments in graphene with vacancies. *Nanoscale*, 6:8814, 2014. doi: 10.1039/c3nr06892g.

[284] E. J. G. Santos, S. Riikonen, D. Sánchez-Portal, and A. Ayuela. Magnetism of single vacancies in rippled graphene. *J. Phys. Chem. C*, 116:7602–7606, 2012. doi: 10.1021/jp300861m.

[285] N. Mounet and N. Marzari. First-principles determination of the structural, vibrational and thermodynamic properties of diamond, graphite, and derivatives. *Phys. Rev. B*, 71:205214, 2005. doi: 10.1103/PhysRevB.71.205214.

[286] D. Yoon, Y.-W. Son, and H. Cheong. Negative Thermal Expansion Coefficient of Graphene Measured by Raman Spectroscopy. *Nano Lett.*, 11:3227, 2011. doi: 10.1021/nl201488g.

[287] A. S. Fedorov, Z. I. Popov, D. A. Fedorov, N. S. Eliseeva, M. V. Serjantova, and A. A. Kuzubov. DFT investigation of the influence of ordered vacancies on elastic and magnetic properties of graphene and graphene-like SiC and BN structures. *Phys. Status Solidi B*, 249:2549, 2012.

[288] S. K. Georgantzinos, D. E. Katsareas, and N. K. Anifantis. Limit load analysis of graphene with pinhole defects: A nonlinear structural mechanics approach. *Int. J. Mech. Sci.*, 55:85, 2012. doi: 10.1016/j.ijmecsci.2011.12.006.

[289] N. Jing, Q. Xue, C. Ling, M. Shan, T. Zhang, X. Zhoub, and Z. Jiaob. Effect of defects on Young's modulus of graphene sheets: A molecular dynamics simulation. *Rsc Adv.*, 2:9124, 2012. doi: 10.1039/C2RA21228E.

[290] Curie supercomputer web. http://www-hpc.cea.fr/en/complexe/tgcc-curie.htm.

[291] O. Lehtinen, I.-L. Tsai, R. Jalil, R. R. Nair, J. Keinonen, U. Kaiser, and I. V. Grigorieva. Non-invasive transmission electron microscopy of vacancy defects in graphene produced by ion irradiation. *Nanoscale*, 6:6569, 2014. doi: 10.1103/PhysRevB.90.014401.

[292] S. Nosé. A Unified Formulation of the Constant Temperature Molecular Dynamics Methods. *J. Chem. Phys.*, 81(1):511–519, 1984. doi: 10.1063/1.447334.

[293] S. Nosé. A Molecular Dynamics Method for Simulations in the Canonical Ensemble. *Mol. Phys.*, 52(2):255–268, 1984. doi: 10.1080/00268978400101201.

[294] W. G. Hoover. Canonical Dynamics: Equilibrium Phase-space Distributions. *Phys. Rev. A*, 31:1695–1697, 1985. doi: 10.1103/PhysRevA.31.1695.

[295] R. Khare, S. L. Mielke, J. T. Paci, S. Zhang, R. Ballarini, G. C. Schatz, and T. Belytschko. Coupled quantum mechanical/molecular mechanical modeling of the fracture of defective carbon nanotubes and graphene sheets. *Phys. Rev. B*, 75:075412, 2007. doi: 10.1103/PhysRevB.75.075412.

[296] O. L. Blakslee, D. G. Proctor, E. J. Seldin, G. B. Spence, and T. Weng. Elastic constants of compression-annealed pyrolytic graphite. *Journal of Applied Physics*, 41(8):3373–3382, 1970. doi: 10.1063/1.1659428.

[297] L. A. Girifalco and R. A. Lad. Energy of Cohesion, Compressibility, and the Potential Energy Functions of the Graphite System. *J. Chem. Phys.*, 25(4):693–697, 1956. doi: 10.1063/1.1743030.

[298] G. López-Polín, M. Jaafar, F. Guinea, R. Roldán, C. Gómez-Navarro, and Gómez-Herrero J. Strain dependent elastic modulus of graphene. *arXiv:1504.05521*.

[299] R. Roldán, A. Fasolino, K. V. Zakharchenko, and M. I. Katsnelson. Suppression of anharmonicities in crystalline membranes by external strain. *Phys. Rev. B*, 83:174104, 2011. doi: 10.1103/PhysRevB.83.174104.

[300] K. V. Zakharchenko, M. I. Katsnelson, and Fasolino A. Finite Temperature Lattice Properties of Graphene beyond the Quasiharmonic Approximation. *Phys. Rev. Lett.*, 102:046808, 2011. doi: 10.1103/PhysRevLett.102.046808.

[301] Stephen R. Forrest. Ultrathin Organic Films Grown by Organic Molecular Beam Deposition and Related Techniques. *Chem. Rev.*, 97(6):1793–1896, 1997. doi: 10.1021/cr941014o.

[302] J. V. Barth, G. Costantini, and K. Kern. Engineering atomic and molecular nanostructures at surfaces. *Nature*, 437(7059):671–9, 2005. doi: 10.1038/nature04166.

[303] F. Schreiber. Structure and growth of self-assembling monolayers. *Prog. Surf. Sci.*, 65(5-8):151–257, 2000. doi: 10.1016/S0079-6816(00)00024-1.

[304] D. K. Schwartz. Mechanisms and kinetics of self-assembled monolayer formation. *Annu. Rev. Phys. Chem.*, 52(1):107–137, 2001. doi: 10.1146/annurev.physchem.52.1.107.

[305] H. Y. Mao, Y. H. Lu, J. D. Lin, S. Zhong, A. T. S. Wee, and W. Chen. Manipulating the Electronic and Chemical Properties of Graphene via Molecular Functionalization. *Prog. Surf. Sci.*, 88(2):132–159, 2013. doi: 10.1016/j.progsurf.2013.02.001.

[306] L. Kong, A. Enders, T. S. Rahman, and P. A. Dowben. Molecular adsorption on graphene. *J. Phys.: Condens. Matter*, 26(44):443001, 2014. doi: 10.1088/0953-8984/26/44/443001.

[307] J. D. Wuest and A. Rochefort. Strong adsorption of aminotriazines on graphene. *Chem. Commun.*, 46:2923–2925, 2010. doi: 10.1039/B926286E.

[308] H. Bin, Q. Yong, and C. Quan-Shui. DFT Study on the Effect of Hydrogen-bond Formation on the Adsorption of Aminotriazines on Graphene. *Chinese Journal Of Structural Chemistry*, 30(12):1742–1750, 2011.

[309] C.-H. Chang, X. Fan, L.-J. Li, and J.-L. Kuo. Band Gap Tuning of Graphene by Adsorption of Aromatic Molecules. *J. Phys. Chem. C*, 116(25):13788–13794, 2012. doi: 10.1021/jp302293p.

[310] W. Zhang, C.-T. Lin, K.-K. Liu, T. Tite, C.-Y. Su, C.-H. Chang, Y.-H. Lee, C.-W. Chu, K.-H. Wei, J.-L. Kuo, and L.-J. Li. Opening an Electrical Band Gap of Bilayer Graphene with Molecular Doping. *ACS nano*, 5(9):7517–24, 2011. doi: 10.1021/nn202463g.

[311] F. Huttmann, A. J. Martínez-Galera, V. Caciuc, N. Atodiresei, S. Schumacher, S. Standop, I. Hamada, T. O. Wehling, S. Blügel, and T. Michely. Tuning the van der waals interaction of graphene with molecules via doping. *Phys. Rev. Lett.*, 115:236101, 2015. doi: 10.1103/PhysRevLett.115.236101.

[312] R. Zacharia, H. Ulbricht, and T. Hertel. Interlayer cohesive energy of graphite from thermal desorption of polyaromatic hydrocarbons. *Phys. Rev. B*, 69:155406, 2004. doi: 10.1103/PhysRevB.69.155406.

[313] S. D. Chakarova-Käck, E. Schröder, B. I. Lundqvist, and D. C. Langreth. Application of van der waals density functional to an extended system: Adsorption of benzene and naphthalene on graphite. *Phys. Rev. Lett.*, 96:146107, 2006. doi: 10.1103/PhysRevLett.96.146107.

[314] K. Berland and P. Hyldgaard. Analysis of van der waals density functional components: Binding and corrugation of benzene and c_{60} on boron nitride and graphene. *Phys. Rev. B*, 87:205421, 2013. doi: 10.1103/PhysRevB.87.205421.

[315] A. Martín-Recio, A. J. Martínez-Galera, and J. M. Gómez-Rodríguez. Surface diffusion of azabenzene s-triazine molecules on a strong interacting graphene-metal system. *J. Phys. Chem. C*, 119(1):401–406, 2015. doi: 10.1021/jp509973v.

[316] R. Dovesi, R. Orlando, A. Erba, C. M. Zicovich-Wilson, B. Civalleri, S. Casassa, L. Maschio, M. Ferrabone, M. De La Pierre, P. D'Arco, Y. Noël, M. Causà, M. Rerat, and Kirtman B. CRYSTAL14: A Program for the *Ab Initio* Investigation of Crystalline Solids. *Int. J. Quantum Chem.*, 114:1287, 2014. doi: 10.1002/qua.24658.

[317] R. Dovesi, V. R. Saunders, C. Roetti, R. Orlando, C. M. Zicovich-Wilson, F. Pascale, B. Civalleri, K. Doll, N. M. Harrison, I. J. Bush, P. D'Arco, M. Causà M. Llunell, and Y. Noël. *CRYSTAL14 User's Manual (University of Torino, Torino, 2014)*.

[318] G. Kresse and D. Joubert. From Ultrasoft Pseudopotentials to the Projector Augmented-Wave Method. *Phys. Rev. B*, 1999:1758, 59. doi: 10.1103/PhysRevB.59.1758.

[319] P. Lazar, J. Granatier, J. Klimeš, P. Hobzab, and M. Otyepka. The Nature of Bonding and Electronic Properties of Graphene and Benzene with Iridium Adatoms. *Phys. Chem. Chem. Phys.*, 16:20818, 2014. doi: 10.1039/c4cp02608j.

[320] A. Dewaele, P. Loubeyre, and M. Mezouar. Equations of State of Six Metals above 94 GPa. *Phys. Rev. B*, 70:094112, 2004. doi: 10.1103/PhysRevB.70.094112.

[321] R. Zan, Q. M. Ramasse, R. Jalil, and U. Bangert. Atomic Structure of Graphene and h-BN Layers and Their Interactions with Metals. In M. Aliofkhazraei, editor, *Advances in Graphene Science*, page InTech. World Scientific, 2013. doi: 10.5772/56640.

[322] P. Sutter, J. T. Sadowski, and E. Sutter. Graphene on Pt(111): Growth and Substrate Interaction. *Phys. Rev. B*, 80:245411, 2009. doi: 10.1103/PhysRevB.80.245411.

[323] G. Mills, H. Jónsson, and G. K. Schenter. Reversible work transition state theory: Application to dissociative adsorption of hydrogen. *Surf. Sci.*, 324:305–337, 1995. ISSN 0039-6028. doi: 10.1016/0039-6028(94)00731-4.

[324] H. Jónsson, G. Mills, and K. W. Jacobsen. Nudged elastic band method for finding minimum energy paths of transitions. In B. J. Berne, G. Ciccotti, and D. F. Coker, editors, *Classical and Quantum Dynamics in Condensed Phase Simulations*, page 385. World Scientific, 1998.

[325] H. Hedgeland, P. Fouquet, A. P. Jardine, G. Alexandrowicz, W. Allison, and J. Ellis. Measurement of Single-molecule Frictional Dissipation in a Prototypical Nanoscale System. *Nat. Phys.*, 5:561–564, 2009. doi: 10.1038/nphys1335.